Adsorption of Atoms and Molecules on Surfaces: Density-Functional Theory with Screened van der Waals Interactions

VICTOR GONZALO RUIZ LÓPEZ

MAX-PLANCK-GESELLSCHAFT
Fritz-Haber-Institut

BERLIN • 2016

Adsorption of Atoms and Molecules on Surfaces: Density-Functional Theory with Screened van der Waals Interactions

vorgelegt von
M.Sc.
Victor Gonzalo Ruiz López
geb. in Mexiko Stadt

der Fakultät II Mathematik und Naturwissenschaften
der Technischen Universität Berlin
zur Erlangung des akademischen Grades

Doktor der Naturwissenschaften
Dr.rer.nat

genehmigte Dissertation

Promotionsausschuss:

Vorsitzender: Prof. Dr. Mario Dähne
1. Gutachter: Prof. Dr. Eckehard Schöll
2. Gutachter: Prof. Dr. Alexandre Tkatchenko
Tag der wissenschaftlichen Aussprache: 18. Mai 2016

Berlin – 2016

Abstract

Understanding the properties of novel hybrid interfaces has implications in both fundamental science and technology. The interfaces of hybrid inorganic/organic systems (HIOS), for instance, may lead to the emergence of collective effects that the isolated components forming the interface do not exhibit. The electronic properties and the function of these interfaces are intimately linked to their interface geometry. The interface structure and its properties are a result of the interplay of electron transfer processes, (covalent) hybridization of wave functions, van der Waals (vdW) interactions, and Pauli repulsion. In particular, vdW interactions are fundamental in determining the structure of the interface and the stability of HIOS. Thus, controlling the functionalities of HIOS involves as a first step the prediction and understanding of the structural features of the interface. Since the role of vdW interactions is crucial in the determination of the structural features and stability, their accurate prediction becomes distinctively relevant in this context. From an atomistic perspective within the computational simulation of materials, it follows that modeling the adsorption of atoms and molecules on surfaces requires efficient electronic-structure methods that are able to capture both covalent and non-covalent interactions in a reliable manner.

It is in this context that we propose a method within density-functional approximations (DFA) which includes screened vdW interactions (the so-called DFA+vdW$^{\text{surf}}$ method) to model the adsorption of atoms and molecules on surfaces. Specifically, we combine dispersion-corrected density-functional approximations (the Tkatchenko-Scheffler DFA+vdW method) with the Lifshitz-Zaremba-Kohn theory in order to include the Coulomb screening within the substrate surface in the determination of the vdW C_6 coefficients and vdW radii. Our method includes both image-plane and interface polarization effects via the inclusion of semi-local hybridization due to the dependence of the C_6^{ab} interatomic parameters on the electron density. We show that the inclusion of the non-local many-body response of the substrate electrons is essential to predict the structure and stability of atoms and molecules on surfaces in a reliable manner, taking as examples the adsorption of a Xe monolayer and an aromatic molecule which includes oxygen in its structure.

In particular, we show that the DFA+vdW$^{\text{surf}}$ method yields geometries in remarkable agreement (within approximately 0.1 Å) with normal incidence x-ray standing wave measurements for the adsorption of 3,4,9,10-perylene-tetracarboxylic dianhydride ($C_{24}H_8O_6$, PTCDA) on Ag(111), Au(111), and Cu(111). Additional examples include the

adsorption of Xe on transition-metal surfaces and a comparative study of the interfaces formed by a PTCDA monolayer on the Ag(111), Ag(100), and Ag(110) surfaces, showing that the method also achieves surface-termination sensitivity. These results demonstrate that the DFA+vdW^{surf} method can deal in a reliable manner with a wide range of interactions at HIOS including chemical interactions, electrostatic interactions, Pauli repulsion, and vdW interactions; therefore establishing it as a reasonable option for the accurate treatment of adsorption problems due to its efficiency and affordability in terms of computational time. Nevertheless, cooperative electronic effects between atoms in larger molecules lead to non-additive molecular polarizabilities, effect which is absent in the DFA+vdW^{surf} method. I conclude by commenting this and further remaining challenges left in order to achieve both quantitative accuracy and predictive power in the simulation of the structure and stability of complex interfaces.

Zusammenfassung

Das Verständnis der Eigenschaften von neuartigen Hybrid-Grenzflächen ist sowohl für die Grundlagenforschung als auch für technologische Anwendungen wichtig. Die Grenzflächen von hybriden anorganischen/organischen Systemen (HIOS) führen zum Beispiel zur Entstehung von kollektiven Effekten, welche die isolierten Bausteine nicht besitzen. Die elektronischen Eigenschaften und die Funktionen dieser Grenzflächen hängen stark von ihrer Geometrie ab. Die Grenzflächenstruktur und ihre Eigenschaften resultieren aus dem Wechselspiel zwischen Elektronentransferprozessen, (kovalenter) Hybridisierung von Wellenfunktionen, van-der-Waals-Wechselwirkungen (vdW) und der Pauli-Abstoßung. Die vdW-Wechselwirkungen sind entscheidend für die Struktur und die Stabilität der HIOS. Um schlussendlich die Funktionalitäten der HIOS kontrollieren zu können, ist als erster Schritt die Vorhersage und das Verständnis von strukturellen Merkmalen der Grenzfläche notwendig. Aufgrund der bedeutenden Rolle der vdW-Wechselwirkungen in diesem Kontext ist es besonders wichtig diese Wechselwirkungen präzise berechnen zu können. Von einer atomistischen Perspektive benötigt die Computersimulation der Adsorption von Atomen und Molekülen auf Oberflächen effiziente Elektronenstrukturmethoden, die in der Lage sind sowohl kovalente also auch nichtkovalente Wechselwirkungen verlässlich zu beschreiben.

In diesem Kontext stellen wir eine Methode im Bereich der Dichtefunktionalnäherungen (DFA) vor, die abgeschirmte vdW-Wechselwirkungen beinhaltet (DFA+vdW$^{\text{surf}}$), um die Adsorption von Atomen und Molekülen auf Oberflächen zu modellieren. Im Besonderen kombinieren wir dispersionskorrigierte Dichtefunktionalnäherungen (die Tkatchenko-Scheffler DFA+vdW Methode) mit der Lifshitz-Zaremba-Kohn-Theorie um die Coulomb-Abschirmung innerhalb der Substratoberfläche bei der Berechnung der vdW-C_6-Koeffizienten und vdW-Radien zu berücksichtigen. Unsere Methode inkludiert sowohl Polarisationseffekte der Bildebene und der Grenzfläche durch semilokale Hybridisierung aufgrund der Abhängigkeit der interatomaren C_6^{ab}-Parameter von der Elektronendichte. Wir zeigen, dass die Berücksichtigung der semilokalen Mehrteilchenantwort der Substratelektronen essentiell für eine zuverlässige Vorhersage der Struktur und Stabilität der Atome und Moleküle auf der Oberfläche ist. Als Beispiele verwenden wir die Adsorption einer Xe-Monolage und eines aromatischen Moleküls, das Sauerstoffatome beinhaltet.

Im Speziellen demonstrieren wir, dass die DFA+vdW$^{\text{surf}}$-Methode für die Adsorption von 3,4,9,10-Perylentetracarbonsäuredianhydrid ($C_{24}H_8O_6$, PTCDA) auf Ag(111),

Au(111) und Cu(111) Geometrien liefert, die bemerkenswert gut (innerhalb von etwa 0.1 Å) mit *normal incidence x-ray standing wave* Messunge übereinstimmen. Weitere Beispiele beinhalten die Adsorption von Xe auf übergangsmetall-Oberflächen und eine vergleichende Studie der Grenzflächen, die von einer PTCDA-Monolage auf Ag(111), Ag(100) und Ag(110)-Oberflächen gebildet werden, um zu zeigen, dass diese Methode Oberflächenempfindlichkeit aufweist. Diese Resultate demonstrieren, dass die DFA+vdW$^{\text{surf}}$-Methode verlässlich mit einer großen Bandbreite von Wechselwirkungen der HIOS (chemische Wechselwirkungen, elektrostatische Wechselwirkungen, Pauli-Abstoßung und vdW-Wechselwirkungen) umgehen kann. Daher stellt sie durch ihre Effizienz und Leistbarkeit im Bezug auf Rechenzeit eine vernünftige Option für die präzise Beschreibung von Adsorptionsproblemen dar. Allerdings führen kooperative elektronische Effekte zwischen Atomen in größeren Molekülen zu einer Nicht-Additivität der molekularen Polarisierbarkeiten. Dieser Effekt wird in der DFA+vdW$^{\text{surf}}$ Methode nicht berücksichtigt. Abschließend wird dies und andere verbleibende Herausforderungen für die Erzielung von quantitativer Genauigkeit und Vorhersagekraft bei der Simulation von der Struktur und Stabilität komplexer Grenzflächen diskutiert.

Acknowledgements

I would first like to express my gratitude to my supervisor Alexandre Tkatchenko for his continuous support and invaluable contributions, specially during the last stages, of my doctoral research project. The way he solves complex problems using (relative) simple concepts is the reason for the success of this project. I would also like to thank Matthias Scheffler for giving me the opportunity of pursuing my Ph.D. studies at the Theory Department of the Fritz-Haber-Institut, letting me accomplish an important personal aspiration in my professional life. My sincere gratitude also goes to Wei Liu, whose contributions were key for the success of this project. I would also like to thank Guo-Xu Zhang, Oliver Hofmann, David Egger, and Egbert Zojer for their valuable collaboration and insights throughout the progress of this project.

I would also like to take this opportunity to thank my teachers Rossitza Pentcheva, Nikolaj Moll, and Jan Minar for their help during the transition to my Ph.D. studies and their support beyond that. I also want to express my special gratitude to the members of our group in the department for making all these years special, in particular Nicola, Vivek, Wael, and Johannes for we have shared a very similar path.

Finally and most important, I want to express my special and heartfelt thanks to my family –my parents and my brother– for their tremendous support since I've left Mexico; and my dear girlfriend Isa for her love, patience, and support in these last years. My achievements would mean nothing without them.

VICTOR GONZALO RUIZ LÓPEZ
Berlin
June 2016

Contents

List of Figures

List of Tables

CHAPTER

1 Introduction

It is hard to imagine the world of today without the influence of surface science. In 1909 Fritz Haber developed a catalytic process for the synthesis of ammonia from its constituent elements. His process was later refined and industrially scaled by Carl Bosch and Alwin Mittasch at BASF realizing its potential in the agricultural and military industries while also laying the foundations of modern industrial chemistry [James *et al.*, 2011]. The Haber-Bosch process has been a central process in today's industrial chemistry for a century, supplying the world agriculture with a large-scale production of fertilizers and thus contributing with the food supply for a growing world population [James *et al.*, 2011].

This little extract of history of science, which interestingly initiated at the research institute where this dissertation has been written, shows us the major role that modern surface science has in the world of today. The physical and chemical processes occurring at surfaces have significant implications for basic science and technological applications. In this context, the central topic of the research leading to this dissertation has been the theoretical study of adsorption phenomena at interfaces formed between organic matter (in our case typically comprised by organic aromatic molecules) and inorganic substrates. The main challenge in modeling the adsorption of atoms and molecules on surfaces is developing efficient electronic-structure methods that are able to capture both covalent and non-covalent interactions in a reliable manner. In particular, we focus on the role of collective effects –up to now often underestimated or simply ignored– in the van der Waals (vdW) interaction of molecules on surfaces, aiming for an accurate description of the structure and stability of these complex systems in the context of density-functional theory (DFT).

1.1 Van der Waals interactions in hybrid inorganic/organic systems

Understanding the electronic properties of hybrid inorganic/organic systems (HIOS) has implications in both fundamental science and technology. In terms of basic science, these interfaces may lead to the emergence of collective effects that the isolated components forming the interface do not exhibit [Kronik and Koch, 2010; Cahen *et al.*, 2005]. Among these effects, Kronik and Koch [2010] mention the emergence of magnetic phenomena at the interface formed by non-magnetic components (including closed-shell

molecular layers), localization of electron-hole pairs at the interface, and electronic or transport properties of molecular ensembles that differ from those of the isolated molecule(s) [see references within Kronik and Koch, 2010].

The eventual control of the function of HIOS has also substantial technological importance. Organic light emitting diodes, organic thin film transistors, and low cost and efficient organic solar cells are examples of emerging technologies based on organic thin films, which some of them are now reaching the consumer market [Forrest and Thompson, 2007; Kronik and Koch, 2010]. Potential future applications also include organic memories and chemical sensors [Forrest and Thompson, 2007; Kronik and Koch, 2010]. The performance and future design of these devices are clearly related to the electronic properties of the interface in which the interface geometry plays a fundamental role [Duhm *et al.*, 2008; Tkatchenko *et al.*, 2010]. A balanced description of both the structural and electronic properties of these interfaces is thus critical for controlling their functionality.

The interface properties that HIOS exhibit, including their interface structure, are a result of the interplay of electron transfer processes, (covalent) hybridization of wave functions, van der Waals (vdW) interactions, and Pauli repulsion. In particular, vdW forces play an essential part in the structure and stability of these systems [Tkatchenko *et al.*, 2010; Atodiresei *et al.*, 2009; Mercurio *et al.*, 2010; Stradi *et al.*, 2011; Olsen *et al.*, 2011; McNellis, 2010; Lazić *et al.*, 2014]. It becomes clear that controlling the functionalities of HIOS involves as a first step the prediction and understanding of the structural features of the interface as these features will determine the electronic properties. It is in this regard where the accurate prediction of vdW forces becomes distinctively relevant since their role in the determination of the structural features and stability is crucial.

In this context, DFT has become the method of choice in the calculation of interfaces and adsorption phenomena due to its good compromise between accuracy and efficiency. Unfortunately, modeling vdW interactions in DFT is not an easy task as standard density-functional approximations (DFA) within DFT do not include them properly. In this regard, the role of vdW interactions in the binding between small molecules in the gas phase has been extensively studied and is fairly well understood. Unlike standard DFA, the hierarchy of methods in quantum chemistry can describe vdW interactions properly; but recent years have also seen the development of several promising vdW-inclusive schemes in DFT [see Klimeš *et al.*, 2012; Tkatchenko *et al.*, 2010, for a concise review of vdW-inclusive methods in DFT]. Nevertheless, we have observed that their application to HIOS is questionable due to either the absence or inaccuracy of the nonlocal (inhomogeneous) collective electron response of the extended surface in the vdW energy. This problem has been exemplified in previous publications for the case of the adsorption of 3,4,9,10-perylene-tetracarboxylic dianhydride (PTCDA, chemical formula: $C_{24}H_8O_6$) on coinage metal surfaces [Rohlfing and Bredow, 2008; Rohlfing *et al.*, 2007; Romaner *et al.*, 2009; McNellis, 2010; Tkatchenko *et al.*, 2010; Ruiz *et al.*, 2012] and in general for other adsorption systems [Nguyen *et al.*, 2010; Olsen *et al.*, 2011; Stradi *et al.*, 2011; Atodiresei *et al.*, 2009; Mercurio *et al.*, 2010; Lüder *et al.*, 2014].

It follows from this evidence that modeling HIOS requires efficient methods that are able to describe a range of interactions in an accurate manner. The main contribution that we present in this dissertation is regarding this particular issue. We have developed a method within DFT, the DFA+vdW$^{\text{surf}}$ method [Ruiz *et al.*, 2012], to model *screened* vdW interactions for the adsorption of atoms and molecules which incorporates the col-

lective response of the substrate electrons in vdW-inclusive DFT for intermolecular interactions.

The DFA+vdW^{surf} method combines the Lifshitz-Zaremba-Kohn (LZK) theory [Lifshitz, 1956; Zaremba and Kohn, 1976] for the inclusion of the non-local collective response of the substrate surface in the vdW energy with the Tkatchenko-Scheffler (TS) method [Tkatchenko and Scheffler, 2009] for intermolecular interactions. We have demonstrated with this method that the collective response of the substrate electrons can modify vdW coefficients in HIOS by up to an order of magnitude [see for example section 4.4 or Ruiz *et al.*, 2012]. Calculations using this method have demonstrated that the inclusion of these collective effects, which effectively go beyond an atom-based pairwise description of vdW interactions, is essential to describe the binding properties of HIOS. As a vdW-inclusive DFT method, the DFA+vdW^{surf} method has allowed us to cover a wide range of interactions in the adsorption of molecules on surfaces. These include, for example, the adsorption of a Xe monolayer, aromatic molecules (benzene and derivatives, naphthalene, anthracene, azobenzene, diindenoperylene, and olympicene and derivatives), C_{60}, aromatic molecules including sulfur/oxygen such as thiophene, NTCDA, and PTCDA on several close-packed transition-metal surfaces [Ruiz *et al.*, 2012; Liu *et al.*, 2012; van Ruitenbeek, 2012; Liu *et al.*, 2013b; Bürker *et al.*, 2013; Mercurio *et al.*, 2013b; Schuler *et al.*, 2013; Liu *et al.*, 2013a, 2014]. A study of a Cu-phthalocyanine film on a PTCDA monolayer adsorbed on Ag(111) has also been published recently [Egger *et al.*, 2013]. It is also worth mentioning that Camarillo-Cisneros *et al.* [2015] have studied the adsorption, diffusion, and desorption of benzene and naphthalene on a vicinal Cu(443) surface, showing that the accuracy of the method also extends to adsorption on stepped substrates.

The work we present here forms part of a stimulating context taking place recently in surface science where the emergence of novel single-molecule experiments and theoretical predictions, in which accuracy and further understanding are the main goals, have been received with interest by the scientific community; as evidenced, for example, in the short article "Dispersion forces unveiled" by van Ruitenbeek [2012]. For instance, recent single-molecule experiments have aimed to illustrate and quantify the –often underestimated or ignored– role of dispersion forces in molecule/metal interfaces, work in which we have collaborated from the theoretical perspective [Wagner *et al.*, 2014]. More specifically, the methods that we present in this work have also contributed in illustrating the effects of non-additive vdW contributions in organic/metal interfaces while also testing the asymptotic vdW force law and its validity range.

In short, this work is part of a larger effort trying to develop methods that are able to give a balanced description of adsorption phenomena while treating realistic adsorption systems. This development is still experiencing its early phases, but we expect that our contribution together with the inclusion of all relevant collective many-body effects should take surface science in general and modeling of HIOS in particular to an unprecedented level of accuracy, enabling us to achieve a truly predictive power in the simulation of the structure and stability of complex HIOS.

This dissertation is structured in the following way. Part I contains the description of the theory and methods used (some of them developed) in this work. It starts in chapter 2 by giving a brief introduction of the theoretical background underlying the atomistic methods that we employ to treat molecules interacting with surfaces including DFT, a brief review of vdW interactions in the context of DFT, and a review of vdW interactions

in solids with an emphasis on metals. Part I ends in chapter 3 with a short review of experimental techniques used to analyze the structure and stability of adsorption systems. Part II, which includes chapter 4, is in many ways the central part of this work containing also its original contribution. It starts motivating the need of accurate vdW-inclusive methods to model the structure and energetic stability of HIOS. To this end, we describe the performance of several vdW-inclusive methods in DFT using one of the best experimentally and theoretically characterized inorganic/organic interfaces –the adsorption of PTCDA on Ag(111). This is followed by a review of the general theory of vdW interactions including the particular case of the atom-surface vdW interaction. As we progress in the chapter, we discuss the relation between vdW pairwise interactions and the case of atom-surface vdW interaction as this relation underlines the DFA+vdW^{surf} method. We conclude chapter 4 with a detailed description of the DFA+vdW^{surf} method.

Part III contains the applications of this new methodology to the adsorption of atoms and molecules on surfaces. Chapter 5 briefly revisits the adsorption of PTCDA on Ag(111) as a first example of performance with the DFA+vdW^{surf} method, it also introduces and analyzes the adsorption of a single PTCDA molecule on Au(111) as an example of physisorption in an inorganic/organic interface. It is also important to indicate that the adsorption of noble gases on metal surfaces are prototypical examples of adsorption phenomena where the main attractive forces are given by long-range vdW interactions. More interesting is the fact that they have been studied extensively in experiments [Vidali *et al.*, 1991; Diehl *et al.*, 2004; Bruch *et al.*, 2007, 1997] and theory [Da Silva *et al.*, 2003, 2005; Chen *et al.*, 2011, 2012; Bruch *et al.*, 1997]. Because of their status as benchmark systems for physisorption in vdW-inclusive DFT methods, in chapter 6 we focus on the study of the energetics and structure of the adsorption of Xe on selected transition metal surfaces with the DFA+vdW^{surf} method.

In chapter 7 we finally address in more detail the structure and stability of HIOS, topic which is fundamental to our motivation. Chapter 7 includes an in-depth study of the adsorption structure found in the cases of PTCDA on the Ag(111), Au(111), and Cu(111) close-packed metal surfaces, as well as their energetic stability. In order to analyze the adsorption of an organic adsorbate on a metal surface with different orientations, this chapter also includes the adsorption of an organic monolayer on non-close-packed surfaces. As study case, we take the interface formed by the adsorption of a PTCDA monolayer on the Ag(111), Ag(100), and Ag(110) surfaces and investigate their adsorption structure and energetic stability. We conclude this dissertation in chapter 8 with a summary of our research where we also mention the outstanding challenges that we still face to achieve a truly predictive power in the simulation of the structure and stability of complex HIOS and adsorption phenomena in general.

Part I

Theory and Methods

CHAPTER

2 The many-body problem

The goal behind this dissertation is the first-principles modeling of van der Waals interactions to study the structure and stability of molecules adsorbed on solid surfaces. For this purpose, we require accurate methods that are able to describe efficiently the microscopic properties of surfaces and molecules in an accurate manner. With this idea in mind, in this chapter we briefly introduce the theoretical background behind the atomistic methods required to treat molecules interacting with surfaces.

We start with the basic concepts behind the theoretical description of molecules and solids that lead to the introduction of the electronic problem and electronic-structure theory. In this context, our next step is to introduce density-functional theory as it constitutes our main tool in electronic-structure theory due to its favorable compromise between accuracy and efficiency. Finally, we examine some general ways of including van der Waals interactions within the context of density-functional theory.

The following discussion is mainly based on the monographs by Parr and Yang [1989]; Kohanoff [2006]; Martin [2004]; and Engel and Dreizler [2011]. The reader is referred to these references for an extended treatment of the subjects here presented.

2.1 The Hamiltonian

In general, any molecule or solid can be thought of as an ensemble of interacting atoms. At the microscopic scale, molecules and solids can be unambiguously described as a collection of atomic nuclei and electrons that interact via Coulombic electrostatic forces. The Hamiltonian of such a system with P nuclei and N electrons has the following general form

$$\begin{aligned}\hat{\mathscr{H}} = &-\frac{\hbar^2}{2M_I}\sum_I \nabla_I^2 - \frac{\hbar^2}{2m_e}\sum_i \nabla_i^2 + \frac{e^2}{2}\sum_{I\neq J}\frac{Z_I Z_J}{|\boldsymbol{R}_I - \boldsymbol{R}_J|} \\ &+ \frac{e^2}{2}\sum_{i\neq j}\frac{1}{|\boldsymbol{r}_i - \boldsymbol{r}_j|} - e^2\sum_{i,I}\frac{Z_I}{|\boldsymbol{r}_i - \boldsymbol{R}_I|},\end{aligned} \tag{2.1}$$

where $\boldsymbol{R} = \{\boldsymbol{R}_I,\ I = 1,\ldots,P\}$ is a set of P nuclear coordinates, and $\boldsymbol{r} = \{\boldsymbol{r}_i,\ i = 1,\ldots,N\}$ is a set of N electron coordinates. Z_I and M_I denote the nuclear charges and masses, respectively and m_e is the mass of an electron. The first and second terms in (2.1) are the kinetic energy of the nuclei and electrons, respectively. The last three terms describe the Coulomb interaction between nuclei, between electrons, and between nuclei and

electrons, respectively. In principle, most physical and chemical properties of molecules and solids can be obtained by solving the time-independent many-body Schrödinger equation using the Hamiltonian in (2.1)

$$\hat{\mathscr{H}}\Phi(\boldsymbol{R},\boldsymbol{r}) = \mathscr{E}\Phi(\boldsymbol{R},\boldsymbol{r}), \tag{2.2}$$

where $\mathscr{E}$ is called the total energy and $\Phi(\boldsymbol{R},\boldsymbol{r})$ is the wave function of the system. In solving (2.2), we must take into account the appropriate quantum statistics of the involved particles. Since the electrons are fermions, the electronic wave function must be antisymmetric with respect to the interchange of both the space and spin coordinates of any two electrons. Different nuclear species are distinguishable, but nuclei of the same species can be either bosons or fermions, determining the symmetric or antisymmetric character of the nuclear wave function. In surface science however, the symmetry of the nuclei does not usually play an important role [Groß, 2009].

All the ingredients in the Schrödinger equation are in principle well known. In practice however, it is impossible to solve it analytically with the exception of a few simple cases such as hydrogenoid atoms or the H_2^+ molecule [Kohanoff, 2006]. The most important complications in (2.2) arise from the many-body character of the wave function and the non-linear nature of the Coulomb interaction, making the Schrödinger equation not separable. It is necessary to take into account some approximations to make (2.2) tractable. The first one in this hierarchy of approximations is the Born-Oppenheimer approximation.

2.2 The Born-Oppenheimer approximation

The first major approximation, which is expected to have validity for an important class of systems, consists in decoupling the dynamics of electrons and nuclei. The central idea is that nuclei move more slowly than electrons since they are much heavier. Following this reasoning, Born and Oppenheimer first proposed in 1927 [as cited by Kohanoff, 2006] a scheme to separate the motion of nuclei and electrons. They showed that under certain conditions, the electrons do not undergo transitions between stationary states, which is called the adiabatic approximation. To a good approximation, the electrons are thought as to be in motion in the field of fixed nuclei while staying in their ground state for any configuration of the nuclei. The Born-Oppenheimer approximation serves as an excellent approximation for many purposes in quantum chemistry and computational materials science. It also forms the starting point for perturbation theory in electron-phonon interactions in solids [Martin, 2004; Szabo and Ostlund, 1996].

Following this approximation, the kinetic energy of the nuclei can be neglected and the repulsion of the nuclei can be considered as constant in (2.1). The remaining terms in (2.1) form the electronic Hamiltonian which describes the motion of electrons in the field of P point charges

$$\hat{H} = \hat{T} + \hat{U}_{\mathrm{ee}} + \hat{V}_{\mathrm{ne}}, \tag{2.3}$$

where $\hat{T}$ is the electronic kinetic operator, $\hat{U}_{\mathrm{ee}}$ is the electron-electron interaction, and $\hat{V}_{\mathrm{ne}}$ is the electron-nuclear interaction. The electronic wave function and the energy are then obtained via the solution of the electronic Schrödinger equation

$$\hat{H}\Psi(\boldsymbol{R};\boldsymbol{r}) = E(\boldsymbol{R})\Psi(\boldsymbol{R};\boldsymbol{r}). \tag{2.4}$$

In (2.4), the electronic wave function $\Psi(\boldsymbol{R};\boldsymbol{r})$ and the electronic energy $E(\boldsymbol{R})$ depend both *parametrically* on the $3P$ nuclear coordinates $\boldsymbol{R}$. This means that the electronic wave function is a different function depending on the arrangement of the nuclei and that we must solve (2.4) for all different nuclear configurations. The total energy for a fixed arrangement of nuclei must also include the constant nuclear repulsion V_{nn} [Szabo and Ostlund, 1996]

$$\mathscr{U} = E + V_{\mathrm{nn}}, \tag{2.5}$$

where

$$V_{\mathrm{nn}} = \frac{e^2}{2} \sum_{I \neq J} \frac{Z_I Z_J}{|\boldsymbol{R}_I - \boldsymbol{R}_J|}. \tag{2.6}$$

Equations (2.3)–(2.6) constitute the fundamental equations for the theory of electronic structure. By solving the electronic problem, the nuclear problem can also be solved under the same assumptions. If the electrons move much faster than the nuclei, the electronic coordinates of the Hamiltonian given in (2.1) can be reasonably approximated by taking their values averaged over the electronic wave function [Szabo and Ostlund, 1996]. We can thus assume that the motion of the nuclei in the average field of the electrons follows the Schrödinger equation given by

$$\left[\hat{T}_{\mathrm{n}} + \mathscr{U}(\boldsymbol{R})\right] \Theta(\boldsymbol{R}) = \mathscr{E}_{\mathrm{BO}} \Theta(\boldsymbol{R}), \tag{2.7}$$

where $\hat{T}_{\mathrm{n}}$ is the kinetic energy of the nuclei, $\Theta(\boldsymbol{R})$ is the nuclear wave function, and $\mathscr{E}_{\mathrm{BO}}$ is the Born-Oppenheimer approximation to the total energy in (2.2). Thus, within the Born-Oppenheimer approximation, the nuclei move in the potential energy surface provided by the total energy $\mathscr{U}(\boldsymbol{R})$ which is obtained by solving the electronic problem.

The atomic nuclei can often be treated as *classical* particles hence neglecting the quantum effects involved in their motion [Groß, 2009; Kohanoff, 2006]. This consists in identifying the mean value of the position operator acting on the nuclei with the Cartesian coordinates of the classical particle [Kohanoff, 2006], leading to the equation of motion given by

$$M_I \frac{d^2 \boldsymbol{R}_I(t)}{dt^2} = -\frac{\partial \mathscr{U}(\boldsymbol{R})}{\partial \boldsymbol{R}_I}. \tag{2.8}$$

A final expression for the force acting on the nuclei can be achieved by using the Hellmann-Feynman theorem [see for example Groß, 2009; Kohanoff, 2006; Martin, 2004]

$$\boldsymbol{F}_I = -\frac{\partial \mathscr{U}(\boldsymbol{R})}{\partial \boldsymbol{R}_I} = -\langle \Psi(\boldsymbol{R}) | \frac{\partial \hat{H}(\boldsymbol{R})}{\partial \boldsymbol{R}_I} | \Psi(\boldsymbol{R}) \rangle - \frac{\partial V_{\mathrm{nn}}(\boldsymbol{R})}{\partial \boldsymbol{R}_I}. \tag{2.9}$$

The motion of the nuclei on the potential energy surface is defined by (2.9), its numerical integration using the Newton equation is called *ab initio* molecular dynamics [Kohanoff, 2006]. The minima in the potential energy surface define equilibrium geometries which correspond to the solution of the stationary problem given by $\boldsymbol{F}_I = 0$. The problem of finding the equilibrium geometry is known as a geometry optimization and is equivalent to the mathematical problem of nonlinear unconstrained minimization [Szabo and Ostlund, 1996]. All the *ab initio* single-point molecular simulations and geometry optimizations presented in this dissertation are obtained within the Born-Oppenheimer approximation.

2.3 The electronic problem

As we have established in the previous section, the fundamental equation to study and analyze the structure of matter is the time-independent electronic Schrödinger equation given by

$$\hat{H}|\Psi\rangle = E|\Psi\rangle, \tag{2.10}$$

where $\hat{H}$ is the electronic Hamiltonian

$$\hat{H} = \hat{T} + \hat{U}_{\text{ee}} + \hat{V}_{\text{ext}}, \tag{2.11}$$

and $\hat{V}_{\text{ext}}$ is the interaction with external fields. This term is a generalization of the electron-nuclear interaction $\hat{V}_{\text{ne}}$ defined in (2.3). The many-body wave function is represented by a state vector $|\Psi\rangle$, according to Dirac's bra-ket notation, which is characterized in real space by its projection onto $\langle \boldsymbol{r}|$ given by $\Psi(\boldsymbol{r}) = \langle \boldsymbol{r}|\Psi\rangle$. The main difficulty in solving (2.10) is that electrons interact among themselves via the Coulomb long-range non-linear potential, so the presence of an electron in a region of space will influence the behavior of electrons in other regions. In mathematical terms, it means that the wave function of a many-electron system cannot be simply written as the product of the wave functions of individual electrons [Kohanoff, 2006].

The total energy of the electronic system is the expectation value of the Hamiltonian given by

$$E = \frac{\langle\Psi|\hat{H}|\Psi\rangle}{\langle\Psi|\Psi\rangle}, \tag{2.12}$$

where $|\Psi\rangle$ is the N-electron ground-state wave function. If Ψ is normalized $\langle\Psi|\Psi\rangle = 1$, the expectation value of an operator $\hat{\mathcal{O}}$ in state $|\Psi\rangle$ is given by

$$\langle\hat{\mathcal{O}}\rangle = \langle\Psi|\hat{\mathcal{O}}|\Psi\rangle = \int d\boldsymbol{r}\ \Psi^*(\boldsymbol{r})\hat{\mathcal{O}}\Psi(\boldsymbol{r}). \tag{2.13}$$

In this context, the energy of the electronic system (2.10) with the electronic Hamiltonian given by (2.11) becomes

$$E = \langle\hat{T}\rangle + \langle\hat{U}_{\text{ee}}\rangle + \langle\hat{V}_{\text{ext}}\rangle. \tag{2.14}$$

The electrostatic nuclear repulsion V_{nn} of (2.6) is essential in the total-energy calculation [see (2.5)], but as it only represents a classical additive term in electronic-structure theory [Martin, 2004], we will consistently keep it separated.

In order to provide an expression for each of the terms in (2.14), let us introduce the one- and two-body density matrices in their operator form. They are given, respectively, by [Parr and Yang, 1989; Engel and Dreizler, 2011]

$$\hat{n}_1(\boldsymbol{r},\boldsymbol{r}') = \sum_\sigma \hat{\psi}^\dagger_\sigma(\boldsymbol{r})\hat{\psi}_\sigma(\boldsymbol{r}'), \tag{2.15}$$

$$\hat{n}_2(\boldsymbol{r},\boldsymbol{r}') = \frac{1}{2}\sum_{\sigma,\sigma'} \hat{\psi}^\dagger_\sigma(\boldsymbol{r})\hat{\psi}^\dagger_{\sigma'}(\boldsymbol{r}')\hat{\psi}_{\sigma'}(\boldsymbol{r}')\hat{\psi}_\sigma(\boldsymbol{r}), \tag{2.16}$$

where $\hat{\psi}^\dagger_\sigma(\boldsymbol{r})$ and $\hat{\psi}_\sigma(\boldsymbol{r})$ are the creation and annihilation operators for electrons of spin σ at point $\boldsymbol{r}$. These operators obey the anticommutation relations [Engel and Dreizler,

2011; Kohanoff, 2006; Parr and Yang, 1989]

$$\{\hat{\psi}_\sigma(\boldsymbol{r}), \hat{\psi}_\sigma(\boldsymbol{r})\} = \left\{\hat{\psi}^\dagger_\sigma(\boldsymbol{r}), \hat{\psi}^\dagger_\sigma(\boldsymbol{r}')\right\} = 0, \tag{2.17}$$

$$\left\{\hat{\psi}_\sigma(\boldsymbol{r}), \hat{\psi}^\dagger_{\sigma'}(\boldsymbol{r}')\right\} = \delta_{\sigma\sigma'}\delta(\boldsymbol{r}-\boldsymbol{r}'). \tag{2.18}$$

The diagonal element of $n_1(\boldsymbol{r},\boldsymbol{r}')$ corresponds to the electron density $n(\boldsymbol{r})$ given by

$$\begin{aligned} n(\boldsymbol{r}) &= \left\langle \hat{n}_1(\boldsymbol{r},\boldsymbol{r})\right\rangle \\ &= N \sum_{\sigma_1\ldots\sigma_N} \int \ldots \int d\boldsymbol{r}_2 \ldots d\boldsymbol{r}_N \left|\Psi(\boldsymbol{r}\sigma_1, \boldsymbol{r}_2\sigma_2, \ldots, \boldsymbol{r}_N\sigma_N)\right|^2. \end{aligned} \tag{2.19}$$

The electron density $n(\boldsymbol{r})$ can then be obtained as the expectation value of the density operator $\hat{n}(\boldsymbol{r})$ which can be expressed as [Parr and Yang, 1989; Engel and Dreizler, 2011]

$$\hat{n}(\boldsymbol{r}) = \sum_{i=1}^{N} \delta(\boldsymbol{r}-\boldsymbol{r}_i) = \sum_\sigma \hat{\psi}^\dagger_\sigma(\boldsymbol{r})\hat{\psi}_\sigma(\boldsymbol{r}), \tag{2.20}$$

so that $n(\boldsymbol{r}) = \langle\Psi\,|\,\hat{n}(\boldsymbol{r})\,|\,\Psi\rangle$. The expression for the two-body density matrix in terms of the many-body wave function $|\Psi\rangle$ is [Engel and Dreizler, 2011]

$$\begin{aligned} n_2(\boldsymbol{r},\boldsymbol{r}') &= \left\langle \hat{n}_2(\boldsymbol{r},\boldsymbol{r}')\right\rangle \\ &= \frac{N(N-1)}{2} \sum_{\sigma_1\ldots\sigma_N} \int \ldots \int d\boldsymbol{r}_3 \ldots d\boldsymbol{r}_N \left|\Psi(\boldsymbol{r}\sigma_1, \boldsymbol{r}'\sigma_2, \boldsymbol{r}_3\sigma_3, \ldots, \boldsymbol{r}_N\sigma_N)\right|^2, \end{aligned} \tag{2.21}$$

where the two-body density matrix operator can also be formulated as [Engel and Dreizler, 2011]

$$\hat{n}_2(\boldsymbol{r},\boldsymbol{r}') = \frac{1}{2}\sum_{i\neq j}^{N} \delta(\boldsymbol{r}-\boldsymbol{r}_i)\delta(\boldsymbol{r}'-\boldsymbol{r}_j). \tag{2.22}$$

$n_2(\boldsymbol{r},\boldsymbol{r}')$ can be interpreted as the probability to find one particle with arbitrary spin at position $\boldsymbol{r}$ and, simultaneously, a second particle with arbitrary spin at $\boldsymbol{r}'$ [see, for example, Engel and Dreizler, 2011; Martin, 2004; Dobson, 1991]. This interpretation will be useful to treat and understand the electron-electron interaction.

In the case of local one-particle operators, only the diagonal part is conventionally written given the fact that it is always possible to find a matrix representation of these operators which is diagonal, that is; $\hat{\mathcal{O}}_1 = \sum_i \mathcal{O}_1(\boldsymbol{r}_i)$. The corresponding expectation value is given by [Parr and Yang, 1989]

$$\left\langle \hat{\mathcal{O}}_1 \right\rangle = \int d\boldsymbol{r}\, \mathcal{O}_1(\boldsymbol{r}) \left[n_1(\boldsymbol{r},\boldsymbol{r}')\right]_{\boldsymbol{r}'=\boldsymbol{r}}. \tag{2.23}$$

This is the case, in particular, for the kinetic energy and the external potential energy operators of (2.11) which take the following form (adopting atomic units)

$$T = -\frac{1}{2}\sum_{i=1}^{N} \left\langle \Psi \left| \nabla_i^2 \right| \Psi \right\rangle = -\frac{1}{2}\int d\boldsymbol{r} \left[\nabla^2_{\boldsymbol{r}} n_1(\boldsymbol{r},\boldsymbol{r}')\right]_{\boldsymbol{r}'=\boldsymbol{r}}, \tag{2.24}$$

$$V_{\text{ext}} = \langle\Psi|\sum_{i=1}^{N} v_{\text{ext}}(\boldsymbol{r}_i)|\Psi\rangle = \int d\boldsymbol{r}\, v_{\text{ext}}(\boldsymbol{r})\, n(\boldsymbol{r}). \tag{2.25}$$

The electron-electron Coulomb interaction term U_{ee} in (2.11) is responsible of introducing many-body effects. It consists of a two-body operator which is given by $\hat{\mathcal{O}}_2 = \sum_{i<j}\mathcal{O}_2(\boldsymbol{r}_i,\boldsymbol{r}_j)$ and is local with respect to the coordinates of the two particles involved [Engel and Dreizler, 2011]. Such an operator can be written in terms of the two-body density matrix defined in (2.21) as [as found in Parr and Yang, 1989; Kohanoff, 2006]

$$U_{\text{ee}} = \frac{1}{2}\sum_{i=1}^{N}\sum_{j\neq i}^{N}\langle\Psi|\frac{1}{|\boldsymbol{r}_i-\boldsymbol{r}_j|}|\Psi\rangle = \int\int d\boldsymbol{r}\,d\boldsymbol{r}'\,\frac{n_2(\boldsymbol{r},\boldsymbol{r}')}{|\boldsymbol{r}-\boldsymbol{r}'|}. \tag{2.26}$$

Recalling here that $n_2(\boldsymbol{r},\boldsymbol{r}')$ can be interpreted as the probability to find one particle with arbitrary spin at position $\boldsymbol{r}$ and a second particle with arbitrary spin at $\boldsymbol{r}'$ [see (2.21)], we can write [Kohanoff, 2006; Engel and Dreizler, 2011]

$$n_2(\boldsymbol{r},\boldsymbol{r}') = \frac{1}{2}n(\boldsymbol{r})n(\boldsymbol{r}')g(\boldsymbol{r},\boldsymbol{r}'), \tag{2.27}$$

where we have defined the pair-correlation function $g(\boldsymbol{r},\boldsymbol{r}')$ which measures the departure of $n_2(\boldsymbol{r},\boldsymbol{r}')$ from a simple product $n(\boldsymbol{r})n(\boldsymbol{r}')$ that corresponds to the case of uncorrelated particles. The symmetric function $g(\boldsymbol{r},\boldsymbol{r}')$ is an object that is different from one only when $\boldsymbol{r}$ is sufficiently close to $\boldsymbol{r}'$. If the electron-electron interaction of (2.26) were purely classical, meaning that $g(\boldsymbol{r},\boldsymbol{r}')=1$ everywhere, the electron-electron interaction could be written as the classical electrostatic interaction energy of a charge distribution $n(\boldsymbol{r})$ [Parr and Yang, 1989]

$$E_{\text{H}}[n] = \frac{1}{2}\int\int d\boldsymbol{r}\,d\boldsymbol{r}'\frac{n(\boldsymbol{r})n(\boldsymbol{r}')}{|\boldsymbol{r}-\boldsymbol{r}'|}, \tag{2.28}$$

where the factor 1/2 is present to avoid double counting. Expression (2.28) is known as the Hartree term, its square brackets indicate a functional dependence on the electronic density $n(\boldsymbol{r})$. Expressions (2.27) and (2.28) point in the direction of separating the electron-electron interaction of (2.26) into two terms [Kohanoff, 2006]

$$U_{\text{ee}} = E_{\text{H}}[n] + \frac{1}{2}\int\int d\boldsymbol{r}\,d\boldsymbol{r}'\,\frac{n(\boldsymbol{r})n(\boldsymbol{r}')}{|\boldsymbol{r}-\boldsymbol{r}'|}\left[g(\boldsymbol{r},\boldsymbol{r}')-1\right], \tag{2.29}$$

where the first term ignores correlation altogether by taking $g(\boldsymbol{r},\boldsymbol{r}')=1$, thus corresponding to the classic Hartree term defined in (2.28). The second term incorporates all nonclassical effects due to the correlation of electrons by taking into account the departure of $g(\boldsymbol{r},\boldsymbol{r}')$ from 1. In this manner, the function $g(\boldsymbol{r},\boldsymbol{r}')$ incorporates all nonclassical effects due to the correlation of electrons [Kohanoff, 2006].

The pair-correlation function $g(\boldsymbol{r},\boldsymbol{r}')$ takes into account the fact that the presence of an electron at $\boldsymbol{r}$ reduces the probability of finding a second electron located at a position $\boldsymbol{r}'$ in the vicinity of $\boldsymbol{r}$ due to the Coulomb repulsion. In addition, this probability will be further diminished if the electrons have the same spin projection due to Pauli's exchange principle [Kohanoff, 2006]. Correspondingly, the second term in (2.29) includes the so called effects of exchange and correlation which we will briefly describe next.

2.3.1 Exchange and correlation

Independent (quasi-)particle approximations are at the heart of understanding electronic-structure theory methods. The simplest possible approximation consists in

neglecting the second term in (2.29) by taking $g(\boldsymbol{r},\boldsymbol{r}')=1$ everywhere. This leads to a completely uncorrelated system in which the two-particle interaction becomes the classical self-repulsion energy of a continuous charge distribution $n(\boldsymbol{r})$, namely the Hartree term in (2.28). This is known as the Hartree approximation [Martin, 2004; Kohanoff, 2006]. The Hartree approximation treats electrons as distinguishable particles but electrons are indistinguishable particles with spin, that is, they are fermions. The next step is to introduce the exchange interaction, which can be achieved through the Hartree-Fock approximation.

The Hartree-Fock approximation

Pauli's exclusion principle states that two fermions cannot occupy the same quantum state because the many-fermion wave function must be antisymmetric upon particle exchange. The Hartree-Fock (HF) approximation consists in improving over the simple Hartree approximation by adding Pauli's exclusion principle, thus taking into account that the motion of two electrons with parallel spins must be correlated. It can be fulfilled by proposing an antisymmetric many-body wave function as a solution to (2.10).

The simplest antisymmetric wave function which can be used to describe the ground-state of an $N-$electron system is a Slater determinant

$$\Psi^{\mathrm{HF}} = \frac{1}{\sqrt{N!}}\begin{vmatrix} \psi_1(\boldsymbol{r}_1\sigma_1) & \psi_2(\boldsymbol{r}_1\sigma_1) & \cdots & \psi_N(\boldsymbol{r}_1\sigma_1) \\ \psi_1(\boldsymbol{r}_2\sigma_2) & \psi_2(\boldsymbol{r}_2\sigma_2) & \cdots & \psi_N(\boldsymbol{r}_2\sigma_2) \\ \vdots & \vdots & & \vdots \\ \psi_1(\boldsymbol{r}_N\sigma_N) & \psi_2(\boldsymbol{r}_N\sigma_N) & \cdots & \psi_N(\boldsymbol{r}_N\sigma_N) \end{vmatrix} \tag{2.30}$$

$$= \frac{1}{\sqrt{N!}}\det\left[\psi_1\psi_2\ldots\psi_N\right] \tag{2.31}$$

where the functions $\psi_i(\boldsymbol{r}_j\sigma_j)=\phi_i(\boldsymbol{r}_j)\chi_i(\sigma_j)$ are single-particle spin orbitals. Each of them is the product of a function of the position $\phi_i(\boldsymbol{r}_j)$ and a function of the spin variable $\chi_i(\sigma_j)$. The mathematical properties of the determinantal expression (2.31) ensure that the wave function changes sign when exchanging the coordinates of two of the electrons. The variational principle states that the ground-state wave function of the form (2.31) is the one which gives the lowest possible energy $E_0^{\mathrm{HF}}=\langle\Psi_0^{\mathrm{HF}}|\,\hat{h}\,|\Psi_0^{\mathrm{HF}}\rangle$, where $\hat{h}$ is the electronic Hamiltonian given in (2.11) [Szabo and Ostlund, 1996]. The variational flexibility in the wave function Ψ^{HF} is the choice of single-spin orbitals.[1]

In terms of the pair-correlation function $g(\boldsymbol{r},\boldsymbol{r}')$ discussed above, the electron-electron interaction in the HF approximation becomes [Kohanoff, 2006]

$$U_{\mathrm{ee}}^{\mathrm{HF}} = \frac{1}{2}\int\int d\boldsymbol{r}\,d\boldsymbol{r}'\,\frac{n(\boldsymbol{r})n(\boldsymbol{r}')}{|\boldsymbol{r}-\boldsymbol{r}'|} + \frac{1}{2}\int\int d\boldsymbol{r}\,d\boldsymbol{r}'\,\frac{n(\boldsymbol{r})n(\boldsymbol{r}')}{|\boldsymbol{r}-\boldsymbol{r}'|}\left[g_{\mathrm{x}}(\boldsymbol{r},\boldsymbol{r}')-1\right], \tag{2.32}$$

where the contribution of exchange to the pair-correlation function is given by

$$g_{\mathrm{x}}(\boldsymbol{r},\boldsymbol{r}') = 1-\frac{\left|n_1(\boldsymbol{r},\boldsymbol{r}')\right|^2}{n(\boldsymbol{r})n(\boldsymbol{r}')}. \tag{2.33}$$

[1] The reader is referred to the book written by Szabo and Ostlund [1996] for a detailed description regarding the derivation of the HF equations and the determination of the optimal spin orbitals.

The HF density and density matrix in (2.32) and (2.33) are calculated from the ground-state Slater determinant[2] Ψ_0^{HF}. The next step is to include effects that go beyond those of exchange.

Effects beyond exchange: the correlation energy

The HF approximation incorporates exchange effects by proposing a wave function made from a single Slater determinant. However, since the motion of electrons with opposite spins remains uncorrelated, a single-determinant wave function is usually referred as an uncorrelated wave function [Szabo and Ostlund, 1996]. The improvement of this wave function can be achieved by introducing extra degrees of freedom in the wave function, thus lowering the ground-state energy. The wave-function-based methods that improve the quality of the description upon the HF approximation are commonly known as post-HF methods. These methods include, for example, the linear mixing of many determinants, known as configuration interaction, and the use of many-body perturbation techniques. A detailed description of these methods can be found in the book by Szabo and Ostlund [1996].

The effects of correlation can be cast, in terms of the pair-correlation function $g(\boldsymbol{r},\boldsymbol{r}')$, as the remaining part of the function once the effects of exchange have been taken into account [Kohanoff, 2006],

$$g(\boldsymbol{r},\boldsymbol{r}') = g_{\mathrm{x}}(\boldsymbol{r},\boldsymbol{r}') + g_{\mathrm{c}}(\boldsymbol{r},\boldsymbol{r}'), \tag{2.34}$$

where $g_{\mathrm{c}}(\boldsymbol{r},\boldsymbol{r}')$ is the contribution of electron correlation to the pair-correlation function [Kohanoff, 2006]. In general, since electrons of the same spin are kept apart by the exclusion principle, correlation is most important for electrons with opposite spin.

One possible definition of the correlation energy ($E_{\mathrm{c}}^{\mathrm{HF}}$), in the context of HF based methods (quantum chemistry methods), is given as the difference between the exact nonrelativistic ground-state energy (E_0) within the BO approximation [see (2.4)] and the ground-state HF energy (E_0^{HF}) obtained in the limit where the basis set approaches completeness: $E_{\mathrm{c}}^{\mathrm{HF}} = E_0 - E_0^{\mathrm{HF}}$ [Szabo and Ostlund, 1996]. However, this is not the only possible definition of the correlation energy as it can also be done in terms of another reference state. Another precise definition emerges in the context of density-functional theory where the correlation energy still corresponds to the difference between the total energy and the sum of kinetic, direct and exchange Coulomb energies, but with the condition that the orbitals must give the exact density of the system [Martin, 2004; Kohanoff, 2006]. This fact reveals that a separation of the total energy into different contributions can be done as a matter of convenience, and that such separation depends on the particular theoretical framework.

[2] In the case of single determinants, the one-particle density matrix takes the form

$$n_1(\boldsymbol{r},\boldsymbol{r}') = n_1^{\uparrow\uparrow}(\boldsymbol{r},\boldsymbol{r}') + n_1^{\downarrow\downarrow}(\boldsymbol{r},\boldsymbol{r}'),$$

where $n_1^{\sigma\sigma}(\boldsymbol{r},\boldsymbol{r}') = \sum_i \psi_i(\boldsymbol{r}\sigma)\psi_i^*(\boldsymbol{r}'\sigma')$. The ground-state electron density is calculated by inserting the wave-function Ψ_0^{HF} into the expression for the electron density (2.19), yielding

$$n(\boldsymbol{r}) = \sum_{\sigma}\sum_{i}^{N} \left|\psi_i(\boldsymbol{r}\sigma)\right|^2 = 2\sum_{i}^{N/2} \left|\phi_i(\boldsymbol{r})\right|^2.$$

In the next section we describe another approach to address the electronic problem in which the separation of the total energy into different contributions shall play an important role. This approach is density-functional theory, which considers the electronic density to be the fundamental variable in electronic-structure theory. It has been the preferred choice in electronic-structure calculations in condensed matter physics for some decades now, but has also become accepted by the quantum chemistry community because of its computational advantages over post-HF methods of comparable quality.

2.4 Density-functional theory

Density-functional theory (DFT) is a theory for the treatment of many-body systems that has become the primary tool for calculation of electronic-structure in condensed matter, molecular, and other finite systems. It considers a special role of the electron density in the ground-state of a quantum many-body system, postulating that all properties of the many-body system can be considered to be unique functionals of the ground-state density [Martin, 2004]. We start by giving a general description of the Thomas-Fermi-Dirac (TFD) approximation which, although is not accurate enough for present-day electronic-structure calculations, constitutes the basis for the development of density-functional theory.

2.4.1 The Thomas-Fermi-Dirac approximation

Thomas and Fermi proposed a method which can be considered as a precursor of density-functional theory of quantum systems around 1927.[3] They gave a prescription for calculating the energy of an electronic system exclusively in terms of the electronic density [Martin, 2004; Kohanoff, 2006]. In the Thomas-Fermi method, the system of electrons is idealized as a noninteracting homogeneous gas. The homogeneous electron gas is the simplest model used to represent condensed matter. It is a system completely determined by its electronic density in which the nuclei are replaced by a homogeneous positive background charge density. In its noninteracting approximation, it involves the solution of a set of one-electron equations with the Hamiltonian given in the Hartree approximation (see section 2.3.1). The ground-state of the system is found by occupying the lowest eigenstates while obeying the exclusion principle. The solutions to this approximation are normalized plane waves $\psi_k = \frac{1}{\Omega^{1/2}} e^{i\boldsymbol{k}\cdot\boldsymbol{r}}$ with energy $\varepsilon_k = \frac{1}{2}k^2$ [Martin, 2004].

The main idea in the Thomas-Fermi method is to construct the same quantities for the inhomogeneous system as

$$E_\alpha[n] = \int d\boldsymbol{r}\; n(\boldsymbol{r})\varepsilon_\alpha^{\text{heg}}[n(\boldsymbol{r})], \tag{2.35}$$

where $\varepsilon_\alpha^{\text{heg}}[n(\boldsymbol{r})]$ is the energy density of the contribution α, which potentially includes the kinetic, exchange, and correlation contributions, determined locally at the value assumed for the density at any given point [Kohanoff, 2006]. This is the first proposal of the local-density approximation (LDA). In the noninteracting homogeneous electron gas,

[3] The original reference(s) can be found in Martin [2004]; Kohanoff [2006]; Parr and Yang [1989]; and Engel and Dreizler [2011].

the electronic density is calculated in terms of the Fermi energy ε_F as [Kohanoff, 2006; Martin, 2004]

$$n = \frac{1}{3\pi^2}\left(2\varepsilon_F\right)^{3/2}, \tag{2.36}$$

the kinetic energy per electron is given by $T_s(V) = \frac{3}{5}\varepsilon_F$, and the kinetic-energy density becomes [Kohanoff, 2006; Engel and Dreizler, 2011]

$$t_s[n] \equiv \frac{T_s(V)}{V} = \frac{3}{5}\left(3\pi^2 n\right)^{2/3}. \tag{2.37}$$

In the approximation by Thomas and Fermi, the kinetic-energy density $t_s(\boldsymbol{r})$ of the inhomogeneous system is replaced by the energy density of the electron gas given in (2.37), but evaluated with the local density $n(\boldsymbol{r})$. As a result, the kinetic energy is given by [Engel and Dreizler, 2011; Kohanoff, 2006]

$$T_s^{\mathrm{TF}}[n] = C_k \int d\boldsymbol{r}\; n(\boldsymbol{r})^{5/3}, \tag{2.38}$$

where $C_k = \frac{3}{10}(3\pi)^{2/3} = 2.871$ hartree. Whereas the rigorous formula of (2.24) for the kinetic energy is given in terms of the one-body density matrix, Thomas and Fermi originally approximated the kinetic energy of the electrons as an explicit functional of the density, but neglected exchange and correlation among the electrons. It was Dirac, in 1930 [as found in Martin, 2004; Kohanoff, 2006], who formulated the local approximation for exchange of an homogeneous electron gas as

$$E_x[n] = -C_x \int d\boldsymbol{r}\; n(\boldsymbol{r})^{4/3}, \tag{2.39}$$

with $C_x = \frac{3}{4}(\frac{3}{\pi})^{1/3} = 0.739$ hartree.

By recalling the general energy expression for a many-body electronic system of (2.14) and keeping in mind that the TFD approximation neglects the correlation energy, the TFD approximation for the energy of a system of electrons in an external potential V_{ext} is obtained by replacing the approximations given in (2.38)–(2.39) as [Kohanoff, 2006]

$$\begin{aligned} E_{\mathrm{TFD}}[n] = C_k \int d\boldsymbol{r}\; n(\boldsymbol{r})^{5/3} + \int d\boldsymbol{r}\; v_{\mathrm{ext}}(\boldsymbol{r}) n(\boldsymbol{r}) + \frac{1}{2}\int\int d\boldsymbol{r}\, d\boldsymbol{r}' \frac{n(\boldsymbol{r})n(\boldsymbol{r}')}{|\boldsymbol{r}-\boldsymbol{r}'|} \\ - C_x \int d\boldsymbol{r}\; n(\boldsymbol{r})^{4/3}, \end{aligned} \tag{2.40}$$

where $E_{\mathrm{TFD}}[n]$ is said to be a functional of the electronic density as its formulation is given in terms of the electronic density alone. The next step is to assume that, by means of a variational principle, we can search for the ground-state density $n(\boldsymbol{r})$ that minimizes the energy functional $E_{\mathrm{TFD}}[n]$ under the constraint that the total integrated charge be equal to the number of electrons

$$\int d\boldsymbol{r}\, n(\boldsymbol{r}) = N. \tag{2.41}$$

This minimization can be evaluated using the method of Lagrange multipliers, so the ground-state density must satisfy the variational principle

$$\delta\left\{E_{\mathrm{TFD}} - \mu_{\mathrm{TFD}}\left[\int d\boldsymbol{r}\, n(\boldsymbol{r}) - N\right]\right\} = 0, \tag{2.42}$$

where the Lagrange multiplier μ_{TFD} is given by

$$\mu_{\mathrm{TFD}} = \frac{\delta E_{\mathrm{TFD}}[n]}{\delta n(\boldsymbol{r})} \tag{2.43}$$

$$= \frac{5}{3} C_{\mathrm{k}} n(\boldsymbol{r})^{2/3} + v_{\mathrm{ext}}(\boldsymbol{r}) + \int d\boldsymbol{r}' \frac{n(\boldsymbol{r}')}{|\boldsymbol{r} - \boldsymbol{r}'|} - \frac{4}{3} C_{\mathrm{x}} n(\boldsymbol{r})^{1/3}. \tag{2.44}$$

Extensions of the TFD energy formula (2.40) include correlation contributions that can be introduced within the same philosophy of a local quantity in the framework of the homogeneous electron gas, as first done for example by Wigner [as cited by Kohanoff, 2006]. Further extensions correspond to those of the Thomas-Fermi kinetic energy, as taken first by von Weizsäcker [see for example Engel and Dreizler, 2011; Martin, 2004], in order to account in a better manner for the inhomogeneity of real systems. A thorough account of these extensions and the related models to the TFD method can be found in Parr and Yang [1989] and Engel and Dreizler [2011].

The idea of expressing the energy of an electronic system exclusively in terms of the three-dimensional quantity that is the electron density is a very attractive feature of the TFD model. However, its approximations result to be too severe, missing essential physics and chemistry such as the shell structure of atoms and binding of molecules [Martin, 2004]. We shall continue by addressing the Hohenberg-Kohn theorems which form the mathematical basis of modern DFT.

2.4.2 The Hohenberg-Kohn theorems

Hohenberg and Kohn [1964] were the first to formulate DFT as an exact theory of many-body systems by proving two theorems in which DFT is based upon. In an $N-$electron system with a Hamiltonian given by (2.11), the external potential $v_{\mathrm{ext}}(\boldsymbol{r})$ defines the nuclear frame for an electronic system which together with the number of electrons N determine all the electronic properties of the ground state [Parr and Yang, 1989]. The formulation of the theorems of Hohenberg and Kohn is restricted to nondegenerate ground states.

The first Hohenberg-Kohn (HK) theorem [Hohenberg and Kohn, 1964] provides the grounds for using the electron density $n(\boldsymbol{r})$ as basic variable in place of N and v_{ext}. It states that[4] *the external potential* $v_{\mathrm{ext}}(\boldsymbol{r})$ *is determined, within a trivial additive constant, by the electron density* $n(\boldsymbol{r})$. Since $n(\boldsymbol{r})$ determines the number of electrons, it also determines the ground-state wave function Ψ and all the other electronic properties of the system [Parr and Yang, 1989]. The proof of this theorem is simple and can be found, for example, in Parr and Yang [1989]; Kohanoff [2006]; and Martin [2004] in addition to the original reference [Hohenberg and Kohn, 1964].

Since the electronic density n determines N and v_{ext}, it follows that n also determines all properties of the ground state as the kinetic energy $T[n]$, the potential energy $V[n]$, and thus the total energy $E[n]$. In place of (2.40), we define the energy E_v, which is a functional of the density because of the previous theorem, as [Parr and Yang, 1989;

[4] Taken from Parr and Yang [1989].

Kohanoff, 2006]

$$\begin{aligned} E_v[n] &= T[n] + V_{\text{ext}}[n] + U_{\text{ee}}[n] \\ &= F_{\text{HK}}[n] + \int d\boldsymbol{r}\, v_{\text{ext}}(\boldsymbol{r})\, n(\boldsymbol{r}), \end{aligned} \tag{2.45}$$

with

$$F_{\text{HK}}[n] = T[n] + U_{\text{ee}}[n]. \tag{2.46}$$

Note that $F_{\text{HK}}[n]$ must be universal (the same for all electron systems) by construction since it is defined independently of the external potential $v_{\text{ext}}(\boldsymbol{r})$ [Parr and Yang, 1989].

The second HK theorem [Hohenberg and Kohn, 1964] provides the variational principle for the energy:[5] *for a trial density* $\tilde{n}(\boldsymbol{r})$*, such that* $\tilde{n}(\boldsymbol{r}) \geq 0$ *and* $\int d\tilde{n}(\boldsymbol{r}) = N$*,*

$$E_0 \leq E_v[\tilde{n}] \tag{2.47}$$

where $E_v[\tilde{n}]$ *is the energy functional of* (2.45). This inequality is analogous to the variational principle for wave functions and provides justification for the variational principle in the TFD theory as $E_{\text{TFD}}[n]$ is just an approximation to $E[n]$ [Parr and Yang, 1989]. The proof of this theorem can also be found in Parr and Yang [1989]; Kohanoff [2006]; Martin [2004]; and the original reference [Hohenberg and Kohn, 1964].

The variational principle of (2.47) requires that the ground-state density satisfies the stationary principle

$$\delta\left\{E_v[n] - \mu\left[\int d\boldsymbol{r}\, n(\boldsymbol{r}) - N\right]\right\} = 0, \tag{2.48}$$

where the Lagrange multiplier μ corresponds to the chemical potential for integer particle number [Parr and Yang, 1989; Engel and Dreizler, 2011] and is given by

$$\mu = \frac{\delta E_v[n]}{\delta n(\boldsymbol{r})} = v_{\text{ext}}(\boldsymbol{r}) + \frac{\delta F_{\text{HK}}[n]}{\delta n(\boldsymbol{r})}. \tag{2.49}$$

Equation (2.49) is the basic equation of DFT given the fact that if we knew the exact form of $F_{\text{HK}}[n]$, (2.48) would be an exact expression for the ground-state electron density [Parr and Yang, 1989]. Unfortunately, the explicit form of $F_{\text{HK}}[n]$ is (unsurprisingly) not known.

The fact that the ground-state electron density uniquely determines the properties of a ground state brings us to the definition of $v-$representability. An electron density is defined as $v-$representable if it is associated to the antisymmetric ground-state wave function of a Hamiltonian of the form (2.11) with *some* external potential $v_{\text{ext}}(\boldsymbol{r})$ (not necessarily a Coulomb potential). In these terms, a given density may or may not be $v-$representable [Parr and Yang, 1989]. The first HK theorem can then be thought as the existence of a one-to-one mapping between ground-state wave functions and $v-$representable densities, via which a $v-$representable density determines the properties of its associated ground state [Parr and Yang, 1989]. The HK functional $F_{\text{HK}}[n]$ is then defined only for trial densities that can be generated by some external potential [Martin, 2004]. It is clear that $F_{\text{HK}}[n]$ and the variational principle of (2.47) both depend on the $v-$representability of trial densities, but the conditions for such representability are, in general, not known [Parr and Yang, 1989; Martin, 2004].

[5] Taken from Parr and Yang [1989].

Constrained search formulation in density-functional theory

The question of $v-$representability is solved by an alternative construction due to Levy and Lieb [as found in Martin, 2004; Parr and Yang, 1989]. The idea behind the Levy-Lieb (LL) formulation is to define a two-step minimization procedure starting with the general expression for the energy in terms of the many-body wave function Ψ given by (2.14). Instead of minimizing the energy with respect to all variables in Ψ, the LL formulation first considers the energy only for the class of many-body wave functions Ψ that have the same density $n(\boldsymbol{r})$ [Martin, 2004]. The total energy for any wave function can be written

$$E = \langle \Psi \,|\, \hat{T} \,|\, \Psi \rangle + \langle \Psi \,|\, \hat{U}_{\text{ee}} \,|\, \Psi \rangle + \int d\boldsymbol{r}\, v_{\text{ext}}(\boldsymbol{r}) n(\boldsymbol{r}). \tag{2.50}$$

If we minimize the energy (2.50) over the class of wave functions with the same density $n(\boldsymbol{r})$, it is possible to define a unique lowest energy for that density

$$\begin{aligned} E[n] &= \min_{\Psi \to n(\boldsymbol{r})} \left\{ \langle \Psi \,|\, \hat{T} \,|\, \Psi \rangle + \langle \Psi \,|\, \hat{U}_{\text{ee}} \,|\, \Psi \rangle \right\} + \int d\boldsymbol{r}\, v_{\text{ext}}(\boldsymbol{r}) n(\boldsymbol{r}) \\ &= F[n] + \int d\boldsymbol{r}\, v_{\text{ext}}(\boldsymbol{r}) n(\boldsymbol{r}), \end{aligned} \tag{2.51}$$

where the LL functional of the density is defined by [as found in Martin, 2004]

$$F[n] = \min_{\Psi \to n(\boldsymbol{r})} \langle \Psi \,|\, \hat{T} + \hat{U}_{\text{ee}} \,|\, \Psi \rangle. \tag{2.52}$$

The variational search is constrained in (2.52) because the space of trial wave functions comprises only those giving $n(\boldsymbol{r})$ [Parr and Yang, 1989]. With the definition of $F[n]$, the energy $E[n]$ is manifestly a functional of the density and the ground-state E_0 is found by minimizing $E[n]$,

$$E_0 = \min_{n(\boldsymbol{r})} E[n] \tag{2.53}$$

where $E[n]$ is given by (2.51).

The LL construction provides a meaning for the functional $F[n]$ and an operational definition given as the minimum of the sum of kinetic plus interaction energies for all possible wave functions having the density $n(\boldsymbol{r})$ [Martin, 2004]. The LL functional $F[n]$ is defined for any density $n(\boldsymbol{r})$ derivable from an antisymmetric wave function for N electrons, condition which is termed $N-$representability [Martin, 2004; Parr and Yang, 1989]. The existence of such representability is satisfied for any reasonable density.[6] The LL functional $F[n]$ thus extends the domain of definition from $v-$representable densities to $N-$representable densities, eliminating the $v-$representability constraint found in the HK functional $F_{\text{HK}}[n]$. Since in the constrained search of $F[n]$ only one of a set of degenerate wave functions is selected, the LL construction also eliminates the restriction to nondegenerate ground states found in the HK formulation [Parr and Yang, 1989]. At the minimum of the total energy of the system in a given external potential, the LL functional $F[n]$ must be equal to the HK functional $F_{\text{HK}}[n]$ since the minimum is a density which can be generated by an external potential [Martin, 2004].

[6] The conditions for a density $n(\boldsymbol{r})$ to be $N-$representable are relatively simple. It is possible to construct any density integrating to N total electrons of a given spin from a single Slater determinant of N one-electron orbitals, subject only to the condition that $n(\boldsymbol{r}) \geq 0$ and $\int d\boldsymbol{r} |\nabla n(\boldsymbol{r})^{1/2}|^2$ is finite [Martin, 2004].

The ground-state density and energy can be determined exactly by means of DFT, provided that $F[n]$ is known. However, the HK theorems do not provide us with any hint concerning its explicit form. In this context, Kohn and Sham [1965] devised a practical scheme for determining the ground-state which we shall discuss next.

2.4.3 The Kohn-Sham equations

We have discussed how the Thomas-Fermi and related models provide a direct approach in which one constructs explicit approximate forms for the kinetic energy $T[n]$ and the electron-electron interaction U_{ee}, producing equations that involve the electron density alone. Unfortunately, the approximations of the TFD related models are too severe. The main problem at this stage is related to the kinetic energy $T = \langle\Psi|\hat{T}|\Psi\rangle$. Its exact calculation –as shown in (2.24)– involves evaluating the Laplacian of the one-body density matrix, which has no straightforward relation to the density. Kohn and Sham [1965] devised an ingenious indirect approach to the kinetic energy functional $T[n]$, turning DFT into a practical tool for rigorous calculations [Parr and Yang, 1989; Kohanoff, 2006].

Kohn and Sham proposed to introduce single-particle orbitals in order to compute the kinetic energy in a simple manner and with good accuracy, leaving a residual correction to it that is handled separately. Let us start by considering a system of noninteracting electrons with the external potential v_{s} described by the Hamiltonian

$$\hat{\mathscr{H}}_{\mathrm{s}} = \sum_{i}^{N} \left[-\tfrac{1}{2}\nabla^2 + v_{\mathrm{s}}(\boldsymbol{r}_i) \right]. \tag{2.54}$$

The corresponding $N-$particle ground state, assumed to be nondegenerate, is a Slater determinant

$$\Psi_{\mathrm{s}} = \frac{1}{\sqrt{N!}} \det\left[\psi_1 \psi_2 \ldots \psi_N\right], \tag{2.55}$$

where the functions ψ_i are the N lowest eigenstates of the one-electron Hamiltonian [Engel and Dreizler, 2011; Parr and Yang, 1989]

$$\hat{h}_{\mathrm{s}}\psi_i = \left[-\tfrac{1}{2}\nabla^2 + v_{\mathrm{s}}(\boldsymbol{r}) \right] \psi_i = \varepsilon_i \psi_i. \tag{2.56}$$

The ground-state density $n_{0\mathrm{s}}(\boldsymbol{r})$, corresponding to (2.55) and (2.56), is given by

$$n_{0\mathrm{s}}(\boldsymbol{r}) = \sum_{\sigma} \sum_{i}^{N} \left|\psi_i(\boldsymbol{r},\sigma)\right|^2 = 2 \sum_{i}^{N/2} \left|\phi_i(\boldsymbol{r})\right|^2. \tag{2.57}$$

The sum over the N energetically lowest single-particle states can be written in the more general form

$$n_{\mathrm{s}}(\boldsymbol{r}) = \sum_{i}^{N} f_i \sum_{\sigma} \left|\psi_i(\boldsymbol{r},\sigma)\right|^2, \tag{2.58}$$

where f_i are the occupation numbers corresponding to the single-electron orbitals ψ_i. Equation (2.57) is the special case of (2.58), having $f_i = 1$ for N orbitals and $f_i = 0$ otherwise [Engel and Dreizler, 2011; Parr and Yang, 1989].

It is convenient at this point to recall that the HK theorems are valid for arbitrary many-particle systems. In particular, they also apply to the case of noninteracting systems. Thus, the nondegenerate ground-state (2.55) is uniquely determined by the

ground-state density (2.57): $\Psi_s = \Psi_s[n]$. We can now define the HK ground-state energy functional of a noninteracting system as [Engel and Dreizler, 2011]

$$E_s[n] = \left\langle \Psi_s[n] \middle| \hat{T} \middle| \Psi_s[n] \right\rangle + \int d\boldsymbol{r}\, v_s(\boldsymbol{r}) n_s(\boldsymbol{r}). \tag{2.59}$$

The functional $E_s[n]$ has the same properties of the functional $E_v[n]$ defined in (2.45). Recalling the expression for $\hat{T}$ given in (2.24), expression (2.59) defines the kinetic energy functional $T_s[n]$ of noninteracting particles for any ground-state density n resulting from a Hamiltonian of the type (2.54). That is, for any noninteracting $v-$representable density n, $T_s[n]$ takes the form [Engel and Dreizler, 2011]

$$\begin{aligned} T_s[n] &= \left\langle \Psi_s[n] \middle| \hat{T} \middle| \Psi_s[n] \right\rangle \\ &= -\frac{1}{2} \sum_i^N \left\langle \psi_i[n] \middle| \nabla^2 \middle| \psi_i[n] \right\rangle, \end{aligned} \tag{2.60}$$

which shows that not only the many-body ground-state Ψ_s is a unique functional of n, but also its components; $\psi_i(r,\sigma) = \psi_i[n](r,\sigma)$. The fact that the orbitals are density functionals becomes evident if one considers that a change in $n(\boldsymbol{r})$ can only be induced by a corresponding change in $v_s(\boldsymbol{r})$ and that any modification of $v_s(\boldsymbol{r})$ leads to a unique change of all orbitals via (2.56) [Engel and Dreizler, 2011].

This leads us to the discussion of the interacting system described by the electronic Hamiltonian (2.11). Kohn and Sham [1965] proved that for any admissible potential v_{ext}, the ground-state density $n_0(\boldsymbol{r})$ of the interacting system is equal to the ground-state density of some yet to be determined system of noninteracting electrons moving in the effective local single-particle potential $v_s(\boldsymbol{r}) = v_{eff}(\boldsymbol{r})$ (different from v_{ext}). The auxiliary system of noninteracting electrons is called the Kohn-Sham (KS) system [Engel and Dreizler, 2011]. Assuming that the KS system exists,[7] the ground-state density of the interacting system can then be represented in terms of the single-particle orbitals $\psi_i(\boldsymbol{r},\sigma)$ of the noninteracting system as [taken from Engel and Dreizler, 2011]

$$n_0(\boldsymbol{r}) \equiv n_{0s}(\boldsymbol{r}) = \sum_\sigma \sum_i^N \left|\psi_i(\boldsymbol{r},\sigma)\right|^2. \tag{2.61}$$

Engel and Dreizler [2011] emphasize the difference between (2.57) and (2.61) by observing that while (2.57) is a straightforward result for the density of a noninteracting system, equation (2.61) corresponds to a highly non-trivial representation of the interacting density.

In this context, the HK energy functional (2.45) can be rewritten as

$$E[n] = T_s[n] + V_{ext}[n] + E_H[n] + E_{xc}[n] \tag{2.62}$$

where all the terms have been defined in the preceding sections except that the exchange-correlation (xc) energy functional $E_{xc}[n]$ is now defined in the context of KS-DFT as

$$E_{xc}[n] \equiv \left\langle \hat{T} \right\rangle - T_s[n] + \left\langle \hat{U}_{ee} \right\rangle - E_H[n]. \tag{2.63}$$

[7] The fact that the exact ground-state density of the interacting system can be represented by the ground-state density of an auxiliary system of noninteracting particles is called noninteracting $v-$representability [Martin, 2004]. The question of such representability; that is, whether the KS system actually exists for arbitrary n_0, is discussed in more detail by Engel and Dreizler [2011] and Parr and Yang [1989]. In the treatment of the Kohn-Sham theory here presented, we proceed assuming its existence.

The xc energy functional of (2.63) contains not only the nonclassical part of U_{ee} but also the difference between T and T_s [Parr and Yang, 1989].

The nature of the interacting system must be reflected in the structure of the effective potential v_{eff} as it ensures that the density of the noninteracting reference system is the same as the true density of the interacting system. To determine it, we look for the minimization of the total-energy functional (2.62) with respect to the density under the constraint that this density integrates to N particles. If we apply the variational principle of (2.48) to the energy functional $E[n]$ of (2.62),

$$\delta\left\{E[n]-\mu\left[\int d\boldsymbol{r}\, n(\boldsymbol{r})-N\right]\right\}=0, \tag{2.64}$$

we obtain the following equation for minimizing the ground-state density [Kohanoff, 2006]

$$\mu=\frac{\delta T_s[n]}{\delta n(\boldsymbol{r})}+v_{ext}(\boldsymbol{r})+\frac{\delta E_H[n]}{\delta n(\boldsymbol{r})}+\frac{\delta E_{xc}[n]}{\delta n(\boldsymbol{r})}. \tag{2.65}$$

The next step is to consider the auxiliary noninteracting system, that is the KS system. Since the particles of such system do not interact between themselves but only with the effective potential v_{eff}, its energy functional $E_s[n]$ is given by (2.59) with $v_s(\boldsymbol{r})=v_{eff}(\boldsymbol{r})$. Its ground state is the same as that of the interacting system because they share the same electronic density. Applying the variational principle of (2.64) to $E_s[n]$, we obtain the chemical potential of the noninteracting system which must be equal to that of the interacting system μ given by (2.65), yielding the following expression for the effective potential

$$\begin{aligned} v_{eff}(\boldsymbol{r}) &= v_{ext}(\boldsymbol{r})+\frac{\delta E_H[n]}{\delta n(\boldsymbol{r})}+\frac{\delta E_{xc}[n]}{\delta n(\boldsymbol{r})} \\ &= v_{ext}(\boldsymbol{r})+\int d\boldsymbol{r}'\,\frac{n(\boldsymbol{r}')}{|\boldsymbol{r}-\boldsymbol{r}'|}+v_{xc}(\boldsymbol{r}), \end{aligned} \tag{2.66}$$

with the exchange-correlation potential $v_{xc}(\boldsymbol{r})$ given by

$$v_{xc}(\boldsymbol{r})=\frac{\delta E_{xc}[n]}{\delta n(\boldsymbol{r})}. \tag{2.67}$$

The well known Kohn-Sham equations result from rewriting the single-particle equations (2.56) with $v_s(\boldsymbol{r})=v_{eff}(\boldsymbol{r})$. If we define the KS effective potential as $v_{KS}(\boldsymbol{r})\equiv v_{eff}(\boldsymbol{r})$, the KS equations are then given by

$$\hat{h}_{KS}\psi_i=\left[-\tfrac{1}{2}\nabla^2+v_{KS}(\boldsymbol{r})\right]\psi_i=\varepsilon_i\psi_i. \tag{2.68}$$

The KS equations have the form of independent-particle equations with a potential that must be found self-consistently, making sure that the density used to construct it coincides with that obtained from the solutions of (2.68) [Kohanoff, 2006; Martin, 2004].

2.4.4 Energy functionals for exchange and correlation

In the KS-DFT framework, all the many-body complexity of the electronic problem is contained in the unknown xc term. This term can be reasonably approximated as an explicit functional of $n(\boldsymbol{r})$ and its local gradients as done in conventional functionals,

or as a functional of the single-particle orbitals $\{\psi_i\}$, themselves functionals of $n(\boldsymbol{r})$, as done in non-local formulations. The different existing approximations have been summarized and classified in a hierarchical scheme by Perdew and Schmidt [1994].[8] As our interest in this thesis is mainly van der Waals interactions, it is illustrative and advantageous to start by discussing a formally exact representation of the xc energy functional before addressing conventional xc functionals. Engel and Dreizler [2011] discuss two different variants to derive the xc functional in the KS-DFT framework: Kohn-Sham perturbation theory and the adiabatic connection. In this work, we shall focus on the adiabatic connection formalism.

Exact formalism: the adiabatic connection

In the adiabatic connection (AC) formalism, the ground state of a many-body Hamiltonian can be obtained by introducing a coupling constant λ into the total Hamiltonian

$$\hat{H}(\lambda) = \hat{H}_0 + \lambda \hat{H}_1 \tag{2.69}$$

that connects a reference Hamiltonian $\hat{H}_0 = \hat{H}(\lambda = 0)$ with the total many-body Hamiltonian $\hat{H} = \hat{H}(\lambda = 1)$ [Ren *et al.*, 2012b]. In the case of an electronic system, the total Hamiltonian for a given λ takes the form [Engel and Dreizler, 2011]

$$\hat{H}(\lambda) = \hat{T} + \int d\boldsymbol{r}\, u_\lambda(\boldsymbol{r})\hat{n}(\boldsymbol{r}) + \lambda \hat{U}_{\mathrm{ee}}, \tag{2.70}$$

in which the external potential, denoted by u_λ, is chosen in such a way that the ground-state density at coupling constant λ is equal to the ground state for any given interaction strength. That is, for all $0 \leq \lambda \leq 1$,

$$n_\lambda(\boldsymbol{r}) = \langle \Psi_\lambda | \hat{n}(\boldsymbol{r}) | \Psi_\lambda \rangle \equiv n(\boldsymbol{r}), \tag{2.71}$$

where we have introduced the ground-state wave function $|\Psi_\lambda\rangle$ for the λ-dependent system such that

$$\hat{H}(\lambda)\,|\Psi_\lambda\rangle = E(\lambda)\,|\Psi_\lambda\rangle\,. \tag{2.72}$$

The external potential u_λ reduces to the physical external potential of the fully interacting system at $\lambda = 1$, $u_{\lambda=1}(\boldsymbol{r}) = v_{\mathrm{ext}}(\boldsymbol{r})$. In the context of KS-DFT, the reference Hamiltonian, given by (2.70) at $\lambda = 0$, is the Hamiltonian of the KS system, meaning that $u_{\lambda=0}(\boldsymbol{r}) = v_{\mathrm{KS}}(\boldsymbol{r})$.

Adopting the normalization condition $\langle \Psi_\lambda | \Psi_\lambda \rangle = 1$, an application of the Hellmann-Feynman theorem [see, for example, Engel and Dreizler, 2011; Nguyen, 2008] leads to the expression

$$\begin{aligned} \frac{d}{d\lambda}E(\lambda) &= \frac{d}{d\lambda}\left\langle \Psi_\lambda \middle| \hat{H}(\lambda) \middle| \Psi_\lambda \right\rangle \\ &= \langle \Psi_\lambda | \int d\boldsymbol{r}\, \hat{n}(\boldsymbol{r}) \frac{\partial u_\lambda}{\partial \lambda} | \Psi_\lambda \rangle + \left\langle \Psi_\lambda \middle| \hat{U}_{\mathrm{ee}} \middle| \Psi_\lambda \right\rangle, \end{aligned} \tag{2.73}$$

[8] This hierarchy is the well known "Jacob's Ladder" of density-functional approximations for the xc energy.

from which we can express the ground-state energy $E_0 = E(\lambda = 1)$ in terms of an integration with respect to the coupling constant as

$$E_0 = E(1) = E(0) + \int d\boldsymbol{r} \left[v_{\text{ext}}(\boldsymbol{r}) - v_{\text{KS}}(\boldsymbol{r}) \right] n(\boldsymbol{r}) + \int_0^1 d\lambda \left\langle \Psi_\lambda \middle| \hat{U}_{\text{ee}} \middle| \Psi_\lambda \right\rangle. \tag{2.74}$$

Recalling that $E(\lambda = 0)$ corresponds to (2.59) with $v_{\text{s}}(\boldsymbol{r}) = v_{\text{KS}}(\boldsymbol{r})$,

$$E(0) = T_{\text{s}}[n] + \int d\boldsymbol{r}\, v_{\text{KS}}(\boldsymbol{r}) n(\boldsymbol{r}), \tag{2.75}$$

and $E(\lambda = 1)$ is the energy of the total many-body electronic Hamiltonian given by (2.50), expression (2.74) leads to the equality

$$\left\langle \hat{T} \right\rangle + \left\langle \hat{U}_{\text{ee}} \right\rangle - T_{\text{s}}[n] = \int_0^1 d\lambda \left\langle \Psi_\lambda \middle| \hat{U}_{\text{ee}} \middle| \Psi_\lambda \right\rangle. \tag{2.76}$$

Recalling the definition of the xc energy functional $E_{\text{xc}}[n]$ within KS-DFT given by (2.63), the first term of (2.76) can be conveniently expressed as $E_{\text{H}}[n] + E_{\text{xc}}[n]$ yielding the identity [Nguyen, 2008]

$$E_{\text{Hxc}}[n] \equiv E_{\text{H}}[n] + E_{\text{xc}}[n] = \int_0^1 d\lambda \left\langle \Psi_\lambda \middle| \hat{U}_{\text{ee}} \middle| \Psi_\lambda \right\rangle. \tag{2.77}$$

Equation (2.77) shows that the unknown xc energy functional in KS-DFT can be formally constructed by adiabatically switching on the Coulomb interaction between electrons while keeping the electron density fixed at its physical value [Ren *et al.*, 2012b]. The right hand side of (2.77) can be rewritten in terms of the two-body density matrix $n_2(\boldsymbol{r}, \boldsymbol{r}')$, in analogy to (2.26), as

$$E_{\text{Hxc}}[n] = \int_0^1 d\lambda \int\int d\boldsymbol{r}\, d\boldsymbol{r}' \frac{n_{2\lambda}(\boldsymbol{r}, \boldsymbol{r}')}{|\boldsymbol{r} - \boldsymbol{r}'|}, \tag{2.78}$$

where $n_{2\lambda}(\boldsymbol{r}, \boldsymbol{r}')$ takes the form, using (2.22), (2.20) and (2.71), of [Dobson, 2006]

$$\begin{aligned} n_{2\lambda}(\boldsymbol{r}, \boldsymbol{r}') &= \left\langle \Psi_\lambda \middle| \hat{n}_2 \middle| \Psi_\lambda \right\rangle \\ &= \frac{1}{2} \langle \Psi_\lambda | \sum_{i \neq j}^{N} \delta(\boldsymbol{r} - \boldsymbol{r}_i) \delta(\boldsymbol{r}' - \boldsymbol{r}_j) | \Psi_\lambda \rangle \\ &= \frac{1}{2} \left\{ \langle \Psi_\lambda | \sum_{i}^{N} \delta(\boldsymbol{r} - \boldsymbol{r}_i) \sum_{j}^{N} \delta(\boldsymbol{r}' - \boldsymbol{r}_j) | \Psi_\lambda \rangle - \delta(\boldsymbol{r} - \boldsymbol{r}') \langle \Psi_\lambda | \sum_{i}^{N} \delta(\boldsymbol{r} - \boldsymbol{r}_i) | \Psi_\lambda \rangle \right\} \\ &= \frac{1}{2} \left\{ \left\langle \Psi_\lambda \middle| \hat{n}(\boldsymbol{r}) \hat{n}(\boldsymbol{r}') \middle| \Psi_\lambda \right\rangle - \delta(\boldsymbol{r} - \boldsymbol{r}') n(\boldsymbol{r}) \right\}. \end{aligned} \tag{2.79}$$

Let us now introduce the density fluctuation operator

$$\delta\hat{n}(\boldsymbol{r}) = \hat{n}(\boldsymbol{r}) - n(\boldsymbol{r}), \tag{2.80}$$

which describes spontaneous density fluctuations around the expectation value of the operator $\hat{n}(\boldsymbol{r})$ [Dobson, 2006; Ren *et al.*, 2012b]. It is worth mentioning that density fluctuations found away from their expectation value $n(\boldsymbol{r})$ produce electric fields leading to the van der Waals energy [Dobson, 2006]. The next step is to insert $\hat{n}(\boldsymbol{r}) = \delta\hat{n}(\boldsymbol{r}) + n(\boldsymbol{r})$

into (2.79) and note that $\langle\Psi_\lambda|\delta\hat{n}(\boldsymbol{r})|\Psi_\lambda\rangle = 0$ in order to obtain the final form of $n_{2\lambda}(\boldsymbol{r},\boldsymbol{r}')$ as

$$n_{2\lambda}(\boldsymbol{r},\boldsymbol{r}') = \frac{1}{2}\left\{\left\langle\Psi_\lambda\left|\,\delta\hat{n}(\boldsymbol{r})\delta\hat{n}(\boldsymbol{r}')\,\right|\Psi_\lambda\right\rangle + n(\boldsymbol{r})n(\boldsymbol{r}') - \delta(\boldsymbol{r}-\boldsymbol{r}')n(\boldsymbol{r})\right\}. \tag{2.81}$$

If we introduce the second term on the right hand side of (2.81) into the AC formula (2.78), we shall notice that the result is the term corresponding to the Hartree energy $E_{\mathrm{H}}[n]$ given by (2.28). The other two terms thus provide us with an exact expression for the xc energy functional which takes the form of [Ren *et al.*, 2012b]

$$E_{\mathrm{xc}}[n] = \frac{1}{2}\int_0^1 d\lambda \int\int d\boldsymbol{r}\, d\boldsymbol{r}' \frac{n_{\mathrm{xc}}^\lambda(\boldsymbol{r},\boldsymbol{r}')n(\boldsymbol{r})}{|\boldsymbol{r}-\boldsymbol{r}'|}, \tag{2.82}$$

where $n_{\mathrm{xc}}^\lambda(\boldsymbol{r},\boldsymbol{r}')$ is known as the xc hole and is given by

$$n_{\mathrm{xc}}^\lambda(\boldsymbol{r},\boldsymbol{r}') = \frac{\left\langle\Psi_\lambda\left|\,\delta\hat{n}(\boldsymbol{r})\delta\hat{n}(\boldsymbol{r}')\,\right|\Psi_\lambda\right\rangle}{n(\boldsymbol{r})} - \delta(\boldsymbol{r}-\boldsymbol{r}'). \tag{2.83}$$

Equations (2.82) and (2.83) show that the xc energy[9] is given in terms of the density-density correlation function $\langle\Psi_\lambda|\delta\hat{n}(\boldsymbol{r})\delta\hat{n}(\boldsymbol{r}')|\Psi_\lambda\rangle$, which describes the correlation between density fluctuations at $\boldsymbol{r}$ with those occurring at $\boldsymbol{r}'$ [Dobson, 2006]. In physical terms, the xc hole $n_{\mathrm{xc}}^\lambda(\boldsymbol{r},\boldsymbol{r}')$ can be interpreted as the depletion of electron density at point $\boldsymbol{r}'$ caused by the presence of an electron at point $\boldsymbol{r}$ [Ren *et al.*, 2012b]. In terms of the pair-correlation function $g(\boldsymbol{r},\boldsymbol{r}')$ defined in (2.27), $n_{\mathrm{xc}}^\lambda(\boldsymbol{r},\boldsymbol{r}')$ takes the form of

$$n_{\mathrm{xc}}^\lambda(\boldsymbol{r},\boldsymbol{r}') = n(\boldsymbol{r}')\left[g_\lambda(\boldsymbol{r},\boldsymbol{r}') - 1\right]. \tag{2.84}$$

Any approximation to n_{xc}^λ or g_λ defines an approximation for the xc energy functional. The density-density correlation function can also be related to the response properties of the system, which we will discuss in more detail later on (see page 29).

The xc energy functional can also be written as the Coulomb interaction between the electron density $n(\boldsymbol{r})$ and a displaced charge density [Kohanoff, 2006; Parr and Yang, 1989]. To this end, we can define the xc hole in terms of its average over the coupling constant λ as

$$\bar{n}_{\mathrm{xc}}(\boldsymbol{r},\boldsymbol{r}') = \int_0^1 d\lambda\; n_{\mathrm{xc}}^\lambda(\boldsymbol{r},\boldsymbol{r}'), \tag{2.85}$$

where $\bar{n}_{\mathrm{xc}}(\boldsymbol{r},\boldsymbol{r}')$ is known as the average xc hole [Martin, 2004; Parr and Yang, 1989]. The xc energy functional can then be written in terms of the average xc hole as

$$E_{\mathrm{xc}}[n] = \frac{1}{2}\int\int d\boldsymbol{r}\, d\boldsymbol{r}' \frac{\bar{n}_{\mathrm{xc}}(\boldsymbol{r},\boldsymbol{r}')n(\boldsymbol{r})}{|\boldsymbol{r}-\boldsymbol{r}'|}. \tag{2.86}$$

The average xc hole $\bar{n}_{\mathrm{xc}}$ can be interpreted according to (2.86) as a fictitious charge depletion due to exchange and correlation effects.[10] This means that the xc hole contains exactly one displaced electron and follows the sum rule given by $\int d\boldsymbol{r}'\,\bar{n}_{\mathrm{xc}}(\boldsymbol{r},\boldsymbol{r}') = \int d\boldsymbol{r}\,\bar{n}_{\mathrm{xc}}(\boldsymbol{r},\boldsymbol{r}') = -1$ [Kohanoff, 2006]. This sum rule places constraints on any approximate forms that may be proposed and serves, along with the analysis of the nature of $\bar{n}_{\mathrm{xc}}(\boldsymbol{r},\boldsymbol{r}')$, as one of the primary approaches to develop improved approximations for $E_{\mathrm{xc}}[n]$ [Martin, 2004].

[9] The important result given in (2.82) was independently developed [see, for example, Kohn, 1999; Parr and Yang, 1989] by Harris and Jones [1974]; Langreth and Perdew [1975]; and Gunarsson and Lundqvist [1976].

[10] The integral given in (2.86) involves only the spherically averaged behavior of $n_{\mathrm{xc}}(\boldsymbol{r},\boldsymbol{r}')$ [Parr and Yang, 1989].

The local-density approximation

The local-density approximation (LDA) is considered the "mother" of almost all approximations in use in DFT [Kohn, 1999]. It was proposed by Kohn and Sham [1965] but its philosophy was already present in TFD theory. Its main idea is to consider a general inhomogeneous electronic system as locally homogeneous using the xc hole corresponding to the homogeneous electron gas [Kohanoff, 2006].[11]

The ingenious explicit separation of the independent-particle kinetic energy and the long-range Hartree terms in KS-DFT offers the possibility of reasonably approximating the xc functional $E_{\rm xc}[n]$ as a local or nearly local functional of the density. In practice, this means that $E_{\rm xc}$ can be given –in analogy to (2.35)– as

$$E_{\rm xc}^{\rm LDA}[n] = \int d\boldsymbol{r}\; n(\boldsymbol{r})\varepsilon_{\rm xc}^{\rm heg}[n(\boldsymbol{r})], \tag{2.87}$$

in which the xc energy density $\varepsilon_{\rm xc}^{\rm heg}$ at each point is assumed to be the same as in a homogeneous electron gas with that density [Martin, 2004]. By comparing (2.86) and (2.87), we shall notice that we can recover an expression for the xc energy in terms of the average xc hole if

$$\varepsilon_{\rm xc}^{\rm heg}[n] = \frac{1}{2}\int d\boldsymbol{r}'\,\frac{\bar{n}_{\rm xc}^{\rm LDA}(\boldsymbol{r},\boldsymbol{r}')}{|\boldsymbol{r}-\boldsymbol{r}'|}, \tag{2.88}$$

where $\bar{n}_{\rm xc}^{\rm LDA}(\boldsymbol{r},\boldsymbol{r}')$ is the average xc hole given in the LDA. In principle, $\varepsilon_{\rm xc}$ is an extremely complex functional of the full density, but in the LDA it becomes just a functional of the local density because it corresponds to a homogeneous system where n is the same everywhere [Kohanoff, 2006]. These considerations finally lead to the form of the average xc hole in the LDA, which is given by

$$\bar{n}_{\rm xc}^{\rm LDA}(\boldsymbol{r},\boldsymbol{r}') = n(\boldsymbol{r})\left[\bar{g}_{\rm heg}\big(|\boldsymbol{r}-\boldsymbol{r}'|;n(\boldsymbol{r})\big)-1\right], \tag{2.89}$$

where $\bar{g}_{\rm heg}\big(|\boldsymbol{r}-\boldsymbol{r}'|;n(\boldsymbol{r})\big)$ is, in analogy to (2.84), the λ-averaged pair correlation function of the homogeneous electron gas of density n.

From a practical point of view, the xc energy within the LDA is calculated via (2.87) using $\varepsilon_{\rm xc}^{\rm heg}[n] = \varepsilon_{\rm x}^{\rm heg}[n] + \varepsilon_{\rm c}^{\rm heg}[n]$ [Kohanoff, 2006]. The exchange energy density $\varepsilon_{\rm x}^{\rm heg}[n]$ is given according to Dirac's expression (2.39) as $\varepsilon_{\rm x}^{\rm heg}[n] = -C_{\rm x}n^{1/3}$. In the case of the correlation energy density $\varepsilon_{\rm c}^{\rm heg}[n]$, the most accurate results are based on the quantum Monte Carlo simulations of Ceperley and Alder [1980], which are exact within numerical accuracy and have been parametrized for the spin-polarized and spin-unpolarized homogeneous electron gas [Kohanoff, 2006]. The expression for $\varepsilon_{\rm c}^{\rm heg}[n]$ and a more in depth treatment of the homogeneous electron gas and the LDA can be found, for example, in Parr and Yang [1989]; Kohanoff [2006]; and Martin [2004].

The LDA is a very successful approximation especially for those systems where the electronic density is quite uniform such as bulk metals, but also for less uniform systems such as molecules, semiconductors, and ionic crystals [Kohanoff, 2006]. However, the LDA tends to overestimate the bonding strength, resulting in bond lengths that are

[11] The xc hole for the homogeneous electron gas is known to an excellent accuracy. It has been calculated by quantum Monte Carlo methods at full coupling strength $\lambda = 1$ [see, for example, Martin, 2004; Kohanoff, 2006].

too short or tending to favor close-packed structures. It also overestimates atomization energies in the order of 1 eV, much larger than the desired "chemical accuracy" of around 0.05 eV [Kümmel and Kronik, 2006].

The generalized-gradient approximation

The first step to go beyond the LDA and address the inhomogeneities in the electron density is to carry out an expansion of the density in terms of the gradient and higher order derivatives. To this end, the xc energy of (2.87) can be written in a generalized form as

$$E_{\mathrm{xc}}^{\mathrm{GE}}[n] = \int d\boldsymbol{r}\; n(\boldsymbol{r})\varepsilon_{\mathrm{xc}}[n(\boldsymbol{r})]\, F_{\mathrm{xc}}\left[n(\boldsymbol{r}), \nabla n(\boldsymbol{r}), \nabla^2 n(\boldsymbol{r}), \ldots\right], \tag{2.90}$$

where F_{xc} is a dimensionless enhancement factor that modifies the LDA expression according to the variation of the density in the vicinity of the considered point [Kohanoff, 2006]. Gradient expansions are a semi-local approach which, however, will hardly be able to capture non-local effects at longer ranges (vdW interactions, for example).

The low-order expansions of the exchange and correlation energies are known, but the approximations based on gradient expansions do not lead to consistent improvements over the LDA. The expansion breaks down because of the large gradients present in real materials. The generalized gradient approximations (GGAs) correspond to a number of proposed second-order gradient expansions which behavior at large gradients is modified to preserve certain desired properties such as the exact conditions required for the exchange and correlation holes [Martin, 2004; Kohanoff, 2006]. In this regard, there is only one defined LDA but many possible GGAs.

We rewrite equation (2.90) in its GGA form as [Martin, 2004; Perdew *et al.*, 1996]

$$\begin{aligned} E_{\mathrm{xc}}^{\mathrm{GGA}}[n] &= \int d\boldsymbol{r}\; n(\boldsymbol{r})\varepsilon_{\mathrm{xc}}^{\mathrm{GGA}}[n(\boldsymbol{r}), |\nabla n(\boldsymbol{r})|] \\ &= \int d\boldsymbol{r}\; n(\boldsymbol{r})\varepsilon_{\mathrm{x}}^{\mathrm{heg}}\big(n(\boldsymbol{r})\big) F_{\mathrm{xc}}\big(n(\boldsymbol{r}), |\nabla n(\boldsymbol{r})|\big), \end{aligned} \tag{2.91}$$

where the best choice for the enhancement factor F_{xc} is the subject matter in the development of GGAs. Much work has been done on GGAs [see for example Kohanoff, 2006; Martin, 2004], but we focus here on the first-principles GGAs proposed by Perdew, Burke, and Ernzerhof (PBE) [Perdew *et al.*, 1996].

A first-principles GGA is constructed [as found in Perdew *et al.*, 1996] starting from the second-order density gradient expansion for the xc hole surrounding an electron in a system of slowly varying density and finally cutting off its long-range parts to satisfy sum rules on the exact hole. The functional proposed by Perdew and Wang (PW91) [Perdew and Wang, 1992] is an analytic fit to this numerical GGA which is designed to satisfy several exact conditions. The PBE functional takes the general features of the underlying construction given by the PW91 functional, but in contrast to the latter, it is designed to satisfy only those exact conditions –not necessarily unique however– that are deemed to be energetically significant [Perdew *et al.*, 1996].

The PBE functional for exchange is given by a simple form of the enhancement factor F_{x} over local exchange –as defined in (2.91)– which depends on the local Seitz radius[12]

[12] The Seitz radius or density parameter r_s is defined as the radius of a sphere containing one electron on average: $\frac{4}{3}\pi r_s^3 = n^{-1}$. In the homogeneous electron gas, it constitutes a measure of the average distance between electrons and characterizes its density n [Martin, 2004].

$r_s = \left(\frac{3}{4\pi n}\right)^{1/3}$, the magnetization density ζ (in the spin-dependent case),[13] and the dimensionless density gradient $s = |\nabla n(\boldsymbol{r})|/(2k_F n)$, where $k_F = (\frac{9}{4}\pi)/r_s$ is the Fermi wave vector. It takes the form

$$F_{\mathrm{x}}(s) = 1 + \kappa - \frac{\kappa}{1 + \mu s^2/\kappa}, \tag{2.92}$$

where κ, μ, and the specific form of (2.92) are chosen to satisfy several formal conditions and recover some limits found in the LDA [see Perdew *et al.*, 1996].

The correlation energy in PBE is expressed as the local correlation plus a correction term $H(r_s, \zeta, t)$ defined to satisfy several conditions and properties [see Perdew *et al.*, 1996]. It has the following form

$$E_{\mathrm{c}}^{\mathrm{GGA}}[n] = \int d\boldsymbol{r}\; n\left[\varepsilon_{\mathrm{c}}^{\mathrm{heg}}(r_s, \zeta) + H(r_s, \zeta, t)\right], \tag{2.93}$$

where the correlation correction term $H(r_s, \zeta, t)$ depends on the local Seitz radius r_s, the magnetization density ζ, and another dimensionless gradient t.[14] The PBE functional is very satisfactory from the theoretical point of view: it satisfies many of the exact conditions for the xc hole and it does not contain any empirical fitting parameters [Kohanoff, 2006].

In comparison to the LDA, GGAs tend to improve total energies, atomization energies, energy barriers, and structural energy differences [Perdew *et al.*, 1996]. GGAs also typically favor density inhomogeneities more than the LDA does. An important deficiency in the GGAs (and the LDA as well) however is the presence of the self-interaction present in the Hartree term. The KS-DFT energy functional of (2.62) partitions arbitrarily the energy due to the electron-electron interaction into a classical term, the Hartree term of (2.28), and a nonclassical part found in the definition of the xc energy of (2.63). The Hartree term has an inherent error in its expression caused by the self-interaction of an electron with itself, which is known as self-interaction error (SIE) [Kümmel and Kronik, 2006; Martin, 2004].

The electron-electron interaction could, in principle, be handled exactly in DFT, consequently canceling any error that is present in the Hartree term. However, complete error cancellation is only guaranteed for the exact xc functional. Hence, only partial cancellation is obtained within the LDA or the GGAs. The SIE is one of the most fundamental deficiencies in approximate KS-DFT that could lead to important consequences. Kümmel and Kronik [2006] point out that the SIE leads to a destabilization of localized orbitals, diminishing their binding energy. This causes that the LDA or the GGAs may fail in the qualitative treatment of localized states, resulting in a qualitative erroneous picture of the electronic-structure whenever there is a significant interaction between localized and delocalized states [Kümmel and Kronik, 2006]. A scenario like this is common when studying defects in solids, transition-metal oxides, or the interaction between localized $4f$ electrons and itinerant s-d electrons in rare-earth metals for example. The erroneous treatment within KS-DFT of the photoemission spectra and electron transfer processes in interfaces formed between organic molecules and metal surfaces are also a consequence of the SIE [Tkatchenko *et al.*, 2010].

[13] The magnetization or spin-polarization density ζ is defined as $\zeta(\boldsymbol{r}) = n^{\uparrow}(\boldsymbol{r}) - n^{\downarrow}(\boldsymbol{r})$.

[14] See Martin [2004]; Kohanoff [2006]; or Perdew *et al.* [1996] for details on the form of the correction term $H(r_s, \zeta, t)$ and the dimensionless gradient t.

Beyond the GGAs lies the meta-generalized gradient approximations (which consider the fourth-order gradient expansion of the xc energy) and orbital-dependent functionals within the KS framework [see Perdew and Schmidt, 1994, for a hierarchical scheme of approximations for the xc functional]. Treatments including exact exchange or orbital-dependent functionals are ways to overcome the SIE in KS-DFT. As a special case of orbital-dependent functionals, the so-called hybrid functionals combine a fraction of exact exchange (defined in the context of KS-DFT) with a fraction of semi-local exchange and correlation.[15] As a final remark, the LDA and its improvements are naturally inappropriate for all those systems for which the starting point of an electron gas of slowly varying density is fundamentally incorrect, such as van der Waals energies between nonoverlapping subsystems or materials with strongly correlated electrons [Kohn, 1999].

The random-phase approximation for the electron correlation

The computational efficiency and the relative accuracy in many polyatomic systems of conventional xc functionals such as the LDA or GGAs have a major contribution to the success of DFT in first-principles materials science. However, as mentioned before, these approximations have well-known shortcomings such as the self-interaction error in the Hartree term and the lack of non-local effects in the correlation energy. It is in this context that the treatment of exchange and correlation in terms of exact exchange plus correlation in the random-phase approximation (RPA) [Ren *et al.*, 2012b] becomes a promising approach. Especially, we are interested in the fact that the correlation energy in the RPA is fully non local and includes long-range van der Waals interactions automatically and seamlessly [Ren *et al.*, 2012b]. Because of this fact, the RPA correlation energy can also be used as a tool in testing and developing approximations for vdW-inclusive DFT approaches.

The RPA for correlation energy can be introduced in the context of KS-DFT via the adiabatic connection fluctuation-dissipation theorem (ACFD). This is achieved by formulating the density-density correlation function, found implicitly in the AC formula for exchange and correlation (2.82), in terms of the linear density-response function, $\langle\Psi_\lambda|\delta\hat{n}(\boldsymbol{r})\delta\hat{n}(\boldsymbol{r}')|\Psi_\lambda\rangle$, of the $\lambda-$scaled system described in page 23. The fluctuation-dissipation theorem (FDT) is the technique that can be used to make this connection. The FDT states that the response of a system at thermodynamic equilibrium to a small external perturbation is the same as its response to the spontaneous internal fluctuations in the absence of the perturbation [as found in Ren *et al.*, 2012b]. Thus, the FDT relates the correlations of electron positions in the absence of an external influence to the response of the electrons in the presence of a time-dependent external influence [Dobson, 1994]. The zero temperature FDT leads to [see for example Ren *et al.*, 2012b]

$$\left\langle \Psi_\lambda \left| \delta\hat{n}(\boldsymbol{r})\delta\hat{n}(\boldsymbol{r}') \right| \Psi_\lambda \right\rangle = -\frac{1}{\pi}\int_0^\infty d\omega \,\mathrm{Im}\,\chi_\lambda(\boldsymbol{r},\boldsymbol{r}',\omega), \tag{2.94}$$

where $\chi_\lambda(\boldsymbol{r},\boldsymbol{r}',\omega)$ is the linear density-response function of the $\lambda-$scaled system. By using expressions (2.82), (2.83), (2.94), and $v(\boldsymbol{r},\boldsymbol{r}') = |\boldsymbol{r}-\boldsymbol{r}'|^{-1}$, the ACFD formula for the

[15] See Kümmel and Kronik [2006] for a detailed review on orbital-dependent functionals.

xc energy within KS-DFT is obtained as

$$E_{\mathrm{xc}} = \frac{1}{2}\int_0^1 d\lambda \int\int d\boldsymbol{r}\, d\boldsymbol{r}'\, v(\boldsymbol{r},\boldsymbol{r}') \left[-\frac{1}{\pi}\int_0^\infty d\omega \chi_\lambda(\boldsymbol{r},\boldsymbol{r}',i\omega) - \delta(\boldsymbol{r}-\boldsymbol{r}')n(\boldsymbol{r})\right], \tag{2.95}$$

where we have used the fact that, because of its analytical structure, $\chi_\lambda(\boldsymbol{r},\boldsymbol{r}',\omega)$ becomes real on the imaginary axis so the frequency integration can also be performed along the imaginary axis [Ren *et al.*, 2012b]. An equivalent expression based on (2.95) can be obtained for the exact-exchange energy within KS-DFT,

$$E_{\mathrm{x}} = \frac{1}{2}\int_0^1 d\lambda \int\int d\boldsymbol{r}\, d\boldsymbol{r}'\, v(\boldsymbol{r},\boldsymbol{r}') \left[-\frac{1}{\pi}\int_0^\infty d\omega \chi_0(\boldsymbol{r},\boldsymbol{r}',i\omega) - \delta(\boldsymbol{r}-\boldsymbol{r}')n(\boldsymbol{r})\right], \tag{2.96}$$

and the correlation energy

$$E_{\mathrm{c}} = -\frac{1}{2\pi}\int_0^1 d\lambda \int\int d\boldsymbol{r}\, d\boldsymbol{r}'\, v(\boldsymbol{r},\boldsymbol{r}') \left[\int_0^\infty d\omega \chi_\lambda(\boldsymbol{r},\boldsymbol{r}',i\omega) - \chi_0(\boldsymbol{r},\boldsymbol{r}',i\omega)\right]. \tag{2.97}$$

In a system with a coupling constant λ, the density-response function χ_λ can be related to the noninteracting limit ($\lambda = 0$) response function via the self-consistent Dyson-like screening equation [see, for example, Gross and Burke, 2006; Dobson, 2006; Lu *et al.*, 2010],

$$\begin{aligned}\chi_\lambda(\boldsymbol{r},\boldsymbol{r}',i\omega) = \chi_0(\boldsymbol{r},\boldsymbol{r}',i\omega) \\ + \int\int d\boldsymbol{r}_1\, d\boldsymbol{r}_2 \chi_0(\boldsymbol{r},\boldsymbol{r}_1,i\omega)\left[\frac{\lambda}{|\boldsymbol{r}_1-\boldsymbol{r}_2|} + f_{\mathrm{xc}}^\lambda(\boldsymbol{r}_1,\boldsymbol{r}_2,i\omega)\right]\chi_\lambda(\boldsymbol{r}_2,\boldsymbol{r}',i\omega),\end{aligned} \tag{2.98}$$

where χ_0 is the response function of the system at $\lambda = 0$ which in this case corresponds to the response function of the KS reference system. It is known in terms of the single-particle KS orbitals ψ_i, along with the corresponding eigenvalues ε_i and occupation numbers f_i [see (2.58)], as

$$\chi_0(\boldsymbol{r},\boldsymbol{r}',i\omega) = \sum_{\sigma,\sigma'}\sum_{ij}(f_i - f_j)\frac{\psi_i^*(\boldsymbol{r},\sigma)\psi_j(\boldsymbol{r},\sigma')\psi_j^*(\boldsymbol{r}',\sigma')\psi_i(\boldsymbol{r}',\sigma)}{\varepsilon_i - \varepsilon_j + i\omega}. \tag{2.99}$$

The exchange-correlation kernel $f_{\mathrm{xc}}^\lambda(\boldsymbol{r}_1,\boldsymbol{r}_2,i\omega)$ of (2.98) is on the other hand not known. The RPA consists in setting $f_{\mathrm{xc}}^\lambda = 0$, providing a simple approximation to the linear density-response function χ_λ. The xc energy can then be separated in the RPA into two terms, one for the exact-exchange energy and another for the RPA-correlation energy as

$$E_{\mathrm{xc}}^{\mathrm{RPA}} = E_{\mathrm{x}}^{\mathrm{EX}} + E_{\mathrm{c}}^{\mathrm{RPA}}, \tag{2.100}$$

where the exact non-local exchange (EX) energy $E_{\mathrm{x}}^{\mathrm{EX}}$ is given in the framework of KS-DFT by inserting the expression for χ_0 of (2.99) into the formula (2.96) [see, for example, Dobson and Gould, 2012; Ren *et al.*, 2012a]. The RPA-correlation energy (cRPA) $E_{\mathrm{c}}^{\mathrm{RPA}}$ takes the form, in accordance to (2.97), of

$$E_{\mathrm{c}}^{\mathrm{RPA}} = -\frac{1}{2\pi}\int\int d\boldsymbol{r}\, d\boldsymbol{r}'\, v(\boldsymbol{r},\boldsymbol{r}')\int_0^\infty d\omega\left[\int_0^1 d\lambda \chi_\lambda^{\mathrm{RPA}}(\boldsymbol{r},\boldsymbol{r}',i\omega) - \chi_0(\boldsymbol{r},\boldsymbol{r}',i\omega)\right], \tag{2.101}$$

where $\chi_\lambda^{\mathrm{RPA}}$ is given by (2.98) with $f_{\mathrm{xc}}^\lambda = 0$. The correlation energy of the system is now written in terms of the response functions of a series of fictitious systems along the AC

path. The λ integration of (2.101) can be carried out analytically yielding [Dobson and Gould, 2012; Ren *et al.*, 2012a]

$$E_{\rm c}^{\rm RPA} = \frac{1}{2\pi}\int_0^\infty d\omega \mathrm{Tr}\left[\log(1-\chi_0(i\omega)v)+\chi_0(i\omega)v\right] \tag{2.102}$$

$$= -\frac{1}{2\pi}\int_0^\infty d\omega \sum_{n=2}^{\infty}\frac{1}{n}\mathrm{Tr}\left[(\chi_0(i\omega)v)^n\right], \tag{2.103}$$

where

$$\mathrm{Tr}[AB] = \int d\boldsymbol{r}\, d\boldsymbol{r}' A(\boldsymbol{r},\boldsymbol{r}')B(\boldsymbol{r}',\boldsymbol{r}). \tag{2.104}$$

Alternatively, the RPA correlation energy (2.101) can be written in terms of the expansion in powers of the fully interacting RPA response function $\chi \equiv \chi_1^{\rm RPA}$ as [Lu *et al.*, 2010]

$$E_{\rm c}^{\rm RPA} = -\frac{1}{2\pi}\int_0^\infty d\omega \sum_{n=2}^{\infty}(-1)^n\left(1-\frac{1}{n}\right)\mathrm{Tr}\left[(\chi(i\omega)v)^n\right]. \tag{2.105}$$

The EX+cRPA method is an orbital-dependent functional within the KS-DFT framework that can be solved self-consistently, but this represents a formidable task in numerical terms. In practical terms, EX+cRPA calculations are commonly performed based on preceding reference calculations in a post-processing fashion where single-particle orbitals from a self-consistent KS-DFT calculation in the LDA or GGA are used to evaluate both the EX and cRPA terms.

Despite the fact that the EX+cRPA technique is a very promising non-local method to include correlation energy in the KS-DFT framework, there are some shortcomings of this method like its systematic underestimation of binding energies and the fact that it is sometimes sensitive to the input orbitals. Another well-accepted fact is that short-range correlations are not adequately described within the RPA, which has triggered the development of range-separated frameworks in which the long-range part of the cRPA energy is explicitly included but the short/mid-range correlation is treated in a different manner. Moreover, the development of methods that go beyond the standard RPA has become a very active research field in recent years. We refer the interested reader to the reviews by Ren *et al.* [2012b]; Eshuis *et al.* [2012]; and Dobson and Gould [2012].

2.5 Practical methods to include van der Waals interactions in density-functional approximations

The need for efficient methods that incorporate vdW forces with accuracy has come along with the rise of DFT as the theoretical method of choice for many applications in physics, chemistry, and materials science. The vdW forces are essential in determining the properties of many systems such as biomolecules, molecular crystals, and organic/inorganic interfaces. The term vdW forces is sometimes associated with different types of long-range intermolecular interactions such as electrostatics, induction, and dispersion. These correspond, respectively, to a permanent multipole-permanent multipole interaction, permanent multipole-induced multipole interaction, and the induced multipole-induced multipole interaction [Stone, 2013; Tkatchenko *et al.*, 2010]. In this work, our main concern is the dispersion energy, but as done frequently, we will use the terms “vdW energy” and “dispersion energy” as interchangeable.

Dispersion energy is a quantum-mechanical phenomenon whose origin lies in the correlated motion of electrons. Unfortunately, its modeling in DFT is not an easy task as (semi–)local and hybrid functionals used to approximate the xc energy functional do not include them properly. Due to its importance in many applications, several promising vdW-inclusive approaches in DFT have been developed in recent years. This section is a general review of these methods. As base for our discussion, we follow the classification done in the review by Klimeš *et al.* [2012], meaning that the complexity grows with each tier of methods. We also use concepts from the review papers by Tkatchenko *et al.* [2010] and Dobson and Gould [2012].

2.5.1 Empirical pairwise corrections

The simplest approach to recover the correct long-range asymptotic behavior for particles in the gas phase is to add an additional attractive energy term to the KS-DFT total energy. In this context, the total energy is given by

$$E_{\text{tot}} = E_{\text{DFA}} + E_{\text{vdW}}, \tag{2.106}$$

where E_{DFA} corresponds to the energy of a density-functional approximation (DFA) computed within KS-DFT [see (2.62)] and E_{vdW} is the vdW energy. The vdW energy in this approximation is typically written as a sum of $-C_6^{ab}R_{ab}^{-6}$ terms over all pairs of atoms a and b, where R_{ab} is the distance between atoms a and b and C_6^{ab} is the associated dispersion coefficient, thus considering only the leading-order term for the vdW energy and assuming its pairwise additivity. The fact that the $-C_6R^{-6}$ term diverges at short-range inter-atomic separations is solved by damping the vdW-energy term. These methods have the following general expression for the vdW energy

$$E_{\text{vdW}} = -\frac{1}{2}\sum_{a,b} f_{\text{damp}}\left(R_{ab}, a, b\right)\frac{C_6^{ab}}{R_{ab}^6}, \tag{2.107}$$

where the damping function f_{damp} is equal to one for large R and decreases E_{vdW} to zero or to a constant for small R, eliminating the R^{-6} divergence at short inter-atomic separations. The damping function depends on the definition of the atomic size of pairs a and b (usually vdW radii are used) and must be adjusted with each xc functional in order to be compatible.

Among these type of methods, the schemes developed by Grimme are widely used, in particular the method known as DFT-D2 [Grimme, 2006]. In this method, the computation of dispersion coefficients is based on calculated atomic ionization potentials and static polarizabilities with data given for all elements up to Xe. Although its popularity, low computational cost, and good accuracy for small molecules[16] are attractive features of the DFT-D2 method, it shares some severe limitations along with other methods using empirical pairwise corrections,[17] such as neglecting many-body dispersion effects by only taking the leading term of the vdW interaction. In addition, it is not clear what

[16] 15%-20% error for energies and 0.1-0.2 Å for equilibrium distances [see for example Tkatchenko *et al.*, 2010].

[17] See Klimeš *et al.* [2012] and references within for a comprehensive list of methods including empirical pairwise corrections for the vdW energy.

is the best manner to obtain the C_6 coefficients involving, sometimes, experimental polarizabilities and ionization potentials that are not transferable as data often come from species in organic molecules. Furthermore, the C_6 coefficients are kept constant, ignoring the possibility of effects due to different possible hybridization/oxidation states of atoms in different chemical or geometrical environments [Tkatchenko *et al.*, 2010; Klimeš *et al.*, 2012].

2.5.2 Environment-dependent pairwise methods

The second tier of methods is characterized by the fact that the influence of the environment is incorporated in the determination of the parameters involved in the calculation of the dispersion energy. We focus, in particular, on three methods: the Becke-Johnson (BJ) method, the Tkatchenko-Scheffler (TS) DFA+vdW method [2009], and the DFT-D3 method developed by Grimme *et al.* [2010]. All these three methods are still based on a separation of terms according to (2.106) but share a novel concept, namely the fact that the dispersion coefficient of an atom in a molecule depends on the effective volume of the atom, thus exploiting the relation between volume and polarizability in an atom.

The proposal in the BJ model is that the exchange hole instantaneous dipole moment is the source of dispersion interactions behind nonoverlapping systems. This model exploits the physical interpretation of the xc hole in which there exists a region where the electron density is depleted due to the presence of an electron [see (2.83)]. The asymmetric electron density that follows such depletion creates non-zero dipole and higher electrostatic moments. This causes polarization in other atoms given in some extent by their polarizability. The BJ method then generates dispersion interactions by using the dipole moment of the exchange hole. The dispersion coefficients are calculated using the average square of the hole dipole moment together with isotropic polarizabilities. Two effects modify the dispersion coefficients in the BJ method. The first one is the change given by scaling the polarizabilities of atoms in molecules from their reference values according to their effective atomic volumes. The second is through the changes of the exchange hole, which are a respond to the chemical environment, but are also difficult to quantify in a precise manner.

The DFA+vdW method by Tkatchenko and Scheffler [2009] starts by taking high level quantum-chemistry calculations of atomic polarizabilities and dispersion coefficients for free atoms. Using these as a reference, C_6 coefficients for heteronuclear atoms can be calculated by a simple but powerful combination rule.[18] The next step consists in including the changes that result from the chemical environment, which are obtained from the electron density of the polyatomic system by using effective atomic volumes. The system of interest is divided between the individual atoms using the Hirshfeld partitioning scheme [Hirshfeld, 1977], and for each atom its density is compared to the density of the free atom. The factor that is obtained by this comparison is then used to scale the reference C_6 coefficient, the atomic polarizability, and the vdW radius thus changing the value of the dispersion energy. We will describe this method in more detail in chapter 4 (see section 4.4), where we develop a methodology to include vdW interactions within DFT for adsorption phenomena. As a final remark, it is worth to mention that

[18] See Tkatchenko and Scheffler [2009] or expression (4.29) in section 4.4.

the DFA+vdW method is also a true functional of the density as its recent self-consistent implementation within KS-DFT exemplifies [Ferri *et al.*, 2015].

The DFT-D3 method by Grimme *et al.* [2010] incorporates the effect of the environment in the C_6 coefficient by considering the number of neighbors that each atom has. In this manner, the dispersion coefficient will decrease when an atom has more neighbors. These effects are taken into account by having a set of precalculated C_6 coefficients for various pairs of elements in difference reference states (or, equivalently, different hybridization states). The function calculating the number of neighbors is defined so that it continuously interpolates between the precalculated reference values. As a result, the C_6 coefficient can change continuously if the hybridization state of an atom is changing during a simulation.

2.5.3 Non-local density functionals

The methods in the preceding subsections require the input of predetermined parameters in order to determine the dispersion interaction. We now describe the methods that add the long-range correlations to (semi-)local correlation functionals. These methods are termed non-local vdW functionals.

The non-local (long-range) correlation energy in these functionals is calculated with

$$E_{\mathrm{c}}^{\mathrm{nl}}[n] = \int\int d\boldsymbol{r}\, d\boldsymbol{r}'\, n(\boldsymbol{r})\phi(\boldsymbol{r},\boldsymbol{r}')n(\boldsymbol{r}'), \tag{2.108}$$

where $\phi(\boldsymbol{r},\boldsymbol{r}')$ is an integration kernel with a complicated expression that includes the $\mathcal{O}(|\boldsymbol{r}-\boldsymbol{r}'|^{-6})$ asymptotic behavior. A number of approaches have been proposed in the literature for $E_{\mathrm{c}}^{\mathrm{nl}}$ [see Klimeš *et al.*, 2012; Dobson and Gould, 2012, and references within]. Within these functionals, Dion *et al.* [2004] proposed an approximated ACFD type functional, known as van der Waals density functional (vdW-DF), that is able to evaluate the non-local energy correlation for overlapping molecules and arbitrary geometries. In the vdW-DF, the xc energy is calculated as

$$E_{\mathrm{xc}}^{\mathrm{vdW-DF}}[n] = E_{\mathrm{x}}^{\mathrm{GGA}}[n] + E_{\mathrm{c}}^{\mathrm{LDA}}[n] + E_{\mathrm{c}}^{\mathrm{nl}}[n], \tag{2.109}$$

where the exchange energy is given in the revPBE approximation [Zhang and Yang, 1998]. The vdW-DF is an important conceptual development since it is a functional that combines correlations of all ranges in a single formula, adding dispersion interactions within DFT. A detailed description of the steps to derive the ACFD-type non-local functional, as well as its approximations within the vdW-DF, can be found, for example, in the works by Dobson and Gould [2012] and Lu *et al.* [2010].

The vdW-DF itself overestimates the long-range dispersion but since its development, many studies and proposals have emerged to improve and better understand the method. We find, among these proposals, the vdW-DF2 [Lee *et al.*, 2010], developed by the same group behind the vdW-DF, and the vdW-DF-type functionals with modified (optimized) exchange termed optB88-vdW and optPBE-vdW [Klimeš *et al.*, 2010]. The reader is referred once more to the review by Klimeš *et al.* [2012] and the references found in there for additional information on the developments of non-local functionals.

2.5.4 Methods going beyond pairwise additivity

The methods that we have reviewed in section 2.5.1 and section 2.5.2 so far consider dispersion to be pairwise additive. This assumption has the consequence of, for example, ignoring the role that collective excitations would have in the polarizability of the atoms involved. Let us take for instance the description of organic molecules adsorbed on an inorganic surface, where pairwise interactions vdW methods are frequently employed without any consideration of the relatively strong electrodynamic response screening present within bulk materials [Mercurio *et al.*, 2010; Atodiresei *et al.*, 2009; Stradi *et al.*, 2011; Tonigold and Gross, 2010].[19]

The next tier in vdW-inclusive DFT methods consists in approximations that go beyond the assumption of pairwise additivity. The EX+cRPA method described in page 29 includes many-body effects in the vdW interaction, but it is still computationally expensive for the calculation of realistic systems and sometimes sensitive to the input orbitals [Tkatchenko *et al.*, 2010]. Efforts have recently started to focus on methods treating the vdW interaction beyond the pairwise additivity that are accurate and efficient enough to treat realistic systems such as extended molecules, molecular crystals, and adsorption systems [see, for example, DiStasio Jr. *et al.*, 2014; Klimeš *et al.*, 2012]. Many-body effects in the vdW energy may not play a decisive role in small molecules, but recent studies show that a many-body description of vdW interactions is essential, for example, in extended molecules, molecular solids, and even organic molecules of intermediate size [Tkatchenko *et al.*, 2012; DiStasio Jr. *et al.*, 2012]. Our own recent work has been directed to investigate the influence of many-body dispersion effects in the adsorption of atoms and molecules on metal surfaces [Maurer *et al.*, 2015].

We focus on the approach termed many-body dispersion (MBD) by Tkatchenko *et al.* [2012] which is an efficient and accurate approach that incorporates higher order dispersion terms in the context of DFT. The MBD method maps the atoms in the system onto a set of atom-centered quantum harmonic oscillators using an effective oscillator Hamiltonian and interacting via the dipole-dipole interaction potential. The long-range correlation is treated based on a range-separation of the interelectronic Coulomb potential [Tkatchenko *et al.*, 2013]. Its formulation in terms of the RPA shows that it includes many-body effects in the long-range correlation energy to all orders and that it becomes a very accurate technique when correct polarizabilities are used as input [Ambrosetti *et al.*, 2014a]. This representation, however, assumes a finite electronic gap in order to divide the system into effective atomic fragments, fact which does not provide a complete description of delocalized electrons present, for example, in metallic systems.

2.6 Van der Waals interactions in solids

The role of vdW interactions in solids had not been a matter of extensive study due to the long-time belief that vdW interactions were relatively not important or determinant in the cohesive properties of solids. From a historical perspective, Zhang [2014] traces back the earliest studies of vdW forces in solids to the x-ray measurements of noble-gas solid structures performed in the 1920s [see the text by Zhang, 2014, for the original ref-

[19] A more detailed analysis of the performance of several vdW-inclusive DFT methods is left for later on in chapter 4, section 4.1.

erences]. It was necessary, however, the development of quantum mechanics to fully explain the origin of the interaction among rare gas atoms. The origin of these interactions was solved by London [1930, 1937] with the development of the theory of dispersion forces.[20] The studies on noble-gas solids were eventually followed up by research showing that dispersion interactions can actually contribute to the bonding of ionic and metallic solids as well [see Zhang, 2014, for a more detailed account on the topic].

From a modern materials perspective, it has become clear in the last few years that vdW interactions can play a nonnegligible role in the cohesive properties of hard solids such as ionic solids, semiconductors, and metals [Woods *et al.*, 2015]. For instance, Zhang *et al.* [2011] demonstrated that dispersion interactions account for 10-15% of the cohesive energy and bulk modulus of Si, Ge, GeAs, NaCl, and MgO. In a similar manner, Klimeš *et al.* [2011] found a systematic improvement in the cohesive properties of alkali metals and alkali halides when nonlocal correlations are accounted for through vdW-DF-type functionals with modified (optimized) exchange. Tao *et al.* [2010] also found improvements in the lattice constant of alkali metals by including nonlocal correlation within KS-DFT. Relative stabilities of different solid phases, phase transition pressures, phase diagrams, and defect formation energies are additional solid properties that can be influenced by the description of vdW interactions [see Woods *et al.*, 2015, for a more detailed account].

The description of vdW interactions in metals is a difficult task because of the simultaneous presence of localized and delocalized electronic states. The free electrons in metals give rise to a dynamically screened interaction between the ions that modifies modifying the vdW interaction between atoms. The accurate determination of the vdW contribution in metals has consequently proven to be challenging for theory as estimates have ranged in the past from being negligible to roughly a third of the total cohesive energy [Rehr *et al.*, 1975; Richardson and Mahanty, 1977; Zhang, 2014]. Before addressing the theory of vdW interactions in bulk metals, it is useful to review the phenomenon of screening because an analogous effect plays an important role in the adsorption of atoms and molecules on inorganic substrates such as metal surfaces. It is, in addition, the foundation of the methodology that we propose in the next chapter for the treatment of vdW interactions in adsorption phenomena. As such, we first give a general description of the phenomenon of screening in metals and finally, we address its influence on vdW interactions in metals.

2.6.1 Screening in solids (metals)

A detailed theory describing the screening in a realistic periodic potential of a metal is a very complex problem. A simple way to analyze this problem is to imagine a test positively charged particle placed and held at a specific position inside the electron gas. Our interest is in the dielectric properties of the electron gas, that is, its response to this perturbation. This positive charge will attract electrons in its surroundings creating an excess of negative charge which in turn will reduce (screen) its field. The total effective potential ϕ_{eff} generated like this is formed by two contributions, the first as a consequence of the positively charged particle itself, which we will call ϕ_{ext}, and the second contribution, which is the potential $\delta\phi$ induced by the cloud of screening electrons, so

[20] See the textbook by Kaplan [2006] for a historical survey of intermolecular interactions in general.

that

$$\phi_{\text{eff}} = \phi_{\text{ext}} + \delta\phi. \tag{2.110}$$

These potentials satisfy Poisson's equation,

$$\begin{aligned} -\nabla^2\phi_{\text{eff}} &= 4\pi n_{\text{eff}}, \\ -\nabla^2\phi_{\text{ext}} &= 4\pi n_{\text{ext}}, \\ -\nabla^2\delta\phi &= 4\pi\delta n, \end{aligned} \tag{2.111}$$

where n_{ext} corresponds in this case to the charge density of the positive particle, δn is the electron density induced in the electron gas due to the presence of the positive charged particle, and the effective charge density n_{eff} is given by

$$n_{\text{eff}} = n_{\text{ext}} + \delta n, \tag{2.112}$$

thereby relating each charge distribution with its associated potential.

The external and the effective potentials are related, in analogy to the theory of dielectric media, linearly by [see, for example, Ashcroft and Mermin, 1976; Bruus and Flensberg, 2004]

$$\phi_{\text{ext}}(\boldsymbol{r}, t) = \int dt' \int d\boldsymbol{r}' \epsilon(\boldsymbol{r}\, t, \boldsymbol{r}'\, t')\phi_{\text{eff}}(\boldsymbol{r}, t), \tag{2.113}$$

where $\epsilon(\boldsymbol{r}\, t, \boldsymbol{r}'\, t')$ is the dielectric function which is, in general, non local both in time and space. In the translation-invariant case (the homogeneous electron gas, for example), the dielectric function depends only on the differences of the argument, that is $\epsilon(\boldsymbol{r}\, t, \boldsymbol{r}'\, t') = \epsilon(\boldsymbol{r} - \boldsymbol{r}', t - t')$, so that (2.113) can be formulated in the frequency and momentum space such that after a Fourier transformation in space and time,[21], it assumes the product form of

$$\phi_{\text{ext}}(\boldsymbol{q}, \omega) = \epsilon(\boldsymbol{q}, \omega)\phi_{\text{eff}}(\boldsymbol{q}, \omega). \tag{2.114}$$

Expression (2.114) can be rewritten as

$$\phi_{\text{eff}}(\boldsymbol{q}, \omega) = \frac{1}{\epsilon(\boldsymbol{q}, \omega)}\phi_{\text{ext}}(\boldsymbol{q}, \omega), \tag{2.115}$$

which shows that the q_{th} component of the total potential is equal to the external potential reduced by the factor $1/\epsilon(\boldsymbol{q}, \omega)$ [Ashcroft and Mermin, 1976].

To calculate the dielectric function $\epsilon(\boldsymbol{q}, \omega)$, which is the physical quantity that we are interested in when dealing with screening in metals, we must, however, first turn our attention to the charge density $\delta n(\boldsymbol{r}, t)$ induced in the electron gas by the perturbation, that is, the external potential $\phi_{\text{ext}}(\boldsymbol{r}, t)$. In the case of a self-consistent theory, linear-response theory relates the induced density to the external potential as

$$\delta n(\boldsymbol{q}, \omega) = \chi(\boldsymbol{q}, \omega)\phi_{\text{ext}}(\boldsymbol{q}, \omega), \tag{2.116}$$

[21] The Fourier transforms in this case are defined as

$$\begin{aligned} \epsilon(\boldsymbol{q}, \omega) &= \int d(\boldsymbol{r} - \boldsymbol{r}') \int_{-\infty}^{\infty} d(t - t') e^{-i\boldsymbol{q}\cdot(\boldsymbol{r} - \boldsymbol{r}')} e^{i\omega(t - t')} \epsilon(\boldsymbol{r} - \boldsymbol{r}', t - t'), \\ \epsilon(\boldsymbol{r} - \boldsymbol{r}', t - t') &= \int \frac{d\boldsymbol{q}}{(2\pi)^3} \int_{-\infty}^{\infty} \frac{d\omega}{2\pi} e^{i\boldsymbol{q}\cdot(\boldsymbol{r} - \boldsymbol{r}')} e^{-i\omega(t - t')} \epsilon(\boldsymbol{q}, \omega), \end{aligned}$$

with similar equations for each potential.

where χ is the density-density response function or density-density correlation function which we have first encountered in the RPA for the electron correlation in section 2.4.4 (see page 29). The next step is to write the Fourier transform in space and time of the induced density given in the set of expressions (2.111),

$$q^2\delta\phi = 4\pi\delta n, \tag{2.117}$$

which together with (2.116) lead to the following expression for the induced potential

$$\delta\phi(\boldsymbol{q},\omega) = v_q\chi(\boldsymbol{q},\omega)\phi_{\text{ext}}(\boldsymbol{q},\omega), \tag{2.118}$$

where $v_q = 4\pi q^{-2}$ is the Fourier transform of the Coulomb potential. Using expressions (2.118) and (2.110), the total effective potential can be written in terms of the response function as

$$\phi_{\text{eff}}(\boldsymbol{q},\omega) = \Big[1 + v_q\chi(\boldsymbol{q},\omega)\Big]\,\phi_{\text{ext}}(\boldsymbol{q},\omega). \tag{2.119}$$

By comparing (2.119) and (2.115), we identify the expression for the dielectric function as [Bruus and Flensberg, 2004]

$$\frac{1}{\epsilon(\boldsymbol{q},\omega)} = 1 + v_q\chi(\boldsymbol{q},\omega). \tag{2.120}$$

Expression (2.120) shows us that, in order to calculate the dielectric function and estimate the screening effects in the system, we need to evaluate the response function of the electron gas. In practice, (2.120) can be evaluated under a number of approximations for the density-density response function. Depending on these approximations, it is possible to propose a microscopic dielectric function for metallic systems based, for example, on the homogeneous electron gas.

Several formulations for the response function χ –all of them intimately related– can be found in the literature depending on the particular context. For our discussion we make use of the retarded response function which is given in statistical physics as [Engel and Dreizler, 2011]

$$\begin{aligned}\chi(\boldsymbol{r}\,t,\boldsymbol{r}'\,t') &= -i\Theta(t-t')\left\langle[\delta\hat{n}(\boldsymbol{r},t),\delta\hat{n}(\boldsymbol{r}',t')]\right\rangle \\ &= -i\Theta(t-t')\left\langle[\hat{n}(\boldsymbol{r},t),\hat{n}(\boldsymbol{r}',t')]\right\rangle,\end{aligned} \tag{2.121}$$

where the expectation value is taken for the unperturbed system, $\Theta(t-t')$ is the step function, and the operators $\hat{n}(\boldsymbol{r},t)$ and $\delta\hat{n}(\boldsymbol{r},t)$ have been defined in expressions (2.20) and (2.80), respectively. Solving the density-density response function for the fully interacting system is a very complicated task to which we have already discussed some approximations, within KS-DFT, in the previous section. Because of this reason, it is convenient to first address the case of the noninteracting homogeneous electron gas[22] since an expression for its response function is well known. It becomes an integral over states where $|\boldsymbol{k}| < k_F$ is occupied and $|\boldsymbol{k}+\boldsymbol{q}| > k_F$ is empty with the following expression [Martin, 2004]

$$\chi_0(\boldsymbol{q},\omega) = 2\int^{k=k_F}\frac{d\boldsymbol{k}}{(2\pi)^3}\frac{\Theta(|\boldsymbol{k}+\boldsymbol{q}|-k_F)}{\varepsilon_k - \varepsilon_{|\boldsymbol{k}+\boldsymbol{q}|} - \omega + i\eta}, \tag{2.122}$$

[22] See section 2.4.1.

where $\varepsilon_k = \frac{1}{2}k^2$ and $(k_F)^3 = 3\pi^2 n$. Expression (2.122) is known as the Lindhard function, its explicit expression can be obtained by inserting the eigenstates of the noninteracting homogeneous electron gas in (2.122) and integrating with limit $\eta \to 0^+$.

In the case of theories in which the electrons interact via an effective field, such as those reviewed in this chapter, the Dyson screening equation can be used to expand the response function in terms of its basic building blocs, with an expression of the form [see for example Engel and Dreizler, 2011; Bruus and Flensberg, 2004]

$$\begin{aligned}\chi(\boldsymbol{q},\omega) = &\ \Pi(\boldsymbol{q},\omega) + \Pi(\boldsymbol{q},\omega)\, v_q(\boldsymbol{q})\chi(\boldsymbol{q},\omega) \\ = &\ \frac{\Pi(\boldsymbol{q},\omega)}{1 - v_q(\boldsymbol{q})\Pi(\boldsymbol{q},\omega)},\end{aligned} \tag{2.123}$$

where $\chi(\boldsymbol{q},\omega)$ is expanded in terms of the irreducible or proper polarization $\Pi(\boldsymbol{q},\omega)$. We have already used an equation of the type of (2.123) for expression (2.98) within the context of KS-DFT. With the result given by (2.123), the dielectric function is determined according to (2.120) as

$$\frac{1}{\epsilon(\boldsymbol{q},\omega)} = 1 + v_q \frac{\Pi(\boldsymbol{q},\omega)}{1 - v_q(\boldsymbol{q})\Pi(\boldsymbol{q},\omega)} = \frac{1}{1 - v_q(\boldsymbol{q})\Pi(\boldsymbol{q},\omega)}. \tag{2.124}$$

The lowest-order contribution to χ is the response function of the noninteracting homogeneous electron gas χ_0 given by (2.122). In the RPA, the irreducible polarization is approximated by the noninteracting response function which corresponds to $\Pi(\boldsymbol{q},\omega) \simeq \chi_0(\boldsymbol{q},\omega)$, leading to the full response function in the RPA as [Bruus and Flensberg, 2004]

$$\chi^{\mathrm{RPA}}(\boldsymbol{q},\omega) = \frac{\chi_0(\boldsymbol{q},\omega)}{1 - v_q(\boldsymbol{q})\chi_0(\boldsymbol{q},\omega)}. \tag{2.125}$$

Consequently, the dielectric function in the RPA is given according to (2.124) as

$$\epsilon(\boldsymbol{q},\omega) \simeq \epsilon^{\mathrm{RPA}}(\boldsymbol{q},\omega) = 1 - v_q(\boldsymbol{q})\chi_0(\boldsymbol{q},\omega). \tag{2.126}$$

Static regime $\omega = 0$

This brings us to the first approximation for screening in the static regime $\omega = 0$, which is the Thomas-Fermi approximation for the electron gas (see also section 2.4.1). It describes the effect of a static potential (zero frequency) at long wavelength by taking the limit $\omega = 0, q \to 0$ of $\chi_0(q,\omega)$. At $T = 0$, $\chi_0(q \to 0, 0) = -\partial n/\partial \varepsilon_F$, leading to the following expression for the dielectric function in the long wavelength

$$\epsilon(q,0) \simeq 1 + \frac{4\pi}{q^2}\frac{\partial n}{\partial \varepsilon_F} = 1 + \frac{k_{TF}^2}{q^2}, \tag{2.127}$$

where k_{TF} is the Thomas-Fermi wave vector which is given for the homogeneous electron gas by

$$k_{TF} = \sqrt{4\pi \frac{\partial n}{\partial \varepsilon_F}} = \sqrt{\frac{6\pi n}{\varepsilon_F}}. \tag{2.128}$$

The positively charged particle that we have placed in the electron gas would produce a potential $\phi_{\text{ext}}(q) = 4\pi/q^2$ everywhere in space. The effective potential in the medium is then given, according to (2.115), as [Ashcroft and Mermin, 1976]

$$\phi_{\text{eff}}(q) = \frac{\phi_{\text{ext}}(q)}{\epsilon(q)} = \frac{4\pi}{q^2 + k_{TF}^2}, \tag{2.129}$$

showing that the Thomas-Fermi wave vector cuts off the divergence of the bare Coulomb interaction. In real space, the effective potential becomes the Yukawa or screened Coulomb potential given by

$$\phi_{\text{eff}}(\boldsymbol{r}, \boldsymbol{r}') = \int \frac{d\boldsymbol{q}}{(2\pi)^3} e^{i\boldsymbol{q}\cdot(\boldsymbol{r}-\boldsymbol{r}')} \phi_{\text{eff}}(q) = \frac{1}{|\boldsymbol{r}-\boldsymbol{r}'|} e^{-k_{TF}|\boldsymbol{r}-\boldsymbol{r}'|}. \tag{2.130}$$

Expression (2.130) shows the importance of including screening effects: the fact that the effective or *screened* interaction at long wavelength is finite. The long-range Coulomb interaction has been reduced due to the rearrangement of the electron gas.

The Thomas-Fermi theory describes how screening is responsible of cutting off the singularities of the long-range Coulomb potential. However, expression (2.129) is valid only when $q << k_F$. Due to its long wavelength approximation, it cannot reproduce the response of the electron gas to a short-range perturbation in an adequate manner. We must then incorporate the finite $-q$ behavior in the response function $\chi_0(\boldsymbol{q}, 0)$. This gives rise to a modification in the dielectric function, leading to the following expression for the dielectric function

$$\epsilon(q, 0) \simeq 1 + \frac{k_{TF}^2}{q^2} F(x), \tag{2.131}$$

where $x = q/(2k_F)$ and $F(x)$ is the Lindhard correction to the Thomas-Fermi result.[23] It is equal to one when limit $q/(2k_F) \to 0$ but is not analytic at $q = 2k_F$. The result is that, at large distances, the effective potential at $T = 0$ goes as [Ashcroft and Mermin, 1976]

$$\phi_{\text{eff}}(\boldsymbol{r}, \boldsymbol{r}') \sim \frac{1}{|\boldsymbol{r}-\boldsymbol{r}'|^3} \cos\left(2k_F|\boldsymbol{r}-\boldsymbol{r}'|\right). \tag{2.132}$$

The screened potential of (2.132) has not an exponential decay anymore but an oscillatory decaying behavior instead, showing that the potential is quite sensitive to the behavior of the density-density response function at $q = 2k_F$.

Dynamic regime $\omega \neq 0$

We now investigate the case in which the external potential has a frequency ω and how this affects the dielectric function. In the limit of $T = 0$, for $|\omega| > k_F q + \frac{q^2}{2}$, the imaginary part of χ_0 vanishes ($\text{Im}\chi_0 = 0$). In this region of the (q, ω) plane, the real part of χ_0 at long-wavelength (small q) and $T = 0$ can be expanded to give

$$\begin{aligned} \chi_0(q, \omega) &\simeq \frac{k_F^3}{3\pi^2} \frac{q^2}{\omega^2} \left[1 + \frac{3}{5}\left(\frac{k_F q}{\omega}\right)^2\right] \\ &\simeq \frac{nq^2}{\omega^2} \left[1 + \frac{3}{5}\left(\frac{k_F q}{\omega}\right)^2\right]. \end{aligned} \tag{2.133}$$

[23] With $F(x) = \frac{1}{2}\left[1 + \frac{1-x^2}{2x} \ln\left(\frac{1+x}{|1-x|}\right)\right]$.

Using (2.133) and (2.126) lead to the following expression for the frequency-dependent dielectric function

$$\epsilon(q,\omega) \simeq 1 - \frac{\omega_p^2}{\omega^2}\left[1 + \frac{3}{5}\left(\frac{k_F q}{\omega}\right)^2\right], \tag{2.134}$$

where we have introduced the characteristic frequency ω_p, known as the electronic plasma frequency

$$\omega_p = (4\pi n)^{1/2}. \tag{2.135}$$

The plasma frequency sets the energy scale of several processes in the interacting electron gas. For instance, it determines the limit above which metals become transparent. A direct manifestation of the plasma frequency is the existence of collective charge density oscillations known as plasmons. These spontaneous oscillations can be found if we consider the case in which $\epsilon(\boldsymbol{q},\omega) = 0$. In this condition, the system responds very strongly to a small perturbation as (2.114) and (2.115) show. The plasmon frequency for the electron gas is given in the RPA by setting $\epsilon(q,\omega) = 0$ in (2.134), which leads to [Bruus and Flensberg, 2004]

$$\omega(q) \simeq \omega_p\left[1 + \frac{9}{10}\mathcal{O}\left(\frac{q}{k_{TF}}\right)^2\right]. \tag{2.136}$$

The plasma oscillations are examples of undamped excitations. The damping of excitations is described by the imaginary part of χ_0, which is non zero if the real part of the denominator in the integrand of (2.122) vanishes. This is possible for wave vectors $\boldsymbol{k}$ such that $\pm\omega_{\boldsymbol{k}} = \varepsilon_{\boldsymbol{k}+\boldsymbol{q}} - \varepsilon_{\boldsymbol{k}}$ where $|\boldsymbol{k}+\boldsymbol{q}|$ is always above the Fermi surface and $\boldsymbol{k}$ is always below. The physical origin of this resonance condition is the ability of the electron gas to absorb incoming energy by generating electron-hole pairs [Bruus and Flensberg, 2004]. For fixed q, there is a maximum frequency where there are no more possible particle-hole excitations. Outside of this (q,ω) area, the electron gas cannot absorb energy by the excitation of electron-hole pairs. The plasmon excitation starts in the (q,ω) space where dissipation is zero, which occurs at small values of q yielding infinite life times for them. At some point, the plasmon dispersion curve crosses into the dissipative region where $\mathrm{Im}\chi_0 \neq 0$ and the plasmon acquires a finite life time. This damping mechanism is called Landau damping [Bruus and Flensberg, 2004].

2.6.2 Van der Waals interactions in metals

In their work dealing with vdW forces in noble metals, Rehr, Zaremba, and Kohn [1975] already mentioned that attractive vdW interactions between ions in a metal had long been recognized to contribute effectively to the total cohesive energy. They also stated, however, that the magnitude and relative importance of this contribution had remained as an open question, where the estimates had ranged from being negligible to approximately a third of the total cohesive energy [see Rehr *et al.*, 1975].

The main reasons for these discrepancies reflect the differences when estimating the ionic polarizabilities and the screening of the polarization forces due to the free electrons in metals. The free electrons in metals give rise to a dynamically screened interaction between the ions which is reflected in the vdW interaction among the ions in the metallic system. As we have mentioned above, the importance of this effect lies in the fact that an analogous mechanism takes place in the adsorption of atoms and molecules on inorganic substrates such as metal surfaces. With this in mind, we review the work

of Rehr *et al.* [1975], who calculated the interaction between ions using diagrammatic techniques within many-body perturbation theory.

We start by considering the interaction between two ions a and b separated by a distance R which are embedded in an homogeneous electron gas with density n. The distance R is large enough that their ionic charge distributions are spherically symmetric and there exists no overlap between them. The Hamiltonian of the system is given by

$$\hat{\mathscr{H}} = \hat{\mathscr{H}}_0 + \hat{\mathscr{H}}_1, \tag{2.137}$$

where the unperturbed part $\hat{\mathscr{H}}_0$ consists of two effective one-electron Hamiltonians which describe the ions in the metal and a Hamiltonian for a noninteracting electron gas,

$$\hat{\mathscr{H}}_0 = \hat{\mathscr{H}}_e + \hat{\mathscr{H}}_a + \hat{\mathscr{H}}_b. \tag{2.138}$$

The perturbation $\hat{\mathscr{H}}_1$ consists in the Coulomb interaction between the charge distributions of the ions and the electron gas,

$$\hat{\mathscr{H}}_1 = \hat{\mathscr{H}}_{ab} + \hat{\mathscr{H}}_{ae} + \hat{\mathscr{H}}_{be} + \hat{\mathscr{H}}_{ee}. \tag{2.139}$$

In this context, the treatment by Rehr *et al.* [1975] consisted in including the interactions between ions themselves and between the ions and the electron gas to non vanishing order while keeping the electron-electron interactions to all orders, leading to the following expression for the dispersion energy between ions

$$U_{\text{disp}}(R) = -\int_0^\infty \frac{d\omega}{2\pi} \int\int \frac{d\boldsymbol{q}}{(2\pi)^3} \frac{d\boldsymbol{q}'}{(2\pi)^3} \, \chi_a^T(\boldsymbol{q},\boldsymbol{q}',i\omega) V(\boldsymbol{q}',i\omega) \chi_b^T(\boldsymbol{q}',\boldsymbol{q},i\omega) V(\boldsymbol{q},i\omega), \tag{2.140}$$

where $\chi_j^T (j = a,b)$ is the continuation to complex frequencies of the Fourier transform of the time-ordered density-density response function. A relevant result found in (2.140) is that the summation of the electron-electron interactions originates a frequency-dependent screened interaction of the same form of (2.115),

$$V(\boldsymbol{q},\omega) = \frac{v(\boldsymbol{q})}{\epsilon(\boldsymbol{q},i\omega)}, \tag{2.141}$$

with the same dielectric function $\epsilon(\boldsymbol{q},i\omega)$ of (2.124).

The time-ordered response function χ_j^T is intimately related to the retarded response function of (2.121) that we have encountered in the context of linear response theory. The relation between them can be solved in terms of the Lehmann representation [see for example Fetter and Walecka, 1971; Engel and Dreizler, 2011]. Given the assumption of spherically symmetric ions, χ_j^T is proportional to the ionic dipole polarizability $\alpha^j(i\omega)$ to leading order in $\boldsymbol{q}$ and $\boldsymbol{q}'$,

$$\chi_j^T \simeq -\boldsymbol{q}\cdot\boldsymbol{q}' e^{i(\boldsymbol{q}-\boldsymbol{q}')\cdot\boldsymbol{R}_j} \alpha^j(i\omega). \tag{2.142}$$

Using the approximation of (2.142) in expression (2.140), the dipole-dipole polarization forces between the ions in real space takes the form of

$$U_{\text{disp}}(R) \simeq -\int_0^\infty \frac{d\omega}{2\pi} \alpha^a(i\omega)\alpha^b(i\omega) \left[\left(\frac{\partial^2 V(R,i\omega)}{\partial R^2} \right) + \frac{2}{R^2} \left(\frac{\partial V(R,i\omega)}{\partial R} \right)^2 \right], \tag{2.143}$$

where $V(R, i\omega)$ is the screened Coulomb interaction at separation R and frequency $i\omega$ given as

$$V(R, i\omega) = \int \frac{d\boldsymbol{q}}{(2\pi)^3} \frac{4\pi}{q^2} \frac{e^{i\boldsymbol{q}\cdot\boldsymbol{R}}}{\epsilon(\boldsymbol{q}, i\omega)} = \frac{2}{\pi} \int dq \frac{\sin qR}{qR} \frac{1}{\epsilon(\boldsymbol{q}, i\omega)}. \tag{2.144}$$

One of the essential ingredients to evaluate the dipole-dipole contribution to the vdW interaction between the ions in the metal is the screened Coulomb interaction, given by (2.144), together with its first and second derivatives with respect to R. This term is given by the term in brackets of expression (2.143). For the case of a very dilute electron gas or for frequencies much larger than the plasma frequency, $\epsilon(\boldsymbol{q}, i\omega) \to 1$ and the bracketed quantity of (2.143) goes as R^{-6}, leading to the reduction of $U_{\text{disp}}(R)$ to the pairwise expression for the vdW interaction between atoms or molecules. The screening is, however, most effective at frequencies lower than the plasma frequency, reducing considerably the magnitude of the ion-ion interaction at low frequencies. The resulting values of evaluating expression (2.143) neglecting the screening effects are 2-3 times larger according to the work of Rehr *et al.* [1975].

The other ingredient in (2.143) is the evaluation of the frequency-dependent dipole polarizabilities of the ions. Rehr *et al.* [1975] extracted them from the optical data for the noble metals given the fact that the ionic polarizabilities can be expressed by the long-wavelength limit of the dielectric function. This was done by subtracting the free electron part from the imaginary part of the observed dielectric function using a Drude formula past the onset of the $d-$electron transitions. Finally, they also took into consideration local-field effects by a Lorentz-Lorentz relation for the final ionic polarizability of each core. For the dielectric function, they performed a numerical evaluation of its RPA form. Furthermore, they also found that only the small$-q$ behavior is relevant in the evaluation of the screened potential $V(R, i\omega)$, behavior which corresponds to taking the limit $q \to 0$ of (2.134).

With the model described above and estimating the contribution of higher order polarization forces, they calculated the total dispersion energy for Cu, Ag, and Au to be 0.21, 0.42, and 0.63 eV per atom, respectively. These values correspond to an approximate contribution of 6%, 14%, and 17% to the total cohesive energy of Cu, Ag, and Au, respectively. Richardson and Mahanty [1977] also estimated the contribution of the vdW energy to the binding energy of Au and Cu, obtaining a reasonable agreement with the work of Rehr *et al.* [1975]. Most importantly, both works show that the vdW energy makes an important contribution from the structural point of view to the stability of these noble metals. We must also mention that the same contribution considered by Rehr *et al.* [1975] has also been investigated by Maggs and Ashcroft [1987] and Mon *et al.* [1979].

2.6.3 Screening in density-functional approximations including van der Waals interactions

The previous section has shown the effect of free-electron screening in the vdW interaction between ions in metals, an example of a highly polarizable material. From a more general perspective, the screening of the Coulomb interaction couples fluctuations between two atoms resulting from the polarization of the electronic charge on other atoms [Dobson and Gould, 2012]. These collective effects go beyond the physics described by simple pairwise interatomic vdW methods, especially for anisotropic and highly polarizable systems in which this behavior becomes stronger. It is evident that an analogous

mechanism can then take place in complex systems such as adsorption systems, hybrid interfaces, or nanostructures to name a few, whose electronic properties are determined by a non-trivial interplay between localized and free electrons.

We have emphasized the reduction of the vdW interaction between ions as a very important result of these collective effects. This result is, however, given at a sufficiently large distance R such that there is no overlap between the ions in a metal. But from the perspective of modeling complex systems such as adsorption systems, this also leads to inaccurate magnitudes of vdW interactions between atoms at short to intermediate distances where wave-function hybridization takes place. From this context, it is necessary to examine the theory behind the vdW-inclusive DFT methods that we have reviewed in section 2.5, and their potential quantitative accuracy on systems in which screened vdW interactions may be relevant.

The simple pairwise interactions described in section 2.5.1 are based on the pairwise expression (2.107), where the C_6 coefficients are evaluated by a simple average of atomic C_6 coefficients. Such a simple consideration is not sufficient to capture the collective effects among atoms that lead to the emergence of screened vdW interactions. As a consequence, these methods will overestimate the contribution of vdW interactions between atoms in highly polarizable systems such as metals or complex interfaces determined by the presence of free electrons. The environment-dependent methods of section 2.5.2 go beyond the simple pairwise methods by taking into account the chemical environment of each atom. In this regard however, these methods suffer from the same limitation implicit in their asymptotic R^{-6} behavior and the fact that the C_6 coefficients are calculated from atomic polarizabilities taking into account the chemical environmental effects, which are only semi-local in their character, but do not represent the collective non-local nature of the screening effects.

The ACFD theorem of section 2.4.4 is a method to include many-body dispersion interactions seamlessly within KS-DFT. For a system with the electron-electron coupling constant λ, vdW interactions are included automatically in the total correlation energy of expression (2.97) in terms of the retarded density-response function χ_λ. The nonlocal density functionals of section 2.5.3 and the RPA correlation energy are both based on this formula to include dispersion interactions within KS-DFT. There are, however, differences in both methods, some of which we will briefly examine [see especially Dobson and Gould, 2012; Lu *et al.*, 2010, for a discussion of these differences].

The first difference that we address is the model used to define the dielectric response function. In the RPA, the dielectric function is given from a fully microscopic theory by expression (2.126), which along with expression (2.102), leads to

$$\begin{aligned} E_{\mathrm{c}}^{\mathrm{RPA}} &= \frac{1}{2\pi}\int_0^\infty d\omega \mathrm{Tr}\left\{\log\left[1-\chi_0(i\omega)v\right]+\chi_0(i\omega)v\right\} \\ &= \frac{1}{2\pi}\int_0^\infty d\omega \mathrm{Tr}\left\{\log[\epsilon(i\omega)]+[1-\epsilon(i\omega)]\right\}. \end{aligned} \tag{2.145}$$

In the vdW-DF of Dion *et al.* [2004], the density-response function to the full effective potential $\delta n = \widetilde{\chi}\phi_{\mathrm{eff}}$ is used as alternative to expression (2.116). From classical electrodynamics, the polarization $\boldsymbol{P}$ of a dielectric material is given in terms of the macroscopic dielectric function ϵ^{M} and the total electric field $\boldsymbol{E}_{\mathrm{tot}}$ by

$$\boldsymbol{P} = \frac{\epsilon^{\mathrm{M}}-1}{4\pi}\boldsymbol{E}_{\mathrm{tot}}. \tag{2.146}$$

The macroscopic dielectric function is then introduced to relate the induced charge density δn to the polarization $\boldsymbol{P}$ as [Dion, 2004; Langreth *et al.*, 2005]

$$\delta n = -\nabla \cdot \boldsymbol{P} = -\nabla \cdot \left(\frac{\epsilon^{\mathrm{M}} - 1}{4\pi} \boldsymbol{E}_{\mathrm{tot}} \right) = \nabla \cdot \left(\frac{\epsilon^{\mathrm{M}} - 1}{4\pi} \nabla \phi_{\mathrm{eff}} \right), \tag{2.147}$$

which implies that the dielectric function is given by $\epsilon^{\mathrm{M}} = 1 + 4\pi\alpha$ given that $\boldsymbol{P} = \alpha \boldsymbol{E}_{\mathrm{tot}}$, where the dipole polarizability α has the general form of a matrix in spatial positions [Rydberg *et al.*, 2000]. If we compare expression (2.147) to $\delta n = \widetilde{\chi} \phi_{\mathrm{eff}}$, the following expression is obtained [Langreth *et al.*, 2005]

$$\widetilde{\chi}_\lambda = \nabla \cdot \frac{\epsilon_\lambda^{\mathrm{M}} - 1}{4\pi\lambda} \nabla. \tag{2.148}$$

This representation for $\epsilon_\lambda^{\mathrm{M}}$ differs from the quantum-mechanical microscopic representation of ϵ in the RPA [see expression (2.126)]. The macroscopic representation of the dielectric function is in general not equal to its microscopic representation due to local-field effects.

Another difference lies in the approximation to perform the λ integration of expression (2.97). In the RPA, the xc kernel f_{xc}^λ is neglected in the Dyson equation (2.98) of the density-response χ_λ, leading to (2.102). In the vdW-DF, on the other hand, the full potential approximation (FPA) is introduced, that is $\widetilde{\chi}_\lambda \equiv \widetilde{\chi}_1$, assuming that the λ integration in expression (2.97) can be done analytically to give a logarithmic operator; so that [Dobson and Gould, 2012; Langreth *et al.*, 2005]

$$E_{\mathrm{c}}^{\mathrm{nl}} = \frac{1}{2\pi} \int_0^\infty d\omega \mathrm{Tr} \left\{ \log \left[1 - \widetilde{\chi}_1(i\omega) v \right] - \log \left[\epsilon^{\mathrm{M}}(i\omega) \right] \right\}. \tag{2.149}$$

The analogous expression in the RPA is exactly true where χ_0 is independent of λ, but constitutes an approximation in other formalisms [Dobson and Gould, 2012]. Since $\widetilde{\chi}_1$ can be given in terms of ϵ^{M} according to (2.148), the correlation energy of (2.149) can be expressed in terms of ϵ^{M} alone. As a final approximation, the correlation energy given by (2.149) is solved in the vdW-DF by expanding the logarithm in second order in the quantity $\left(\epsilon^{\mathrm{M}}\right)^{-1} - 1$ termed as 'S' [see Dion *et al.*, 2004; Dobson and Gould, 2012].

The RPA correlation energy includes, at least qualitatively, the correct screening behavior at the long-range regime, where the expression (2.140) by Rehr *et al.* [1975] is evaluated. In fact, an analogous expression can be recovered when the RPA correlation energy is evaluated in the limit of non-overlapping fragments [Dobson and Gould, 2012]. In the case of the vdW-DF, the approximations behind its derivation yield a density-dependent pairwise additive behavior of the form $-\sum_{ab} C^{ab} R_{ab}^{-6}$ at large separations [see for example Dobson and Gould, 2012]. This implies the same asymptotic behavior both for insulators and metallic systems, contradicting the result obtained by Rehr *et al.* [1975] given in (2.143). A final and most important remark is the fact that the same pairwise behavior eventually leads to an overestimation of vdW interactions in highly polarizable and anisotropic systems at intermediate and short distances, region in which we are interested in the case of inorganic/organic systems for instance.

The MBD method [Tkatchenko *et al.*, 2012; Ambrosetti *et al.*, 2014b], which consists in an efficient dipole approximation to the RPA, includes many-body effects in the long-range correlation energy to all orders, but does not include a simultaneous description

of localized and metallic states. The quantum harmonic oscillators, which represent the basic model elements of the MBD method, have a non zero excitation gap and are initially localized. The coupling of the whole system eventually can induce a delocalization of the polarizability, which can be significantly closer to the correct metallic response in comparison to a pairwise response. This means that, together with the accurate input polarizability of each of the atomic components in a given metallic system, the MBD method has the potential to capture many-body dispersion effects with reasonable accuracy in metallic systems [Maurer *et al.*, 2015]. The challenge in the MBD method still remains, however, to introduce the correct free-electron screening in metallic systems in a fully microscopic manner.

In this last section we have analyzed, from a theoretical perspective, the effect of free-electron screening in the vdW interactions of metallic systems focusing in metals and the inclusion of screening effects in vdW-inclusive KS-DFT. It remains only to recall that an analogous mechanism can take place in adsorption systems where free electrons play a similar role, this is the case, for example, of the adsorption of atoms and molecules on metal surfaces. We will address the specific theory of vdW interactions in adsorption phenomena in chapter 4, focusing also on the practical perspective of the computational simulation of materials.

CHAPTER

3 Brief review of experimental techniques

Validation is a major part of any approximate model since it tests the accuracy of our representation of the real system. As we want to model the structure and stability of adsorption systems in an accurate manner, the validity of our model is given by a direct comparison with results found in experiments. For this reason, before entering into the discussion of vdW interactions in adsorption phenomena, we briefly review some experimental techniques that are used to determine the important quantities involved in the structure and stability of adsorption systems.

We first give a brief review of the normal incidence x-ray standing wave technique, which is frequently referred to throughout this text as it has become one of the most favored methods to determine accurate adsorption geometries of inorganic/organic systems. In section 3.2, we briefly address the temperature programed desorption technique, one of the favored methods to measure the adsorption energies of rare gases and organic molecules on metal surfaces. Finally, in section 3.3 we discuss a recent technique which combines scanning tunneling microscopy (STM) and non-contact atomic force microscopy (NC-AFM) to manipulate the adsorption of large organic molecules on metal surfaces at the single-molecule level.

3.1 The normal incidence x-ray standing wave technique

The normal incidence x-ray standing wave technique (NIXSW) is a powerful experimental tool to determine accurate geometries of molecular adsorbates. In the last decade, it has become the method of choice in this regard and contributed largely to further understand the adsorption properties of organic films adsorbed on different surfaces [Hauschild *et al.*, 2005, 2010; Mercurio *et al.*, 2013a; Bauer *et al.*, 2012; Gerlach *et al.*, 2007; Mercurio, 2012; Stadtmüller, 2013; Mercurio *et al.*, 2014]. The NIXSW technique combines x-ray diffraction and inelastic x-ray scattering (photoelectric effect, Auger effect, fluorescence) using the coherent interference between the incident and diffracted waves to create a standing wave inside and above the crystal. The spatial distribution of the atoms can then be determined from their characteristic scattering response within the standing wavefield [Mercurio, 2012].

Among the main advantages of the NIXSW technique we can mention that long-range order of the adsorbate under study is not required in addition to the inherent chemical sensitivity that the technique provides [Mercurio *et al.*, 2014; Mercurio, 2012].

This last point is of great importance for the validation of our electronic-structure methods in the context of adsorption phenomena given the fact that the structural information –more specifically the vertical adsorption height– of each chemical species forming the molecular adsorbate can be obtained. Not only the position of each chemical element can be determined, but also the position of atoms of the same element in different chemical environments within a molecular adsorbate [Mercurio *et al.*, 2014]. We shall now briefly discuss the fundamentals of the NIXSW method based mainly on the works by Mercurio [2012] and Stadtmüller [2013]. A more detailed treatment of the NIXSW technique can be found in these works along with the reviews by Zegenhagen [1993] and Woodruff [2005], for example.

3.1.1 Fundamentals of the normal incidence x-ray standing wave method

The NIXSW technique consists of an incoming x-ray wave $\mathscr{E}_0$ illuminating a crystalline sample in a direction perpendicular to the Bragg planes of the sample. If the photon energies of the incident wave are close to the Bragg condition, a Bragg-reflected wave $\mathscr{E}_H$ will be generated. The x-ray standing wave (XSW) is then formed inside and above the crystalline sample by the coherent interference of both wavefields. Assuming the two waves to be planar, linearly polarized, and with parallel electric field vectors, both wave fields $\mathscr{E}_0$ and $\mathscr{E}_H$ can be characterized by the complex amplitude of the electric field of the electromagnetic wave as [Mercurio, 2012]

$$\mathscr{E}_0 = E_0 e^{2\pi i(\nu_0 t - \boldsymbol{K}_0 \cdot \boldsymbol{r})}, \tag{3.1}$$

$$\mathscr{E}_H = E_H e^{2\pi i(\nu_H t - \boldsymbol{K}_H \cdot \boldsymbol{r})}, \tag{3.2}$$

where ν_0 and ν_H are the respective frequencies of the radiation, $\boldsymbol{K}_0$ and $\boldsymbol{K}_H$ are the propagation vectors, and $\boldsymbol{r}$ is a coordinate vector with respect to an arbitrary origin. The total wavefield $\mathscr{E}$ of the XSW is given by the superposition of $\mathscr{E}_0$ and $\mathscr{E}_H$, that is $\mathscr{E} = \mathscr{E}_0 + \mathscr{E}_H$. Its intensity I_{XSW}, normalized to the incoming beam, at a position $\boldsymbol{r}$ of the real space is given by [Mercurio, 2012; Stadtmüller, 2013]

$$I_{\mathrm{XSW}} = \frac{\mathscr{E}\mathscr{E}^*}{|E_0|^2} = \left| 1 + \left(\frac{E_H}{E_0} \right) e^{-2\pi i \boldsymbol{H} \cdot \boldsymbol{r}} \right|^2. \tag{3.3}$$

In expression (3.3), E_0 and E_H are the incident and reflected complex amplitudes of the electric field of the electromagnetic wave, respectively, and $\boldsymbol{H}$ corresponds to the reciprocal lattice vector of the Bragg reflection that generates the standing wave, that is $\boldsymbol{K}_H = \boldsymbol{K}_0 + \boldsymbol{H}$.

Considering the coherence between $\mathscr{E}_0$ and $\mathscr{E}_H$, the ratio of the complex wavefield amplitudes E_H/E_0 can be expressed as a complex number containing a phase factor υ given by [Zegenhagen, 1993; Mercurio, 2012]

$$\frac{E_H}{E_0} = \sqrt{R} e^{i\upsilon}, \tag{3.4}$$

where υ defines the phase relationship of E_0 to E_H, and R, which represents the reflectivity, relates the amplitude of E_H to E_0. Using (3.4), expression (3.3) takes the form

[Zegenhagen, 1993; Mercurio, 2012] of

$$\begin{aligned} I_{\mathrm{XSW}} &= \left|1+\sqrt{R}e^{i(\upsilon-2\pi\boldsymbol{H}\cdot\boldsymbol{r})}\right|^2 \\ &= 1+R+2\sqrt{R}\,\cos(\upsilon-2\pi\boldsymbol{H}\cdot\boldsymbol{r}). \end{aligned} \tag{3.5}$$

Expression (3.5) shows how the standing wave probes the position $\boldsymbol{r}$ in space. According to expression (3.5), the pattern of the wavefield is determined through $\boldsymbol{H}$, so the nodes and antinodes (minima and maxima of intensity respectively) of the wavefield intensity lie on planes; whereas its intensity at a particular location $\boldsymbol{r}$ in space, whether a maximum or a minimum intensity can be found at this point, is determined by the phase υ.

The planar wavefield described by (3.5) has a spacing d_{s} which is determined by the relationship between $\boldsymbol{K}_0$ and $\boldsymbol{K}_H$. This relationship is associated to the specific Bragg reflection from the (hkl) scatterer planes separated by d_{hkl}, which is in turn given by $\boldsymbol{H}$ since $\boldsymbol{K}_H = \boldsymbol{K}_0 + \boldsymbol{H}$. Thus, the spacing d_{s} between the maxima of the wavefield is given by the spacing d_{hkl} of the Bragg planes, yielding [Mercurio, 2012; Zegenhagen, 1993]

$$d_{\mathrm{s}} = d_{hkl} = |\boldsymbol{H}|^{-1}. \tag{3.6}$$

Expressing $\boldsymbol{H}\cdot\boldsymbol{r} = Hz$, where $H = |\boldsymbol{H}|$ and z is the vertical distance of the real space point defined by $\boldsymbol{r}$ from the nearest Bragg plane below, expression (3.5) can be written as [Mercurio, 2012]

$$I_{\mathrm{XSW}}(z,E) = 1+R(E)+2\sqrt{R(E)}\,\cos\left(\upsilon-2\pi\frac{z}{d_{hkl}}\right). \tag{3.7}$$

The vertical z position of the atom can be analyzed through expression (3.7). Furthermore, changing υ by π exchanges the positions of the nodal and antinodal planes, that is a shift of the wavefield by $d_{hkl}/2$.

3.1.2 The normal incidence x-ray standing wave experiment

As the fundamental principle behind the NIXSW technique is to use the XSW as a probe to determine the spatial distribution of the atoms in the sample, the x-ray intensity at the position of a scatterer atom must be experimentally detected. In this regard, we focus on the photoelectric effect rather than on the decay processes as the Auger effect or x-ray fluorescence.[1] If the incident photon energy $h\nu$ is greater than the sum of the electron binding energy E_b and the work function W, that is $h\nu > E_b + W$, the electron is emitted. The detection of the emitted photoelectrons at position z, known as the electron yield $Y(z)$, is proportional to the absorption $I_a(z)$ of the XSW from a given element at position z. Within the dipole approximation, the photon absorption I_a is at the same

[1] The experiments that we use to validate our theoretical predictions in this dissertation have been mainly performed in the last decade. We believe that research using this specific technique are well represented in the works by Mercurio [2012]; Mercurio *et al.* [2014]; and Stadtmüller [2013]. In this context, Mercurio [2012] mentions the advantages of detecting photoelectrons over Auger electrons or x-ray fluorescence. Among these advantages, the most important from our perspective is that photoelectrons are both element specific and bonding-environment specific.

time proportional to the intensity I_{XSW} of the XSW given by (3.5) [Mercurio, 2012]. In simple terms,

$$Y(z) \propto I_{\mathrm{XSW}}(z). \tag{3.8}$$

Expression (3.8) is the link between the probe and the measured electron yield corresponding to a spatial distribution of atoms located, in the case of the adsorption systems of our interest, at different positions z on top of an inorganic substrate.

In general, during an XSW experiment, either the incident angle or the energy of the incoming photon varies. In the experiments that we cite in this dissertation, the NIXSW technique was used, meaning that the incident angle is perpendicular to the set of Bragg planes. As a result, the incident photon energy is the variable quantity, being scanned through the finite range of energies, changing the phase v, and eventually including the Bragg energy $E_{\mathrm{Bragg}} = hc/\lambda_{\mathrm{Bragg}}$. This leads to diffraction and the generation of the standing wave. The photon absorption $Y(z)$ is then quantified by recording secondary emission processes, mainly photoelectrons. The position z is finally determined using (3.7), by fitting photoemission yield curves $Y(z)$ together with the calculated R and phase v [Stadtmüller, 2013; Mercurio, 2012].

The coherent fraction F_c and coherent position P_c

There are two structure parameters that are extracted from fitting the photoemission yield profile: the coherent fraction F_c and the coherent position P_c. The origin of these is that different vertical positions can occur in complex adsorbate systems due to vertical disorder, surface defects, or thermally induced vibrations [Stadtmüller, 2013; Mercurio *et al.*, 2014]. These aspects are introduced in (3.7) with a distribution function $f(z)$ which describes the vertical position of all atoms of one species so that $\int_0^{d_{hkl}} f(z)\,dz = 1$. Expression (3.7) then takes the form of [Mercurio, 2012]

$$\begin{aligned} I_{\mathrm{XSW}} &= 1 + R + 2\sqrt{R}\int_0^{d_{hkl}} f(z)\cos\left(v - 2\pi\frac{z}{d_{hkl}}\right)dz \\ &= 1 + R + 2F_c\sqrt{R}\,\cos\left(v - 2\pi P_c\right), \end{aligned} \tag{3.9}$$

where the parameters F_c and P_c, which take values between 0 and 1, are defined. The coherent position P_c is related to the averaged vertical position in fractions of the Bragg plane distance $P_c = \frac{D_c}{d_{hkl}}$ above the nearest Bragg plane. $P_c = 0$ and $P_c = 1$ correspond to a Bragg plane position while any value between 0 and 1 corresponds to a position between two consecutive Bragg planes. The coherent fraction F_c refers to the fraction of photoemitters found at the position P_c. An homogeneous distribution of adsorbates relative to the Bragg planes is indicated by $F_c = 0$ while $F_c = 1$ indicates that all photoemitters are located at the same height associated to the coherent position P_c [Stadtmüller, 2013; Mercurio *et al.*, 2014].

3.2 The temperature programed desorption technique

The adsorption energy is often used to validate the predictions of electronic-structure methods. Campbell and Sellers [2013] review some of the experimental techniques to

measure adsorption energies of adsorbates on single-crystalline surfaces such as single-crystal adsorption calorimetry, equilibrium adsorption isotherms, and temperature programed desorption (TPD). Here, we limit our discussion to the TPD method because this technique is highly favored in the case of the adsorption of rare gases and organic molecules on metal surfaces in part because of its simplicity and power. We base our discussion of this technique on the works by Campbell and Sellers [2013] and King [1975].

The TPD method is an experimental technique used to characterize the energetics of adsorbates on single-crystalline surfaces since the late 1950's [King, 1975]. It is not a direct method in the sense that it only provides an accurate activation energy for desorption $\left(E_{\mathrm{d}}\right)$ in the best case. This energy can only be equated to the adsorption energy when the adsorption $\rightleftharpoons$ desorption process is reversible and the activation energy for adsorption is negligible [Campbell and Sellers, 2013].

During a TPD experiment, a sample with the preadsorbed species is heated in ultra-high vacuum at a constant heat rate, preferably linear in time, while monitoring at the same time the rate of appearance of gases emitted by the surface [Campbell and Sellers, 2013]. The desorption rate is typically recorded with a mass spectrometer. The desorption energy E_{d} is then determined by analyzing the measured desorption rate data versus temperature and coverage [see, for example, Figure 3 in Campbell and Sellers, 2013]. Other kinetic parameters can be also be obtained from this analysis. We shall now discuss briefly some of the methods to obtain the desorption energy.

If the adsorption $\rightleftharpoons$ desorption process is reversible and the activation energy for adsorption is negligible, the desorption energy can be related to the enthalpy of adsorption ΔH^0_{ad} (where the superscript 0 refers to its value at the standard pressure of 1 bar) by

$$q_{\mathrm{ad}} = -\Delta H^0_{\mathrm{ad}} = E_{\mathrm{d}} + \tfrac{1}{2}RT, \tag{3.10}$$

where q_{ad} is the differential heat of adsorption, R is the universal gas constant, and T is the average sample temperature where the desorption rates were measured. One can safely assume that the activation energy for adsorption is negligible when the sticking probability for adsorption is nearly unity, which is usually the case for simple molecular adsorption [Campbell and Sellers, 2013].

For the case of a reversible molecular adsorption $\rightleftharpoons$ desorption process, where it is reasonable to assume that desorption is a first-order process, the Polanyi-Wigner equation reads [Campbell and Sellers, 2013]

$$r(\Theta, T) = -\frac{d\Theta}{dt} = \nu_1 \Theta \, e^{-E_{\mathrm{d}}(\Theta)/(RT)}, \tag{3.11}$$

where the desorption rate $r(\Theta, T)$ is a single-valued function of the coverage Θ and temperature T, ν_1 is the pre-exponential factor, generally assumed not to vary with coverage or temperature, and $E_{\mathrm{d}}(\Theta)$ is the coverage-dependent desorption activation energy. The desorption energy clearly changes with the coverage as the adsorption energy does since it depends on the adsorbate-adsorbate distance or the adsorption site (defects, terraces, for example). We will partially address this effect in section 5.2. From (3.11), the value of $E_{\mathrm{d}}(\Theta)$ can be obtained with the knowledge of ν_1 using

$$E_{\mathrm{d}}(\Theta) = -RT \ln\left[-\frac{d\Theta}{dt}(\nu_1 \Theta)^{-1}\right]. \tag{3.12}$$

The pre-exponential factor ν_1 in (3.12) is treated as a variational parameter by optimizing the fit between experimental and simulated TPD spectra, finding the prefactor that best describes the kinetics of the desorption process [Campbell and Sellers, 2013].

Another option, commonly used, to calculate E_d is by using the first-order Redhead equation [Redhead, 1962; Campbell and Sellers, 2013]. This equation relates E_d to the temperature T_p at which the desorption maximizes, the heating rate β, and ν_1 as

$$\frac{E_\mathrm{d}}{RT_\mathrm{p}^2} = \frac{\nu_1}{\beta} e^{-E_\mathrm{d}/(RT_\mathrm{p})}. \tag{3.13}$$

In this case, E_d is commonly calculated using expression (3.13) assuming a value for ν_1. Extracting E_d from the Redhead equation (3.13) is a highly favored method which gives reasonable accuracy if the value ν_1 is approximately correct [Campbell and Sellers, 2013]. For simple adsorbates such as small molecules, small prefactors of the order of $10^{11} - 10^{12}$ s^{-1} are expected and sometimes assumed (such as the case of the adsorption of small alkanes for instance) [Fichthorn and Miron, 2002; Liu *et al.*, 2013b]. However, recent experimental and theoretical studies have shown that the value of ν_1 is significantly increased for larger molecules, reflecting a discrepancy between the adsorbed and the gas-phase (transition-state) entropies [Fichthorn and Miron, 2002; Tait *et al.*, 2005]. Campbell and Sellers [2012] have tackled this issue by estimating values of ν_1 from a discovered relation between the pre-exponential factor for desorption and the entropy of the gas-phase product [see also Campbell and Sellers, 2013]. Liu *et al.* [2012] have applied this methodology to revisit experimental adsorption energies for benzene on coinage metal surfaces in order to validate theoretical predictions, finding that a prefactor of 10^{15} s^{-1} describes more accurately the kinetics of the desorption process of benzene on coinage metal surfaces. As we can infer from this discussion, the correct interpretation of experimental results is highly important in order to achieve an adequate validation of our theoretical methods.

3.3 Combining experimental microscopy techniques for single-molecule manipulation

In this last section, we briefly review a recent experimental technique which combines scanning tunneling microscopy (STM) and non-contact atomic force microscopy (NC-AFM) aiming to investigate, at the single-molecule level, the energetic features of large organic molecules adsorbed on surfaces [Wagner *et al.*, 2012, 2014]. An important part of this research is unveiling the influence of vdW interactions in the adsorption of organic molecules on metal surfaces [van Ruitenbeek, 2012]. We only give here a brief review of this experimental technique. More detailed information can be found, for example, in Fournier *et al.* [2011]; Wagner *et al.* [2012, 2014]; and Wagner and Temirov [2015].

This novel experimental technique uses a low-temperature, ultrahigh-vacuum scanning tunneling microscope whose tip is glued to a tuning-fork-type quartz mechanical sensor [van Ruitenbeek, 2012]. The mechanical sensor uses a piezoelectric tuning fork resonator as tip mount which measures the shift of the resonance frequency f_0 of the resonator with the stiffness k_0 at any given spatial position of the tip. The frequency shift Δf of the tip oscillating with a small amplitude along the $z-$axis perpendicular to

the surface is related to the first derivative of the force F_z acting from the surface on the tip along z [Wagner and Temirov, 2015],

$$\frac{dF_z}{dz} = -\frac{2k_0}{f_0}\Delta f. \tag{3.14}$$

This configuration extends the capabilities that STM provides in imaging individual molecules and their functional groups while adsorbed on metal surfaces. Such a combined NC-AFM/STM working at temperatures of approximately 5 K was the first instrument used to obtain images of the structure of a large organic molecule, namely pentacene [Gross *et al.*, 2009].

Wagner *et al.* [2012] used this technique to obtain experimental information in order to partition the overall binding energy of the adsorption of a single PTCDA molecule on Au(111) into its different bonding channels. They were able to establish contact between the microscope tip and the corner of the molecule, forming a chemical bond between the molecule and the outermost tip apex atom, then retract the tip from the surface, lifting the molecule, and eventually approaching the tip back to the surface, thus restoring the bond between PTCDA and Au(111). They measured the stiffness of the surface-molecule-tip junction throughout the complete removal process, probing all the interaction potentials that form the bond between PTCDA and Au(111).

To retrieve the quantitative shape of all the interaction potentials –Pauli repulsion, local chemical bonds, and dispersion interactions– they used the information contained in the curve generated with expression (3.14). By modeling the various components of the molecule-substrate interaction with generic potentials, simulating the junction stiffness $\frac{dF_z}{dz}$ based on these potentials, and eventually fitting them to the experimental data throughout the whole manipulation process, they finally extracted the potential parameters and retrieve the desired partitioning [Wagner *et al.*, 2012]. The adsorption potentials generated with this technique serve as a direct benchmark for the potentials calculated with electronic-structure methods. Furthermore, this technique also provides the adsorption energy and distance of single molecules adsorbed on surfaces, providing another source of validation for our theoretical methods.

Part II

Method development: including screened van der Waals interactions in density-functional approximations

CHAPTER

4 Van der Waals interactions in adsorption phenomena

This chapter includes our original work and specific topic of interest in this dissertation, namely accurately modeling vdW interactions in DFT within the context of adsorption phenomena. We are especially interested in the interfaces formed by inorganic/organic systems as they are of great interest to both basic science and technology. The interface geometry of these systems plays a fundamental role in their electronic properties in such a way that a balanced description of both their structural and electronic properties is critical for their understanding [Tkatchenko *et al.*, 2010].

We start by describing the performance of several vdW-inclusive methods in KS-DFT using one of the best experimentally and theoretically characterized inorganic/organic interfaces. We continue by describing the theory behind vdW forces in the context of adsorption phenomena. From this analysis, an expression for the vdW interaction between an atom and a solid surface can be obtained. We conclude by describing the development of a method (which we call DFA+vdW$^{\text{surf}}$) to treat vdW forces between complex adsorbates and surfaces within DFT. Much of the work here presented is based on our own previously published work [Ruiz *et al.*, 2012, 2016].

4.1 State of the art

The reliable prediction of the equilibrium structure and dynamic properties of hybrid inorganic/organic systems (HIOS) from first principles represents a great challenge to the state-of-the-art theoretical methods due to the interplay of covalent interactions, electron transfer processes, van der Waals (vdW) interactions, and Pauli repulsion. In particular, vdW interactions are fundamental in determining the structure and stability of organic molecules on solid surfaces [Atodiresei *et al.*, 2009; Mercurio *et al.*, 2010; Stradi *et al.*, 2011; McNellis, 2010; Tkatchenko *et al.*, 2010; Olsen *et al.*, 2011; Lazić *et al.*, 2014].

Routine KS-DFT calculations using (semi-)local and hybrid functionals to approximate the xc energy functional do not include vdW interactions at all, but recent years have seen the development of several promising vdW-inclusive approaches in KS-DFT. In this context, the role of vdW interactions in the binding between small molecules in the gas phase has been extensively studied and is fairly well understood. Methods such as the ones we have described in section 2.5 have shown to be remarkably accurate for intermolecular interactions but their application to HIOS is questionable due to either the absence or inaccuracy of the impact that the non-local (inhomogeneous) collective

electron response of the extended substrate has on the vdW energy of the system. The foundation of this statement is given, from the theoretical point of view, in the discussion of section 2.6.3. From the practical perspective of the computational simulation of materials, this problem has been exemplified for several adsorption systems [see for example Nguyen *et al.*, 2010; Olsen *et al.*, 2011; Stradi *et al.*, 2011; Atodiresei *et al.*, 2009; Mercurio *et al.*, 2010; Lüder *et al.*, 2014].

Within the large variety of HIOS, 3,4,9,10-perylene-tetracarboxylic dianhydride (PTCDA, chemical formula: $C_{24}H_8O_6$) on coinage metals is one of the best experimentally and theoretically characterized systems. The adsorption geometry of PTCDA on Ag(111), Au(111), and Cu(111), has been accurately determined by means of the normal incidence x-ray standing wave (NIXSW) technique [Gerlach *et al.*, 2007; Henze *et al.*, 2007; Hauschild *et al.*, 2010], making these systems a suitable choice for testing the predictive power of theoretical methods. In particular, Romaner *et al.* [2009] studied the adsorption of PTCDA on coinage metal surfaces and concluded that a more accurate approach to include vdW interactions is needed. Several other studies for PTCDA on Ag(111) have also been published on the matter [Rohlfing and Bredow, 2008; Rohlfing *et al.*, 2007; Romaner *et al.*, 2009; McNellis, 2010; Tkatchenko *et al.*, 2010; Ruiz *et al.*, 2012].

To illustrate the challenge of predicting the equilibrium structure in HIOS from first principles, we start by comparing the performance of existing theoretical methods for the interaction of PTCDA with Ag(111) in Figure 4.1. The average adsorption height of 2.86 ± 0.05 Å is reliably known from a number of NIXSW studies for the ordered monolayer at room temperature [see Hauschild *et al.*, 2010, and references therein]. From an experimental perspective, the adsorption energy is unavailable because PTCDA breaks down upon thermal desorption in TPD experiments [Zou *et al.*, 2006]. Nevertheless, the adsorption energy of 1.16 ± 0.1 eV has been measured from TPD experiments for the adsorption of 1,4,5,8–naphthalene–tetracarboxylic–dianhydride ($C_{14}H_4O_6$, NTCDA) on Ag(111) by Stahl *et al.* [1998]. Both NTCDA and PTCDA are molecules terminated with two anhydride functional groups, however NTCDA has a smaller aromatic backbone. Based on this information we have initially made an estimate of 2.4 ± 0.2 eV for the adsorption energy of PTCDA on Ag(111) [Tkatchenko *et al.*, 2010; Ruiz *et al.*, 2012].[1] Using KS-DFT with the PBE functional [Perdew *et al.*, 1996] results in no visible minimum in the binding curve [see also Tkatchenko *et al.*, 2010]. The LDA underestimates the binding distance (≈ 2.65 Å), although it (fortuitously) yields a better adsorption energy [see also Rohlfing *et al.*, 2007].

The inclusion of vdW interactions using the non-local vdW-DF [Dion *et al.*, 2004] leads to results that are far off both for the binding distance and the binding energy [Tkatchenko *et al.*, 2010; Romaner *et al.*, 2009]. The interatomic pairwise PBE-D2 correction by Grimme appears to be closer to the experimental binding distance; the calculated binding energy is, however, larger by 1 eV than the above mentioned estimate [McNellis, 2010]. The interatomic pairwise PBE+vdW correction scheme [Tkatchenko and Scheffler, 2009], where the vdW coefficients and radii are determined nonempirically from the electron density, leads to a better prediction for the energy but it still overestimates the equilibrium distance by about 0.35 Å [see also Tkatchenko *et al.*, 2010]. Even the computationally most expensive calculations using exact exchange with elec-

[1] We revisit this estimate for the adsorption energy of PTCDA on Ag(111) later on chapter 7, section 7.3.1.

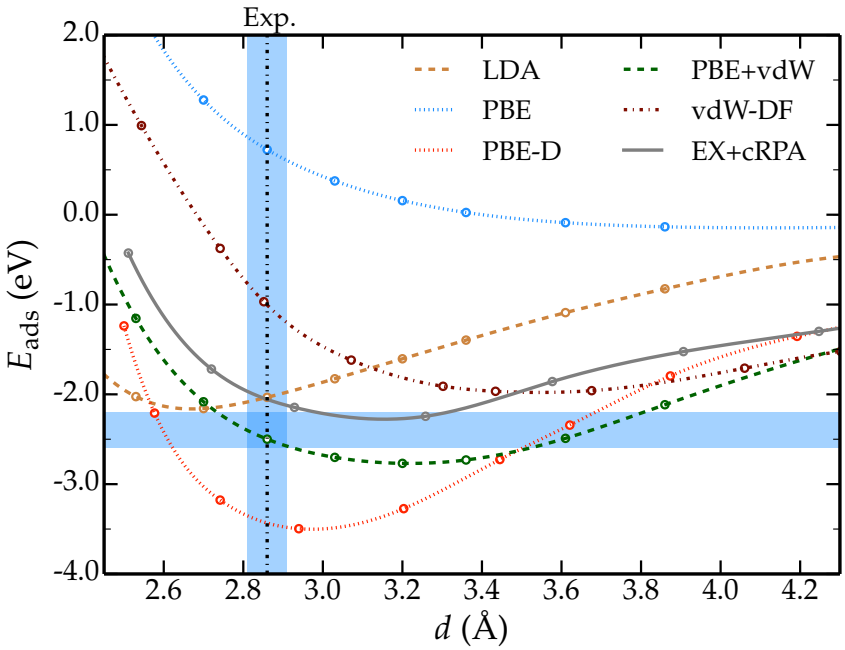

FIGURE 4.1: Adsorption energy E_{ads} as a function of vertical distance d for PTCDA on Ag(111) employing different vdW-inclusive DFT methods. The estimated adsorption energy for the system of -2.4 ± 0.2 eV [Tkatchenko *et al.*, 2010] and the experimental adsorption distance of 2.86 ± 0.05 Å [Hauschild *et al.*, 2010] are indicated by shaded intervals. These error bars correspond to typical experimental error estimates.

tron correlation treated in the RPA (EX+cRPA, with some additional approximations to make these calculations feasible) yield a 0.2 Å overestimation in the equilibrium distance of PTCDA on Ag(111) [Rohlfing and Bredow, 2008].

The discussion above, along with that of section 2.6.3, give us a clear picture of what the state-of-the-art computational modeling of HIOS was at the moment when the research project of this dissertation started. It is evident that modeling HIOS in KS-DFT requires efficient and accurate methods that are able to include a wide range of interactions, especially vdW interactions. It is also evident that the methods which were available did not have the required accuracy to predict the structure and stability of HIOS in a reliable manner. As a result, the prediction, understanding, and eventual control of the functionality of these interfaces would become almost impossible from the computational point of view given the fact that the interface geometry of these systems determines their electronic properties.

It is in this background, and with the intention of solving this problem, that we have developed the DFA+vdW^{surf} method [Ruiz *et al.*, 2012] to calculate the adsorption properties of atoms and molecules on surfaces. This method combines the DFA+vdW method [Tkatchenko and Scheffler, 2009] for intermolecular interactions with the Lifshitz-Zaremba-Kohn (LZK) theory [Lifshitz, 1956; Zaremba and Kohn, 1976] for the inclusion of the non-local collective response of the substrate surface in the vdW energy tail. Calculations using the DFA+vdW^{surf} method have demonstrated that the in-

clusion of these collective effects, which effectively go beyond the atom-based pairwise description of vdW interactions, enables us to reliably describe the binding in many systems, including the adsorption of a Xe monolayer, of aromatic molecules (benzene and derivatives, naphthalene, anthracene, azobenzene, diindenoperylene, and olympicene and derivatives), C_{60}, molecules including sulfur/oxygen such as thiophene, NTCDA, and PTCDA on several close-packed transition-metal surfaces [Ruiz *et al.*, 2012; Liu *et al.*, 2012; van Ruitenbeek, 2012; Liu *et al.*, 2013b; Bürker *et al.*, 2013; Mercurio *et al.*, 2013b; Schuler *et al.*, 2013; Liu *et al.*, 2013a, 2014]. A study of a Cu-phthalocyanine film on a PTCDA monolayer adsorbed on Ag(111) has also been published recently [Egger *et al.*, 2013]. As a final comment, it is worth mentioning that along with our own developed methodology to describe vdW interactions in adsorption phenomena, vdW-DF-type functionals with empirically optimized exchange have emerged which seem to be able to achieve accurate results in describing inorganic/organic adsorption systems [Klimeš *et al.*, 2010; Liu *et al.*, 2012; Carrasco *et al.*, 2014].

We shall continue by presenting a detailed description of the DFA+vdW$^{\text{surf}}$ method. We start in section 4.2 by reviewing the general theory of vdW interactions followed by a discussion regarding the case of the atom-surface vdW interaction in section 4.3, where we also discuss its relation to the vdW pairwise interactions. Finally, in section 4.4 we show how this relation determines the development of the DFA+vdW$^{\text{surf}}$ method.

4.2 The van der Waals interaction between polarizable fragments

As a starting point, we consider the case of two neutral polarizable fragments $\mathscr{S}_a$ and $\mathscr{S}_b$ in the well-separated regime, that is, separated at large distances where there is no wave-function overlap between fragments. If we treat the inter-fragment Coulomb interaction v_{ab} as a perturbation, expressions (2.103) and (2.105) become particularly useful in relating the ACFD-RPA approach described in section 2.4.4 with a formal perturbative description of the dispersion energy [Dobson, 1994; Lu *et al.*, 2010]. If χ_{aa} and χ_{bb} correspond to the fully interacting intra-system response function of each isolated fragment and v_{ab} is the inter-fragment Coulomb interaction treated as a perturbation, the total inter-fragment response function can be written in terms of the sum of the individual interacting responses plus a correction term $\delta\chi$ [Dobson, 1994; Lu *et al.*, 2010]

$$\chi = \chi_{aa} + \chi_{bb} + \delta\chi, \tag{4.1}$$

where $\delta\chi \simeq \delta\chi_{aa} + \delta\chi_{ab} + \delta\chi_{bb} + \delta\chi_{ba}$ at the lowest order of v_{ab}. By including first order changes to the cross responses [Dobson, 1994; Lu *et al.*, 2010]

$$\delta\chi_{ab} \simeq \chi_{aa} v_{ab} \chi_{bb},$$
$$\delta\chi_{ba} \simeq \chi_{bb} v_{ba} \chi_{aa},$$

and second order changes to the intra-responses

$$\delta\chi_{aa} \simeq \chi_{aa} v_{ab} \chi_{bb} v_{ba} \chi_{aa},$$
$$\delta\chi_{bb} \simeq \chi_{bb} v_{ba} \chi_{aa} v_{ab} \chi_{bb};$$

the contribution to the correlation energy (2.105), keeping only second order ($n = 2$) terms and using (4.1), can be expressed as [Dobson, 1994, 2006; Lu *et al.*, 2010]

$$E_{\text{vdW}}^{(2)} = -\frac{1}{2\pi}\int_0^\infty d\omega \int \ldots \int d\boldsymbol{r}_a\, d\boldsymbol{r}'_a\, d\boldsymbol{r}_b\, d\boldsymbol{r}'_b\, \chi_a(\boldsymbol{r}_a, \boldsymbol{r}'_a, i\omega)\, v(\boldsymbol{r}'_a, \boldsymbol{r}_b)\chi_b(\boldsymbol{r}_b, \boldsymbol{r}'_b, i\omega)\, v(\boldsymbol{r}'_b, \boldsymbol{r}_a), \tag{4.2}$$

where χ_a and χ_b are the linear density response functions of fragments $\mathscr{S}_a$ and $\mathscr{S}_b$ respectively and $v(\boldsymbol{r}, \boldsymbol{r}') = \left|\boldsymbol{r} - \boldsymbol{r}'\right|^{-1}$ is the bare Coulomb interaction. Position vectors $\boldsymbol{r}_a$ and $\boldsymbol{r}'_a$ are restricted to fragment $\mathscr{S}_a$, while $\boldsymbol{r}_b$ and $\boldsymbol{r}'_b$ are restricted to fragment $\mathscr{S}_b$. Expression (4.2) corresponds to the Zaremba-Kohn [Zaremba and Kohn, 1976] (ZK) formula which was derived following second-order perturbation theory. The ZK expression corresponds to the dispersion energy between two neutral polarizable fragments in terms of the charge fluctuations of each fragment. Within the ACFD-RPA formalism of section 2.4.4, Dobson [1994] showed that the ZK formula is obtained when the response function is formulated in terms of the RPA.

We consider now the response function of each fragment $\mathscr{S}_i$ to be characterized by an isotropic point dipole polarizability $\alpha^i(i\omega)$ located at $\boldsymbol{R}_i$ [Dobson, 1994]

$$\chi_i(\boldsymbol{r}_i, \boldsymbol{r}'_i, i\omega) = -\alpha^i(i\omega)\nabla_{\boldsymbol{r}_i}\delta^3(\boldsymbol{r}_i - \boldsymbol{R}_i) \otimes \nabla_{\boldsymbol{r}'_i}\delta^3(\boldsymbol{r}'_i - \boldsymbol{R}_i), \tag{4.3}$$

where $\delta^3(\boldsymbol{r} - \boldsymbol{r}')$ is the three-dimensional (3D) Dirac delta function and $\otimes$ corresponds to the tensor (outer) product. Given (4.3) for χ_a and χ_b, the vdW interaction for two well-separated fragments given by (4.2) becomes [Dobson, 1994]

$$E_{\text{vdW}}^{(2)} \simeq -\frac{3}{\pi R^6}\int_0^\infty d\omega\, \alpha^a(i\omega)\alpha^b(i\omega) = -\frac{C_6^{ab}}{R^6}, \tag{4.4}$$

where the Casimir-Polder formula [Casimir and Polder, 1948; McLachlan, 1963] has been used to calculate C_6^{ab} from the dipole polarizabilities of each fragment and $R = |\boldsymbol{R}_a - \boldsymbol{R}_b|$. The equation above corresponds to the pairwise formula known since the work of London [1930, 1937] and, as it has been summarized by Dobson [2006] can be derived in several ways. For the general case of N polarizable dipoles in the well-separated regime, Tkatchenko *et al.* [2013] showed that the second-order expansion of the correlation energy given within the ACFD-RPA scheme leads, in the dipole approximation, to [Tkatchenko *et al.*, 2013; DiStasio Jr. *et al.*, 2014]

$$E_{\text{vdW}}^{(2)} = E_{c,\text{RPA}}^{(2)} = -\frac{1}{2}\sum_i \sum_j \frac{C_6^{ij}}{R_{ij}^6}. \tag{4.5}$$

The reader will note that (4.5) corresponds to the expression for the pairwise dispersion energy of N atoms as used in the DFT-D [Grimme, 2004, 2006; Grimme *et al.*, 2010] and DFA+vdW [Tkatchenko and Scheffler, 2009] methods.

4.3 Atom-surface van der Waals interaction (Lifshitz-Zaremba-Kohn theory)

The vdW interaction between a semi-infinite crystalline solid and a neutral atom can be derived starting from (4.2) in the limit where there is no wave-function overlap between

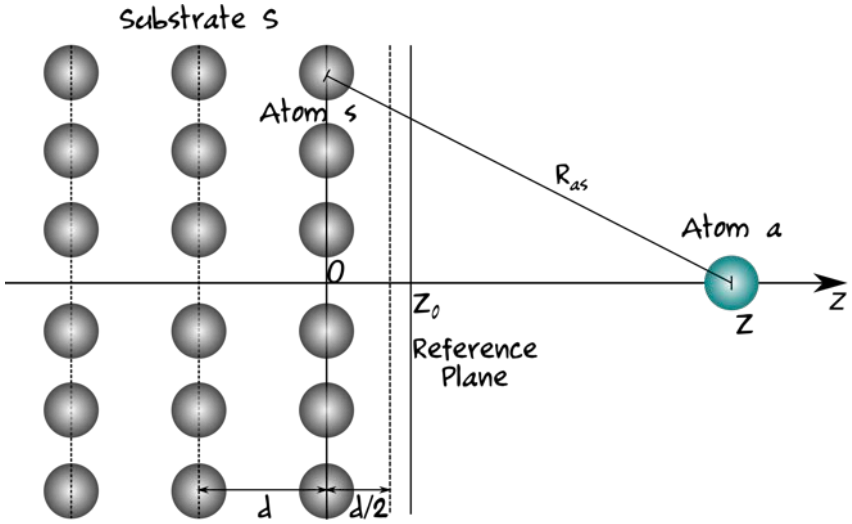

FIGURE 4.2: Geometry of the atom-surface system.

the atom and the surface [Zaremba and Kohn, 1976]. Figure 4.2 features the geometric arrangement of the atom-surface system. In this arrangement, fragment $\mathscr{S}_a$ is the atom located at a distance Z from the topmost layer of the surface, which corresponds to fragment $\mathscr{S}_S$. The origin of the coordinate system is chosen to lie in the plane of the topmost surface atoms. For the case of the atom-surface interaction, the ZK formula (4.2) correlates the charge fluctuations between adsorbate and substrate and does not rely on any specific model for the involved fragments [Bruch *et al.*, 1997].

In this case, the Coulomb potential between fragments can be expressed in terms of two-dimensional (2D) Fourier decompositions in order to incorporate the symmetry of the planar semi-infinite substrate as

$$v(\boldsymbol{r}) = \int d\boldsymbol{q} \frac{2\pi}{q} e^{i\boldsymbol{q}\cdot\boldsymbol{\rho} - qz}, \tag{4.6}$$

where $\boldsymbol{q}$ is a 2D wave vector that lies parallel to the plane of the surface and the 3D position vector is $\boldsymbol{r} = (\boldsymbol{\rho}, z)$. After expressing the Coulomb potential in terms of $\boldsymbol{q}$ and incorporating the complex wave vector $\boldsymbol{\kappa} = \boldsymbol{q} + iq\hat{\boldsymbol{z}}$, the atom-surface dispersion interaction takes the following form [Zaremba and Kohn, 1976; Bruch *et al.*, 1997]

$$E^{(2)}_{\mathrm{vdW}} = -\frac{1}{2\pi}\int_0^\infty d\omega \int \frac{d^2q}{(2\pi)^2} \int \frac{d^2q'}{(2\pi)^2} \frac{2\pi}{q}\frac{2\pi}{q'}\, e^{-Z(q+q')} e^{i\boldsymbol{R}\cdot(\boldsymbol{q}-\boldsymbol{q}')} A(\boldsymbol{x},\boldsymbol{x}',i\omega) S(\boldsymbol{r},\boldsymbol{r}',i\omega). \tag{4.7}$$

$A(\boldsymbol{x},\boldsymbol{x}',i\omega)$ represents the adsorbate response function and is given by

$$A(\boldsymbol{x},\boldsymbol{x}',i\omega) = \int d\boldsymbol{x} \int d\boldsymbol{x}'\, e^{i\boldsymbol{\kappa}\cdot\boldsymbol{x} - i\boldsymbol{\kappa}^*\cdot\boldsymbol{x}'}\, \chi_a(\boldsymbol{x},\boldsymbol{x}',i\omega), \tag{4.8}$$

where the position vector $\boldsymbol{x}$ is taken relative to the center of the adatom located at $\boldsymbol{R} = (0,0,Z)$, that is $\boldsymbol{x} = \boldsymbol{r} - \boldsymbol{R}$. The surface response function $S(\boldsymbol{r},\boldsymbol{r}',i\omega)$ is the analog to (4.8) and is given by

$$S(\boldsymbol{r},\boldsymbol{r}',i\omega) = \int d\boldsymbol{r} \int d\boldsymbol{r}'\, e^{i\boldsymbol{\kappa}\cdot\boldsymbol{r} - i\boldsymbol{\kappa}^*\cdot\boldsymbol{r}'}\, \chi_S(\boldsymbol{r},\boldsymbol{r}',i\omega). \tag{4.9}$$

Due to the periodicity of the surface, the integral over $\boldsymbol{q}'$ in (4.7) is restricted to $\boldsymbol{q}' = \boldsymbol{q} + \boldsymbol{G}$, where $\boldsymbol{G}$ is a reciprocal lattice vector in the plane of the surface. Only the terms where $\boldsymbol{G} = 0$ give rise to a power-law dependence characteristic of the vdW interaction [Zaremba and Kohn, 1976]. Taking only the $\boldsymbol{G} = 0$ terms, (4.7) reduces to [Bruch *et al.*, 1997]

$$E_{\mathrm{vdW}}^{(2)} = -\frac{1}{2\pi}\int_0^\infty d\omega \int \frac{d^2q}{(2\pi)^2}\,\frac{2\pi}{q} e^{-2qZ} A(q,i\omega) S(q,i\omega). \tag{4.10}$$

The factor e^{-2qZ} appearing in (4.10) cuts off the sum of q values to $q \gtrsim 1/Z$. Therefore, it is sufficient to determine only the small-q behavior of functions $A(q,i\omega)$ and $S(q,i\omega)$. $A(q,i\omega)$ contains the fluctuations in the density of the adsorbate due to the dipole and higher-multipole moments of the atom. It can be expanded in terms of even powers of q as [Zaremba and Kohn, 1976; Bruch *et al.*, 1997]

$$A(q,i\omega) = 2\alpha_1^a(i\omega)q^2 + \frac{2}{3}\alpha_2^a(i\omega)q^4 + \mathcal{O}(q^6) + \ldots, \tag{4.11}$$

where α_1^a and α_2^a are the frequency-dependent dipole and quadrupole polarizabilities of atom a, respectively, evaluated at imaginary frequency. Higher-multipole polarizabilities correspond to higher even powers of q.

The surface response function $S(q,i\omega)$, which has the form of

$$S(q,i\omega) = \frac{2\pi}{q}\int dz \int dz'\, e^{q(z+z')}\,\chi_S(z,z',i\omega), \tag{4.12}$$

contains all the information of the substrate, that is, its structure and the response given by its electronic structure. $S(q,i\omega)$ can also be formulated as [Zaremba and Kohn, 1976; Persson and Zaremba, 1984]

$$S(q,i\omega) = \int dz\, e^{qz}\delta n(z,q,i\omega), \tag{4.13}$$

where $\delta n(z,q,i\omega)$ is the surface electron density induced by an external charge of the form $\rho_{\mathrm{ext}}(\boldsymbol{r},t) = \delta(z-Z)e^{i\boldsymbol{q}\cdot\boldsymbol{\rho}}e^{\omega t}$ [Zaremba and Kohn, 1976; Persson and Zaremba, 1984]. The surface response function gives the relative amplitude of the induced electrostatic potential. It can also be seen, according to (4.13), as an exponentially weighted integral of the surface charge density [Persson and Zaremba, 1984]. It includes effects due to the diffuseness of the surface charge density and the nonlocal dielectric response of the surface and the bulk. Expression (4.13) can be expanded in terms of q as [Bruch *et al.*, 1997]

$$S(q,i\omega) = \sigma_0(i\omega) + q\sigma_1(i\omega) + \mathcal{O}(q^2) + \ldots, \tag{4.14}$$

where the term σ_0, corresponding to the limit $q = 0$ of $S(q,i\omega)$, is the total surface charge density and can be expressed in terms of the bulk dielectric function $\epsilon_S(i\omega)$ of substrate S as

$$\sigma_0(i\omega) = \frac{\epsilon_S(i\omega) - 1}{\epsilon_S(i\omega) + 1}. \tag{4.15}$$

The expansion of $S(q,i\omega)$ in powers of q generates a series for $E_{\mathrm{vdW}}^{(2)}$ which can be in consequence given in terms of inverse powers of Z [Zaremba and Kohn, 1976; Bruch

et al., 1997]. Given the expansions of (4.11) and (4.14), the vdW interaction of (4.10) can be expressed as

$$E_{\mathrm{vdW}}^{(2)} \simeq -\frac{C_3^{aS}}{Z^3} - \frac{C_4^{aS}}{Z^4} - \mathcal{O}(Z^{-5}) + \ldots, \tag{4.16}$$

where

$$C_3^{aS} = \frac{1}{4\pi}\int_0^\infty d\omega\, \alpha_1^a(i\omega)\sigma_0(i\omega), \tag{4.17}$$

and

$$C_4^{aS} = \frac{3}{8\pi}\int_0^\infty d\omega\, \alpha_1^a(i\omega)\sigma_1(i\omega). \tag{4.18}$$

The leading term of (4.16) shows the characteristic Z^{-3} behavior of the atom-surface vdW interaction [see London and Polanyi, 1930; Lifshitz, 1956; Zaremba and Kohn, 1976], which depends on the dipole polarizability of the adsorbate and the surface charge density of the substrate [see (4.17)]. Higher-Z^{-n} terms and their respective interaction coefficients C_n^{aS} correspond to complex expressions involving both adsorbate and substrate response properties [Bruch *et al.*, 1997].

With the identification of σ_0 in terms of the macroscopic bulk dielectric function of the substrate in (4.15), the interaction coefficient C_3^{aS} is given by

$$C_3^{aS} = \frac{1}{4\pi}\int_0^\infty d\omega\, \alpha_1^a(i\omega)\frac{\epsilon_S(i\omega)-1}{\epsilon_S(i\omega)+1}. \tag{4.19}$$

Lifshitz [1956] originally gave a macroscopic formulation of the attractive vdW forces between two bodies. His formulation characterized each body in terms of spatially nondispersive ($q = 0$) frequency-dependent dielectric functions such as σ_0 in (4.19) and resulted in the same inverse third power dependence on the distance between bodies. The approach of Zaremba and Kohn [1976] that yields the asymptotic expansion in (4.16) has the advantage of taking into account the microscopic details of the surface in the atom-surface vdW interaction. However, expression (4.16) cannot be applied directly to the atom-surface vdW interaction since the choice of the origin of coordinates in the expansion is not obvious considering the distances typically found in physisorption. The first two terms in (4.16) can be recovered by writing [Zaremba and Kohn, 1976; Bruch *et al.*, 1997]

$$E_{\mathrm{vdW}}^{(2)} \simeq -\frac{C_3^{aS}}{(Z-Z_0)^3}, \tag{4.20}$$

where Z_0 is the position of the reference plane for the atom-surface vdW interaction and is defined as

$$Z_0 \equiv \frac{C_4^{aS}}{3C_3^{aS}}. \tag{4.21}$$

The vdW reference plane Z_0 can be understood as a consequence of the spatially dispersive character found in the density-response function of the substrate as its definition in terms of C_4^{aS} indicates [Zaremba and Kohn, 1976; Bruch *et al.*, 1997]. The physical importance of C_4^{aS} lies in its dependence on σ_1 in (4.18), which corresponds to the linear term in q found in the expansion of the surface response function $S(q, i\omega)$. We note that the relationship among the Lifshitz theory, the ZK theory, and the RPA approximation within the ACFD formalism is discussed by Dobson and Gould [2012].

4.3.1 Atom-surface van der Waals interaction as a sum of interatomic pairwise potentials

In order to give a theoretical basis to Polanyi's potential theory of adsorption [Polanyi, 1932, 1963], London and Polanyi [1930] first proposed the inverse third power dependence on the distance for the adsorption of particles in a gas on a flat surface. Based on the work in dispersion forces between atoms by London [1930, 1937], their approach consisted in the summation of pairwise vdW interactions between a single gas particle and each of the atoms contained in the volume of the solid, yielding an inverse third power dependence on the distance between particle and substrate.

Let us consider a homogeneous distribution of attractive forces within the substrate between atom a and each of the atoms s constituting substrate S given by the leading $-C_6R^{-6}$ term of the vdW interaction between two atoms. We can recover the inverse third power dependence on the distance by integrating the pairwise interaction over the volume of the substrate spanning the region $\mathscr{S}_S$ [Hamaker, 1937; Cole *et al.*, 2012]

$$E_{\mathrm{vdW}}^{(2)} \simeq -\int_{\mathscr{S}_S} dV\, n_S \frac{C_6^{as}}{R^6}, \tag{4.22}$$

where dV is the volume element of substrate S and n_S is the number of atoms per unit volume in the bulk of the substrate. Starting from expression (4.22), the Lifshitz-Zaremba-Kohn (LZK) formula given in (4.20) can be recovered exactly [Zaremba and Kohn, 1976; Bruch *et al.*, 1997; Patil *et al.*, 2002] by setting

$$C_3^{aS} = n_S\left(\frac{\pi}{6}\right) C_6^{as}, \tag{4.23}$$

and

$$Z_0 = \frac{d}{2}, \tag{4.24}$$

where d is the interlayer distance between equally spaced lattice planes parallel to the surface. In the jellium model of a metal, $d/2$ corresponds to the position of the jellium edge [Zaremba and Kohn, 1976; Bruch *et al.*, 1997]. Deviations from this position occur due to local-field effects in the dielectric function and reflect surface polarization. The magnitude of these deviations also constitutes a measure of the importance of many-body forces in the potential between the atom and the solid [Zaremba and Kohn, 1976].

4.4 Density-functional approximations with screened van der Waals interactions to model adsorption phenomena

Our discussion of vdW interactions so far has emphasized the well-separated regime where there is no wave-function overlap between the interacting fragments. This regime is a natural starting point for vdW interactions as the origin of these lies in the induced polarization which results from instantaneous fluctuations of the electronic density, effects which are part of the electronic correlation energy of the interacting system. However, in order to provide a quantitative account even in model adsorption systems –such as the adsorption of noble gases on metal surfaces– it is necessary to incorporate the (chemical) interactions that occur at the short-range regime where the wave-function

hybridization becomes important. This can be understood in the context of electronic-structure theory as treating the exchange and correlation energies on an equal footing.

We have mentioned in chapter 2 how DFT has become the primary tool for treating exchange and correlation effects in electronic-structure calculations of condensed matter and molecular systems due to its good compromise between accuracy and efficiency. Unfortunately, the subtle (and relatively weak)[2] nature of vdW interactions introduces a great deal of complexity for standard approximations in DFT –(semi)-local and hybrid xc functionals– which are able to give a relatively good and quantitative account of covalent bonds but fail to give even a qualitative account of bonds originated in vdW interactions. Equally, we have briefly reviewed in section 2.5 the main strategies to include vdW interactions in the context of DFT, but evidenced in section 4.1 the inaccuracy of these methods to describe the structure and stability of realistic adsorption systems such as HIOS due to the absence or inaccuracy of the non-local collective electron response of the extended surface in the vdW energy.

It is evident that the main challenge in modeling the adsorption of atoms and molecules on surfaces is to develop methods that are able to capture both covalent and non-covalent interactions in a reliable manner while at the same time being capable of dealing with realistic adsorption systems in an efficient fashion. It is with these features in mind that we present in this section a method to model *screened* vdW interactions for the adsorption of atoms and molecules on surfaces: the DFA+vdW$^{\text{surf}}$ method. The DFA+vdW$^{\text{surf}}$ scheme combines methods for molecules and solids with the purpose of an accurate description of vdW interactions in modeling the adsorption of atoms and molecules on surfaces. We accomplish this by linking the LZK theory of the vdW interaction between an atom and a solid surface to include the collective response of the substrate electrons with the DFA+vdW method to include intermolecular interactions. We illustrate this conceptual link in Figure 4.3.

The DFA+vdW$^{\text{surf}}$ method consists in a vdW energy correction to the total DFT energy in the same spirit of (2.106), where the vdW energy of the system is calculated as a sum of pairwise interaction terms

$$E_{\text{vdW}} = -\frac{1}{2}\sum_a \sum_b f_{\text{damp}}(R_{ab}, R_a^0, R_b^0)\frac{C_6^{ab}}{R_{ab}^6}, \tag{4.25}$$

where R_{ab} is the distance between atoms a and b and C_6^{ab} is the corresponding C_6 coefficient given by the Casimir-Polder integral of (4.4). The damping function f_{damp} eliminates the R_{ab}^{-6} singularity found at small distances and is a function of the vdW radii R_a^0 and R_b^0. In analogy to the DFA+vdW method, we adopt a Padé approximant[3] model [Tang and Karplus, 1968] for the frequency-dependent dipole polarizability of atom $i = \{a, b\}$.

[2] The long-range vdW energy represents a small fraction of approximately 0.001% of the total electronic energy of a system [Ferri *et al.*, 2015]. Bonds originated from vdW interactions can be considered relatively weak in magnitude in comparison to covalent bonds. However, research in the last few years has revealed the quantitative importance of vdW interactions in bonding scenarios within the context of adsorption phenomena and large extended molecular systems; even for the cases in which strong chemical interactions are present [see for example the works by Liu *et al.*, 2013b, 2014, or our discussion in inorganic/organic systems present in chapter 7].

[3] The Padé approximant $P(N, M)$ to a function $F(x)$ is the ratio of two polynomials of degree N and M, $P(N, M) = P_N(x)/Q_M(x)$. The polynomial coefficients are chosen so that the series expansion of $P(N, M)$ agrees with the first $N + M + 1$ terms in the expansion of $F(x)$ [taken from Tang and Karplus, 1968].

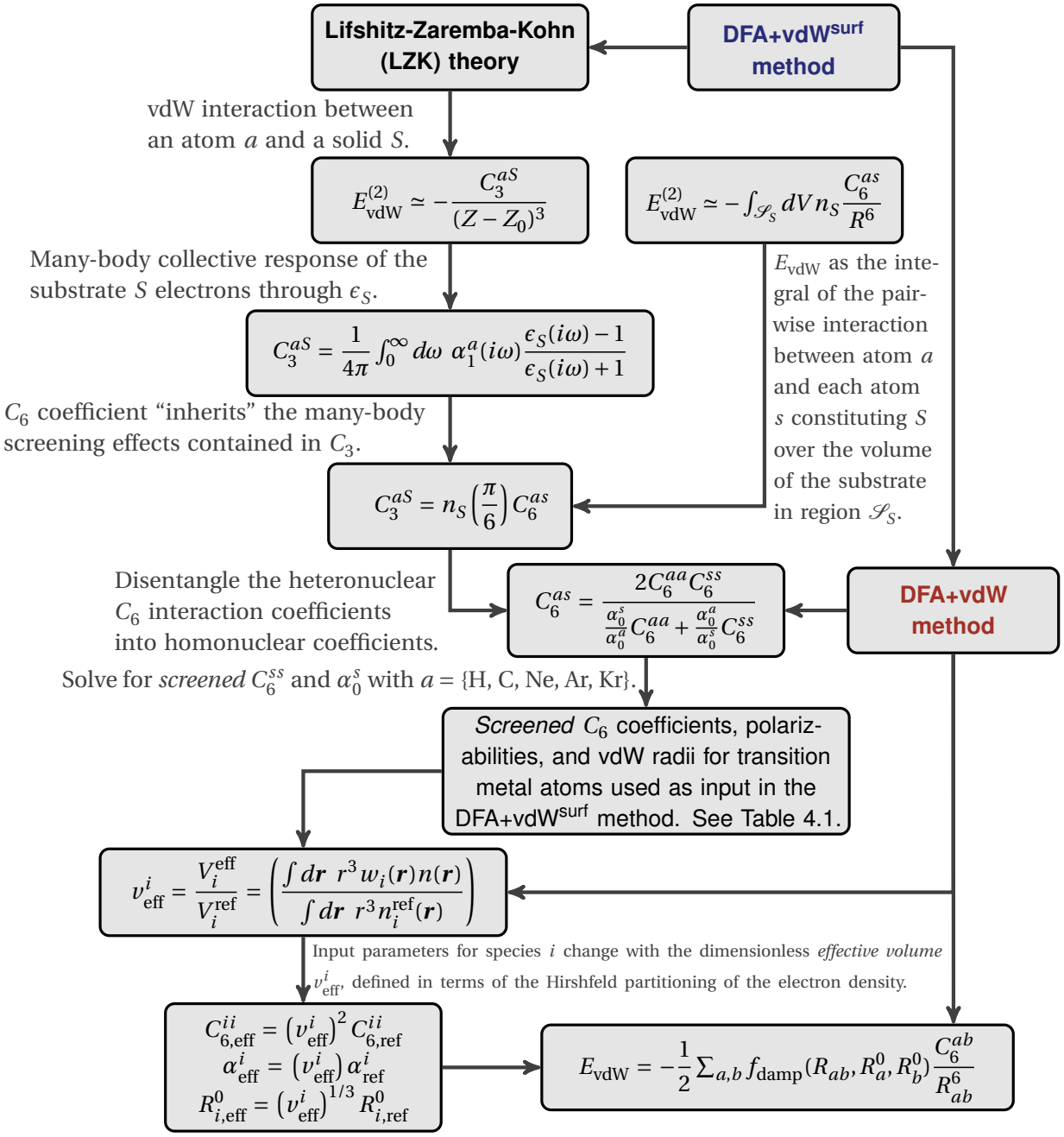

FIGURE 4.3: Conceptual link between the LZK theory and the DFA+vdW leading to the DFA+vdW$^{\rm surf}$ method. The DFA+vdW$^{\rm surf}$ method combines vdW-inclusive DFT for the intermolecular interactions (the DFA+vdW method) together with the collective response of the electrons (the LZK theory) to model *screened* vdW interactions in the adsorption of atoms and molecules on surfaces.

Taking the leading term of the Padé series leads to

$$\alpha_1^i(\omega) = \frac{\alpha_0^i}{1-(\omega/\eta_i)^2}, \tag{4.26}$$

where α_0^i is the static dipole polarizability of atom i and η_i is an effective excitation frequency [Tang, 1969; Tkatchenko and Scheffler, 2009]. The Casimir-Polder integral can be solved analytically with $\alpha_1(i\omega)$ given by (4.26) leading to a London-type formula [Tang, 1969; Tkatchenko and Scheffler, 2009]

$$C_6^{ab} = \frac{3}{2}\left(\frac{\eta_a\eta_b}{\eta_a+\eta_b}\right)\alpha_0^a\alpha_0^b, \tag{4.27}$$

with the effective frequency of atom i given when $a = b$ as [Tkatchenko and Scheffler, 2009]

$$\eta_i = \frac{4}{3}\frac{C_6^{ii}}{(\alpha_0^i)^2}. \tag{4.28}$$

With expressions (4.27) and (4.28), a simple combination rule for C_6^{ab} is found [Tkatchenko and Scheffler, 2009]

$$C_6^{ab} = \frac{2C_6^{aa}C_6^{bb}}{\frac{\alpha_0^b}{\alpha_0^a}C_6^{aa} + \frac{\alpha_0^a}{\alpha_0^b}C_6^{bb}}. \tag{4.29}$$

Expression (4.29) gives the interaction coefficient C_6^{ab} between atoms a and b in terms of the homonuclear parameters C_6^{ii} and α_0^i. We will refer to these in the following as vdW parameters.

Each atom conforming a molecule or material is subject to a dynamical internal electric field that depends on both local and non-local fluctuations associated with the surrounding atoms. Effects due to the environmental screening and anisotropy are absent from a description of the polarizabilty given by expression (4.26) [DiStasio Jr. *et al.*, 2014]. Incorporating local effects due to the chemical environment is the goal of the DFA+vdW method of Tkatchenko and Scheffler [2009] with the assumption of a system with a finite electronic gap and, therefore, the possibility of an atomic partition scheme. The frequency-dependent polarizabilities defined in the DFA+vdW method yield C_6 coefficients that are accurate to 5.5% when compared to reference experimental values for small molecular dimers. For a system with a finite electronic gap, the long-range electrodynamic response screening and anisotropy effects are taken into account for the polarizabilities in the MBD method [see Tkatchenko *et al.*, 2012; Ambrosetti *et al.*, 2014b; DiStasio Jr. *et al.*, 2014]. The environmental effects due to free-electron screening in metallic systems are, however, strictly absent from the atomic definition found in both the DFA+vdW and MBD methods. We shall now address how to take into account this effect in the definition of the reference vdW parameters.

4.4.1 Reference van der Waals parameters

For the case of free-atom reference vdW parameters, accurate values are given in the database of Chu and Dalgarno [2004] [see also Tkatchenko and Scheffler, 2009]. In the

case of solids, the reference vdW parameters for an atom must be determined taking into account the environmental effects that an *atom-in-a-solid* is subject to [Zhang *et al.*, 2011]. We rely on the LZK theory to achieve this. We start by noting that for the atom-surface vdW interaction, we can recover the LZK formula (4.20) exactly starting from a summation of pairwise potentials between the adsorbate and each of the atoms in the solid. The pairwise C_6^{as} coefficient between atom a and atom s in the solid can be obtained from (4.23) and (4.19) as

$$\begin{aligned} C_6^{as} &= \frac{1}{n_S}\left(\frac{6}{\pi}\right) C_3^{aS} \\ &= \frac{1}{n_S}\left(\frac{3}{2\pi^2}\right)\int_0^\infty d\omega\, \alpha_1^a(i\omega)\frac{\epsilon_S(i\omega)-1}{\epsilon_S(i\omega)+1}. \end{aligned} \tag{4.30}$$

The effective vdW coefficient C_6^{as} given in (4.30) inherits the many-body collective response (*screening*) of the solid as indicated by its dependence on the dielectric function ϵ_S. In this context, the adsorbate corresponds to a free atom in the gas phase, which allows us to evaluate $\alpha_1^a(i\omega)$ with (4.26) using the values of C_6^{aa} and α_0^a given by Chu and Dalgarno [2004]. Expression (4.30) can then be determined by calculating the dielectric function $\epsilon_S(i\omega)$ of the solid. We use the Kramers-Kronig relation to determine $\epsilon_S(i\omega)$ in terms of the absorptive part of the dielectric function ϵ_2 at real frequencies. We mainly take data from reflection energy-loss spectroscopy (REELS) experiments by Werner *et al.* [2009] for this purpose. In the case of Rh and Ir, optical constants were taken from the reflectance measurements of Windt *et al.* [1988]. Finally, in the case of Ru, the optical measurements were taken from Choi *et al.* [2006]. We may note in passing that the determination of the dielectric function as input for the coefficients in the present method is not limited to experimental results. It may also be accurately computed from first-principles as demonstrated by Werner *et al.* [2009] whose DFT calculations agree reasonably well with REELS results within the experimental uncertainties involved.

Having determined C_6^{as}, the reference vdW parameters C_6^{ss} and α_0^s for the atom-in-a-solid can be calculated by a system of two equations like (4.29) with $b = s$ and two different adsorbing atoms a. Take, for example, Cu interacting with Ne and Ar. Two equations of the type given by (4.29) with s = Cu can be set for C_6^{NeCu} and C_6^{ArCu} where C_6^{CuCu} and α_0^{Cu} are the only two unknown parameters. We take any two atoms from the list: H, C, Ne, Ar, and Kr and solve the set of two equations for C_6^{ss} and α_0^s for a given substrate. The resulting vdW reference parameters of different substrate atoms are displayed in Table 4.1. For comparison, the reference parameters of the free atoms are presented as well. The vdW radius for the atom-in-a-solid R_s^0 is obtained via the relation

$$R_s^0 = \left(\frac{\alpha_0^s}{\alpha_{0,\mathrm{free}}^s}\right)^{1/3} R_{s,\mathrm{free}}^0, \tag{4.31}$$

where $R_{s,\mathrm{free}}^0$ corresponds to the vdW radius of the same species s but as a free atom. We use the TS ansatz to determine the free-atom vdW radii.[4]

The values in Table 4.1 for the *screened* vdW parameters for an atom-in-a-solid show that the environmental effects in a solid cannot be neglected in the calculation of vdW

[4] For the (spherical) free atoms, the electron density contour value corresponding to the vdW radius can be determined for the rare-gas atoms and then used to define R_{free}^0 free for other elements in the same row of the periodic table [Tkatchenko and Scheffler, 2009].

Table 4.1: Screened vdW parameters as used in the DFA+vdW$^{\text{surf}}$ method. For comparison, the free-atom parameters as used in the DFA+vdW method are also shown. C_6 (in hartree·bohr^6), α_0 (in bohr^3), and R^0 (in bohr) denote the dispersion coefficient, polarizability, and vdW radius respectively. The experimental lattice constants [King, 2015] have been employed to calculate n_S in (4.23).

Substrate	*Screened*			*Free atom*		
	C_6	α_0	R^0	C_6	α_0	R^0
Ti	116	16.8	2.51	1044	98.0	4.51
V	80	13.3	2.40	832	84.0	4.44
Fe	61	11.0	2.46	482	56.0	4.23
Co	55	10.5	2.50	408	50.0	4.18
Ni	59	10.2	2.28	373	48.0	3.82
Cu	59	10.9	2.40	253	42.0	3.76
Zn	62	12.9	2.76	284	40.0	4.02
Ru	53	13.6	2.36	610	65.9	4.00
Rh	84	13.0	2.42	469	56.1	3.95
Pd	102	13.9	3.07	158	23.7	3.66
Ag	122	15.4	2.57	339	50.6	3.82
Ir	98	13.2	2.71	359	42.5	4.00
Pt	120	14.5	2.80	347	39.7	3.92
Au	134	15.6	2.91	298	36.5	3.86

interactions. The inclusion of the collective response of the solid in the determination of the vdW parameters for transition metals can lead to pronounced differences with respect to the free-atom reference values by reducing the vdW C_6 coefficients up to an order of magnitude (in the cases of Ti and V for example). Significant effects can be observed in static polarizabilities (α_0) and vdW radii (R^0) as well. The sensitive dependence of the dielectric screening on the substrate is manifested clearly by these results. We note that the parameters here calculated can be considered as intrinsic properties of the bulk as they are essentially invariant to the nature of the adsorbed atom.

4.4.2 Hybridization and interface polarization effects

A set of accurate reference vdW parameters has been established so far for both free atoms and atoms inside a solid. However, the effects of charge polarization that an atom in a molecule or an interface would experience are not included yet. In the case of adsorption phenomena, there will be effects related to the polarization of the interface. These effects are manifested as the spatial dispersion in the dielectric function close to the surface of the system. They are included in higher $q-$dependent terms of the substrate response function given by (4.14).

The effects of charge polarization are included in the case of molecules in the DFA+vdW method by renormalizing the vdW parameters using the ground-state electron density obtained from DFT calculations [Tkatchenko and Scheffler, 2009]. We adopt the same strategy to account for interface polarization in adsorption phenomena

by defining an *effective volume* v^i_{eff} for species i as

$$v^i_{\text{eff}} = \frac{V^{\text{eff}}_i}{V^{\text{ref}}_i} = \left(\frac{\int d\boldsymbol{r}\; r^3 w_i(\boldsymbol{r}) n(\boldsymbol{r})}{\int d\boldsymbol{r}\; r^3 n^{\text{ref}}_i(\boldsymbol{r})} \right), \tag{4.32}$$

$$w_i(\boldsymbol{r}) = \frac{n^{\text{ref}}_i(\boldsymbol{r})}{\sum_j n^{\text{ref}}_j(\boldsymbol{r})}, \tag{4.33}$$

where r^3 is the cube of the distance from the nucleus of atom i, $w_i(\mathbf{r})$ is the Hirshfeld atomic partitioning weight of the species i [Hirshfeld, 1977], $n(\mathbf{r})$ is the total electron density, $n^{\text{ref}}_i(\mathbf{r})$ is the reference electron density for atom i, and the sum goes over all atoms of the system [Tkatchenko and Scheffler, 2009; Johnson and Becke, 2005]. For the solid, the reference corresponds to the spherical electron density of an atom in the bulk, and for a molecule, it corresponds to the free-atom electron density. By exploiting the direct relation between polarizability and volume [Brink *et al.*, 1993; Tkatchenko and Scheffler, 2009], the effective $C_{6,\text{eff}}$ coefficient, the effective polarizability α_{eff}, and the effective vdW radius $R^0_{i,\text{eff}}$ are determined as [Tkatchenko and Scheffler, 2009]

$$C^{ii}_{6,\text{eff}} = \left(v^i_{\text{eff}} \right)^2 C^{ii}_{6,\text{ref}}, \tag{4.34}$$

$$\alpha^i_{\text{eff}} = \left(v^i_{\text{eff}} \right) \alpha^i_{\text{ref}}, \tag{4.35}$$

$$R^0_{i,\text{eff}} = \left(\frac{\alpha^i_{\text{eff}}}{\alpha^i_{\text{ref}}} \right)^{1/3} R^0_{i,\text{ref}}. \tag{4.36}$$

Effects beyond the pairwise approximation are achieved by the inclusion of semi-local effects through the dependence of the vdW parameters on the electron density as given by (4.34)–(4.36). For example, we have reported significant interface polarization in systems such as PTCDA on Ag(111) and benzene on Pt(111) manifested in the value of the C_6 coefficients in the region of the metal-molecule interface [Ruiz *et al.*, 2012; Liu *et al.*, 2013b].

4.4.3 Empirical short-range damping function

The fact that we adopt an interatomic pairwise expression as (4.25) in order to compute vdW interactions leads to the presence of a R^{-6}_{ab} singularity at small distances. We couple the vdW energy to a given semi-local xc functional via a short range damping function. The damping function f_{damp} in the DFA+vdW$^{\text{surf}}$ method follows the same strategy as the DFA+vdW method, having the following form [Tkatchenko and Scheffler, 2009]

$$f_{\text{damp}}(R_{ab}, R^0_{ab}) = \frac{1}{1 + \exp\left[-d \left(\frac{R_{ab}}{s_R R^0_{ab}} - 1 \right) \right]}, \tag{4.37}$$

where $R^0_{ab} = R^0_a + R^0_b$, $d = 20$ determines the steepness of the damping, and s_R determines the range of the damping. The range parameter s_R is the only parameter that is determined empirically. This is done by fitting s_R for each underlying xc functional to the S22 data set of Jurečka *et al.* [2006]. The S22 data set contains binding energies of 22 different weakly bound systems, calculated using the coupled-cluster method with

single, double, and triple excitations, where triple excitations are treated perturbatively [CCSD(T)] [see Tkatchenko and Scheffler, 2009; Marom *et al.*, 2011].

In the DFA+vdW^{surf} method, the inclusion of the LZK theory leads to a set of effective C_6 coefficients -see Table 4.1- that are determined by the dielectric screening of the bulk and the electronic environment of each atom, yielding a smaller long-range vdW energy. On the other hand, the DFA+vdW^{surf} method also carries a larger relative weight of the vdW contributions at shorter range due to the effect that the reduction of the vdW radii has on the damping function. The non-trivial coaction of these effects and the underlying xc functional enables an accurate treatment of complex interfaces where the interplay of different interactions is present. We also mention that the DFA+vdW^{surf} method does not depend on the nature of the substrate, and in principle it is equally applicable to insulators, semiconductors, and metals.

4.5 Metal bulk lattice constants with density-functional approximations including screened van der Waals interactions

Liu *et al.* [2013b] have calculated the bulk lattice constant of several transition metals in a previous work using the DFA+vdW^{surf} method with the PBE approximation as underlying xc functional, which we refer to as PBE+vdW^{surf}. As we have discussed above, the PBE+vdW^{surf} method includes the *screening* due to metallic bulk electrons in the computation of the long-range vdW energy tail. However, since the PBE functional is reduced to the local-density approximation (LDA) for homogeneous electron densities, the metallic electrons are already accurately described within the PBE functional. This fact results in a partial "double counting" of the interaction between metallic electrons with the PBE+vdW^{surf} method, leading to an overestimation of the vdW energy inside the metal bulk. This effect yields a slight increase of the lattice constants compared to the PBE functional in some transition metals while decreasing it in some other cases [see Liu *et al.*, 2013b]. But, even if the present method can actually lead to an improvement in the bulk lattice constant for some of the transition metals here studied, there is no straightforward way to quantify the overestimation effects. On the other hand, these effects do not pose a problem in the adsorption of molecules on surfaces because the adsorbate interacts both with the localized ions and the delocalized metallic electrons. Further improvement of the lattice constants requires a full microscopic treatment of the polarizability due to localized ions and metallic electrons.

Part III

Applications

CHAPTER

5 Adsorption-potential energies with density-functional approximations including screened van der Waals interactions

A major part of our motivation to develop efficient vdW-inclusive methods for modeling adsorption phenomena is the treatment of realistic adsorption systems such as HIOS. We have presented in section 4.1 an analysis on the performance of vdW-inclusive DFT methods regarding the adsorption of one of the best experimentally and theoretically characterized HIOS: PTCDA on Ag(111). Our analysis has shown the limited power of standard vdW-inclusive DFT methods to predict the structure of PTCDA on Ag(111) mainly due to the absence of the many-body collective electron response of the extended surface in the long-range vdW energy. Our proposal to solve this problem was the subject of chapter 4, namely the DFA+vdW$^{\text{surf}}$ method. In this chapter we begin with the applications of the DFA+vdW$^{\text{surf}}$ method taking the adsorption potential energies of PTCDA on Ag(111) and Au(111) as our first study cases. Because of the analysis presented in section 4.1, we first revisit the adsorption-potential energy of PTCDA on Ag(111) in section 5.1 as first example of performance with the DFA+vdW$^{\text{surf}}$ method. In section 5.2 we show the adsorption-potential energy of a single PTCDA molecule on Au(111) and conclude by analyzing some of the aspects in the DFA+vdW$^{\text{surf}}$ method that lead to the characteristics of the observed adsorption potential energy. This chapter is based on our own previously published work [Ruiz *et al.*, 2012, 2016].

5.1 3,4,9,10-Perylene-tetracarboxylic dianhydride on Ag(111) revisited

We revisit the adsorption of PTCDA on Ag(111) in Figure 5.1, where we reproduce the adsorption potential energy curves discussed in section 4.1 (see Figure 4.1) with the inclusion of the curve calculated with the DFA+vdW$^{\text{surf}}$ method using PBE [Perdew *et al.*, 1996] as underlying xc functional. The calculations have been performed with the all-electron/full-potential electronic-structure code FHI-AIMS which uses numerical atomic-orbital (NAO) as basis sets [Blum *et al.*, 2009]. We employ *tight* numerical basis

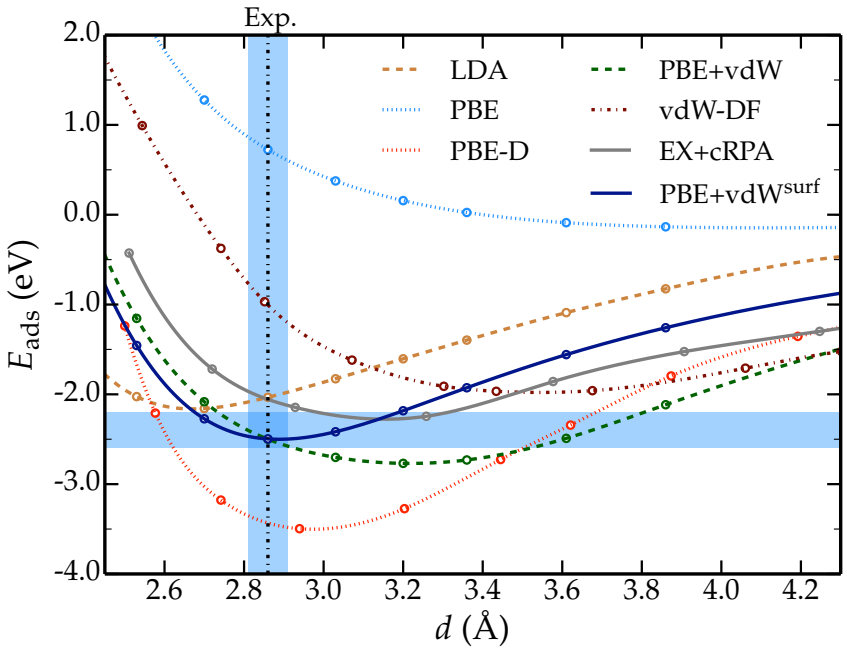

FIGURE 5.1: Adsorption energy E_{ads} as a function of vertical distance d for PTCDA on Ag(111) employing different vdW-inclusive DFT methods including the DFA+vdW$^{\text{surf}}$ method using the PBE xc functional. The estimated adsorption energy for the system of -2.4 ± 0.2 eV [Tkatchenko *et al.*, 2010] and the experimental adsorption distance of 2.86 ± 0.05 Å [Hauschild *et al.*, 2010] are indicated by shaded intervals. These error bars correspond to typical experimental error estimates.

settings, which include the *tier 1* standard basis set for the metallic substrate and the *tier 2* basis set for C, H, and O[1]. The adsorption potential energy curve was calculated using a $\begin{pmatrix} 6 & 1 \\ -3 & 5 \end{pmatrix}$ surface unit cell in accordance to experimental results [Glöckler *et al.*, 1998]. For reasons of computational tractability, the PBE calculations have been performed with a Ag(111) surface slab with three metallic layers generated with the PBE bulk lattice constant (4.149 Å), a vacuum gap of 50 Å, and a Monkhorst-Pack grid of $4 \times 4 \times 1$ k points in the reciprocal space.[2] For the vdW and vdW$^{\text{surf}}$ calculations on top of PBE, we have used a Ag(111) surface slab consisting of five metallic layers to converge the vdW binding energy. All binding curves have been calculated using unrelaxed structures.

The adsorption energy per adsorbed molecule in the monolayer was calculated us-

[1] Further convergence criteria include 10^{-5} electrons for the electron density and 10^{-6} eV for the total energy of the system. Relativistic effects were included via the atomic scalar zeroth-order regular approximation [van Lenthe *et al.*, 2000].

[2] We note that a surface slab of three layers is not enough to reproduce the electronic properties of a Ag(111) surface. However, in this section we are only interested in calculating the structural and energetic features of the system and compare them with results available from other density-functional approximations. We leave the full structural relaxation of the system with a surface slab of five layers as a matter of analysis for chapter 7.

ing

$$E_{\text{ads}} = \frac{1}{N}\left[E_{\text{AdSys}} - \left(E_{\text{Me}} + E^{\text{ml}}_{\text{PTCDA}}\right)\right], \tag{5.1}$$

where E_{AdSys} is the energy per unit cell of the system (PTCDA + metallic surface), E_{Me} is the energy per unit cell of the bare metal slab, $E^{\text{ml}}_{\text{PTCDA}}$ is the energy per unit cell of of the PTCDA monolayer, and N is the number of molecules in the monolayer. In this case, $N = 2$ because there are two molecules per unit cell in our model, corresponding to a coverage of one monolayer as defined in experiments [Glöckler *et al.*, 1998]. The unrelaxed surface and a planar PTCDA monolayer were employed for all the calculated points. The vertical distance d was defined as the difference of the position of the monolayer with respect to the position of the unrelaxed topmost metallic layer.

The first interesting observation comes from comparing the binding curves calculated with the PBE+vdW$^{\text{surf}}$ and PBE+vdW methods in Figure 5.1. The reduced *effective* C_6 coefficient, determined by the dielectric screening of the bulk and the electronic environment of each atom in the PBE+vdW$^{\text{surf}}$ method, yields a smaller long-range vdW energy. However, the vdW radius of the Ag atoms is also reduced in the PBE+vdW$^{\text{surf}}$ method leading to larger values of the damping function at shorter distances, which produces a larger relative weight of the vdW contributions at shorter range in the PBE+vdW$^{\text{surf}}$ method in comparison to the PBE+vdW method. The coaction of these effects causes a non-trivial reduction of both the adsorption energy and the adsorption distance, which modifies the binding-energy curve of PTCDA on Ag(111) as observed in Figure 5.1. The improved description of the binding with the PBE+vdW$^{\text{surf}}$ method leads to an adsorption distance of 2.89 Å and an adsorption energy of approximately −2.5 eV. These results are in an excellent agreement within 0.1 Å with respect to experiment regarding the adsorption distance, and within 0.2 eV in the adsorption energy with respect to the estimated (still uncertain) experimental value. Geometry relaxations , missing in these adsorption potential energy calculations, induce relatively small differences in the binding energy and the adsorption height of the perylene core (see section 7.3.1).

5.2 Adsorption-potential energy of 3,4,9,10-perylene-tetracarboxylic dianhydride on Au(111)

Experimental studies observe that PTCDA is physisorbed on Au(111), hence its bonding interaction is governed mainly by vdW forces [Henze *et al.*, 2007; Tautz, 2007; Wagner *et al.*, 2012; Ziroff *et al.*, 2009]. Wagner *et al.* [2012] studied the system based on single-molecule manipulation experiments. By combining scanning tunneling microscopy and frequency-modulated atomic force microscopy, they reported an adsorption energy of about −2.5 eV per molecule of PTCDA and an adsorption distance of approximately 3.25 Å, a value which is displayed as a blue shaded region in Figure 5.2. The case of PTCDA on Au(111) has also been measured using the NIXSW technique by Henze *et al.* [2007] and Hauschild *et al.* [2010], where they found an approximate adsorption distance of 3.31 Å for the PTCDA monolayer. In addition, TPD experiments performed to study the adsorption of the monolayer reveal an adsorption energy of approximately −1.94 eV per molecule [Stremlau, 2015]. For these reasons and the experimental information that is

available, PTCDA on Au(111) serves as an interesting example of physisorption in an organic/inorganic interface.

System specifications and calculational details. The DFT calculations were performed using the electronic-structure code FHI-AIMS [Blum *et al.*, 2009]. As in section 5.1, we have used the PBE [Perdew *et al.*, 1996] xc functional and *tight* settings for the calculations. Further convergence criteria include 10^{-5} electrons for the electron density and 10^{-6} eV for the total energy of the system. Relativistic effects were included via the atomic scalar zeroth-order regular approximation [van Lenthe *et al.*, 2000]. The system consisted of a single molecule adsorbed on a Au(111) surface modeled with three metallic layers using the repeated-slab method in-line with previous investigations [Ruiz *et al.*, 2012; Romaner *et al.*, 2009; Hauschild *et al.*, 2005; Rohlfing *et al.*, 2007; Rohlfing and Bredow, 2008]. The surface unit cell was modeled with a $\begin{pmatrix} 6 & -6 \\ 1 & 10 \end{pmatrix}$ supercell and a vacuum width of 40 Å in order to minimize the interactions between neighboring molecules. We used a Monkhorst-Pack grid of $2 \times 2 \times 1$ k points in the reciprocal space for the DFT calculations.

Adsorption potential energy curve. We have calculated the adsorption potential energy curve of a single PTCDA molecule on Au(111) using the PBE, PBE+vdW, and PBE+vdW$^{\text{surf}}$ methods, which are displayed in Figure 5.2(a). The adsorption energy per adsorbed molecule was calculated using (5.1) with $N = 1$ since the monolayer in this case is composed of one molecule per unit cell, which consists of a larger super cell in comparison to the case of Ag(111) to minimize the interactions between neighboring molecules (see above). The calculations correspond to the unrelaxed system where the metal slab was generated using the experimental lattice constant of Au in order to have a direct comparison with the single-molecule experimental results of Wagner *et al.* [2012]. From Figure 5.2(a), it is clear that the PBE functional cannot accurately describe the adsorbate-substrate interaction as it leads to an exceptionally small adsorption energy. Both PBE+vdW and PBE+vdW$^{\text{surf}}$ calculations show a stronger interaction due to the inclusion of vdW interactions. Figure 5.2(a) shows that a single molecule of PTCDA adsorbs at a height of approximately 3.44 Å with an adsorption energy of approximately -2.69 eV per molecule with the PBE+vdW method. On the other hand, the PBE+vdW$^{\text{surf}}$ curve yields an adsorption distance of approximately 3.23 Å and an adsorption energy of approximately -2.23 eV per molecule. We have performed the same calculation using the PBE lattice constant of Au [4.159 Å, in accordance to our previous work, see Liu *et al.*, 2013b] to generate the surface slab. The adsorption potential curve yields in this way an adsorption distance of 3.21 Å and an adsorption energy of -2.17 eV with the PBE+vdW$^{\text{surf}}$ method. These values do not change considerably with respect to the lattice constant used so we proceed now to compare the values that we obtain when the experimental lattice constant is used.

We observe differences in the adsorption distance predicted by the PBE+vdW and PBE+vdW$^{\text{surf}}$ methods, resulting in a larger distance with the PBE+vdW method by approximately 0.21 Å with respect to its PBE+vdW$^{\text{surf}}$ counterpart. The PBE+vdW adsorption distance result is overestimated if we consider the values of 3.25 and 3.31 Å found in experiments for the single molecule and monolayer respectively [Wagner *et al.*, 2012; Henze *et al.*, 2007]. These values are, on the other hand, in remarkable agreement with

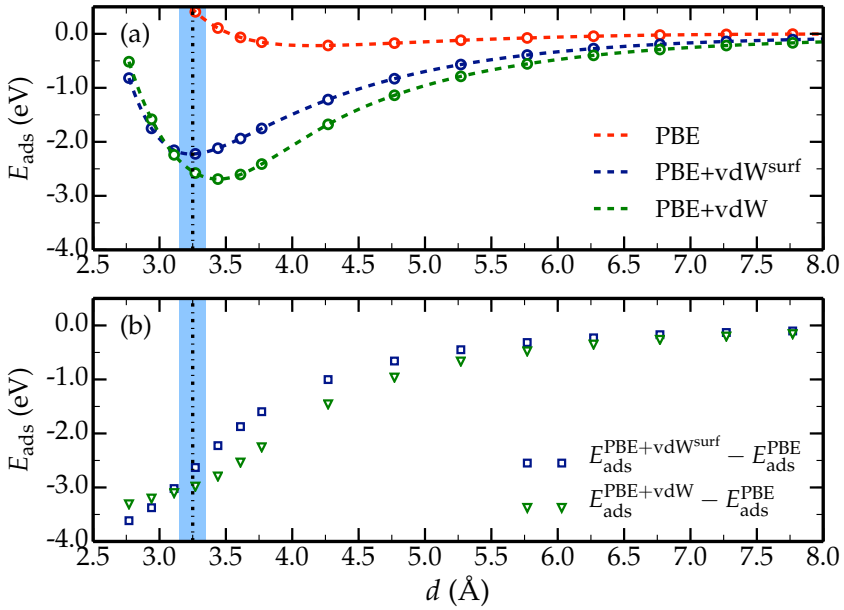

FIGURE 5.2: Adsorption energy E_{ads} as a function of vertical distance d for PTCDA on Au(111). The distance d is evaluated with respect to the position of the unrelaxed topmost metal layer. The blue shaded region corresponds to the experimental adsorption distance of 3.25 ± 0.1 Å as determined by Wagner *et al.* [2012]. The error bar corresponds to typical experimental error estimates. (b) Contribution of vdW interactions to the adsorption energy as a function of vertical distance d for PTCDA on Au(111), which is defined as the difference between either the PBE+vdW^{surf} or the PBE+vdW energy and the PBE energy.

the PBE+vdW^{surf} calculations. With respect to the binding strength, the PBE+vdW adsorption energy also seems overestimated with respect to the experimental values of −2.5 and −1.9 eV measured for the single molecule and monolayer respectively [Wagner *et al.*, 2012; Stremlau, 2015]. Regarding the PBE+vdW^{surf} adsorption energy for the single molecule, its value of −2.23 eV lies in between these two experimental results.

The effect of dielectric screening on the vdW parameters. The differences in these results reflect the impact of the vdW parameters on the accuracy when it comes to the structure of organic/inorganic interfaces. As we have mentioned above, the set of screened C_6 coefficients in the PBE+vdW^{surf} method yields a smaller long-range vdW energy. We show this effect in Figure 5.2(b) where we display the contribution of vdW interactions to the adsorption potential energy curve, showing how the reduced C_6 coefficient of Au yields a smaller vdW energy in the PBE+vdW^{surf} method. This feature modifies the adsorption-potential energy in a non-trivial manner, with particular relevance at the range of the adsorption distance. In addition, the coefficients are effectively changed by the electronic environment of each atom reflecting the interface polarization due to local hybridization effects. Taking PTCDA on Au(111) as example, Figure 5.3(a) demonstrates how the C_6 coefficient between a C atom of the adsorbate molecule and a Au

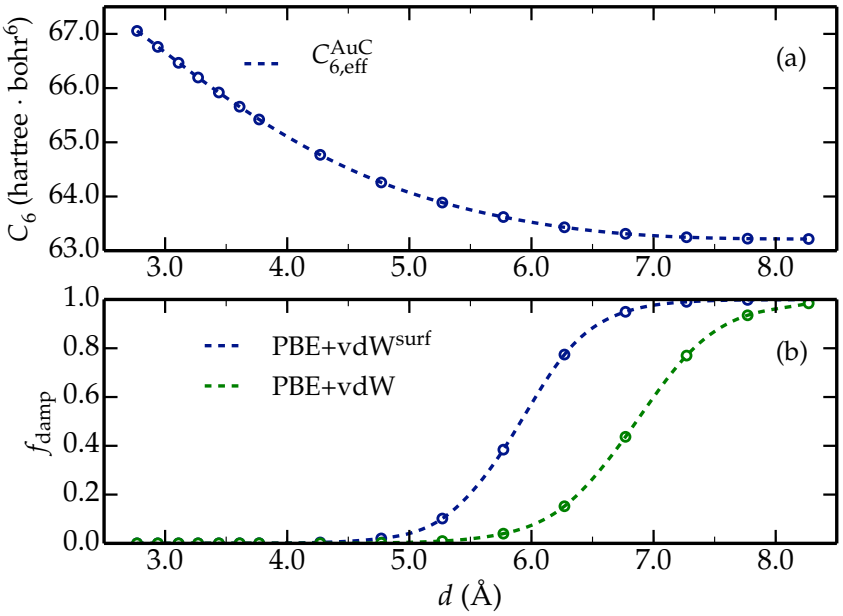

FIGURE 5.3: (a) Changes in the C_6 coefficient between Au and C with respect to the adsorption distance d for a single PTCDA molecule on Au(111) calculated with the PBE+vdW^{surf} method. (b) Variations of the damping function f_{damp} with respect to the adsorption distance d when using the PBE+vdW and PBE+vdW^{surf} methods. The onset of f_{damp} occurs at a smaller distance in the PBE+vdW^{surf} method.

atom of the surface changes as the adsorption distance d does. It displays the variations in the average effective C_6 coefficient between C atoms and the topmost layer of the Au(111) surface as the adsorption distance d is changed. The changes occurring at each distance are a consequence of variations in the electronic environment of each atom. Furthermore, the reduction of the vdW radii in the surface atoms leads to a larger relative weight of the vdW contributions at shorter range with the PBE+vdW^{surf} method in comparison to the PBE+vdW method. This can be observed in Figure 5.3(b) as the onset of the damping function f_{damp} in the PBE+vdW^{surf} method occurs at smaller adsorption distances due to the reduced vdW radius of Au. The coaction of the effects in the C_6 coefficients and the vdW radii causes a non-trivial reduction of both the adsorption energy and the adsorption distance, which modifies the potential energy curve of PTCDA on Au(111) as observed in Figure 5.2.

CHAPTER

6 Structure and stability of Xe on metal surfaces

6.1 Introduction

We have developed in chapter 4 a method within KS-DFT that includes screened vdW interactions for treating adsorption phenomena. We have also performed a preliminary test of the method in chapter 5 by reproducing the adsorption potential energy curves of a couple of experimentally well characterized organic/inorganic interfaces and comparing the results from the curves directly with experiments. We now present a more thorough analysis of the application of the methodology in model adsorption systems.

Before addressing in more detail the case of HIOS in chapter 7, the effects of modeling vdW interactions within KS-DFT in adsorption phenomena can be evaluated by investigating the interaction between noble gases and metallic surfaces. The adsorption interaction in these prototypical physisorption systems is the result of a balance between attractive vdW interactions and Pauli repulsion. We shall address in this chapter the energetics and structure of the adsorption of Xe on selected transition-metal surfaces.

6.1.1 Experimental perspective

The adsorption of noble gases on metal surfaces has been extensively studied as prototypical example of physisorption. A historical perspective of these studies can be found in the works, for example, by Diehl *et al.* [2004] and Da Silva [2002]. An exhaustive historical survey is out of the scope of this disseration, so we restrict the discussion to the experimental data on structure and adsorption energetics for the adsorption of Xe on metal surfaces. From this perspective, the most important fact is the paradigm shift that occurred 25 years ago with respect to the preferred adsorption site of Xe. The general assumption prior to 1990 was that the adsorption potential of noble gases on surfaces would be more attractive in high-coordination sites than those with lower coordination. In the case of Xe, for instance, experimental studies using spin-polarized low-energy electron diffraction (LEED) suggested the hollow site as the preferred adsorption site on close-packed metal surfaces [Potthoff *et al.*, 1995; Hilgers *et al.*, 1995]. This changed with the dynamical LEED studies of adsorbed Xe on Ru(0001) Narloch and Menzel [1997], Cu(111) [Seyller *et al.*, 1998], Pt(111) Seyller *et al.* [1999], and Pd(111) [Caragiu *et al.*, 2002]; which showed that Xe atoms reside on top of the substrate atoms instead of higher-coordination sites [Diehl *et al.*, 2004]. The other important experimental find-

ing is that Xe adopts the $(\sqrt{3} \times \sqrt{3})$R30° structure on Cu(111), Pt(111), and Pd(111). In the case of Xe on Cu(110), a (12×2) structure can be formed at low temperature, which consists of rows of adatoms that are commensurate with the substrate, having higher-order commensurate periodicity along the substrate rows of the surface and a spacing between the rows that is equal to the Cu row spacing [Caragiu *et al.*, 2003; Diehl *et al.*, 2004]. Most importantly, the LEED studies by Caragiu *et al.* [2003] indicate that Xe rows are located on top of the Cu substrate rows.

For our analysis, we take the review papers by Diehl *et al.* [2004] and Vidali *et al.* [1991] as our guidelines for the experimental data on the adsorption of Xe on transition-metal surfaces. The details of each experiment can be found in the original references. The adsorption distances in these systems were mainly obtained using with the low-energy electron diffraction technique. This technique uses electrons of a few hundred eV to penetrate an adsorbed layer generating diffraction peaks corresponding to the substrate surface and to the adsorbed layer; from which the adlayer-substrate separation can be inferred [Bruch *et al.*, 1997]. The experimental adsorption energies are mostly a result of TPD experiments. These experiments report exponential prefactors for desorption of the order of $10^{12} - 10^{13}$ s^{-1}, which are in the expected range for simple adsorbates and small molecules [Fichthorn and Miron, 2002; Tait *et al.*, 2005].

6.1.2 Theoretical perspective

Even if the experiments have identified the low-coordination top site as the preferred adsorption site for Xe on transition-metal surfaces, they have not been able to identify the origin of this preference. It is in this regard that first-principles calculations have the potential to contribute to the atomistic understanding of the origin of this preference. For an extensive review of first-principles simulation of the adsorption of nobel gases, we point the interested reader to the works of Diehl *et al.* [2004], Da Silva [2002], and Chen *et al.* [2012]. The study of noble gases on metal surfaces using KS-DFT is an intricate task because (semi-)local approximations to the exchange-correlation energy in KS-DFT do not include vdW interactions properly, which represent the governing mechanism of attraction in these systems. In general, before the advent of several vdW-inclusive DFT based methods in the last years, LDA had been used extensively to study the adsorption of Xe on metals [Müller, 1990; Da Silva *et al.*, 2003, 2005], where it has been found that the top site is energetically more stable by, at most, 50 meV with respect to the hollow adsorption site. In addition, Da Silva and Stampfl [2008] also studied the adsorption of additional noble gases on metal surfaces using GGAs as xc functional, where they found that these other noble gases also prefer the top adsorption site with the exception of Ar and Ne on Pd(111) [Da Silva *et al.*, 2005; Chen *et al.*, 2012]. In general, Chen *et al.* [2012] mention that GGA xc functionals tend to underestimate the adsortion energy of these systems by a great margin whereas LDA yields equilibrium adsorption distances that are too short in comparison to experiments.

In this respect, it is currently well established that GGA functionals such as PBE cannot describe systems that are dominated by vdW interactions in an accurate manner. The studies performed by Chen *et al.* [2011, 2012] report the performance of several vdW-inclusive DFT methods, such as vdW-DF, vdW-DF2, and DFT-D2, on the adsorption of noble gases on metal surfaces. In this chapter, we analyze the structure and stability of the adsorption of Xe on selected transition-metal surfaces with the PBE+vdW and

PBE+vdW^{surf} methods. We have presented some of these results previously [Ruiz *et al.*, 2012] but here we extend the analysis by including PBE+vdW calculations and studying the perpendicular-vibrational energy of Xe in each case to probe the curvature around the minimum of the potential-energy curves calculated with the PBE+vdW^{surf} method [see also Ruiz *et al.*, 2016]. We also present a preliminary assessment of the performance of the PBE+vdW^{surf} method for adsorption on non-close-packed surfaces. For this, we analyze the differences between the adsorption of Xe on Cu(111) and Cu(110).

We start this chapter by describing the specifications of the systems and the computational details of our calculations. We continue by analyzing the adsorption of Xe on selected transition-metal surfaces using the PBE+vdW and PBE+vdW^{surf} methods, discussing the differences between the two methods while taking into consideration that the latter includes the collective response of the substrate electrons in the determination of the vdW parameters.

6.2 System specifications and calculation details

We performed DFA+vdW and DFA+vdW^{surf} structure optimizations for Xe on five transition-metal surfaces. The DFT calculations were performed using the all-electron/full-potential electronic-structure code FHI-AIMS. The FHI-AIMS code provides a hierarchy of predefined settings which give access to basis set levels and other settings at which fast relaxations can be safely performed. For all calculations in this chapter, we used *tight* settings, which include the *tier 1* standard basis set for the transition metals and Xe. The convergence criteria in the calculations were 10^{-5} electrons for the electron density and 10^{-6} eV for the total energy of the system. For all structure relaxations, 0.01 eVÅ^{-1} was established as convergence criterion for the maximum final force. Relativistic effects were included via the atomic scalar zeroth-order regular approximation [van Lenthe *et al.*, 2000]. We used the repeated-slab method to model all the systems together with the PBE xc functional [Perdew *et al.*, 1996].

The PBE+vdW^{surf} method includes the *screening* due to metallic bulk electrons in the computation of the long-range vdW energy tail. However, since the PBE functional is reduced to the LDA for homogeneous electron densities, the metallic electrons are already accurately described with the PBE functional. This fact results in a partial "double counting" of the interaction between metallic electrons with the PBE+vdW^{surf} method, leading to an overestimation of the vdW energy inside the metal bulk. Even if the present method can lead to an improvement in the bulk lattice constant for some of the transition metals here studied [see Liu *et al.*, 2013b], there is no straightforward way to quantify the overestimation effects. For this reason, we have used the PBE optimized lattice constant to generate most of the metal slabs: 4.149, 3.631, 3.971, and 3.943 Å for Ag, Cu, Pt, and Pd, respectively [Liu *et al.*, 2013b].

For the adsorption structure of the systems, we adopted the experimentally reported $(\sqrt{3}\times\sqrt{3})$R30° structure with top and fcc hollow adsorption sites for the (111) surface of Pt, Pd, and Cu. For the case of the Cu(110) surface, we present the results for a 2 × 2 surface unit cell. We used a Monkhorst and Pack [1976] grid of $15\times15\times1$ k points in the reciprocal space and six metallic layers to perform the calculations, except for Cu(110), where we used seven metallic layers. The width of the vacuum gap was 20 Å. For the relaxation of the systems, the Xe atom and the atoms in the topmost and first subsurface

Table 6.1: Comparison of adsorption energies E_{ads} between PBE+vdW and PBE+vdW^{surf} for the top adsorption site of Xe on transition-metal surfaces. PBE+vdW^{surf} calculations for the fcc hollow adsorption sites are also presented. Experimental data, shown for comparison, are taken from Diehl *et al.* [2004]; Vidali *et al.* [1991]; Seyller *et al.* [1998]; Caragiu *et al.* [2003]; Pouthier *et al.* [1998]; Zhu *et al.* [2003]; Caragiu *et al.* [2002]; Hilgers *et al.* [1995]; Widdra *et al.* [1998]; Seyller *et al.* [1999]; Bruch *et al.* [1998]; Hall *et al.* [1989]; Braun *et al.* [1998]; Zeppenfeld *et al.* [1994]; and Ramseyer *et al.* [1997].

	E_{ads} [meV]			
	top		fcc hollow	Exp.
	PBE+vdW	PBE+vdW^{surf}	PBE+vdW^{surf}	
Xe/Pt(111)	−331	−254	−253	−260 to −280
Xe/Pd(111)	−325	−276	−272	−310 to −330
Xe/Cu(111)	−335	−248	−249	−173 to −200
Xe/Cu(110)	−326	−249	−239	−212 to −224
Xe/Ag(111)	−244	−237	−232	−196 to −226

layers of the surface slab were allowed to relax. As we generated the substrates using the PBE lattice constant, we did not consider vdW interactions between metal atoms in order to avoid an artificial relaxation of the surfaces. The vdW interactions were taken into consideration only in final adsorption energy calculations.

6.3 Results

6.3.1 Adsorption energies

Figure 6.1 and Table 6.1 show the adsorption energies calculated with PBE+vdW^{surf} for both the top and fcc hollow adsorption sites. The adsorption energies were computed using

$$E_{ads} = E_{AdSys} - \left(E_{Me} + E_{Xe}\right), \tag{6.1}$$

where E_{AdSys} is the total energy of the adsorption system (gas + metal surface) after relaxation, E_{Me} is the energy of the bare slab after relaxation, and E_{Xe} is the energy of the isolated Xe gas atom. In all cases, we find that both adsorption sites, top and fcc hollow, are nearly degenerate within vdW-inclusive DFT. Using the PBE+vdW^{surf} method, the top adsorption site is energetically favored in the cases of Pd(111), Cu(110), and Ag(111) by approximately 5 meV for Pd(111) and Ag(111), and 10 meV for Cu(110). Both adsorption sites are virtually degenerate within our calculation settings in the cases of Pt(111) and Cu(111). Figure 6.1 also displays the contribution to E_{ads} coming from PBE and vdW interactions upon relaxing the system. More specifically, the PBE contribution destabilizes the fcc hollow adsorption site in the Cu substrates upon relaxation, as it becomes more positive for both surface orientations. The same finding holds for Ag(111). Although the differences in energy between adsorption sites are too small –a few meV– to regard them as definitive, it is clear that an accurate determination of exchange and correlation effects (particularly related to vdW interactions) is essential in the structural and energetic features of these systems.

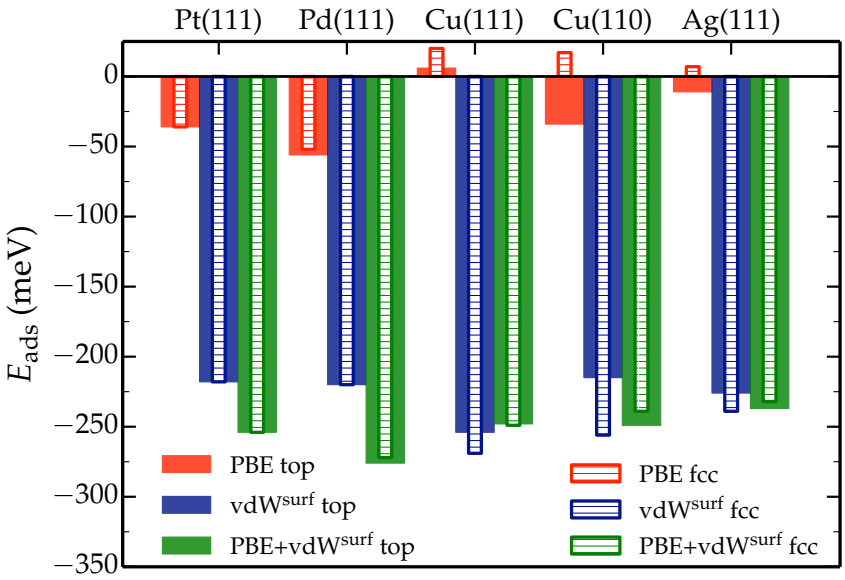

FIGURE 6.1: Adsorption energies E_{ads} calculated with PBE+vdW^{surf} for Xe on transition-metal surfaces. The contributions of PBE and vdW interactions after relaxing the system with the PBE+vdW^{surf} are shown in red and blue, respectively. Total adsorption energies after relaxation are displayed in green. Top sites are displayed with plain color filled bars, whereas fcc hollow sites are displayed with pattern-filled bars.

The fact that both adsorption sites in the adsorption of Xe on transition-metal surfaces are nearly degenerate within KS-DFT methods has also been addressed most recently by Chen *et al.* [2011], who reported differences of a few meV in their PBE and vdW-DF2 calculations between top and fcc hollow adsorption sites. They found, however, that results from experiments cannot be explained by energy differences between top and fcc hollow adsorption sites. Instead, by examining the 2D potential energy surface (PES) of Xe on Pt(111), they found that the fcc hollow adsorption sites correspond to local maxima in the PES, while top sites correspond to a true minimum. Hence, fcc hollow sites are transient states and thus not easily observed in experiments [Chen *et al.*, 2011, 2012; Bruch *et al.*, 1997]. This result is general, according to their calculations, for the adsorption of noble gases on transition-metal surfaces. They further showed that this fact holds no matter the xc functional that is employed. In the case of Xe/Pt(111), experimental measurements by Seyller *et al.* [1999] indeed showed that Xe adsorbs on top sites of the Pt(111) surface at $T = 80$ K. Furthermore, measurements also showed that at low coverage, the diffusion barrier for lateral movement of the Xe atoms on the surface is less than 10 meV [Ellis *et al.*, 1999].

Because of the aforementioned reasons, we now discuss the results for the top adsorption site. For comparison, Table 6.1 also presents PBE+vdW adsorption energies for the top adsorption site as well as the available experimental results. The mentioned Table 6.1 shows that the PBE+vdW^{surf} adsorption energies are in very good agreement with experimental results. These calculations slightly underestimate the adsorption energy in the case of Pt(111) and Pd(111), while slightly overestimating in the case of both Cu sur-

faces and Ag(111). Nevertheless, these discrepancies amount to approximately 50 meV out of the range of experimental results in the worst case. The PBE+vdW method yields larger adsorption energies with respect to PBE+vdW^{surf} calculations, this result stems from the free-atom nature of the vdW reference parameters employed in the PBE+vdW method.

6.3.2 Adsorption distances

Table 6.2 shows the vertical adsorption distances calculated with the PBE+vdW and PBE+vdW^{surf} methods. The results correspond to the top adsorption site and are reported with respect to the average position of the atoms in the topmost metal layer after relaxation of the system. Experimental results are shown for comparison as well. In general, the calculated adsorption distances with both methods are within 0.10 Å of experimental results except for Xe/Cu(111), in which the agreement is within 0.15 Å of the experimental value. We did not find significant differences between PBE+vdW and PBE+vdW^{surf} calculations with the exception of Xe on Cu(110), in which the distance predicted by the PBE+vdW method is 0.12 Å shorter than the PBE+vdW^{surf} result. Overall, we find that the PBE+vdW^{surf} results are in closer agreement (within 0.10 Å) to experimental results than those calculated with other vdW inclusive DFT methods such as those benchmarked in the work of Chen *et al.* [2011, 2012]. We note that the experimental adsorption distances that we report in Table 6.2 follow the analysis presented by Diehl *et al.* [2004] in their review of the topic.

6.3.3 Perpendicular vibrational frequencies of Xe

We have also computed the perpendicular vibrational frequencies of Xe on the metal surfaces to probe the curvature of the potential energy curves around the minimum in each case. For this, we have calculated the adsorption potential energy curve for Xe residing on top sites of each transition-metal surface. We take the case of Xe on Pt(111) as an example: Figure 6.2 shows its adsorption potential energy E_{ads} as a function of vertical distance d of the Xe monolayer employing the PBE and the PBE+vdW^{surf} methodologies. The adsorption energy per adsorbed atom was calculated using (6.1) where the unrelaxed system was employed for all the calculated points. The vertical distance d was defined as the difference of the position of the atom in the monolayer with respect to the position of the unrelaxed topmost metallic layer. The experimental adsorption distance and energy are displayed in blue shaded regions. The adsorption distance and energy observed in the potential curve of Figure 6.2 agree very well with the ones presented in Table 6.2, which shows a summary of the PBE+vdW^{surf} results for Xe on metal surfaces after relaxing each system. This fact holds also for the case of the other metal surfaces here studied. It shows that, in the case of Xe on metal surfaces, the adsorption potential energy curves provide relevant information on the adsorption process. Based on them, we have calculated the perpendicular vibrational energy of Xe in each adsorption case.

Following previous works [Bruch *et al.*, 1997; Da Silva *et al.*, 2005; Chen *et al.*, 2011, 2012], we have modeled the gas-surface adsorption potential energy with the following function given by the sum of repulsive and attractive vdW interactions

$$E(d) = \alpha_1 e^{-\alpha_2 d} - \frac{C_3}{(d - Z_0)^3} + E_{\mathrm{ml}}, \tag{6.2}$$

Table 6.2: Summary of results for the adsorption of Xe on transition-metal surfaces including the equilibrium distances $d_{\mathrm{Xe-Sub}}$, adsorption energies E_{ads}, and perpendicular vibrational energies E_{vib} of Xe. Experimental results are also displayed for comparison. The distances $d_{\mathrm{Xe-Sub}}$ are reported with respect to the average distance of the topmost metal layer and correspond to the top adsorption site on each system. Both adsorption distances and energies correspond to the system after relaxation. The values of $d_{\mathrm{Xe-Sub}}$ and E_{ads} for Ag(111) correspond to the best estimates by Vidali *et al.* [1991]. The experimental data are taken from Diehl *et al.* [2004]; Vidali *et al.* [1991]; Seyller *et al.* [1998]; Caragiu *et al.* [2003]; Pouthier *et al.* [1998]; Zhu *et al.* [2003]; Caragiu *et al.* [2002]; Hilgers *et al.* [1995]; Widdra *et al.* [1998]; Seyller *et al.* [1999]; Bruch *et al.* [1998]; Hall *et al.* [1989]; Braun *et al.* [1998]; Zeppenfeld *et al.* [1994]; Ramseyer *et al.* [1997]; and Gibson and Sibener [1988].

	$d_{\mathrm{Xe-Sub}}$ [Å]			E_{ads} [meV]			E_{vib} [meV]	
	PBE+vdW	PBE+vdW$^{\mathrm{surf}}$	Exp.	PBE+vdW	PBE+vdW$^{\mathrm{surf}}$	Exp.	PBE+vdW$^{\mathrm{surf}}$	Exp.
Xe/Pt(111)	3.39	3.46	3.4 ± 0.1	−331	−254	−260 to −280	3.9	3.5, 3.70
Xe/Pd(111)	3.13	3.12	3.07 ± 0.06	−325	−276	−310 to −330	4.2	–
Xe/Cu(111)	3.48	3.46	3.60 ± 0.08	−335	−248	−173 to −200	3.8	2.6
Xe/Cu(110)	3.17	3.29	3.3 ± 0.1	−326	−249	−212 to −224	4.0	2.5, 2.6
Xe/Ag(111)	3.60	3.57	3.6 ± 0.05	−244	−237	−196 to −226	3.8	2.79

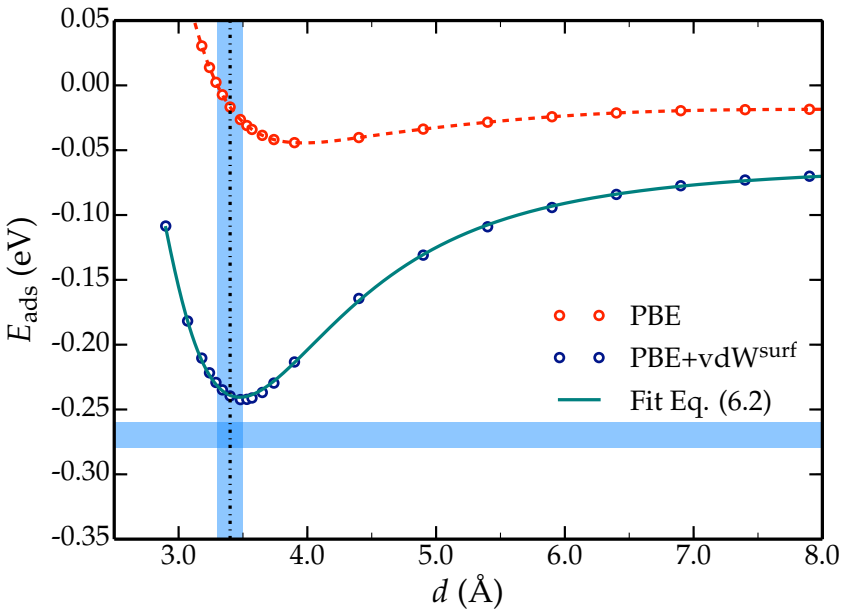

FIGURE 6.2: Potential-energy curve as a function of vertical distance d of a Xe monolayer on top of Pt(111) with different approximations within DFT. The blue shaded regions correspond to the experimental adsorption distance [Seyller *et al.*, 1999] of 3.4 ± 0.1 Å and to the interval of experimental adsorption energy [Diehl *et al.*, 2004] that ranges from −260 to −280 meV.

where $E(d)$ is the adsorption potential energy between Xe and the metal substrate at a distance d from the surface and E_{ml} is a constant that corresponds approximately to the formation energy of the Xe monolayer. We have determined the parameters α_1, α_2, C_3, Z_0, and E_{ml} by fitting (6.2) to the PBE+vdW$^{\mathrm{surf}}$ calculations. The resulting curve of the fit is depicted with a solid line in Figure 6.2 for the case of Xe on Pt(111). The vibrational energy E_{vib} is then given by

$$E_{\mathrm{vib}} = h\nu = \frac{h}{2\pi}\sqrt{\frac{k_e}{m_{\mathrm{Xe}}}}, \tag{6.3}$$

where ν, h, and m_{Xe} are the vibrational frequency, Planck's constant, and the mass of an atom of Xe, respectively. The force constant k_e corresponds to the second derivative evaluated at the minimum of the potential given by (6.2). Following this procedure, the results for E_{vib} are given in Table 6.2.

To the best of our knowledge, experimental measurements for the perpendicular vibrational energy exist for Xe/Pt(111), Xe/Cu(111), Xe/Cu(110), and Xe/Ag(111). In the case of Pt(111), the values of 3.5 and 3.70 meV have been reported [Bruch *et al.*, 1998; Hall *et al.*, 1989]. The PBE+vdW$^{\mathrm{surf}}$ calculations yield a perpendicular vibrational energy of 3.9 meV which is in fair agreement to the experimental results. In the cases of Cu(111), Cu(110), and Ag(111), the PBE+vdW$^{\mathrm{surf}}$ values overestimate the experimental values by 1.2, 1.4, and 1.0 meV respectively [Braun *et al.*, 1998; Ramseyer *et al.*, 1997; Gibson and Sibener, 1988]. With the exception of Pt(111), the results show that the PBE+vdW$^{\mathrm{surf}}$ method overestimates the curvature around the minimum, yielding higher perpendicu-

lar vibrational energies by approximately 1.2 meV with respect to experiment and other vdW inclusive DFT methods such as vdW-DF2 [Chen *et al.*, 2011, 2012]. The overestimation of the curvature with the PBE+vdW^{surf} method is probably related to an overestimation of the adsorption energy with the PBE+vdW^{surf} due to the absence of many-body dispersion effects as we have found in recent work [Maurer *et al.*, 2015]. On the other hand, Carrasco *et al.* [2014] has observed that the vdW-DF2 method yields underestimated C_3 coefficients that are approximately two times smaller than the ones obtained in methods such as the PBE+vdW^{surf} or (the empirically optimized vdW-DF-type functional) optB88-vdW [Klimeš *et al.*, 2010], thus yielding smaller perpendicular vibrational energies with vdW-DF2.

We present a summary of the PBE+vdW^{surf} results for Xe on metal surfaces in Table Table 6.2. The noticeable agreement of both adsorption distances and energies with respect to experimental values indicates the importance of the inclusion of the nonlocal collective effects present in the surface when calculating vdW interactions. With the exception of the vibrational energies, we find that the PBE+vdW^{surf} results are in closer agreement to experimental results than those calculated with other vdW inclusive DFT methods such as the ones benchmarked in the work of Chen *et al.* [2011, 2012]. We must mention that accurate results might also be achieved by vdW-DF-type functionals with empirically optimized exchange [Klimeš *et al.*, 2010; Liu *et al.*, 2012; Carrasco *et al.*, 2014].

In spite of the essential difference between the PBE+vdW^{surf} and PBE+vdW methods, our calculations show that the PBE+vdW adsorption distances are also in very good agreement with experimental results –see Table 6.2– in the case of the adsorption of Xe on transition-metal surfaces. Regardless of this agreement, the PBE+vdW scheme leads to an overestimation of the adsorption energy as the input vdW parameters for the metal atom correspond to the free atom, neglecting the effects of the collective response of the solid (see Table 4.1). Of particular relevance is the fact that we have observed that neglecting the environmental effects of the solid in the determination of the vdW parameters can lead to inaccurate equilibrium structures and an overestimation of the binding strength with respect to experiments in more complex systems such as organic/inorganic interfaces [Ruiz *et al.*, 2012].

6.3.4 Comparison between close-packed and non-close-packed surfaces: Xe on Cu(110) and Cu(111)

So far we have analyzed the performance of the PBE+vdW^{surf} method in the case of the adsorption of Xe on close-packed (111) surfaces of some transition metals. Here, we analyze the case of a non-close-packed surface. We compare the case of a Xe monolayer on the Cu(110) and Cu(111) surfaces. The adsorption potential energy of Xe on Cu(110) is depicted in Figure 6.3. In the blue shaded region, the adsorption distance of 3.3 ± 0.1 Å is shown as measured by Caragiu *et al.* [2003] using LEED. The excellent agreement of the PBE+vdW^{surf} curve within 0.1 Å of the experimental result is evident from Figure 6.3.

The vdW parameters used as an input for the PBE+vdW^{surf} method are calculated according to the dielectric function of the bulk material. As a consequence, the input parameters for a given surface are the same no matter the orientation of the surface termination. The method relies on the differences in the electronic environment given as a result of different surface terminations, which are reflected in the reevaluation of the vdW

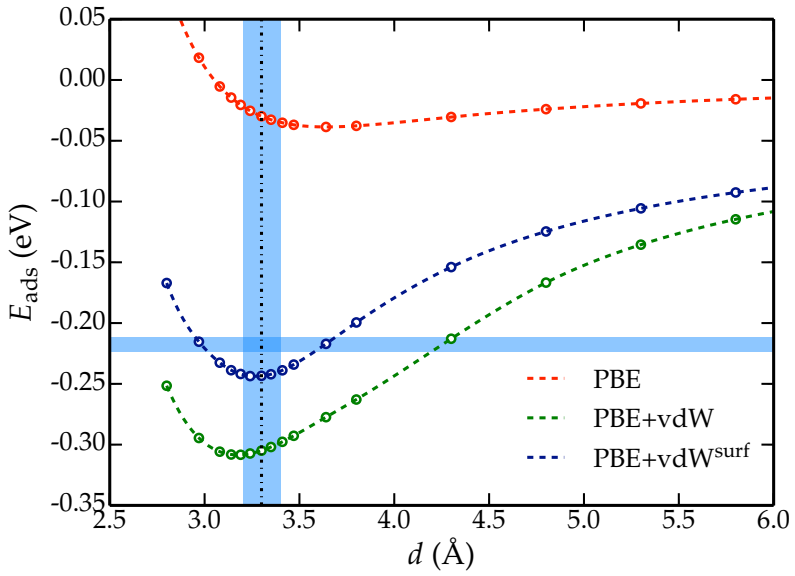

FIGURE 6.3: Potential-energy curve as a function of vertical distance d of a Xe monolayer on top of Cu(110) with different approximations within DFT. The blue shaded region corresponds to the experimental adsorption distance of 3.3 ± 0.1 Å [Caragiu *et al.*, 2003].

parameters based on the Hirshfeld partitioning scheme [see expressions (4.34)-(4.36)]. As an example of this, Figure 6.4(a) shows the effective C_6 parameters for the interaction Xe-Cu as calculated in the PBE+vdW^{surf} method for the adsorption of a Xe monolayer on both the Cu(110) and Cu(111) surfaces. It displays the variations in the average effective C_6 coefficient between Xe and the topmost Cu layer as the distance d is changed. The differences in the electronic environments result in slightly different values for the C_6 coefficients, which gives rise to surface termination sensitivity. This has a contribution in the adsorption potential energies shown in Figure 6.4(b) and the adsorption distances reported in Table 6.2. It is worth mentioning that greater differences may be found in more complex systems like the case of inorganic/organic interfaces. For instance, Al-Saidi *et al.* [2012] found significant surface sensitivity in the adsorption of 2-pyrrolidone on Ag(111) and Ag(100) which was better understood when including vdW interactions with the PBE+vdW^{surf} method. We shall address the case of inorganic/organic systems in section 7.3.2.

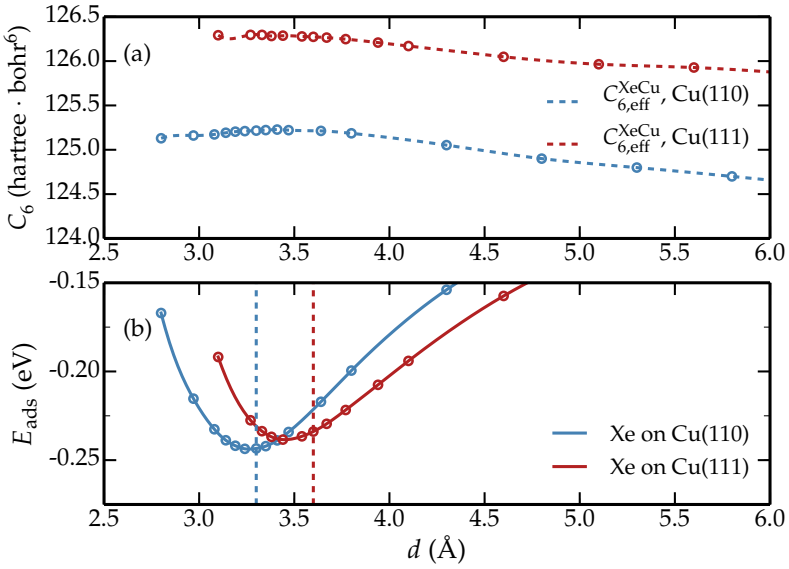

FIGURE 6.4: (a) Changes in the C_6 coefficient between Xe and Cu with respect to the adsorption distance d for Xe on Cu(110) (blue) and Cu(111) (red) calculated with the PBE+vdW$^{\mathrm{surf}}$ method. (b) Potential-energy curve as a function of vertical distance d of Xe on top of Cu(110) (blue) and Cu(111) (red) calculated with the PBE+vdW$^{\mathrm{surf}}$ method. The blue dashed line corresponds to the experimental adsorption distance of 3.3 ± 0.1 Å corresponding to Xe on Cu(110) [Caragiu *et al.*, 2003]. The red dashed line corresponds to the experimental adsorption distance of 3.60 ± 0.08 Å corresponding to Xe on Cu(111) [Seyller *et al.*, 1998].

CHAPTER

7 Structure and stability of inorganic/organic systems

7.1 Introduction

We have discussed the importance of understanding interfacial electronic properties in hybrid inorganic/organic systems (HIOS) from both a basic science and a technological perspective. Among the possible HIOS, the interfaces formed between an organic material and a metal have received much attention. Besides of the possible emergence of novel collective phenomena –as we have mentioned in section 1.1– at these interfaces, these systems have the potential of being relevant in promising technologies such as electronic and opto-electronic devices (transistors and light-emitting diodes for instance) and organic photovoltaics [see for example Kronik and Koch, 2010; Forrest and Thompson, 2007].

The role that these interfaces might play in the future of these potential technologies depends on the eventual control of their functionality, which is clearly related to the properties of the interface. We have already discussed the fact that the interface geometry of these systems has a strong influence on their electronic properties [Duhm *et al.*, 2008; Tkatchenko *et al.*, 2010], so that a balanced description of both their structural and electronic properties is critical for their modeling and understanding. An essential part in the structure and stability of HIOS is played in particular by vdW forces [Tkatchenko *et al.*, 2010; Atodiresei *et al.*, 2009; Mercurio *et al.*, 2010; Stradi *et al.*, 2011; Olsen *et al.*, 2011; McNellis, 2010]. It is therefore evident that the prediction and understanding of the functionalities in HIOS involve as a first step the prediction and understanding of the structural features of the interface as these features will determine the electronic properties. It is in this regard where the accurate prediction of vdW forces becomes distinctively relevant since their role in the determination of the structural features and stability is crucial.

Within the large variety of HIOS, the interfaces formed by the adsorption of PTCDA on coinage metals are among the best experimentally and theoretically characterized systems. PTCDA is a chemical compound formed by an aromatic perylene core (C_{peryl}) terminated with two anhydride functional groups, each of them containing two carbon atoms (C_{func}), two carboxylic oxygens (O_{carb}) and one anhydride oxygen (O_{anhyd}) [see Bauer *et al.*, 2012, and Figure 7.1(b)]. Due to their accurate experimental characterization, the adsorption of PTCDA on coinage metals arise as a relevant study case to analyze the influence of dispersion interactions between an organic (aromatic) molecule

and a metallic substrate while testing the predictive power of vdW-inclusive theoretical methods. In regard to the adsorption of organic molecules on close-packed metal surfaces, the adsorption geometries of a PTCDA monolayer on Ag(111), Au(111), Cu(111) have been studied and determined by using the NIXSW technique [Gerlach *et al.*, 2007; Henze *et al.*, 2007; Hauschild *et al.*, 2010; Stanzel *et al.*, 2004; Stadler *et al.*, 2007]. The NIXSW experimental studies have also been extended to the study of a PTCDA monolayer adsorbed on non-close-packed Ag surfaces, namely on the Ag(100) and Ag(110) surfaces [Bauer *et al.*, 2012; Mercurio *et al.*, 2013a].

In addition, as we have discussed in section 4.1, extensive theoretical work has also been performed on the adsorption of PTCDA on Ag(111) showing the essential role that vdW interactions –including molecule-molecule and molecule-substrate– play in this system [Tkatchenko *et al.*, 2010; Romaner *et al.*, 2009; Hauschild *et al.*, 2005; Rohlfing *et al.*, 2007; Rohlfing and Bredow, 2008; Ruiz *et al.*, 2012]. Furthermore, a recent theoretical study with vdW-inclusive DFT methods on the adsorption of PTCDA on Ag(100) and Ag(110) analyze, along with experimental findings, the existing trends in the bonding mechanism of PTCDA on Ag(111), Ag(100), and Ag(110) [Bauer *et al.*, 2012]. These studies were very helpful to the analysis that we present here.

In chapter 5, we have shown the adsorption potential energies of a monolayer of PTCDA on Ag(111) and a single PTCDA molecule on Au(111) calculated with the PBE+vdW$^{\text{surf}}$ method. Despite the remarkable results in the adsorption height of the perylene core observed in these curves, experiments show that the PTCDA molecule is significantly distorted upon adsorption on Ag(111) and Cu(111). Moreover, NIXSW studies on Ag surfaces performed by Bauer *et al.* [2012] show that the adsorption structure of the PTCDA monolayer also present differences according to the surface termination.

In this context, we demonstrate in this chapter the importance of the inclusion of screened vdW interactions in density-functional theory (DFT) to reproduce the structural distortion and energetic features of HIOS. For this purpose, we start with a study of the structure of PTCDA on Ag surfaces in section 7.3. Here, we first do an in-depth analysis of the structural features and the adsorption energy of a PTCDA monolayer on Ag(111) addressing the effects of the basis set and the lattice constant of the substrate. In order to analyze the influence of the surface termination in the structure of the monolayer and test the sensitivity of the DFA+vdW$^{\text{surf}}$ method, we conclude section 7.3 with a comparative study of the interfaces formed by the adsorption of a PTCDA monolayer on Ag(111), Ag(100), and Ag(110).

The structure of the adsorbate in any HIOS is clearly dependent on the chemical nature of the surface. As we have just mentioned above, several experimental studies have also been performed on the adsorption of PTCDA on the close-packed surfaces of coinage metals: Ag(111), Au(111), and Cu(111). Two different aspects of the existing interaction between substrate and molecule in these systems are related to: *i*) the adsorption height of the perylene core with respect to the metal substrate and *ii*) the distortion of the internal structure of the two inequivalent molecules in the monolayer. Considering that the DFA+vdW$^{\text{surf}}$ method takes into account screened vdW interactions, we study these aspects in the adsorption of a PTCDA monolayer on Au(111) and Cu(111) in section 7.4 and section 7.5 respectively. We also include in these studies an estimation of the adsorption energy of each system with the DFA+vdW$^{\text{surf}}$ method and compare them to available experimental results.

Finally, we must mention that many of the results that we analyze and present in this

chapter follow a similar format to the ones presented by Rohlfing *et al.* [2007] and Bauer *et al.* [2012]. That is, we employ similar definitions to study the distortion and structural features of the interfaces that we study in this chapter. The work we present here has been previously published [see Ruiz *et al.*, 2016].

7.2 General calculation settings

We present the general calculation settings for the DFT calculations analyzed in this chapter, particular settings are mentioned throughout the text. All calculations were performed using the all-electron/full-potential electronic-structure code FHI-AIMS [Blum *et al.*, 2009]. This chapter comprises calculations with both *light* and *tight* settings, where *light* settings include the *tier 1* NAO basis set for C, H, O, and the metal substrate; while *tight* settings include the *tier 1* NAO basis set for the metal substrate and the *tier 2* NAO basis set for C, H, and O. The convergence criteria were 10^{-5} electrons for the electron density and 10^{-6} eV for the total energy of the system in all calculations. For all structure relaxations, we used 0.01 eV Å^{-1} as convergence criterion for the maximum final force. Relativistic effects were included via the atomic scalar zeroth-order regular approximation [van Lenthe *et al.*, 2000]. We used the repeated-slab method to model all the systems together with the PBE xc functional [Perdew *et al.*, 1996].

7.3 3,4,9,10-Perylene-tetracarboxylic dianhydride on Ag surfaces

7.3.1 3,4,9,10-Perylene-tetracarboxylic dianhydride on Ag(111)

Adsorption model and calculation details

PTCDA forms a commensurate monolayer structure on the Ag(111) surface with a herringbone structure having two molecules per unit cell in non-equivalent adsorption configurations [Glöckler *et al.*, 1998; Kraft *et al.*, 2006]. We have modeled the system using a $\begin{pmatrix} 6 & 1 \\ -3 & 5 \end{pmatrix}$ surface unit cell consisting of thirty three Ag atoms per substrate layer and two inequivalent PTCDA molecules with the adsorption site chosen in agreement with experimental results [see also section 7.3.2 and Glöckler *et al.*, 1998; Ikonomov *et al.*, 2008, for detailed information]. The calculations were performed using a slab with a vacuum gap of 50 Å, five metallic layers, and a Monkhorst and Pack [1976] of $4 \times 4 \times 1$ k points in the reciprocal space, including both *tight* and *light* settings (as described in section 7.2). To generate the surface slab, we used both the PBE lattice constant of 4.149 Å and the PBE+vdW$^{\text{surf}}$ lattice constant of 4.007 Å in accordance to the previous work by Liu *et al.* [2013b]. We have taken the experimental configuration as starting point for each structural optimization, allowing the PTCDA molecule and the atoms in the topmost two metal layers to relax. Considering vdW interactions between metal atoms in the slabs built with the PBE lattice constant would result in artificial relaxations within the surface. Hence, in the cases in which the PBE lattice constant was used to generate the surface slab, the vdW interactions between metal atoms were not considered when performing the structural relaxation. They were taken into consideration only in final adsorption energy calculations. A brief discussion of the differences between the PBE and the PBE+vdW$^{\text{surf}}$ lattice constant was given in section 4.5.

Table 7.1: Comparison of results after performing a structural relaxation of PTCDA on Ag(111) with the PBE+vdW^{surf} method using *light* and *tight* settings. The PBE lattice constant was employed to generate the slab. Experimental results are also shown for comparison [Hauschild *et al.*, 2010]. We use $d_{Th/Exp}$ to denote the averaged vertical adsorption heights of the specific atoms obtained from PBE+vdW^{surf} calculations and NIXSW studies. The adsorption height is given in Å with respect to the topmost unrelaxed metal layer for a direct comparison to NIXSW experiments. The specification of the atoms can be seen in Figure 7.1(b). The carbon backbone distortion is given as $\Delta C = d(C_{peryl}) - d(C_{func})$ and the O difference as $\Delta O = d(O_{anhyd}) - d(O_{carb})$.

	d_{Th}		d_{Exp}
	light	*tight*	
C total	2.82	2.80	2.86 ± 0.01
C_{peryl}	2.83	2.80	–
C_{func}	2.79	2.78	–
ΔC	0.04	0.02	–
O total	2.72	2.73	2.86 ± 0.02
O_{carb}	2.68	2.68	2.66 ± 0.03
O_{anhyd}	2.82	2.83	2.98 ± 0.08
ΔO	0.14	0.15	0.32 ± 0.09

Structural features

Influence of the basis set. We performed a structural relaxation with two levels of numerical hierarchy defined in FHI-AIMS, namely *light* and *tight* settings using the PBE lattice constant for the Ag(111) slab. Table 7.1 shows the general structural features obtained from PBE+vdW^{surf} calculations, where we use d_{Th} to denote the averaged vertical adsorption heights of each of the atoms forming the molecule. All distances were calculated with respect to the unrelaxed topmost substrate layer to have a direct comparison with NIXSW experiments. The carbon backbone distortion is given as $\Delta C = d(C_{peryl}) - d(C_{func})$ and the O difference as $\Delta O = d(O_{anhyd}) - d(O_{carb})$. The adsorption height of the monolayer, measured in terms of the vertical distance of the carbon atoms (C total), shows an absolute difference of 0.02 Å when comparing both predefined settings. The carbon backbone of the molecules in the monolayer is given mainly by the aromatic perylene core, which differs in 0.03 Å when comparing both settings. Regarding the position of the oxygen atoms, Table 7.1 shows a small absolute difference of 0.01 Å. Finally, the distortion of the monolayer, given by ΔC and ΔO, takes the values of 0.02 and 0.01 Å, respectively. The results show that *light* settings are sufficient for reproducing the structural features of the system to an accurate level.

Influence of the lattice constant. The lateral ordering found in the room temperature (RT) structure of PTCDA on Ag(111) has been revealed by Kilian *et al.* [2008] to be a consequence of attractive intermolecular interactions between neighboring molecules. To obtain more information regarding the influence of the lattice constant on this particular issue, we performed an additional relaxation of PTCDA on Ag(111) using the PBE+vdW^{surf} lattice constant for Ag (4.007 Å) including vdW interactions between metal atoms. We show the results in Figure 7.1(a) and Table 7.2. We observe an increase of 0.08 Å in the

Table 7.2: Comparison of results after performing a structural relaxation with PBE+vdW^{surf} for the adsorption geometry of PTCDA on Ag(111) under *tight* settings, using the PBE and PBE+vdW^{surf} lattice constants of Ag (4.149 Å and 4.007 Å, respectively) to generate the Ag(111) slab. Experimental results are also shown for comparison [Hauschild *et al.*, 2010]. We use $d_{\mathrm{Th/Exp}}$ to denote the averaged vertical adsorption heights of the specific atoms obtained from PBE+vdW^{surf} calculations and NIXSW studies. The adsorption height is given in Å with respect to the topmost unrelaxed metal layer for a direct comparison with NIXSW experiments. The specification of the atoms can be seen in Figure 7.1(b). The carbon backbone distortion is given as $\Delta\mathrm{C} = d(\mathrm{C_{peryl}}) - d(\mathrm{C_{func}})$ and the O difference as $\Delta\mathrm{O} = d(\mathrm{O_{anhyd}}) - d(\mathrm{O_{carb}})$.

	d_{Th} Lattice constant		d_{Exp}
	PBE	PBE+vdW^{surf}	
C total	2.80	2.88	2.86 ± 0.01
$\mathrm{C_{peryl}}$	2.80	2.88	–
$\mathrm{C_{func}}$	2.78	2.84	–
ΔC	0.02	0.04	–
O total	2.73	2.77	2.86 ± 0.02
$\mathrm{O_{carb}}$	2.68	2.71	2.66 ± 0.03
$\mathrm{O_{anhyd}}$	2.83	2.89	2.98 ± 0.08
ΔO	0.15	0.18	0.32 ± 0.09

adsorption height (C total) of the monolayer and an increase of 0.04 Å in the distance of the oxygen atoms when the surface slab was generated with the PBE+vdW^{surf} lattice constant. In addition, the results show the attraction of the carboxylic oxygen atoms to the surface –as found in experiments– independently of the lattice constant used, with an increase of 0.03 Å when we adopted the PBE+vdW^{surf} lattice constant.

In terms of the comparison with experiments, Table 7.2 shows that the adsorption height of the monolayer calculated with the PBE+vdW^{surf} method is within 0.1 Å of the experimental results regardless of which lattice constant we used for generating the surface slab. A closer look at the results, however, reveals that the adsorption geometry of the structure with the PBE+vdW^{surf} lattice constant is closer to the values found in experiments. The distances of the perylene core and the oxygen atoms are closer to the results observed in experiments, yielding an adsorption height of the monolayer which is just 0.02 Å larger than the one reported by Hauschild *et al.* [2010]. Although the results that we have found with the PBE+vdW^{surf} lattice constant are in better agreement with experiments, the distortion of the molecule remains relatively unchanged. This becomes clear if we examine ΔC and ΔO in Table 7.2, as the differences in these two quantities are of 0.02 Å and 0.03 Å, respectively, between both cases.

A more profound insight into the origin of these differences can be obtained by observing the resolved structural features for each of the structurally inequivalent molecules that conform the monolayer. The experimental unit cell of PTCDA on Ag(111) has an area of 238.7 Å^2, deviating from the rectangular shape by just 1°. These lattice parameters match almost perfectly (deviating by less than 2%) to those of the (102) plane of the β-bulk phase of PTCDA, while its area is smaller only by 0.67% [Glöckler *et al.*,

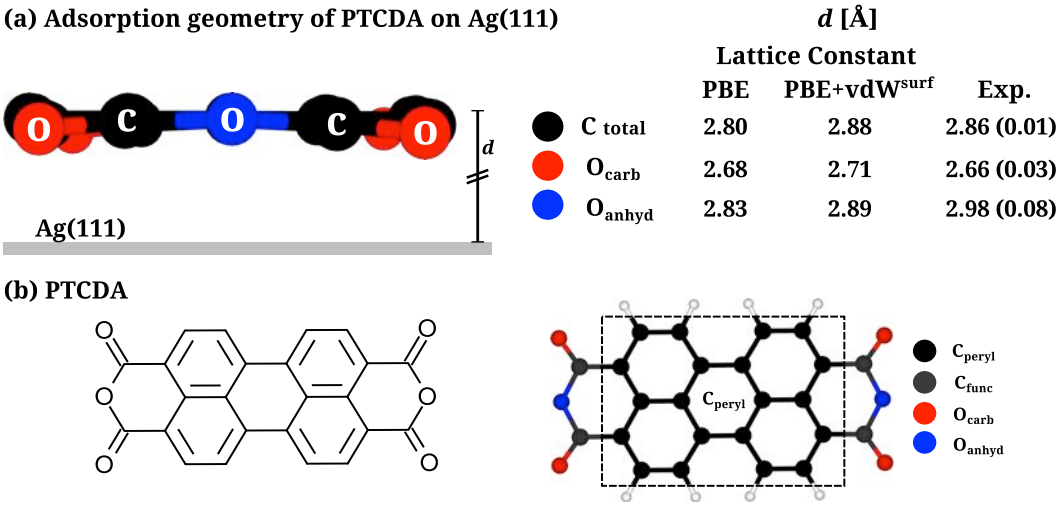

FIGURE 7.1: (a) Geometry of PTCDA adsorbed on Ag(111). The equilibrium distances d for each chemically inequivalent atom calculated with the PBE+vdW^{surf} method are displayed. Two cases are presented: *i*) the structure using a surface slab generated with the PBE lattice constant of Ag and *ii*) the structure using a surface slab generated with the PBE+vdW^{surf} lattice constant (see text). Experimental values by Hauschild *et al.* [2010] from NIXSW studies are also shown for comparison. The distinction between chemically inequivalent atoms is displayed. (b) Chemical structure of PTCDA. The distinction between carbon atoms belonging to the perylene core (C_{peryl}, black) and to the functional groups (C_{funct}, dark gray) is also displayed. In a similar fashion, oxygen atoms are shown in red for the case of the carboxylic oxygen (O_{carb}) and blue for the anhydride oxygen (O_{anhyd}). Images of the structures were produced using the visualization software VESTA [Momma and Izumi, 2011].

1998; Kilian *et al.*, 2004]. This almost perfect match allows the possibility of the growth of a commensurate monolayer of PTCDA on the Ag(111) surface with two molecules per unit cell in non-equivalent adsorption configurations [Glöckler *et al.*, 1998; Kraft *et al.*, 2006]. Both molecules are adsorbed on bridge position, molecule A is practically aligned with the substrate in the [10$\bar{1}$] direction with its carboxylic oxygen atoms on top position and the anhydride oxygen atoms located on bridge sites. Molecule B, on the other hand, is rotated with respect to the [01$\bar{1}$] direction with most atoms in its functional groups located closely to adsorption bridge positions [Kraft *et al.*, 2006; Bauer *et al.*, 2012]. Figure 7.2 depicts how this configuration is well reproduced in our calculations after relaxing the system regardless of the lattice constant used to generate the substrate. Table 7.3 shows the structural features of each molecule after relaxing with PBE+vdW^{surf} for each lattice constant used to generate the substrate.

In contrast to experiments, the unit cells for PTCDA on Ag(111) in our calculations have an area of 245.9 Å^2 and 229.4 Å^2 corresponding to the PBE and PBE+vdW^{surf} lattice constants, respectively. The PBE+vdW^{surf} lattice constant, being smaller than its PBE counterpart, leads to a reduction of the unit cell area. This reduction causes an increase in the adsorption height of the monolayer, a slight misalignment of molecule A with

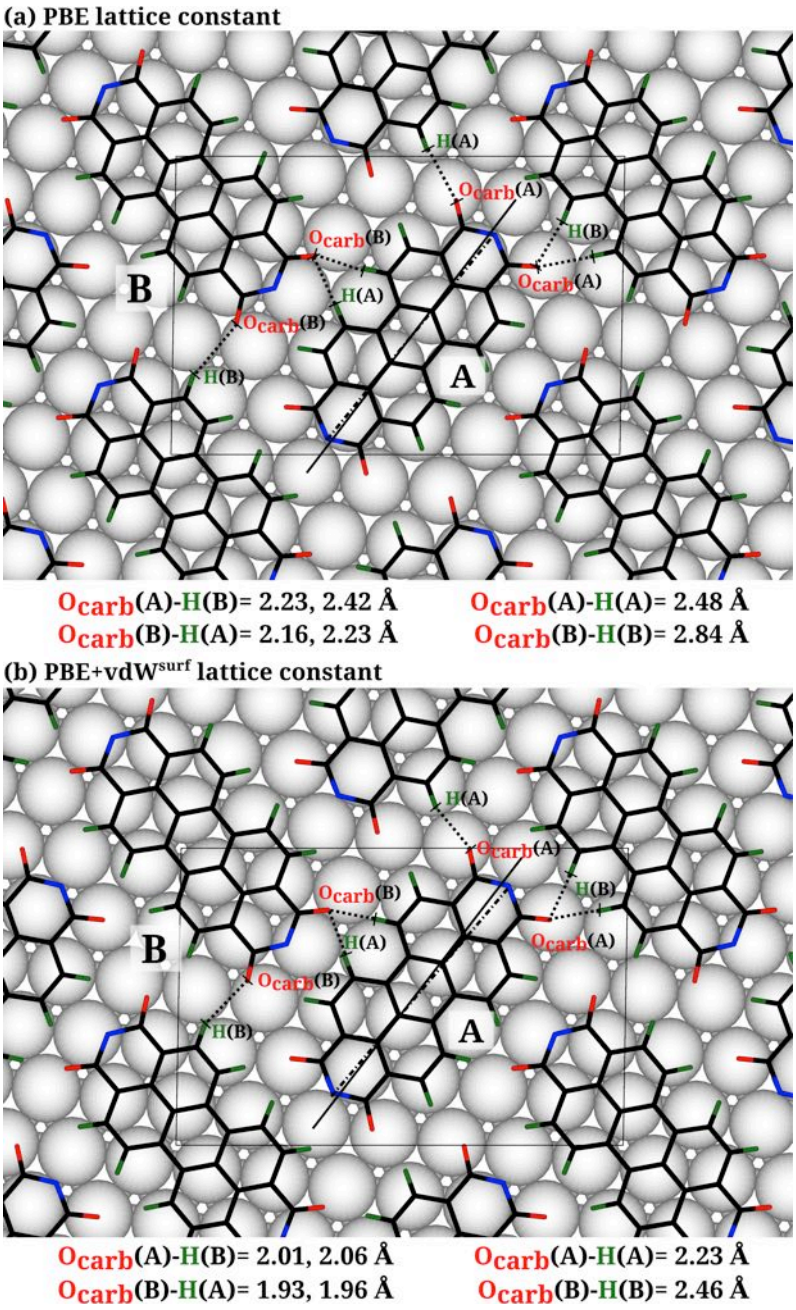

FIGURE 7.2: Top view of the relaxed structure of PTCDA on Ag(111) with a surface slab generated with the PBE lattice constant of Ag (a) and a surface slab generated with the PBE+vdW^{surf} lattice constant (b). Both inequivalent molecules of the structure are labeled A and B. The distinction between chemically inequivalent atoms is displayed including hydrogen atoms in green [see also Figure 7.1(b)]. The bond distances between carboxylic oxygen atoms of molecule A and hydrogen atoms of molecule B are labeled as O_{carb}(A)-H(B). The bond distances between carboxylic oxygen atoms of molecule B and hydrogen atoms of molecule A are labeled as O_{carb}(B)-H(A). The bond distances between carboxylic oxygen atoms of molecule A (B) and hydrogen atoms of a neighboring molecule A (B) are labeled as O_{carb}(A)-H(A) $\left(O_{carb}(B)\text{-}H(B)\right)$. Images of the structures were produced using the visualization software VESTA Momma and Izumi [2011].

Table 7.3: Results after performing a structural relaxation with PBE+vdW^{surf} for the adsorption geometry of PTCDA on Ag(111) using *tight* settings. We show the structural features resolved for each of the non-equivalent adsorbed molecules A and B in the PTCDA monolayer. The PBE and PBE+vdW^{surf} lattice constants of Ag (4.149 Å and 4.007 Å, respectively) were used to generate the Ag(111) slab. Experimental results are also shown for comparison [Hauschild *et al.*, 2010]. We use $d_{Th/Exp}$ to denote the averaged vertical adsorption heights of the specific atoms obtained from PBE+vdW^{surf} calculations and NIXSW studies. The adsorption height is given in Å with respect to the topmost unrelaxed metal layer for a direct comparison to NIXSW experiments. The specification of the atoms can be seen in Figure 7.1(b). The carbon backbone distortion is given as $\Delta C = d(C_{peryl}) - d(C_{func})$ and the O difference as $\Delta O = d(O_{anhyd}) - d(O_{carb})$. The carboxylic oxygen atoms with one and two hydrogen bonds are labeled as O_{carb} 1 H-bond and O_{carb} 2 H-bond respectively.

	d_{Th} Molecule A Lattice constant		d_{Th} Molecule B Lattice constant		d_{Exp}
	PBE	PBE+vdW^{surf}	PBE	PBE+vdW^{surf}	
C total	2.80	2.88	2.80	2.87	2.86 ± 0.01
C_{peryl}	2.80	2.88	2.80	2.88	–
C_{func}	2.77	2.87	2.80	2.82	–
ΔC	0.03	0.01	0.00	0.06	–
O_{carb}	2.68	2.74	2.69	2.69	2.66 ± 0.03
O_{carb} 1 H-bond	2.67	2.76	2.70	2.78	–
O_{carb} 2 H-bond	2.72	2.71	2.65	2.59	–
O_{anhyd}	2.80	2.92	2.84	2.86	2.98 ± 0.08
ΔO	0.12	0.18	0.15	0.17	0.32 ± 0.09

respect to the topmost surface layer –see Figure 7.2(b)–, and a slight increment in the distortion of the oxygen atoms within each molecule as shown by the oxygen difference ΔO in Table 7.2 and Table 7.3.

In addition to a different adsorption site depending on the position of the molecule, the distortion of the carboxylic oxygen atoms is also influenced by the number of hydrogen atoms surrounding each of them, giving rise to either 1 or 2 hydrogen bonds (H-bond) for each carboxylic oxygen atom. As a consequence of the reduction of the unit cell area with the PBE+vdW^{surf} lattice constant, the O-H bond lengths between neighboring molecules also become smaller –see Figure 7.2. This reduction seems to have an opposite effect on each type of carboxylic oxygen atom. In the case of the carboxylic oxygen atoms with 1 H-bond, the Ag-O bond length increases by approximately 0.09 and 0.08 Å in molecules A and B, respectively, in comparison to the substrate generated with the PBE lattice constant. This fact suggests a stabilizing effect (hindering a further distortion) driven by a shorter O-H bond length in both molecules A and B as seen when we look at the values of O_{carb}(A)-H(A) and O_{carb}(B)-H(B) in Figure 7.2(b).

However, we can also notice a stronger distortion on the carboxylic oxygen atoms

of molecule B when the substrate is built with the PBE+vdW^{surf} lattice constant as we observe a difference of approximately 0.19 Å between carboxylic oxygen atoms with 1 H-bond and 2 H-bond in molecule B. The latter fact comes along, due to the reduction of the unit cell area, with a significant decrease in the O-H bond distances when the substrate is generated with the PBE+vdW^{surf} lattice constant. In particular, the O-H bonds between carboxylic oxygen atoms of molecule B and hydrogen atoms of molecule A, labeled as O_{carb}(B)-H(A) in Figure 7.2, are slightly smaller than 2.00 Å (1.93 and 1.96 Å); in comparison to the same O-H bonds when the PBE lattice constant is used to generate the substrate (2.16 and 2.23 Å). These facts suggest that the proximity of neighboring molecules may contribute, not just to a H-bond stabilization, but also to a distortion of the carboxylic oxygen atoms; thus leading to a smaller Ag-O bond length in the case of the carboxylic oxygen atoms with 2 H-bond in molecule B.

From this analysis, we can extract some general recommendations and conclusions. In the first place it is essential to have a consistent adsorption model at the moment of performing the structural optimization of the system. In this particular case, this refers to the fact that including vdW interactions between metal atoms, but modeling the substrate with the lattice constant of an exchange-correlation approximation which is not vdW-inclusive, leads to an inconsistent model with respect to the forces in the system. Certainly, the optimized lattice constant obtained with an exchange-correlation approximation such as PBE (or any other GGA) does not take into consideration (beyond the model of the homogeneous electron gas) that metal atoms within the substrate surface also experience the effects of vdW forces. As a consequence, an artificial relaxation of the system can occur, which would result in notable uncertainties regarding the accuracy of the calculations along with the related conclusions. From this perspective, our analysis of the structural features involving the influence of the lattice constant in this section is consistent. Moreover, our analysis shows that the adsorption height of the monolayer obtained with both the PBE and PBE+vdW^{surf} optimized lattice constants lie within 0.1 Å of the experimental results.

Nevertheless, our analysis also shows that it is necessary to keep in mind that intermolecular forces may also play an important role in the formation and structure of the monolayer, depending on the particular chemical structure of the molecules involved. In this sense, the packing density of the monolayer in the calculations is also dependent on the area of the surface unit cell used in the adsorption model. In our particular case, hydrogen bonding is a major influence in the formation of the monolayer and its structure. This influence also extends to the distortion, both of the carbon backbone and the oxygen difference, found in the molecules forming the monolayer. These considerations must be taken into account for the analysis of similar inorganic/organic interfaces.

Adsorption energy

We have reviewed how several theoretical methods perform on predicting the adsorption energy in section 5.1. From an experimental perspective, the adsorption energy is unavailable because PTCDA breaks down upon thermal desorption in TPD experiments [Zou *et al.*, 2006]. Nevertheless, the adsorption energy of 1.16 ± 0.1 eV has been measured from TPD experiments for the adsorption of 1,4,5,8-naphthalene-tetracarboxylic-dianhydride (NTCDA) on Ag(111) by Stahl *et al.* [1998]. NTCDA is related to PTCDA since both molecules are terminated with two anhydride functional groups, however NTCDA

has a smaller aromatic backbone of approximately 40% less molecular surface area than PTCDA. Based on this information and comparative studies of the adsorption of PTCDA and NTCDA on Au(111), we have recently estimated the adsorption energy of PTCDA on Ag(111) to be between −1.4 and −2.1 eV [see Maurer *et al.*, 2015, for detailed information]. This estimation is more reasonable than the one we have used in section 4.1 and section 5.1 since it is based on more experimental information and takes into consideration the actual differences in size between NTCDA and PTCDA.

We now analyze the adsorption energy of PTCDA on Ag(111) with the PBE+vdW$^{\text{surf}}$ method. We have calculated the adsorption energy per molecule for a coverage Θ of 1.0 monolayer (ml). In our model, Θ = 1.0 ml corresponds to the adsorption of two PTCDA molecules per surface unit cell. As we have mentioned above, the surface unit cell here studied is characterized by an area of 246 Å^2 with the PBE lattice constant and 229 Å^2 using the PBE+vdW$^{\text{surf}}$ lattice constant (see also Figure 7.2). The adsorption energy per molecule in the monolayer was calculated using

$$E_{\text{ads}}^{\Theta(\text{ml})} = \frac{1}{2\Theta}\left[E_{\text{AdSys}}^{\Theta} - \left(E_{\text{Me}} + E_{\text{PTCDA}}^{\Theta}\right)\right], \tag{7.1}$$

$$E_{\text{ads}}^{\Theta(\text{gas})} = \frac{1}{2\Theta}\left[E_{\text{AdSys}}^{\Theta} - \left(E_{\text{Me}} + 2\Theta \cdot E_{\text{PTCDA}}^{\text{gas}}\right)\right], \tag{7.2}$$

where $E_{\text{AdSys}}^{\Theta}$ is the energy of the complete system formed by the monolayer and the slab, E_{Me} is the energy of the slab, and $E_{\text{PTCDA}}^{\Theta}$ corresponds to the energy of the monolayer in periodic boundary conditions. Expression (7.1) considers the adsorption energy with the monolayer in periodic boundary conditions as a reference. On the other hand, the adsorption energy calculated with expression (7.2) considers the formation of the monolayer from gas phase by incorporating $E_{\text{PTCDA}}^{\text{gas}}$, term which corresponds to the energy of a single PTCDA molecule in gas phase after relaxation, thus incorporating the stabilizing formation energy of the monolayer into the adsorption energy $E_{\text{PTCDA}}^{\text{gas}}$.

All terms in (7.1) and (7.2) are calculated at the coverage Θ = 1.0 ml. Considering all quantities after relaxation of the system, the adsorption energies with PBE+vdW$^{\text{surf}}$ are shown in Table 7.4. In the case of the substrate generated with the PBE+vdW$^{\text{surf}}$ lattice constant, the herringbone structure of the free monolayer in periodic boundary conditions is not stable for the structural optimization performed under the calculations settings employed. This fact alters $E_{\text{PTCDA}}^{\Theta}$ in (7.1) leading to an adsorption energy with the monolayer as reference $\left(E_{\text{ads}}^{\Theta(\text{ml})}\right)$ which is not comparable to the case in which the PBE lattice constant was used to generate the surface slab. For this reason, we only report in Table 7.4 the adsorption energy with the gas phase molecule as reference for the case in which the slab was generated with the PBE+vdW$^{\text{surf}}$ lattice constant. The fact that the herringbone structure of the free monolayer in the unit cell generated with the PBE+vdW$^{\text{surf}}$ lattice constant is not stable during the structural optimization is most probably due to the proximity of the neighboring molecules, consequence of the smaller surface unit cell. The closer proximity of the neighboring molecules may be contributing to the destabilization of the herringbone structure of the free monolayer.

From the perspective of our calculations, the first feature that we note in Table 7.4 is that the vdW interactions are the bonding mechanism in this system since the contribution of PBE is repulsive in all cases, confirming what we have already observed in the adsorption potential energy of section 5.1 (see also Figure 5.1). Given the fact that our calculations for the adsorption energy only included a coverage Θ of 1.0 ml, we cannot

Table 7.4: Adsorption energies for PTCDA on Ag(111) calculated with the PBE+vdW^{surf} method. $E_{ads}^{\Theta(ml)}$ refers to the adsorption energy with the monolayer in periodic boundary conditions as a reference while $E_{ads}^{\Theta(gas)}$ has a single molecule in gas phase as reference, thus incorporating the formation of the monolayer in the adsorption energy. $E_{ads}^{\Theta(ml)}$ is not shown for the case of the substrate generated with the PBE+vdW^{surf} lattice constant because the herringbone structure of the free monolayer in periodic boundary conditions is not stable during the structural optimization (see text). The contributions coming from chemical (PBE) and vdW interactions after relaxing the systems are also shown.

	$E_{ads}^{\Theta(ml)}$ [eV]			$E_{ads}^{\Theta(gas)}$ [eV]		
Lattice constant	Total	PBE	vdW	Total	PBE	vdW
PBE	−2.86	0.61	−3.47	−3.77	0.01	−3.78
PBE+vdW^{surf}	–	–	–	−3.38	0.57	−3.95

estimate the adsorption energy in the limit of low coverage, that is, for a single molecule. In the limit of low coverage, the adsorption energy for both reference states (monolayer and gas phase molecule) should be virtually equivalent as well as the proper reference value to compare with single-molecule experimental results. Recognizing that we would need to investigate coverage effects in order to quantify the adsorption energy for a single molecule, the PBE+vdW^{surf} method overestimates the adsorption energy independently of the reference or the lattice constant employed to generate the substrate if we take into consideration the above estimated interval in the adsorption energy. Our current research efforts show that one reason for this overestimation, besides of the possible coverage effects, is the absence of many-body dispersion energy effects, which decrease the effective interaction between the monolayer and the substrate [Maurer *et al.*, 2015].

7.3.2 3,4,9,10-Perylene-tetracarboxylic dianhydride on non-close-packed Ag surfaces

Up to this point we have addressed the performance of the DFA+vdW^{surf} method in the adsorption of PTCDA on the close-packed (111) surfaces of Ag (previous section and section 5.1) and Au (section 7.4), but we are also interested in the performance and sensitivity of the DFA+vdW^{surf} method when the adsorption occurs on non-close-packed surfaces. In this section, we address this aspect by doing a comparative analysis of the adsorption of PTCDA on a surface with different orientations: PTCDA on Ag(111), Ag(100), and Ag(110). The adsorption geometries of these systems have been investigated using the NIXSW technique [Hauschild *et al.*, 2010; Bauer *et al.*, 2012; Mercurio *et al.*, 2013a]. A novel feature in the studies including PTCDA on Ag(100) and Ag(110) is their higher chemical resolution resulting in the extraction of the adsorption position of each of the chemically inequivalent atoms in PTCDA, which offers us the invaluable opportunity of comparing these results to the ones obtained with the PBE+vdW^{surf} method.

Adsorption model and calculation details

As we have mentioned above, PTCDA forms a commensurate monolayer structure on silver surfaces. The lateral ordering of the molecules in the monolayer depends on the

orientation of the surface (see section 7.3.1). The surface unit cells for the calculations were modeled with a $\begin{pmatrix} 6 & 1 \\ -3 & 5 \end{pmatrix}$, $\begin{pmatrix} 4 & 4 \\ -4 & 4 \end{pmatrix}$, and a $\begin{pmatrix} 3 & 2 \\ -3 & 2 \end{pmatrix}$ super cell for the case of Ag(111), Ag(100), and Ag(110), respectively, in accordance to experimental results [Glöckler *et al.*, 1998; Ikonomov *et al.*, 2008]. We generated all surface slabs with the PBE lattice constant of Ag, which is 4.149 Å, in accordance with the work by Liu *et al.* [2013b]. The slabs consisted of five layers for Ag(111) and Ag(100) and seven layers for Ag(110) each with a vacuum gap of 50 Å. We used a Monkhorst and Pack [1976] grid of $4\times4\times1$ for Ag(111) and $6\times6\times1$ k points for Ag(100) and Ag(110) in the reciprocal space. We performed a structural relaxation of each of these systems where the molecule and the atoms in the topmost two metal layers were allowed to relax using the PBE+vdW$^{\text{surf}}$ method taking the experimental configuration as starting point for each structural relaxation. We did not take into account vdW interactions between metal atoms in the structural relaxations in order to avoid an artificial relaxation of the surface due to the fact that the surface slab was created using the PBE lattice constant. They were taken into consideration only in final adsorption energy calculations. All calculations were performed using *tight* settings as described in section 7.2.

Adsorption structures

PTCDA forms a commensurate monolayer structure on silver surfaces. On Ag(111), it forms a herringbone structure with two molecules per unit cell in non-equivalent adsorption configurations [Glöckler *et al.*, 1998; Kraft *et al.*, 2006]. Both molecules are adsorbed on bridge position, molecule A is practically aligned with the substrate in the $[10\bar{1}]$ direction with its carboxylic oxygen atoms on top position and the anhydride oxygen atoms located on bridge sites. Molecule B on the other hand is rotated with respect to the $[01\bar{1}]$ direction, with most atoms in its functional groups located closely to adsorption bridge positions [Kraft *et al.*, 2006; Bauer *et al.*, 2012]. Figure 7.3(b) depicts how this configuration is well reproduced in our calculations after relaxing the system. On Ag(100), a T-shape arrangement with two adsorbed molecules per unit cell can be observed [Ikonomov *et al.*, 2008]. Figure 7.3(c) shows the top view of the system after relaxation, showing that both molecules are aligned with the [110] direction of the substrate with the center of each molecule adsorbed on top position. This result agrees very well with experiments and previous DFT calculations [Bauer *et al.*, 2012]. Finally, in the case of Ag(110), PTCDA forms a brick-wall adsorption pattern with one molecule adsorbed per surface unit cell [Glöckler *et al.*, 1998]. The long axis of the molecule is located parallel to the [001] direction, while the center of the molecule is located on the bridge site between the close-packed atomic rows parallel to the $[\bar{1}10]$ direction [Böhringer *et al.*, 1998]. This configuration is reproduced accurately by the PBE+vdW$^{\text{surf}}$ calculations as Figure 7.3(d) confirms.

The adsorption geometries of these systems have been determined by experiments using the NIXSW technique. We compare these results with PBE+vdW$^{\text{surf}}$ calculations in Table 7.5 and illustrate them in Figure 7.4, in which the adsorption position of each of the atoms is referred to the position of the topmost unrelaxed metal layer. Table 7.5 shows that the PBE+vdW$^{\text{surf}}$ results for the vertical adsorption distance agree very well with experimental results. With the exception of the anhydride oxygen in Ag(111), the calculated distances for all atoms that form the molecule lie within 0.10 Å of the experimental results for all three surfaces. These results also reveal that our calculations

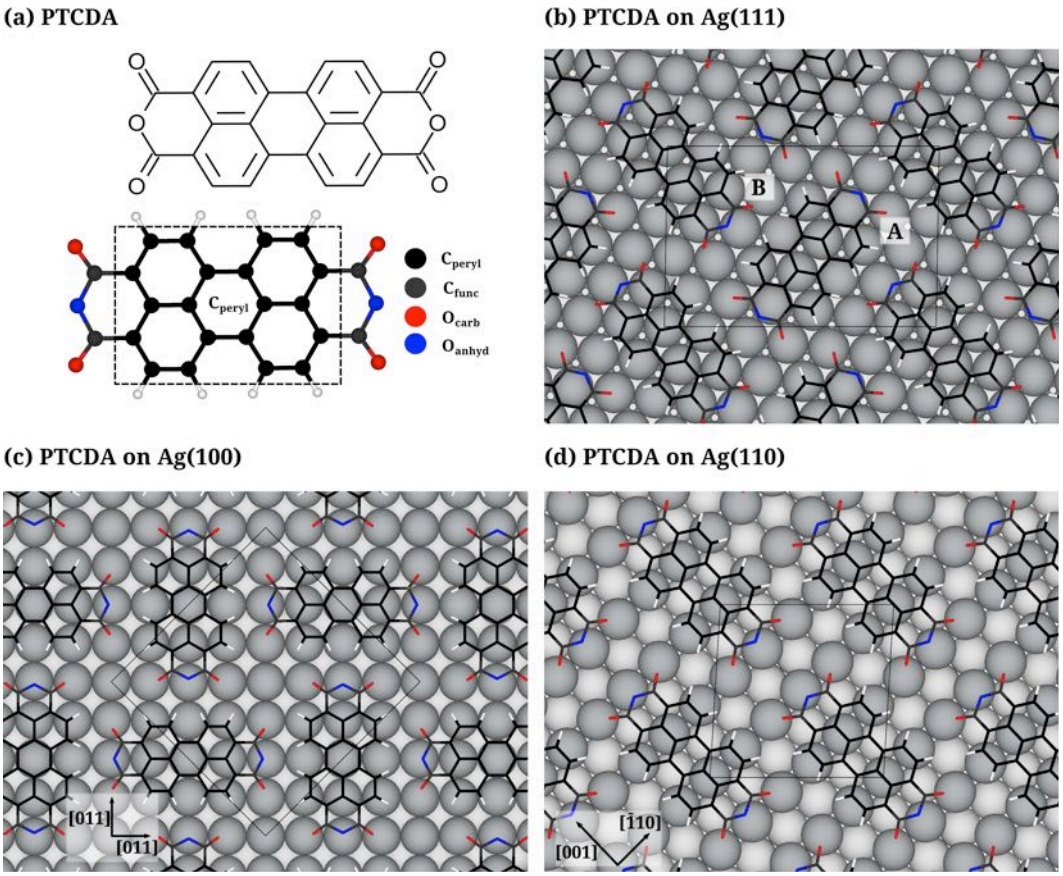

FIGURE 7.3: (a) Chemical structure of PTCDA. The distinction between carbon atoms belonging to the perylene core (C_{peryl}, black) and to the functional groups (C_{funct}, dark gray) is also displayed. In a similar fashion, oxygen atoms are shown in red for the case of the carboxylic oxygen (O_{carb}) and blue for the anhydride oxygen (O_{anhyd}). (b) Top view of the relaxed structure of PTCDA on Ag(111). Both inequivalent molecules of the structure are labeled A and B. (c) Top view of the relaxed structure of PTCDA on Ag(100). (d) Top view of the relaxed structure of PTCDA on Ag(110). The topmost metal layer is displayed in dark gray while the sublayer is light gray. Images of the structures were produced using the visualization software VESTA [Momma and Izumi, 2011].

Table 7.5: Comparison of experimental and theoretical results for the adsorption geometry of PTCDA on Ag(111), Ag(100), and Ag(110). We use $d_{\mathrm{Th/Exp}}$ to denote the averaged vertical adsorption heights of the specific atoms obtained from PBE+vdW$^{\mathrm{surf}}$ calculations and NIXSW studies. The adsorption height is given in Å with respect to the topmost unrelaxed metal layer. The specification of the atoms can be seen in Figure 7.3(a). The carbon backbone distortion is given as $\Delta\mathrm{C} = d(\mathrm{C_{peryl}}) - d(\mathrm{C_{func}})$ and the O difference as $\Delta\mathrm{O} = d(\mathrm{O_{anhyd}}) - d(\mathrm{O_{carb}})$. Experimental results can be found in Hauschild *et al.* [2010]; Bauer *et al.* [2012] and Mercurio *et al.* [2013a]. We cite here the results given by Hauschild *et al.* [2010] and Bauer *et al.* [2012].

	Ag(111)		Ag(100)		Ag(110)	
	d_{Th}	d_{Exp}	d_{Th}	d_{Exp}	d_{Th}	d_{Exp}
C total	2.80	2.86 ± 0.01	2.75	2.81 ± 0.02	2.54	2.56 ± 0.01
$\mathrm{C_{peryl}}$	2.80	–	2.76	2.84 ± 0.02	2.56	2.58 ± 0.01
$\mathrm{C_{func}}$	2.78	–	2.67	2.73 ± 0.01	2.43	2.45 ± 0.11
ΔC	0.02	–	0.09	0.11 ± 0.02	0.13	0.13 ± 0.11
O total	2.73	2.86 ± 0.02	2.59	2.64 ± 0.02	2.33	2.33 ± 0.03
$\mathrm{O_{carb}}$	2.68	2.66 ± 0.03	2.54	2.53 ± 0.02	2.29	2.30 ± 0.04
$\mathrm{O_{anhyd}}$	2.83	2.98 ± 0.08	2.69	2.78 ± 0.02	2.39	2.38 ± 0.03
ΔO	0.15	0.32 ± 0.09	0.15	0.25 ± 0.02	0.10	0.08 ± 0.05

reproduce the experimental trends observed in the sequence of Ag(111), Ag(100), and Ag(110) [Bauer *et al.*, 2012; Mercurio *et al.*, 2013a]. The overall vertical adsorption height –taken as an average over all carbon atoms– given by the calculations decreases in the sequence of Ag(111), Ag(100), and Ag(110) by 0.26 Å, in comparison to the value of 0.30 Å observed in experiments for the same sequence. The calculations reproduce the transition from a *saddlelike* adsorption geometry of PTCDA on Ag(111) to the *archlike* adsorption geometry that can be found in the more open surfaces according to experiments (see Figure 7.4). Finally, for the above mentioned sequence we find an increase in the carbon backbone distortion $\Delta\mathrm{C} = d(\mathrm{C_{peryl}}) - d(\mathrm{C_{func}})$ and a decrease in the O difference $\Delta\mathrm{O} = d(\mathrm{O_{anhyd}}) - d(\mathrm{O_{carb}})$. For ΔC, the calculations yield 0.02, 0.09, and 0.13 Å for Ag(111), Ag(100), and Ag(110), respectively, values which are in excellent agreement with experiments [Bauer *et al.*, 2012; Mercurio *et al.*, 2013a]. In the case of Ag(111), the carbon backbone distortion has not been determined experimentally, but the saddlelike adsorption geometry suggests a minimum distortion of the carbon backbone [Hauschild *et al.*, 2010; Bauer *et al.*, 2012] which we observe in our calculations as well. The carbon backbone distortion in Ag(100) and Ag(110) is then remarkably well reproduced by the calculations.

With respect to the oxygen difference (ΔO), the resulting values are 0.15 Å for Ag(111) and Ag(100), and 0.10 Å for Ag(110). These values reproduce the relative decrease in the distortion of the oxygen atoms in the sequence of Ag(111), Ag(100), and Ag(110) observed in experiments but underestimate the absolute difference by 0.17 Å in Ag(111) and 0.10 Å in Ag(100). This underestimation lies in the fact that the adsorption distances for the anhydride oxygen obtained with the calculations are also underestimated in the cases of Ag(111) and Ag(100). On the other hand, the calculated distance for the anhydride oxygen in Ag(110) agrees well with experiments, leading to a good agreement with

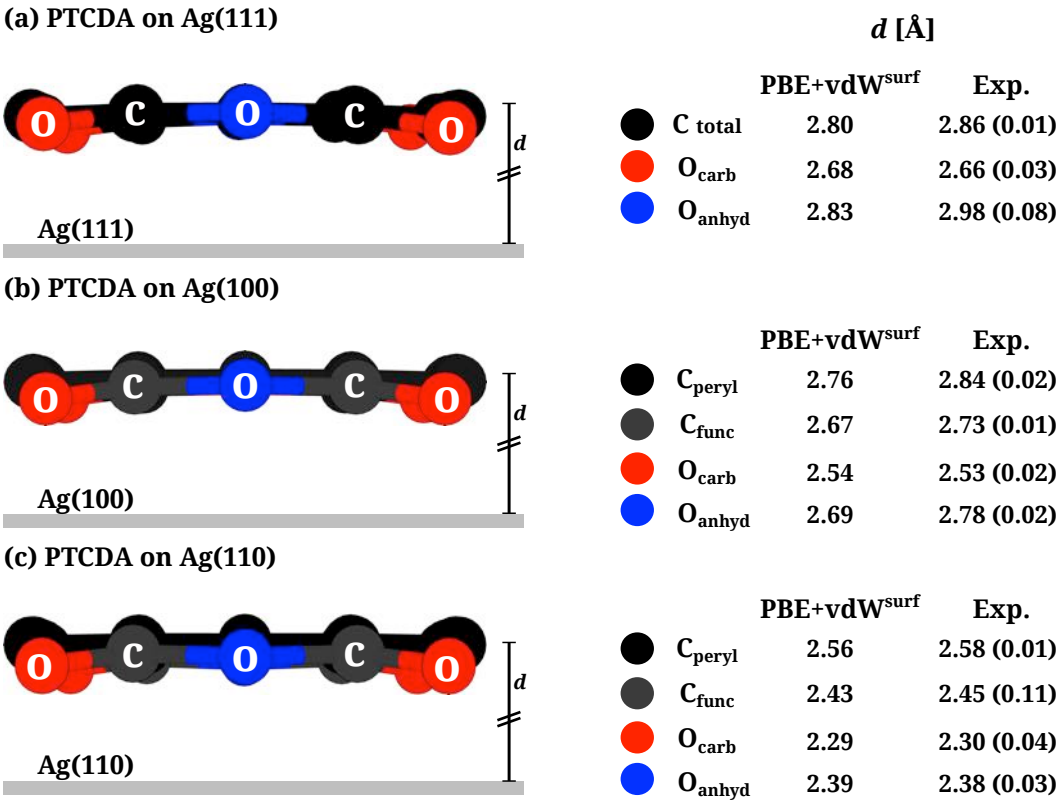

FIGURE 7.4: Geometry of PTCDA when adsorbed on (a) Ag(111), (b) Ag(100), and (c) Ag(110). The equilibrium distances d for each chemically inequivalent atom calculated with the PBE+vdW^{surf} method are displayed. Experimental results by Bauer *et al.* [2012] from NIXSW studies are also shown for comparison. The distinction between carbon atoms belonging to the perylene core (C_{peryl}, black) and to the functional groups (C_{funct}, dark gray) is also displayed. In a similar fashion, oxygen atoms are shown in red for the case of the carboxylic oxygen (O_{carb}) and blue for the anhydride oxygen (O_{anhyd}). Images of the structures were produced using the visualization software VESTA [Momma and Izumi, 2011].

Table 7.6: Adsorption energies $E_{ads}^{\Theta(ml)}$ for PTCDA on Ag(111), Ag(100), and Ag(110) calculated with the PBE+vdW^{surf} method. The contributions coming from chemical (PBE) and vdW interactions after relaxing the systems are also shown.

	$E_{ads}^{\Theta(ml)}$ [eV]		
	Total	PBE	vdW
Ag(111)	−2.86	0.61	−3.47
Ag(100)	−2.93	−0.01	−2.92
Ag(110)	−3.39	−0.90	−2.49

the experimental result of 0.08 ± 0.05 Å in the oxygen difference [Bauer *et al.*, 2012].

Adsorption energies

We have computed the adsorption energy $E_{ads}^{\Theta(ml)}$ of the systems at Θ = 1.0 ml using (7.1), where all the quantities are taken after relaxation of each subsystem. Table 7.6 summarizes the results. The binding strength increases in the above mentioned sequence, yielding the values of −2.86, −2.93, and −3.39 eV for Ag(111), Ag(100), and Ag(110), respectively. The vdW interactions are essential in these systems as they are the larger contribution to the adsorption energy, representing 73% for Ag(110) and the only stabilizing energy in Ag(111) and Ag(100). The chemical interactions become only relevant in Ag(100) and Ag(110). Only in the case of Ag(110) they contribute to the adsorption energy, representing 27% of the binding energy. In Ag(111), the effect is the opposite as a repulsion energy of 0.61 eV is found. We note that the adsorption energy $E_{ads}^{\Theta(ml)}$ is calculated with respect to the PTCDA monolayer, the binding strength will become even larger when calculated with respect to the molecule in gas phase due to the stabilizing formation energy of the monolayer (see for example the case of PTCDA on Au(111) in section 7.4.3). The accuracy of these results confirms the sensitivity to the surface termination that the DFA+vdW^{surf} scheme is able to achieve.

7.4 3,4,9,10-Perylene-tetracarboxylic dianhydride on Au(111)

7.4.1 Adsorption model and calculation details

PTCDA does not form commensurate monolayers on the Au(111) surface but rather exhibits a very close situation to a point-on-line growth on the $(22 \times \sqrt{3})$ reconstructed surface, situation which is not accessible to any type of state of the art modeling [Fenter *et al.*, 1997; Kilian *et al.*, 2006; Mannsfeld *et al.*, 2001; Schmitz-Hübsch *et al.*, 1997]. We generated the surface slab with the PBE lattice constant of Au, which is 4.159 Å, in line with a previous investigation [Liu *et al.*, 2013b]. As a reasonable approximation [see Romaner *et al.*, 2009], we have modeled the system using a $\begin{pmatrix} 6 & 1 \\ -3 & 5 \end{pmatrix}$ surface unit cell consisting of five layers each with thirty three Au atoms. The adsorbed monolayer consists of a herringbone lateral arrangement of two PTCDA molecules per unit cell. We chose the size of the vacuum gap to be approximately 50 Å and a Monkhorst and Pack [1976] grid of $4 \times 4 \times 1$ k points in the reciprocal space. We performed the structural relaxation of the system using the PBE+vdW^{surf} method by fixing the Au atoms in the three bottom

layers. For the structural relaxations, we did not take into account vdW interactions between metal atoms in order to avoid an artificial relaxation of the surface due to the fact that the surface slab was created using the PBE lattice constant. They were taken into consideration only in the calculation of the final adsorption energies. All calculations were performed using *tight* settings as described in section 7.2.

We have calculated the adsorption energy per molecule for two different coverages Θ of 1.0 and 0.5 ml. In this model, Θ = 1.0 ml corresponds to the adsorption of two PTCDA molecules per surface unit cell while Θ = 0.5 ml corresponds to the adsorption of one molecule per surface unit cell. The adsorption energy per molecule was calculated using

$$E_{\mathrm{ads}}^{\Theta(\mathrm{ml})} = \frac{1}{N}\left[E_{\mathrm{AdSys}}^{\Theta} - \left(E_{\mathrm{Au}} + E_{\mathrm{PTCDA}}^{\Theta}\right)\right], \tag{7.3}$$

$$E_{\mathrm{ads}}^{\Theta(\mathrm{gas})} = \frac{1}{N}\left[E_{\mathrm{AdSys}}^{\Theta} - \left(E_{\mathrm{Au}} + N \cdot E_{\mathrm{PTCDA}}^{\mathrm{gas}}\right)\right], \tag{7.4}$$

where $E_{\mathrm{AdSys}}^{\Theta}$ is the energy of the complete system formed by the monolayer and the slab, E_{Au} is the energy of the slab, $E_{\mathrm{PTCDA}}^{\Theta}$ corresponds to the energy of the monolayer in periodic boundary conditions, and N corresponds to the number of molecules in the model of the system. Expression (7.3) does not consider the formation of the monolayer in its definition of adsorption energy, while (7.4) considers the formation of the monolayer from gas phase by using $E_{\mathrm{PTCDA}}^{\mathrm{gas}}$, term which corresponds to the energy of a single PTCDA molecule in gas phase after relaxation. Hence, at Θ = 1.0, the difference between expressions (7.3) and (7.4) corresponds approximately to the formation energy of the monolayer. All terms in (7.3) and (7.4) are calculated at the given coverage value of Θ.

For the calculations with Θ of 0.60, 0.45, 0.30, and 0.15 ml, we have modelled the system with a larger surface unit cell with area of 824 Å^2 and a slab consisting of three layers each with 110 atoms of Au. The surface unit cell in this model is rectangular with unit cell vectors of magnitude a = 32.352 Å and b = 25.471 Å. At Θ = 0.60, the coverage corresponds to the adsorption of four molecules in a herringbone arrangement on top of the surface unit cell, thus being consistent with our above-given definition of monolayer coverage (Θ = 1.0). Coverages of 0.45, 0.30, and 0.15 ml thus correspond to the adsorpiton of 3, 2, and 1 molecule(s) on the same surface unit cell. For these calculations, we chose the size of the vacuum gap to be approximately 50 Å and a Monkhorst and Pack [1976] grid of 2 × 2 × 1 k points in the reciprocal space. We performed the structural relaxation of the system using the PBE+vdW$^{\mathrm{surf}}$ method only at Θ = 0.60 ml by fixing the Au atoms in the two bottom layers. For this structural relaxation, we did not take into account vdW interactions between metal atoms and used *light* settings. The remaining model systems with Θ of 0.45, 0.30, and 0.15 ml were built from the system at Θ = 0.60 ml. Van der Waals interactions were taken into consideration only in the calculation of the final adsorption energies using *tight* settings and expressions (7.3) and (7.4).

7.4.2 Adsorption geometry

Table 7.7 shows the average vertical distance of each species in the PTCDA molecule with respect to the topmost unrelaxed substrate layer using the PBE+vdW$^{\mathrm{surf}}$ method after relaxation of the system. Figure 7.5(a) shows a schematic view of these results, while Figure 7.5(b) depicts the structure of the monolayer after relaxation showing the position of each of the two inequivalent molecules in the unit cell. The bonding distance

Table 7.7: Experimental and theoretical results for the adsorption geometry of PTCDA on Au(111). We use $d_{\mathrm{Th/Exp}}$ to denote the averaged vertical adsorption heights of the specific atoms obtained with PBE+vdW$^{\mathrm{surf}}$ calculations and NIXSW studies respectively. The adsorption height is given in Å with respect to the unrelaxed topmost metal layer for a direct comparison to NIXSW experiments. The specification of the atoms can be seen in Figure 7.5. The carbon backbone distortion is given as $\Delta\mathrm{C} = d(\mathrm{C_{peryl}}) - d(\mathrm{C_{func}})$ and the O difference as $\Delta\mathrm{O} = d(\mathrm{O_{anhyd}}) - d(\mathrm{O_{carb}})$. Experimental results for the adsorption distance can be found in Henze *et al.* [2007]. An estimated experimental adsorption height, which takes into account an estimated outward relaxation of the topmost metal layer by 3%, reduces the adsorption height of the carbon backbone to 3.27 Å. The position of the O atoms was not determined in the experimental studies (see text).

	d_{Th}	d_{Exp}
C total	3.19	3.34 ± 0.02
$\mathrm{C_{peryl}}$	3.18	–
$\mathrm{C_{func}}$	3.23	–
ΔC	−0.05	–
O total	3.23	–
$\mathrm{O_{carb}}$	3.21	–
$\mathrm{O_{anhyd}}$	3.28	–
ΔO	0.07	–

of a PTCDA monolayer on Au(111) was studied by Henze *et al.* [2007] using the NIXSW technique. They found the monolayer, in terms of the carbon backbone of the molecule, located at a distance of 3.34 ± 0.02 Å with respect to the substrate. Their results are also presented in Table 7.7 and Figure 7.5 for comparison. Based on single-molecule manipulation experiments, by combining scanning tunneling microscopy and frequency modulated atomic force microscopy, Wagner *et al.* [2012] proposed a method to quantify the binding energy contributions to an organic-metal bond experimentally. They reported an adsorption distance of approximately 3.25 Å for PTCDA on Au(111).

Calculations with the PBE+vdW$^{\mathrm{surf}}$ method result in an adsorption height of 3.19 Å for the carbon backbone, underestimating the experimental result [Henze *et al.*, 2007] of 3.34 Å by approximately 0.15 Å. The position of the oxygen atoms were not measured in experiment due to an overlap of Au Auger lines with the O 1s core level. The results suggest a minor distortion of the carbon backbone as shown by $\Delta\mathrm{C} = d(\mathrm{C_{peryl}}) - d(\mathrm{C_{func}})$ = −0.05 Å. The negative sign in ΔC indicates that the carbon atoms belonging to the functional groups are located at a higher position than those of the perylene core. This fact is also reflected in the average position of the oxygen atoms which is around 0.04 Å higher than the average carbon backbone position. The results also show a distortion in the oxygen atoms of $\Delta\mathrm{O} = d(\mathrm{O_{anhyd}}) - d(\mathrm{O_{carb}})$ = 0.07 Å. In particular, the anhydride oxygen atoms are located around 0.09 Å higher than the carbon backbone. This behavior suggests a weaker attraction between the functional groups present in the molecule and the Au(111) surface. Overall, the large adsorption height of the monolayer confirms a relatively weak interaction of the molecule with the surface, namely physisorption.

The adsorption of a single PTCDA molecule has also been studied by Mura *et al.*

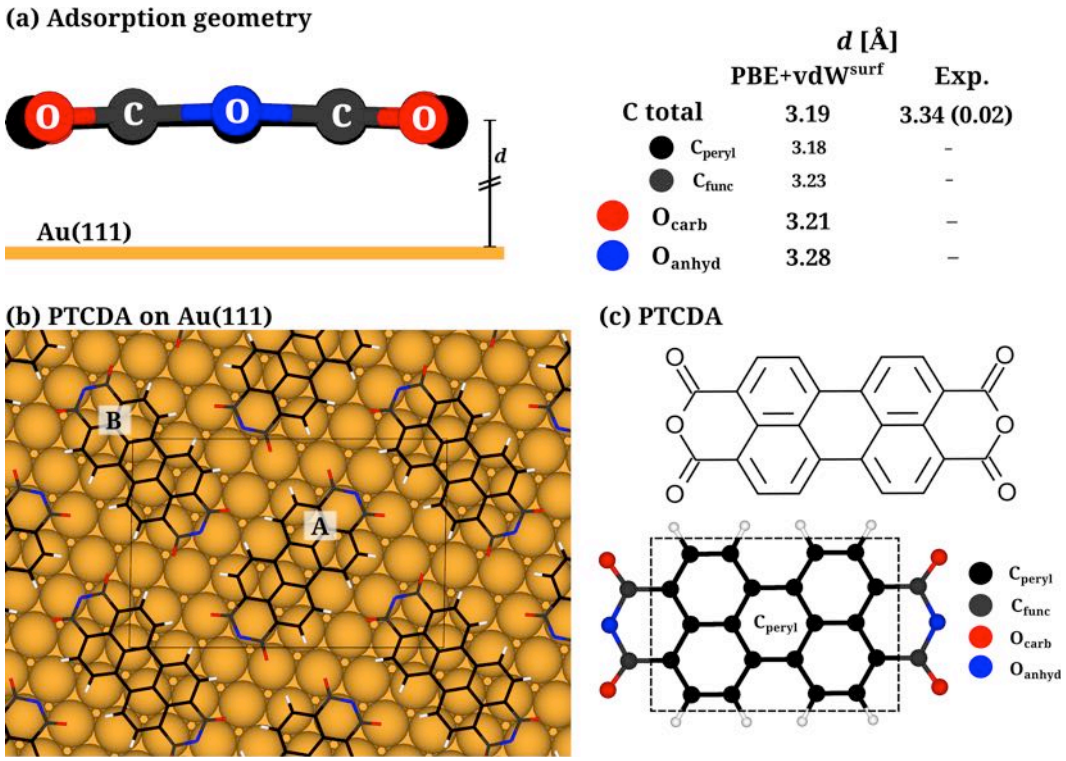

FIGURE 7.5: (a) Geometry of the structure of PTCDA adsorbed on Au(111) where the equilibrium distances d for each chemically inequivalent atom calculated with the PBE+vdW^{surf} method are displayed. Experimental results by Henze *et al.* [2007] from NIXSW studies are also shown for comparison. The distinction between chemically inequivalent atoms is displayed. (b) Top view of the relaxed structure of PTCDA on Au(111). Both inequivalent molecules of the structure are labeled as A and B. (c) Chemical structure of PTCDA. The distinction between carbon atoms belonging to the perylene core (C_{peryl}, black) and to the functional groups (C_{funct}, dark gray) is also displayed. In a similar fashion, oxygen atoms are shown in red for the case of the carboxylic oxygen (O_{carb}) and blue for the anhydride oxygen (O_{anhyd}). Images of the structures were produced using the visualization software VESTA [Momma and Izumi, 2011].

[2010] using the vdW-DF method [Dion *et al.*, 2004] in its self-consistent (scf) version. They performed a full relaxation of the system and obtained an adsorption distance of 3.3 Å, in good agreement with the experimental data. However, Romaner *et al.* [2009] revealed that when applying the vdW-DF to the adsorption of PTCDA on Ag(111), Au(111), and Cu(111), the substrate has a very small impact on the bonding distances; thus contradicting experimental and theoretical results [Tkatchenko *et al.*, 2010; Ruiz *et al.*, 2012]. Hence, the reliability of the vdW-DF method in the treatment of these systems still remains unclear.

The discrepancy of around 0.15 Å between the results here presented and experiment can be attributed to several factors related to both approaches. In the case of the Au(111) surface, PTCDA does not form a commensurate monolayer but rather exhibits a situation very close to a point-on-line correspondence with the $(22 \times \sqrt{3})$ reconstructed surface [Fenter *et al.*, 1997; Kilian *et al.*, 2006; Mannsfeld *et al.*, 2001; Schmitz-Hübsch *et al.*, 1997]. Kilian *et al.* [2006] reported an adsorbate structure at equilibrium conditions (grown at high substrate temperatures and small deposition rates) that suggests an optimal point-on-line relation on each of the three reconstruction domains of the substrate, which results in azimuthal domain boundaries –with an angular misfit of around 2.5°– in the PTCDA monolayer. The adsorbate structure consists of a rectangular unit cell with an area of approximately 232 $Å^2$ and two PTCDA molecules per surface unit cell. The area of the surface unit cell here studied is 247 $Å^2$, which is larger than the area of the experimental surface unit cell by more than 6%. On the other hand, Henze *et al.* [2007] reported an adsorption height that corresponds most probably to the square phase of PTCDA on Au(111) [Mannsfeld *et al.*, 2001; Schmitz-Hübsch *et al.*, 1997], which does not conform the (majority) herringbone type phases observed by LEED [Fenter *et al.*, 1997; Mannsfeld *et al.*, 2001]. Furthermore, neither theory nor experiments take initially into consideration the surface relaxation in the determination of the adsorption height of the carbon backbone. An estimated experimental adsorption height of 3.27 Å [as found in Henze *et al.*, 2007], which takes into account an estimated outward relaxation of the topmost metal layer by 3% reduces the difference between theory and experiment to less than 0.1 Å. Although the correct superstructure of the monolayer including the domain boundaries cannot be achieved by any state-of-the-art modeling, the very good agreement between theory and experiment suggests that the lateral arrangement of the molecule is strong due to the intermolecular interactions and the effect of the exact superstructure of the monolayer on the adsorption height should be minimal; thus yielding the results that we present as relevant. This fact has also been indicated by experimental results [Henze *et al.*, 2007; Kilian *et al.*, 2006].

7.4.3 Adsorption energy

The binding of a single PTCDA molecule on Au(111) was investigated by Wagner *et al.* [2012], where they reported an adsorption energy of approximately −2.5 eV per molecule; while TPD experiments performed to study the adsorption of the monolayer revealed an adsorption energy of approximately −1.94 eV per molecule in the limit of residual coverage [Stremlau, 2015]. The adsorption energy of PTCDA on Au(111) was also studied by Mura *et al.* [2010] by using DFT methods. They found a value of −1.88 eV employing the vdW-DF in its scf version and a value of −2.03 eV when using a classical potential. Romaner *et al.* [2009] reported a value of −2.0 eV based on binding energy

Table 7.8: Adsorption energy E_{ads}^{Θ} for PTCDA on Au(111) at a coverage Θ = 1.0 ml and Θ = 0.5 ml using the PBE+vdW^{surf} method. $E_{ads}^{(ml)}$ is the adsorption energy calculated with the PTCDA monolayer as reference whereas $E_{ads}^{(gas)}$ is the adsorption energy calculated with respect the molecule in gas phase as reference [expressions (7.3) and (7.4) with N =2]. The structure corresponds to the structural relaxation, obtained with the PBE+vdW^{surf} method, of the system modeled with a $\begin{pmatrix} 6 & 1 \\ -3 & 5 \end{pmatrix}$ surface unit cell consisting of five layers each with thirty three Au atoms.

Θ [ml]	$E_{ads}^{\Theta(ml)}$	$E_{ads}^{\Theta(gas)}$
1.0	−2.15	−3.05
0.5	−2.27	−2.50

curves using the vdW-DF with the correction due to nonlocal vdW forces added *a posteriori* on top of the semi-local xc functional. Based on potential-energy curves using the PBE+vdW^{surf} method, we have estimated a value of approximately −2.4 eV per molecule for the case of the adsorbed monolayer [Ruiz *et al.*, 2012] and a value between −2.23 and −2.15 eV for the case of a *single* adsorbed molecule (see section 5.2).

Given the above mentioned experimental results for the adsorption energy, we now analyze the adsorption energy of PTCDA on Au(111) with the PBE+vdW^{surf} method. Under the calculation settings mentioned in section 7.4.1, we have calculated the adsorption energy per molecule for two different coverages Θ of 1.0 and 0.5 ml. In our model, Θ = 1.0 ml corresponds to the adsorption of two PTCDA molecules per surface unit cell while Θ = 0.5 ml corresponds to the adsorption of one molecule per surface unit cell. As we have mentioned above, the surface unit cell here studied is characterized by an area of 247 Å^2 and consists of thirty three Au atoms in its topmost layer –see Figure 7.5(b). The adsorption energy per molecule in the monolayer was calculated using expressions (7.1) and (7.2) with all terms given a the coverage value of Θ. Considering all quantities after relaxation of the system, the adsorption energies with PBE+vdW^{surf} are shown in Table 7.8.

The calculated energies reveal a dependence on the coverage of the monolayer independently of the reference state. In the case in which the reference is the PTCDA monolayer, the adsorption energy $E_{ads}^{\Theta(ml)}$ per molecule for Θ = 0.5 ml *increases* with respect to the case of Θ = 1.0 ml by around 6%. On the other hand, considering the formation of the monolayer from gas phase, $E_{ads}^{\Theta(gas)}$ the adsorption energy per molecule for Θ = 0.5 ml *decreases* with respect to Θ = 1.0 ml by around 18%. It is clear that the adsorption energy calculated in the limit of low coverage for both reference states should be virtually equivalent and the proper reference value to compare with the TPD experimental result. With this in mind, we have included calculations with Θ of 0.60, 0.45, 0.30, and 0.15 ml in order to compare the calculated value of the adsorption energy in the limit of low coverage with the experimental result. For these results, we have modeled the system using a larger unit cell with an area of 824 Å^2 and a slab with three Au layers as we have described above. We present these results in Table 7.9. The results demonstrate that the adsorption energy tends to a converged value as the coverage of the monolayer is reduced to the limit of the single molecule. Notably, at Θ = 0.15, the difference be-

Table 7.9: Adsorption energy E_{ads}^{Θ}, given in eV, for PTCDA on Au(111) at a coverage Θ of 1.00, 0.60, 0.45, 0.30, 0.15 ml, and the limit of residual coverage with the PBE+vdW$^{\text{surf}}$ method. The details of the adsorption model and the structural relaxation are found in section 7.4.1. The experimental result by Stremlau [2015] is also shown for comparison.

Θ [ml]	$E_{\text{ads}}^{\Theta(\text{ml})}$	$E_{\text{ads}}^{\Theta(\text{gas})}$	Exp.
1.00	−2.07	−2.97	–
0.60	−2.05	−2.59	–
0.45	−2.14	−2.40	–
0.30	−2.16	−2.26	–
0.15	−2.17	−2.13	–
$\lim\Theta \to 0$	−2.15		-1.93 ± 0.04

tween $E_{\text{ad}}^{\Theta(\text{ml})}$ and $E_{\text{ad}}^{\Theta(\text{gas})}$ amounts to just 0.04 eV. We take this value as the limit of low coverage for our calculations. Taking the average value between $E_{\text{ad}}^{\Theta(\text{ml})}$ and $E_{\text{ad}}^{\Theta(\text{gas})}$ at $\Theta = 0.15$, the adsorption energy at the limit of the single molecule is −2.15 eV with the PBE+vdW$^{\text{surf}}$ method. This value will be slightly more negative if we consider a small correction due to the number of layers in the surface slab. Nevertheless, it lies, in practical terms, within the interval of our own prediction for the case of a single adsorbed molecule with calculations from a potential-energy curve in section 7.4. In comparison to the experimental result of Stremlau [2015], the PBE+vdW$^{\text{surf}}$ adsorption energy is overestimated by approximately 0.20 eV. Our current research indicates that this overestimation is probably related to the absence of many-body dispersion effects [Maurer *et al.*, 2015, see]. The inclusion of many-body dispersion effects reduces the overbinding found in pairwise vdW-inclusive methods, yielding an improvement, for instance, in the adsorption energy.

7.5 3,4,9,10-Perylene-tetracarboxylic dianhydride on Cu(111)

7.5.1 Adsorption model and calculation details

In the case of PTCDA on Cu(111), a larger unit cell in comparison to Ag and Au is required due to the smaller lattice constant of Cu. We used three models, derived by Romaner *et al.* [2009], which are based on experimental data [Wagner *et al.*, 2007]: structure 1, 2, and 3. The three structures have two inequivalent PTCDA molecules per unit cell and were modeled with slabs consisting of three metallic layers. All slabs were generated with the PW91 lattice constant which is 3.638 Å [Romaner *et al.*, 2009]. Structure 1 consists of a $\left(\begin{smallmatrix} 6 & 2 \\ -4 & 6 \end{smallmatrix}\right)$ surface unit cell with 44 metal atoms per layer and a unit cell area of 252 Å^2, while structure 2 and 3 are conformed by a $\left(\begin{smallmatrix} 5 & 0 \\ -5 & 10 \end{smallmatrix}\right)$ and a $\left(\begin{smallmatrix} 7 & 2 \\ -4 & 6 \end{smallmatrix}\right)$ surface unit cell, respectively; both conformed with 50 atoms per metallic layer and a unit cell area of 286 Å^2. We chose the size of the vacuum gap to be approximately 25 Å and a Monkhorst and Pack [1976] grid of $2 \times 2 \times 1$ k points in the reciprocal space. We performed the structural relaxation of the system using the PBE+vdW$^{\text{surf}}$ method by fixing the Cu atoms in the two bottom layers. For the structural relaxations, we did not take into account vdW interactions between metal atoms in order to avoid an artificial relaxation of the surface due to the

Table 7.10: Specifications for the unit cell of each structure investigated for PTCDA on Cu(111).

Structure	Surface Unit Cell	Area [Å^2]
1	$\begin{pmatrix} 6 & 2 \\ -4 & 6 \end{pmatrix}$	252
2	$\begin{pmatrix} 5 & 0 \\ -5 & 10 \end{pmatrix}$	286
3	$\begin{pmatrix} 7 & 2 \\ -4 & 6 \end{pmatrix}$	286

fact that the surface slab was created using the PW91 lattice constant. They were taken into consideration only in final adsorption energy calculations. All relaxations were performed using *light* settings as described in section 7.2. Final adsorption energies were calculated with *tight* settings, a Monkhorst-Pack grid of $4\times4\times1$ k points in the reciprocal space, and taking into account vdW interactions between metal atoms.

7.5.2 Adsorption structures

The bonding distance of a PTCDA monolayer on Cu(111) was studied by Gerlach *et al.* [2007] using the NIXSW technique. They found the monolayer, in terms of the carbon backbone of the molecule, located at a distance of 2.66 ± 0.02 Å with respect to the substrate. Their studies also include the adsorption distances of the oxygen atoms in PTCDA. The adsorption unit cell of the system was characterized by Wagner *et al.* [2007] by STM experiments. However, the lateral arrangement of the molecules in the monolayer has not been yet clearly established beyond the herringbone arrangement. In this context, we investigated three possible adsorption structures –labeled as 1, 2, and 3– with different surface unit cells and lateral position of the molecules. The features of these structures were mentioned above and are summarized in Table 7.10. Structure 1 corresponds to a smaller surface unit cell than the one proposed by Wagner *et al.* [2007]. Structure 2 corresponds to the experimental surface unit cell [found in Wagner *et al.*, 2007] whereas structure 3 corresponds to a different (however possible) surface unit cell with the same area as structure 2.

Table 7.11 shows the average vertical distance of each species in the PTCDA molecule with respect to the topmost unrelaxed substrate layer after relaxation of each of the structures studied. We show a schematic view of these results in Figure 7.6. The maximum difference in the adsorption distance of the carbon backbone among the three structures is approximately 0.07 Å, which is found between structures 1 and 3; while a similar difference of 0.06 Å is found between structures 2 and 3. The calculations show, however, that the adsorption distance in structure 3 agrees remarkably better (slightly larger by 0.02 Å) with the NIXSW results. On the other hand, the final position of the oxygen atoms disagree with the experimental results regardless of the structure of the substrate. The averaged position of the carboxylic oxygen atoms are below the carbon backbone in contrast to the findings of Gerlach *et al.* [2007]. This takes us to discuss the lateral arrangement of the molecules in the monolayer. Figure 7.7 and Figure 7.8 show the top view of each structure after relaxation where two inequivalent molecules

Table 7.11: Comparison of PBE+vdW^{surf} results after relaxation for the three studied structures of PTCDA on Cu(111). Experimental results are also shown for comparison Gerlach *et al.* [2007]. We use $d_{Th/Exp}$ to denote the averaged vertical adsorption heights of the specific atoms obtained with PBE+vdW^{surf} calculations and NIXSW studies respectively. The adsorption height is given in Å with respect to the unrelaxed topmost metal layer for a direct comparison to NIXSW experiments. The specification of the atoms can be seen in Figure 7.5. The carbon backbone distortion is given as $\Delta C = d(C_{peryl}) - d(C_{func})$ and the O difference as $\Delta O = d(O_{anhyd}) - d(O_{carb})$.

	d_{Th} Structure			d_{Exp}
	1	2	3	
C total	2.75	2.74	2.68	2.66 ± 0.02
C_{peryl}	2.74	2.75	2.68	–
C_{func}	2.79	2.69	2.68	–
ΔC	−0.05	0.06	0.00	–
O total	2.75	2.61	2.62	2.81 ± 0.03
O_{carb}	2.70	2.55	2.56	2.73 ± 0.06
O_{anhyd}	2.86	2.73	2.75	2.89 ± 0.06
ΔO	0.16	0.18	0.19	0.16 ± 0.08

per unit cell are present in each. Label A corresponds to the molecule which is aligned with the topmost layer of the substrate and label B corresponds to the molecule that is misaligned. A comparison among the structures reveal differences in the relative lateral position of each molecule after relaxation. We now mention the main features of each structure.

Structure 1

Figure 7.7(a) shows the top view of structure 1 after relaxation. The effect of a smaller surface unit cell in structure 1 leads to a larger adsorption height of the carbon backbone in comparison to the other structures. Table 7.12 shows the results corresponding to the structure of each molecule in the unit cell, where it can be seen that the adsorption distance and internal distortion of molecule A agree remarkably well with the NIXSW experiments [Gerlach *et al.*, 2007], including the placement of the carboxylic oxygen above the carbon backbone. On the other hand, molecule B resides at approximately 0.13 Å higher than molecule A. This results in the averaged adsorption height of 2.75 Å as observed in the monolayer. As seen in Figure 7.7(a), the central aromatic ring of both molecules resides just on top of a substrate atom. The smaller area of the unit cell results in shorter O-H bonds between neighboring molecules. Because of the latter fact and a very similar adsorption surface site, the carboxylic oxygens in the monolayer do not experience any further distortion. As another result of the similar adsorption site, just one structurally equivalent type of carboxylic oxygen with respect to the substrate can be found in the structure, located at an average height of 2.70 Å. This carboxylic oxygen is labeled as O_{carb} #1 in Figure 7.7(a).

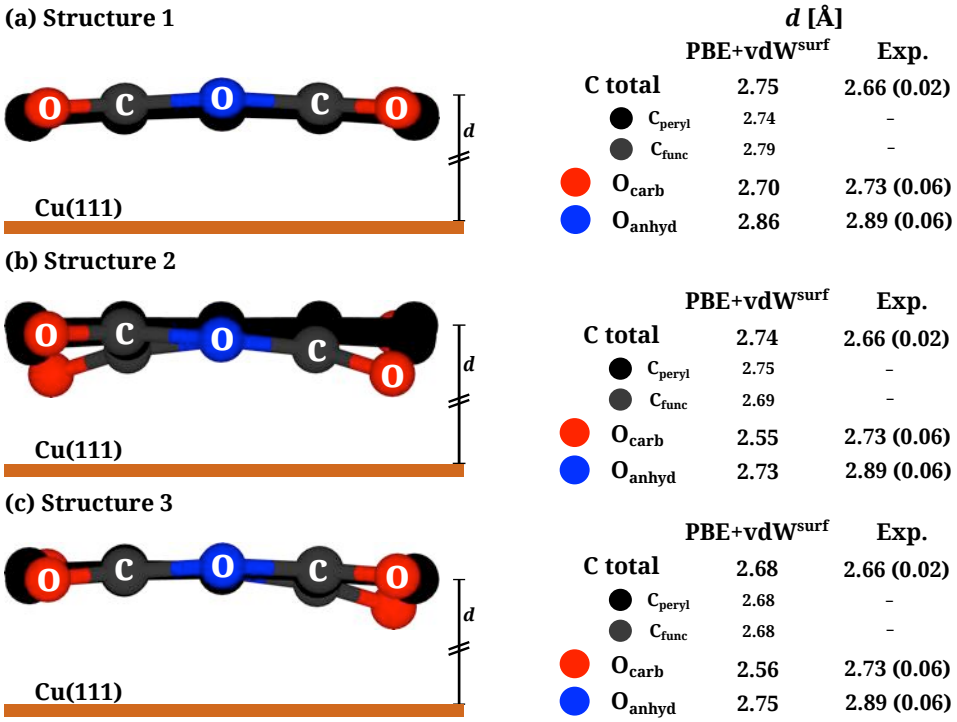

FIGURE 7.6: Geometry of PTCDA adsorbed on Cu(111). The substrate corresponds to (a) structure 1, (b) structure 2, and (c) structure 3 as explained in the text. All substrates were generated with the PW91 lattice constant of Cu (3.638 Å). The equilibrium distances d for each chemically inequivalent atom calculated with the PBE+vdW^{surf} method are displayed. Experimental results from NIXSW studies by Gerlach *et al.* [2007] are also shown for comparison. The distinction between carbon atoms belonging to the perylene core (C_{peryl}, black) and to the functional groups (C_{funct}, dark gray) is also displayed. In a similar fashion, oxygen atoms are shown in red for the case of the carboxylic oxygen (O_{carb}) and blue for the anhydride oxygen (O_{anhyd}). Images of the structures were produced using the visualization software VESTA [Momma and Izumi, 2011].

Structures 2 and 3

Figure 7.8(a) and Figure 7.8(b) show the top view of structures 2 and 3 after relaxation respectively. The main differences in both structures are the relative lateral position of the molecules and the adsorption height of the carbon backbone. The central aromatic ring of both molecules in structure 2 are located on top of copper atoms, while in structure 3, they are adsorbed on a threefold hollow surface site. Both structures present a similar internal distortion. Three different carboxylic oxygen atoms, differing among each other by at least 0.1 Å with respect to the adsorption height, can be found in each structure. They are labeled as O_{carb} #1, #2, and #3 in Figure 7.8(a) and Figure 7.8(b). Structure 2 has four carboxylic oxygen atoms located at an adsorption height of 2.73 Å which reside on a bridge adsorption surface site. These are followed by two located at 2.50 Å and two located at 2.24 Å, all four residing on a similar adsorption site. Structure 3 presents three carboxylic oxygen atoms located at an adsorption height of 2.75 Å, followed by two

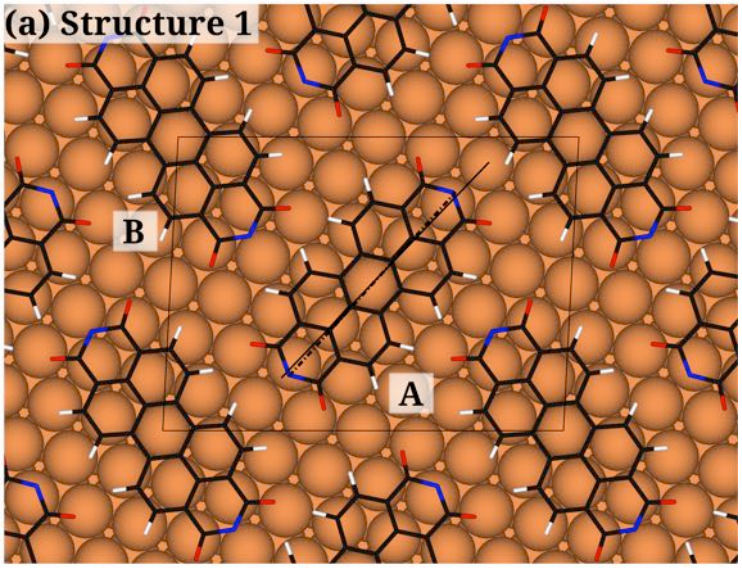

(b) Adsorption distance

	Structure 1	2	3
O_{carb} #1	2.70 Å	2.73 Å	2.75 Å
O_{carb} #2	--	2.50 Å	2.66 Å
O_{carb} #3	--	2.24 Å	2.29 Å

FIGURE 7.7: (a) Top view of the relaxed structure of PTCDA adsorbed on Cu(111). The substrate corresponding to structure 1 is shown. The substrate was generated with the PW91 lattice constant of Cu (3.638 Å). Both inequivalent molecules in the monolayer are labeled A and B. The distinction between chemically inequivalent atoms is displayed [see also Figure 7.1(b)]. (b) Only one type of carboxylic oxygen atom, according to its adsorption site (see text), is found in structure 1. It is labeled as O_{carb} #1 (red) along with its corresponding adsorption distance. Images of the structures were produced using the visualization software VESTA [Momma and Izumi, 2011].

which are located at 2.66 Å and reside on a bridge adsorption surface site. The last three are located at 2.29 Å from the surface and reside practically on top of a substrate atom. Depending on the placement of each of the molecules, carboxylic oxygen atoms which belong to the same molecule can reside in either top or bridge surface sites, giving rise to structurally inequivalent carboxylic oxygens, fact which agrees with the low coherent fraction observed in the NIXSW experiments by Gerlach *et al.* [2007] for the carboxylic oxygen.

7.5.3 Adsorption energies

We investigated the stability of each structure by calculating the adsorption energy for each case employing expressions (7.1) and (7.2) with $\Theta = 1$ ml. The results are summarized in Table 7.13, showing the contribution of vdW and chemical (PBE) interactions to the adsorption energy after relaxation with PBE+vdW^{surf}. These results demonstrate that

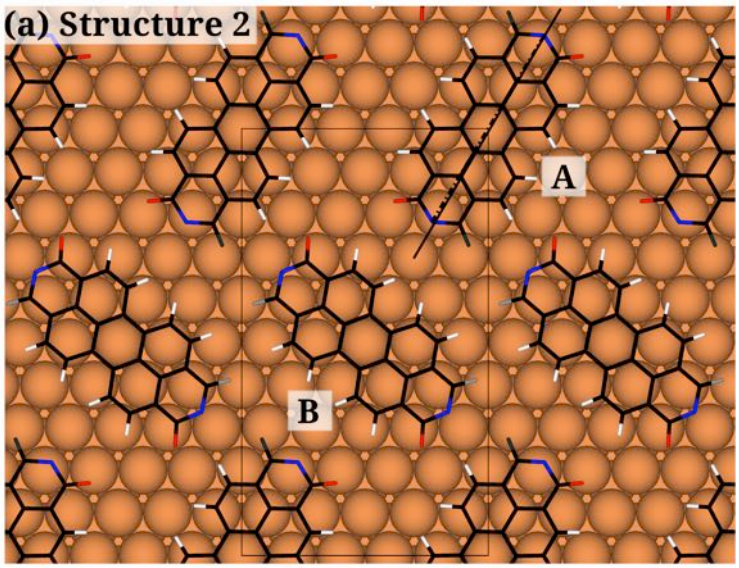

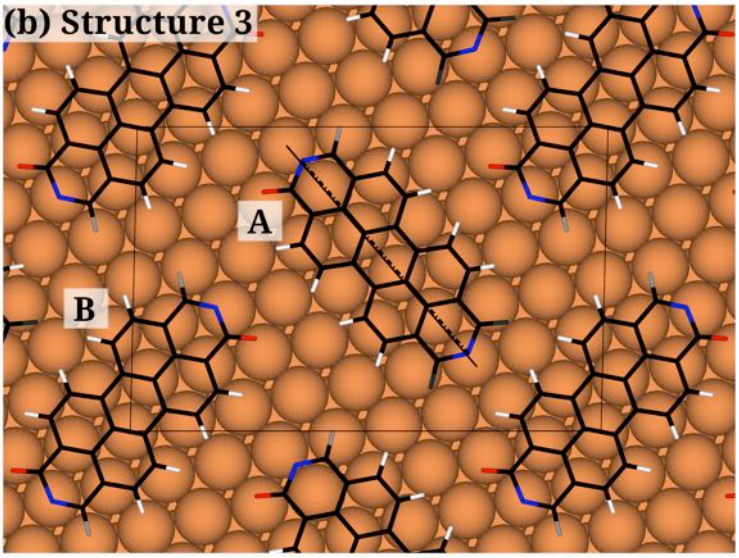

(c) Adsorption distance

	Structure 1	2	3
O_{carb} #1	2.70 Å	2.73 Å	2.75 Å
O_{carb} #2	--	2.50 Å	2.66 Å
O_{carb} #3	--	2.24 Å	2.29 Å

FIGURE 7.8: Top view of the relaxed structure of PTCDA adsorbed on Cu(111). The substrate corresponds to (a) structure 2, and (b) structure 3 as explained in the text. All substrates were generated with the PW91 lattice constant of Cu (3.638 Å). Both inequivalent molecules in the monolayer are labeled A and B. The distinction between chemically inequivalent atoms is displayed [see also Figure 7.1(b)]. (c) Three different carboxylic oxygen atoms, differing in their adsorption site (see text), can be found in structures 2 and 3. They are labeled as O_{carb} #1 (red), #2 (dark green), and #3 (light gray) and listed along with their corresponding adsorption distances. Images of the structures were produced using the visualization software VESTA [Momma and Izumi, 2011].

Table 7.12: Comparison of results after relaxing structure 1 of PTCDA on Cu(111) using the PBE+vdW^{surf} method in which the structure of each inequivalent molecule (A and B, see Figure 7.6) is shown. Experimental results are also shown for comparison [Gerlach *et al.*, 2007]. We use $d_{Th/Exp}$ to denote the averaged vertical adsorption heights of the specific atoms obtained with PBE+vdW^{surf} calculations and NIXSW studies respectively. The adsorption height is given in Å with respect to the unrelaxed topmost metal layer for a direct comparison to NIXSW experiments. The specification of the atoms can be seen in Figure 7.5. The carbon backbone distortion is given as $\Delta C = d(C_{peryl}) - d(C_{func})$ and the O difference as $\Delta O = d(O_{anhyd}) - d(O_{carb})$. Results for each of the molecules in the unit cell corresponding to the structure 1 of PTCDA on Cu(111). Units are Å.

	d_{Th}			d_{Exp}
	Monolayer	Molecule		
		A	B	
C total	2.75	2.68	2.81	2.66 ± 0.02
O_{carb}	2.70	2.73	2.67	2.73 ± 0.06
O_{anhyd}	2.86	2.87	2.85	2.89 ± 0.06
ΔO	0.16	0.14	0.18	0.16 ± 0.08

Table 7.13: Adsorption energy of each investigated structure for PTCDA on Cu(111) calculated with the PBE+vdW^{surf} method. The contributions coming from chemical (PBE) and vdW interactions after relaxing the systems are also shown. $E_{ads}^{(ml)}$ is the adsorption energy calculated with respect to the PTCDA monolayer and $E_{ads}^{(gas)}$ is the adsorption energy calculated with respect to the molecule in gas phase [see expressions (7.1) and (7.2)].

Structure	$E_{ads}^{(ml)}$ [eV]			$E_{ads}^{(gas)}$ [eV]
	Total	PBE	vdW	
1	−2.55	0.93	−3.47	−3.33
2	−2.48	0.94	−3.42	−3.12
3	−2.78	0.74	−3.52	−3.37

the vdW contribution is responsible for the stability of the systems since the energetic contribution from PBE is repulsive regardless of the structure. Table 7.13 also shows that structure 3 is the most favorable in accordance to the adsorption energy per molecule $E_{ads}^{(ml)}$ with the monolayer as reference; while structures 1 and 2 are nearly degenerate. Given all three structures, structure 3 presents the shortest adsorption distance of the carbon backbone, which results in a larger vdW contribution to the adsorption energy. However, Table 7.13 reveals that the vdW interaction energy is not the only factor determining the relative stability of structure 3, but also the smaller repulsive energy from its PBE contribution.

An interesting fact is that structure 1 and structure 3 are nearly degenerate when the molecule in the gas phase is the reference as the adsorption energy $E_{ads}^{(gas)}$ in the structure 1 is just 0.04 eV less stable than the adsorption energy in structure 3. The reason

for this fact could be that the individual molecules are closer in structure 1 due to its smaller surface unit cell; thus favoring the formation of the monolayer through stronger intermolecular forces.

The fact that the formation of the monolayer from gas phase brings the adsorption energy closer in the three cases and the structural differences observed in the structures investigated are evidence that the influence of the lateral placement of the molecules and its relation to the surface unit cell cannot be ignored. The structural and energetic results also suggest that effects beyond the microscopic scale might be at play in the monolayer formation of PTCDA on Cu(111), for example, the statistical average of ordered structures which have subtle structural differences.

CHAPTER

8 Summary and outlook

8.1 Summary

We have presented a DFT-based method with the purpose of modeling screened vdW interactions accurately for the adsorption of atoms and molecules on surfaces. This has been accomplished via the development of the DFA+vdW$^{\text{surf}}$ method by incorporating the collective response of the substrate electrons in vdW-inclusive DFA for intermolecular interactions. The following conclusions can be drawn from our analysis after including screened vdW interactions, within KS-DFT, in the determination of the structure and stability of atoms and molecules on surfaces.

i. The noticeable improvement in the calculation of adsorption distances and energies with the DFA+vdW$^{\text{surf}}$ method indicates the importance of including the collective response of the substrate electrons in the calculation of vdW interactions for adsorption systems. We have shown these effects in prototypical physisorption systems such as the adsorption of a Xe monolayer on transition-metal surfaces; and complex inorganic/organic interfaces such as those formed by the adsorption of aromatic molecules on metal surfaces. In particular, we have emphasized the importance of including screened vdW interactions in the determination of the structure and stability of inorganic/organic interfaces.

ii. Based on our analysis of the structural and stability features of inorganic/organic interfaces, the DFA+vdW$^{\text{surf}}$ method has shown to be successful in dealing with a wide range of interactions present at these interfaces, including chemical interactions, electrostatic interactions, Pauli repulsion, and vdW interactions. Our analysis further shows that the method is also able to capture interface polarization effects and to achieve surface-termination sensitivity as well.

iii. These results establish the DFA+vdW$^{\text{surf}}$ method as a reasonable option for the accurate treatment of realistic adsorption problems, with particular advantage in the calculation of HIOS, due to its efficiency and affordability in terms of computational time. Furthermore, it can be, in principle, equally applied to any polarizable solid with any surface structure.

From a general perspective, however, there are still many important aspects left to consider in order to achieve both quantitative accuracy and predictive power in the simula-

tion of the structure and stability of complex interfaces. Some of which we will address briefly now.

8.2 Inclusion of many-body dispersion effects and full treatment of the collective response of the system

The noticeable improvement in the calculation of adsorption distances and energies with the DFA+vdW^{surf} method establishes the importance of including the non-local many-body response of the substrate electrons for the calculation of vdW interactions, in particular for inorganic/organic interfaces. In a more general perspective, however, the full treatment of the collective response found in the combined system (adsorbate/substrate) would represent an essential step in the direction of improved accuracy and increased reliability in computational studies of adsorption phenomena [Liu *et al.*, 2014]. High-level quantum-chemistry methods or many-body methods such as the RPA for the correlation energy can be used for this purpose. Nevertheless, these approaches either perform well for one of the two subsystems –the solid or the isolated adsorbate– and not for the combined system, or their application to adsorption systems still awaits increasing computer power and more efficient implementations in order to treat larger super cells [Ren *et al.*, 2012b].

An alternative in this regard is the recently developed method, termed as DFT+MBD [Tkatchenko *et al.*, 2012; Ambrosetti *et al.*, 2014b], which consists of an efficient dipole approximation to the RPA. The MBD method includes many-body effects in the long-range correlation energy to all orders. Our current efforts are focused on including many-body dispersion effects in the adsorption of molecules on surfaces with particular focus on organic adsorbates on metal surfaces, systems in which many-body dispersion contributions can play an essential role. In particular, we have studied the adsorption of Xe and PTCDA on Ag(111) [Maurer *et al.*, 2015] as well as the adsorption of PTCDA on Au(111). These studies show that the inclusion of many-body effects in the vdW energy is of great importance to achieve quantitative predictions regarding the stability and properties of HIOS. The inclusion of MBD effects reduces the overbinding typically found in pairwise vdW-inclusive methods, yielding an improvement in the adsorption energies, geometries, and vibrational properties of molecules on surfaces. By using the MBD method, we also capture anisotropic polarization effects and demonstrate strong non-additive effects in the vdW energy of HIOS showing, for example, how these affect the properties of atoms, molecules, and nanostructures adsorbed on metal surfaces.

The challenge that remains for any vdW-inclusive method to model HIOS consists in including a simultaneous accurate description of localized and metallic states. The quantum harmonic oscillators in the MBD calculation have a non zero excitation gap and are initially localized. The coupling of the whole system however induces a delocalization of the polarizability which is significantly closer to the correct metallic response in comparison to a pairwise response. Furthermore, by using the screened vdW parameters generated for DFA+vdW^{surf} method, the initial response of the quantum harmonic oscillators in the MBD can be parametrized in order to serve as a good starting point to capture the response of the extended substrate [see Maurer *et al.*, 2015]. Even if these facts imply that the MBD method can capture many-body dispersion effects with reasonable accuracy in metallic systems, the challenge still consists in extending the method to

introduce both localized and delocalized oscillators for every atom. From this perspective, the question that remains is how to define the oscillators parameters directly from the electron density and its gradient [DiStasio Jr. *et al.*, 2014].

A potential approach to define certain regions in molecules and materials where the characteristics of electrons could be close to those usually defined as free electrons in solid-state physics is through the use of the electron localization functions, introduced initially by Becke and Edgecombe [1990] in the context of quantum-chemistry methods, and later by Savin *et al.* [1992] within KS-DFT. The electron localization function (ELF) was introduced as a measure of the probability of finding an electron in the neighborhood of another electron with the same spin. In this regard, the ELF is a tool created with the intention to serve as a descriptor of the chemical bond. In the case of solids, similar descriptors exist, known as localization and delocalization indices, with the intention of partitioning the space into regions of either localized or mobile electrons [Ponec, 2005, 2011; Baranov and Kohout, 2011]. In particular, Ayers *et al.* [2002] have given an interesting background to the original ELF in terms of the "thermodynamic" description of DFT. In this interpretation, a concept of local temperature is introduced as a result of the varying electronic kinetic density within an inhomogeneous system. The temperature in this interpretation measures the proximity of an electron pair. Therefore, a high local temperature for a given density is associated with strong correlated electrons [Ayers *et al.*, 2002]. These concepts seem attractive options to describe the localization and delocalization of electrons in a material within KS-DFT. However, these descriptors generally depend on the local kinetic energy density which cannot be uniquely defined. Furthermore, they usually depend not only on the electron density and its gradient but also on its Laplacian, which has no simple physical interpretation. Finally, it is clear that, even if there seems to be a relation between them, there is no straightforward equivalence between the concept of free electrons in solid-state physics and "localization" or "delocalization" in electron localization functions. This is, nevertheless, an interesting research venue that would also have potential applications beyond vdW interactions.

8.3 Treating realistic adsorption systems and the comparison between theory and experiment

Along with our interest in adsorption phenomena from a basic science perspective, we also aim to be able to describe and predict, from first principles, processes with technological relevance in which adsorption phenomena play an essential role (catalysis or organic electronics, for example). For this purpose, it is obvious that beyond achieving quantitative predictive level in model systems, we must also address realistic adsorption systems as well as understand surface processes under realistic pressure and temperature conditions. Taking catalysis as an example, Sabbe *et al.* [2012] mention the proper representation of the reactive surface and the treatment of coverage effects (at the electronic structure and mesoscopic level), among other aspects, as crucial. These include, for example, adsorption occurring at multifaceted surfaces or at substrates with the presence of dopant atoms or defects. The addition of first-principles thermodynamic considerations must also be taken into account as thermal effects can lead to restructured surfaces, kinetic effects on adatoms, and vibrational effects on larger (and more flexible) adsorbed molecules [Sabbe *et al.*, 2012].

It is also necessary to take into consideration that many experimental techniques to identify the structure and the energetics of adsorption systems, such as those mentioned in chapter 3, are based on probing the statistics of large adsorbed molecular ensembles, situation which can lead to inconsistent comparisons between DFT and experimental results. Therefore, a correct interpretation of experiments is of vital importance. This takes us full circle back to the introduction given to this dissertation in chapter 1, where we mention how the emergence of novel single-molecule experiments, together with state-of-the-art theoretical predictions, are part of the current context in adsorption studies in which the goals are those of accuracy, further understanding, and consistent comparison between theory and experiment [see also the discussion given by Liu *et al.*, 2014]. Our work has contributed to get closer to these goals and our current efforts are focused in the same direction.

Let us mention, for instance, that part of our ongoing research deals with the importance of coverage effects in adsorption systems as these reflect the complexity of comparing theory and experiment in realistic adsorption systems. To this effect we are currently extending our studies on the adsorption of a monolayer of PTCDA on Au(111). As we have addressed in section 7.4, the energies calculated with the PBE+vdW^{surf} method in this system reveal a dependence on the coverage of the monolayer independently of the reference state. Its importance lies in the comparison between theory and experiment. The TPD experiments for the adsorption of PTCDA on Au(111) have been performed in the limit of low coverage, that is, the adsorption energy of a single PTCDA molecule on Au(111). From this perspective, it is necessary to incorporate this fact in the atomistic adsorption model in order to make a consistent comparison between theory and experiment. Some difficulties are associated to a situation such as this. For example, the atomistic model of the adsorption system requires a larger unit cell, a surface slab with more layers, leading to the possibility of simulations which can become computationally expensive even for a method with a relative good balance between accuracy and efficiency such as DFT.

In relation to the study of molecular processes on imperfect surfaces, Camarillo-Cisneros *et al.* [2015] have studied the adsorption, diffusion, and desorption of benzene and naphthalene on a vicinal Cu(443) surface using the PBE+vdW^{surf} method, proposing a three-step mechanism for the dynamics of these processes. In accordance to their calculations, this mechanism consists in the migration of the molecules, upon strong adsorption on step edges at low temperature, from the step to the (111) terraces, where they can freely diffuse parallel to the step edge. The migration occurs at temperatures below the onset of desorption. Their calculations also show that there is a stronger vdW attraction between the hydrocarbons and the step edges of the Cu(443) surface in comparison to the Cu(111) surface, fact that can explain an increase in the desorption temperature for the Cu(443) observed in experiments. With this, they propose a more complex dynamical picture of the adsorption process in these systems than the one suggested from TPD experiments. From this perspective, the authors emphasize the need of time-resolved experiments to fully understand molecular adsorption on realistic surfaces at finite temperatures.

These examples show that a consistent comparison and feedback between theory and experiment are powerful tools, with the potential of leading joint efforts between theory and experiment, to achieve a deeper understanding of realistic adsorption processes with relevance in both fundamental science and technology.

8.4 Additional remarks concerning electronic-structure theory

Another potential challenge for an accurate description of HIOS is the self-interaction error present in semi-local xc functionals. This can lead to an inaccurate description of charge transfer and electronic level alignment between the adsorbate and the substrate [Liu *et al.*, 2014]. This issue can be solved by adding a fraction of exact exchange as done in hybrid functionals or, in a more general way, by employing orbital-dependent xc functionals [Kümmel and Kronik, 2006]. However, these approaches are still not general and many of them increase computational cost that can become prohibitive for larger systems. The issue at hand is that the screening properties of molecules and solids are rather different and characterized by distinct parameter ranges, leading to the need of a reliable description of the electronic structure not only of the substrate or the adsorbate but also of their coupling [Liu *et al.*, 2014].

An interesting research venue that is just starting to attract attention is the influence of vdW interactions on the electronic properties of molecules and extended systems. Due to the fact that the vdW energy typically represents only a tiny fraction of the total energy of a system [approximately 0.001% of the total energy, see Ferri *et al.*, 2015], the most widely used vdW-inclusive methods in KS-DFT approximate the vdW energy as a perturbation to the total energy which is only added *a posteriori*. That is, after a self-consistent solution of the KS equations has been found and the electronic density $n(\boldsymbol{r})$ is known, which is the case of the DFA+vdW and the DFA+vdW$^{\text{surf}}$ methods. Ferri *et al.* [2015] have recently reported a fully self-consistent implementation of the TS DFA+vdW method [Tkatchenko and Scheffler, 2009] which is achieved by adding the contribution of the electronic vdW potential to the xc potential to form the effective potential in the KS equations. This implementation is consequently also valid for the DFA+vdW$^{\text{surf}}$ method. The most interesting finding of Ferri *et al.* [2015], in our context, is that vdW interactions induce complex and sizable electronic charge redistributions at organic/metal interfaces and in the vicinity of metallic surfaces. These findings affect surface dipoles and work functions for inorganic substrates as well as charge transfer in HIOS [Ferri *et al.*, 2015], opening new interesting research venues in the context of HIOS.

In summary, we have contributed in this dissertation to the development of methods that are able to give a balanced description of adsorption structure and stability, while treating realistic adsorption systems. The development of such methods is still experiencing its early phases, but we expect that the inclusion of all relevant collective many-body effects should take surface science in general, and modeling of HIOS in particular, to an unprecedented level of accuracy, enabling us to achieve a truly predictive power in the simulation of the structure and stability of complex interfaces.

Bibliography

Al-Saidi, W. A., H. Feng, and K. A. Fichthorn (2012), "Adsorption of Polyvinylpyrrolidone on Ag Surfaces: Insight into a Structure-Directing Agent," Nano Letters **12**, 997.

Ambrosetti, A., D. Alfe, R. A. DiStasio Jr., and A. Tkatchenko (2014a), "Hard Numbers for Large Molecules: Toward Exact Energetics for Supramolecular Systems," The Journal of Physical Chemistry Letters **5**, 849.

Ambrosetti, A., A. M. Reilly, R. A. DiStasio Jr., and A. Tkatchenko (2014b), "Long-range correlation energy calculated from coupled atomic response functions," The Journal of Chemical Physics **140**, 18A508.

Ashcroft, N. W., and N. D. Mermin (1976), *Solid state physics* (Saunders College Publishing).

Atodiresei, N., V. Caciuc, P. Lazić, and S. Blügel (2009), "Chemical versus van der Waals Interaction: The Role of the Heteroatom in the Flat Absorption of Aromatic Molecules C_6H_6, C_5NH_5, and $C_4N_2H_4$ on the Cu(110) Surface," Physical Review Letters **102**, 136809.

Ayers, P. W., R. G. Parr, and A. Nagy (2002), "Local kinetic energy and local temperature in the density-functional theory of electronic structure," International Journal of Quantum Chemistry **90**, 309.

Baranov, A. I., and M. Kohout (2011), "Electron localization and delocalization indices for solids," Journal of Computational Chemistry **32**, 2064.

Bauer, O., G. Mercurio, M. Willenbockel, W. Reckien, C. H. Schmitz, B. Fiedler, S. Soubatch, T. Bredow, F. Tautz, and M. Sokolowski (2012), "Role of functional groups in surface bonding of planar π-conjugated molecules," Physical Review B **86**, 235431.

Becke, A. D., and K. E. Edgecombe (1990), "A simple measure of electron localization in atomic and molecular systems," The Journal of Chemical Physics **92**, 5397.

Blum, V., R. Gehrke, F. Hanke, P. Havu, V. Havu, X. Ren, K. Reuter, and M. Scheffler (2009), "Ab initio molecular simulations with numeric atom-centered orbitals," Computer Physics Communications **180**, 2175.

Böhringer, M., W.-D. Schneider, K. Glöckler, E. Umbach, and R. Berndt (1998), "Adsorption site determination of PTCDA on Ag(110) by manipulation of adatoms," Surface Science **419**, L95.

Braun, J., D. Fuhrmann, A. Siber, B. Gumhalter, and C. Wöll (1998), "Observation of a Zone-Center Gap in the Longitudinal Mode of an Adsorbate Overlayer: Xenon on Cu(111)," Physical Review Letters **80**, 125.

Brink, T., J. S. Murray, and P. Politzer (1993), "Polarizability and volume," The Journal of Chemical Physics **98**, 4305.

Bruch, L. W., M. W. Cole, and E. Zaremba (1997), *Physical Adsorption: Forces and Phenomena* (Oxford University Press).

Bruch, L. W., R. D. Diehl, and J. A. Venables (2007), "Progress in the measurement and modeling of physisorbed layers," Reviews of Modern Physics **79**, 1381.

Bruch, L. W., A. P. Graham, and J. P. Toennies (1998), "Vibrations of the commensurate monolayer solid Xe/Pt(111)," Molecular Physics **95**, 579.

Bruus, H., and K. Flensberg (2004), *Many-Body Quantum Theory in Condensed Matter Physics: An Introduction* (Oxford University Press).

Bürker, C., N. Ferri, A. Tkatchenko, A. Gerlach, J. Niederhausen, T. Hosokai, S. Duhm, J. Zegenhagen, N. Koch, and F. Schreiber (2013), "Exploring the bonding of large hydrocarbons on noble metals: Diindoperylene on Cu(111), Ag(111), and Au(111)," Physical Review B **87**, 165443.

Cahen, D., R. Naaman, and Z. Vager (2005), "The Cooperative Molecular Field Effect," Advanced Functional Materials **15**, 1571.

Camarillo-Cisneros, J., W. Liu, and A. Tkatchenko (2015), "Steps or Terraces? Dynamics of Aromatic Hydrocarbons Adsorbed at Vicinal Metal Surfaces," Physical Review Letters **115**, 086101.

Campbell, C. T., and J. R. V. Sellers (2012), "The Entropies of Adsorbed Molecules," Journal of the American Chemical Society **134**, 18109.

Campbell, C. T., and J. R. V. Sellers (2013), "Enthalpies and Entropies of Adsorption on Well-Defined Oxide Surfaces: Experimental Measurements," Chemical Reviews **113**, 4106.

Caragiu, M., T. Seyller, and R. D. Diehl (2002), "Dynamical LEED study of Pd(111) – $(\sqrt{3} \times \sqrt{3})R30^\circ$ – Xe," Physical Review B **66**, 195411.

Caragiu, M., T. Seyller, and R. D. Diehl (2003), "Adsorption geometry of Cu(110) – (12 × 2) – 14Xe," Surface Science **539**, 165.

Carrasco, J., W. Liu, A. Michaelides, and A. Tkatchenko (2014), "Insight into the description of van der Waals forces for benzene adsorption on transition metal (111) surfaces," The Journal of Chemical Physics **140**, 084704.

Casimir, H. B. G., and B. Polder (1948), "The Influence of Retardation on the London-van der Waals Forces," Physical Review **73**, 360.

Ceperley, D. M., and B. J. Alder (1980), "Ground State of the Electron Gas by a Stochastic Method," Physical Review Letters **45**, 566.

Chen, D.-L., W. A. Al-Saidi, and J. K. Johnson (2011), "Noble gases on metal surfaces: Insights on adsorption site preference," Physical Review B **84**, 241405(R).

Chen, D.-L., W. A. Al-Saidi, and J. K. Johnson (2012), "The role of van der Waals interactions in the adsorption of noble gases on metal surfaces," Journal of Physics: Condensed Matter **24**, 424211.

Choi, W. S., S. S. A. Seo, K. W. Kim, T. W. Noh, M. Y. Kim, and S. Shin (2006), "Dielectric constants of Ir, Ru, Pt, and IrO_2: Contributions from bound charges," Physical Review B **74**, 205117.

Chu, X., and A. Dalgarno (2004), "Linear response time-dependent density functional theory for van der Waals coefficients," The Journal of Chemical Physics **121**, 4083.

Cole, M. W., H.-Y. Kim, and M. Liebrecht (2012), "Van der Waals interactions: Accuracy of pair potential approximations," The Journal of Chemical Physics **137**, 194316.

Da Silva, J. L. F. (2002), *The Nature and Behavior of Rare-Gas Atoms on Metal Surfaces*, Ph.D. thesis (Fritz–Haber–Institut der MPG).

Da Silva, J. L. F., and C. Stampfl (2008), "Trends in adsorption of noble gases He, Ne, Ar, Kr, and Xe on Pd(111)$(\sqrt{3}\times\sqrt{3})R30°$: All-electron density-functional calculations," Physical Review B **77**, 045401.

Da Silva, J. L. F., C. Stampfl, and M. Scheffler (2003), "Adsorption of Xe Atoms on Metal Surfaces: New Insights from First-Principles Calculations," Physical Review Letters **90**, 066104.

Da Silva, J. L. F., C. Stampfl, and M. Scheffler (2005), "Xe adsorption on metal surfaces: First-principles investigations," Physical Review B **72**, 075424.

Diehl, R. D., T. Seyller, M. Caragiu, G. S. Leatherman, N. Ferralis, K. Pussi, P. Kaukasoina, and M. Lindroos (2004), "The adsorption sites of rare gases on metallic surfaces: a review," Journal of Physics: Condensed Matter **16**, S2839.

Dion, M. (2004), *Van der Waals Forces in Density Functional Theory*, Ph.D. thesis (Rutgers University).

Dion, M., H. Rydberg, E. Schröder, D. Langreth, and B. Lundqvist (2004), "Van der Waals Density Functional for General Geometries," Physical Review Letters **92**, 246401.

DiStasio Jr., R. A., V. V. Gobre, and A. Tkatchenko (2014), "Many-body van der Waals interactions in molecules and condensed matter," Journal of Physics: Condensed Matter **26**, 213202.

DiStasio Jr., R. A., O. A. von Lilienfeld, and A. Tkatchenko (2012), "Collective many-body van der Waals interactions in molecular system," Proceedings of the National Academy of Sciences of the United States of America **109**, 14791.

Dobson, J. F. (1991), "Interpretation of the Fermi hole curvature," The Journal of Chemical Physics **94**, 4328.

Dobson, J. F. (1994), *Quasi-local-density approximation for a van der Waals energy functional* in Topics in Condensed Matter Physics, edited by M. P. Das (Nova).

Dobson, J. F. (2006), *Dispersion (Van Der Waals Forces),* in Time-Dependent Density Functional Theory Lect. Notes Phys. 706, edited by M. A. L. Marques *et al.* (Springer).

Dobson, J. F., and T. Gould (2012), "Calculation of dispersion energies," Journal of Physics: Condensed Matter **24**, 073201.

Duhm, S., A. Gerlach, I. Salzmann, B. Bröker, R. L. Johnson, F. Schreiber, and N. Koch (2008), "PTCDA on Au(111), Ag(111) and Cu(111): Correlation of interface charge transfer to bonding distance," Organic Electronics **9**, 111.

Egger, D., V. G. Ruiz, W. A. Saidi, T. Bučko, A. Tkatchenko, and E. Zojer (2013), "Understanding Structure and Bonding of Multilayered MetalOrganic Nanostructures," The Journal of Physical Chemistry C **117**, 3055.

Ellis, J., A. P. Graham, and J. P. Toennies (1999), "Quasielastic Helium Atom Scattering from a Two-Dimensional Gas of Xe Atoms on Pt(111)," Phys. Rev. Lett. **82**, 5072.

Engel, E., and R. M. Dreizler (2011), *Density Functional Theory: An Advanced Course* (Springer).

Eshuis, H., J. E. Bates, and F. Furche (2012), "Electron correlation methods based on the random phase approximation," Theoretical Chemistry Accounts **131**, 1084.

Fenter, P., F. Schreiber, L. Zhou, P. Eisenberger, and S. Forrest (1997), "In situ studies of morphology, strain, and growth modes of a molecular organic thin film," Physical Review B **56**, 3046.

Ferri, N., R. A. DiStasio Jr., A. Ambrosetti, R. Car, and A. Tkatchenko (2015), "Electronic Properties of Molecules and Surfaces with a Self-Consistent Interatomic van der Waals Density Functional," Physical Review Letters **114**, 176802.

Fetter, A. L., and J. D. Walecka (1971), *Quantum Theory of many-particle systems* (McGraw Hill).

Fichthorn, K. A., and R. A. Miron (2002), "Thermal Desorption of Large Molecules from Solid Surfaces," Physical Review Letters **89**, 196103.

Forrest, S. R., and S. E. Thompson (2007), "Introduction: Organic Electronics and Optoelectronics," Chemical Reviews **107**, 923.

Fournier, N., C. Wagner, C. Weiss, R. Temirov, and F. S. Tautz (2011), "Force-controlled lifting of molecular wires," Physical Review B **84**, 035435.

Gerlach, A., S. Sellner, F. Schreiber, N. Koch, and J. Zegenhagen (2007), "Substrate-dependent bonding distances of PTCDA: A comparative x-ray standing-wave study on Cu(111) and Ag(111)," Physical Review B **75**, 045401.

Gibson, K. D., and S. J. Sibener (1988), "Inelastic helium scattering studies of ordered Ar, Kr, and Xe monolayers physisorbed on Ag(111): Dispersion curves, scattering cross sections, and excitation line shapes," The Journal of Chemical Physics **88**, 7862.

Glöckler, K., C. Seidel, A. Soukopp, M. Sokolowski, E. Umbach, M. Böhringer, R. Berndt, and W.-D. Schneider (1998), "Highly ordered structures and submolecular scanning tunnelling microscopy contrast of PTCDA and DM-PBDCI monolayers on Ag(111) and Ag(110)," Surface Science **405**, 1.

Grimme, S. (2004), "Accurate description of van der Waals complexes by density functional theory including empirical corrections," Journal of Computational Chemistry **25**, 1463.

Grimme, S. (2006), "Semiempirical GGA-type density functional constructed with a long-range dispersion correction," Journal of Computational Chemistry **27**, 1787.

Grimme, S., J. Antony, S. Ehrlich, and H. Krieg (2010), "A consistent and accurate *ab initio* parametrization of density functional dispersion correction (DFT-D) for the 94 elements H-Pu," The Journal of Chemical Physics **132**, 154104.

Groß, A. (2009), *Theoretical Surface Science: A Microscopic Perspective* (Springer).

Gross, E. K. U., and K. Burke (2006), *Basics,* in Time-Dependent Density Functional Theory Lect. Notes Phys. 706, edited by M. A. L. Marques *et al.* (Springer).

Gross, L., F. Mohn, N. Moll, and P. L. adn G. Meyer (2009), "The Chemical Structure of a Molecule Resolved by Atomic Force Microscopy," Science **325**, 1110.

Gunarsson, O., and B. I. Lundqvist (1976), "Exchange and correlation in atoms, molecules, and solids by the spin-density-functional formalism," Physical Review B **13**, 4274.

Hall, B., D. L. Mills, P. Zeppenfeld, K. Kern, U. Becher, and G. Comsa (1989), "Anharmonic damping in rare-gas multilayers," Physical Review B **40**, 6326.

Hamaker, H. C. (1937), "The London-van der Waals attraction between spherical particles," Physica **4**, 1058.

Harris, J., and R. O. Jones (1974), "The surface energy of a bounded electron gas," Journal of Physics F: Metal Physics **4**, 1170.

Hauschild, A., K. Karki, B. Cowie, M. Rohlfing, F. Tautz, and M. Sokolowski (2005), "Molecular Distortions and Chemical Bonding of a Large π-Conjugated Molecule on a Metal Surface," Physical Review Letters **94**, 036106.

Hauschild, A., R. Temirov, S. Soubatch, O. Bauer, A. Schöll, B. Cowie, and T.-L. Lee (2010), "Normal-incidence x-ray standing-wave determination of the adsorption geometry of PTCDA on Ag(111): Comparison of the ordered room-temperature and disordered low-temperature phases," Physical Review B **81**, 125432.

Henze, S. K. M., O. Bauer, T.-L. Lee, M. Sokolowski, and F. Tautz (2007), "Vertical bonding distances of PTCDA on Au(111) and Ag(111): Relation to the bonding type," Surface Science **601**, 1566.

Hilgers, G., M. Potthoff, N. Müller, , and U. Heinzmann (1995), "Structure investigations of Xe-adsorbate layers by spin-polarized low-energy electron diffraction II. ($\sqrt{3} \times \sqrt{3}$) R30°−Xe/Pd (111) and the dilute phase of Xe/Pd(111)," Surface Science **322**, 207.

Hirshfeld, F. L. (1977), "Bonded-atom fragments for describing molecular charge densities," Theoretica chimica acta **44**, 129.

Hohenberg, P., and W. Kohn (1964), "Inhomogeneous Electron Gas," Physical Review **136**, B864.

Ikonomov, J., O. Bauer, and M. Sokolowski (2008), "Highly ordered thin films of perylene-3,4,9,10-tetracarboxylic acid dianhydride (PTCDA) on Ag(100)," Surface Science **602**, 2061.

James, J., T. Steinhauser, D. Hoffmann, and B. Friedrich (2011), *One hundred years at the intersection of chemistry and physics: the Fritz Haber Institute of the Max Planck Society, 1911-2011* (De Gruyter).

Johnson, E. R., and A. D. Becke (2005), "A post-Hartree-Fock model of intermolecular interactions," The Journal of Chemical Physics **123**, 024101.

Jurečka, P., J. Šponer, J. Černỳ, and P. Hobza (2006), "Benchmark database of accurate (MP2 and CCSD(T) complete basis set limit) interaction energies of small model complexes, DNA base pairs, and amino acid pairs," Physical Chemistry Chemical Physics **8**, 1985.

Kaplan, I. G. (2006), *Intermolecular Interactions: Physical Picture, Computational Methods and Model Potentials* (John Wiley & Sons, Ltd).

Kilian, L., A. Hauschild, R. Temirov, S. Soubatch, A. Schöll, A. Bendounan, F. Reinert, T.-L. Lee, F. S. Tautz, M. Sokolowski, and E. Umbach (2008), "Role of Intermolecular Interactions on the Electronic and Geometric Structure of a Large π-Conjugated Molecule Adsorbed on a Metal Surface," Physical Review Letters **100**, 136103.

Kilian, L., E. Umbach, and M. Sokolowski (2004), "Molecular beam epitaxy of organic films investigated by high resolution low energy electron diffraction (SPA-LEED): 3,4,9,10-perylenetetracarboxylicacid-dianhydride (PTCDA) on Ag(111)," Surface Science **573**, 359.

Kilian, L., E. Umbach, and M. Sokolowski (2006), "A refined structural analysis of the PTCDA monolayer on the reconstructed Au(111) surface–Rigid or distorted carpet?," Surface Science **600**, 2633.

King, D. A. (1975), "Thermal desorption from metal surfaces: A review," Surface Science **47**, 384.

King, H. W. (2014-2015), *Crystal Structures and Lattice Parameters of Allotropes of the Elements,* in CRC Handbook of Chemistry and Physics, edited by W. M. Haynes *et al.* (http://www.hbcpnetbase.com).

Klimeš, J., D. R. Bowler, and A. Michaelides (2010), "Chemical accuracy for the van der Waals density functional," Journal of Physics: Condensed Matter **22**, 022201.

Klimeš, J., D. R. Bowler, and A. Michaelides (2011), "Van der Waals density functionals applied to solids," Physical Review B **83**, 195131.

Klimeš, J., D. R. Bowler, and A. Michaelides (2012), "Perspective: Advances and challenges in treating van der Waals dispersion forces in density functional theory," The Journal of Chemical Physics **137**, 120901.

Kohanoff, J. (2006), *Electronic Structure Calculations For Solids and Molecules: Theory and Computational Methods* (Cambridge University Press).

Kohn, W. (1999), "Nobel Lecture: Electronic structure of matter-wave functions and density functionals," Reviews of Modern Physics **71**, 1253.

Kohn, W., and L. J. Sham (1965), "Self-Consistent Equations Including Exchange and Correlation Effects," Physical Review **14**, A1133.

Kraft, A., R. Temirov, S. K. M. Henze, S. Soubatch, M. Rohlfing, and F. S. Tautz (2006), "Lateral adsorption geometry and site-specific electronic structure of a large organic chemisorbate on a metal surface," Physical Review B **74**, 041402(R).

Kronik, L., and N. Koch (2010), "Electronic Properties of Organic-Based Interfaces," MRS Bulletin **35**, 417.

Kümmel, S., and L. Kronik (2006), "Orbital-dependent density functionals: Theory and applications," Reviews of Modern Physics **80**, 3.

Langreth, D. C., M. Dion, H. Rydberg, E. Schröder, P. Hyldgaard, and B. Lundqvist (2005), "Van der Waals density functional theory with applications," International Journal of Quantum Chemistry **101**, 599.

Langreth, D. C., and J. P. Perdew (1975), "The exchange-correlation energy of a metallic surface," Solid State Communications **17**, 1425.

Lazić, P., V. Caciuc, N. Atodiresei, M. Callsen, and S. Blügel (2014), "First-principles insights into the electronic and magnetic structure of hybrid organic-metal interfaces," Journal of Physics: Condensed Matter **26**, 263001.

Lee, K., E. D. Murray, L. Kong, B. I. Lundqvist, and D. C. Langreth (2010), "Higher-accuracy van der Waals density functional," Physical Review B **82**, 081101.

Lifshitz, E. M. (1956), "The Theory of Molecular Attractive Forces between Solids," Soviet Physics-Journal of Experimental and Theoretical Physics **2**, 73, original version (russian): ZhETF **29**, 94, (1956).

Liu, W., J. Carrasco, B. Santra, A. Michaelides, M. Scheffler, and A. Tkatchenko (2012), "Benzene adsorbed on metals: Concerted effect of covalency and van der Waals bonding," Physical Review B **86**, 245405.

Liu, W., S. N. Filimonov, J. Carrasco, and A. Tkatchenko (2013a), "Molecular switches from benzene derivatives adsorbed on metal surfaces," Nature Communications **4**, 2569.

Liu, W., V. G. Ruiz, G.-X. Zhang, B. Santra, X. Ren, M. Scheffler, and A. Tkatchenko (2013b), "Structure and energetics of benzene adsorbed on transition-metal surfaces: density-functional theory with van der Waals interactions including collective substrate response," New Journal of Physics **15**, 053046.

Liu, W., A. Tkatchenko, and M. Scheffler (2014), "Modeling Adsorption and Reactions of Organic Molecules at Metal Surfaces," Accounts of Chemical Research **47**, 3369.

London, F. (1930), "On some properties and applications of molecular forces," Zeitschrift für Physikalische Chemie (Leipzig) **B11**, 222, found in *Quantum Chemistry: Classic Scientific Papers* (2000), edited by H. Hettema (World Scientific).

London, F. (1937), "The general theory of molecular forces," Transactions of the Faraday Society **33**, 8.

London, F., and M. Polanyi (1930), "Über die atomtheoretische Deutung der Adsorptionskräfte," Naturwissenschaften **18**, 1099.

Lu, D., H.-V. Nguyen, and G. Galli (2010), "Power series expansion of the random phase approximation correlation energy: The role of the third- and higher-order contributions," The Journal of Chemical Physics **133**, 154110.

Lüder, J., B. Sanyal, O. Eriksson, C. Puglia, and B. Brena (2014), "Comparison of van der Waals corrected and sparse-matter density functionals for the metal-free phthalocyanine/gold interface," Physical Review B **89**, 045416.

Maggs, A. C., and N. W. Ashcroft (1987), "Electronic fluctuation and cohesion in metals," Physical Review Letters **59**, 113.

Mannsfeld, S., M. Toerker, T. Schmitz-Hübsch, F. Sellam, T. Fritz, and K. Leo (2001), "Combined LEED and STM study of PTCDA growth on reconstructed Au(111) and Au(100) single crystals," Organic Electronics **2**, 121.

Marom, N., A. Tkatchenko, M. Rossi, V. V. Gobre, O. Hod, M. Scheffler, and L. Kronik (2011), "Dispersion Interactions with Density-Functional Theory: Benchmarking Semiempirical and Interatomic Pairwise Corrected Density Functionals," Journal of Chemical Theory and Computation **7**, 3944.

Martin, R. M. (2004), *Electronic Structure: Basic Theory and Practical Methods* (Cambridge University Press).

Maurer, R. J., V. G. Ruiz, and A. Tkatchenko (2015), "Many-body dispersion effects in the binding of adsorbates on metal surfaces," The Journal of Chemical Physics **143**, 102808.

McLachlan, A. D. (1963), "Retarded Dispersion Forces Between Molecules," Proceedings of the Royal Society A **271**, 387.

McNellis, E. R. (2010), *First-Principles Modeling of Molecular Switches at Surfaces*, Ph.D. thesis (Fritz-Haber-Institut der MPG).

Mercurio, G. (2012), *Study of Molecule-Metal Interfaces by Means of the Normal Incidence X-ray Standing Wave Technique*, Ph.D. thesis (Forschungszentrum Jülich).

Mercurio, G., O. Bauer, M. Willenbockel, N. Fairley, W. Reckien, C. H. Schmitz, B. Fiedler, S. Soubatch, T. Bredow, M. Sokolowski, and F. Tautz (2013a), "Adsorption height determination of nonequivalent C and O species of PTCDA on Ag(110) using x-ray standing waves," Physical Review B **87**, 045421.

Mercurio, G., R. J. Maurer, S. Hagen, F. Leyssner, J. Meyer, P. Tegeder, S. Soubatch, K. Reuter, and F. S. Tautz (2014), "X-ray standing wave simulations based on Fourier vector analysis as a method to retrieve complex molecular adsorption geometries," Frontiers in Physics **2**, 2.

Mercurio, G., R. J. Maurer, W. Liu, S. Hagen, F. Leyssner, P. Tegeder, J. Meyer, A. Tkatchenko, S. Soubatch, K. Reuter, and F. S. Tautz (2013b), "Quantification of finite-temperature effects on adsorption geometries of π-conjugated molecules: Azobenzene/Ag(111)," Physical Review B **88**, 035421.

Mercurio, G., E. McNellis, I. Martin, S. Hagen, F. Leyssner, S. Soubatch, J. Meyer, M. Wolf, P. Tegeder, F. Tautz, and K. Reuter (2010), "Structure and Energetics of Azobenzene on Ag(111): Benchmarking Semiempirical Dispersion Correction Approaches," Physical Review Letters **104**, 036102.

Momma, K., and F. Izumi (2011), "*VESTA 3* for three-dimensional visualization of crystal, volumetric and morphology data," Journal of Applied Crystallography **44**, 1272.

Mon, K. K., N. W. Ashcroft, and G. V. Chester (1979), "Core polarization and the structure of simple metals," Physical Review B **19**, 5103.

Monkhorst, H. J., and J. D. Pack (1976), "Special points for Brillouin-zone integrations," Physical Review B **13**, 5188.

Müller, J. E. (1990), "Interaction of the Pt(111) surface with adsorbed Xe atoms," Physical Review Letters **65**, 3021.

Mura, M., A. Gulans, T. Thonhauser, and L. Kantorovich (2010), "Role of van der Waals interaction in forming molecule-metal junctions: flat organic molecules on the Au(111) surface ," Physical Chemistry Chemical Physics **12**, 4759.

Narloch, B., and D. Menzel (1997), "Structural evidence for chemical contributions in the bonding of the heavy rare gases on a close-packed transition metal surface: Xe and Kr on Ru(001)," Chemical Physics Letters **270**, 163.

Nguyen, H.-V. (2008), *Efficient calculation of RPA correlation energy in the Adiabatic Connection Fluctuation-Dissipation Theory*, Ph.D. thesis (Scuola Internazionale Superiore di Studi Avanzati, SISSA).

Nguyen, M.-T., C. A. Pignedoli, M. Treier, R. Fasel, and D. Passerone (2010), "The role of van der Waals interactions in surface-supported supramolecular networks," Physical Chemistry Chemical Physics **12**, 992.

Olsen, T., J. Yan, J. J. Mortensen, and K. S. Thygesen (2011), "Dispersive and Covalent Interactions between Graphene and Metal Surfaces from the Random Phase Approximation," Physical Review Letters **107**, 156401.

Parr, R. G., and W. Yang (1989), *Density-Functional Theory of Atoms and Molecules* (Oxford University Press).

Patil, S. H., K. T. Tang, and J. P. Toennies (2002), "Damping functions for the pairwise sum model of the atom-surface potential," The Journal of Chemical Physics **116**, 8118.

Perdew, J. P., K. Burke, and M. Ernzerhof (1996), "Generalized Gradient Approximation Made Simple," Physical Review Letters **77**, 3865.

Perdew, J. P., and K. Schmidt (1994), in *Density Functional Theory and Its Application to Materials* (American Institute of Physics).

Perdew, J. P., and Y. Wang (1992), "Accurate and simple analytic representation of the electron-gas correlation energy," Physical Review B **45**, 13244.

Persson, B. N. J., and E. Zaremba (1984), "Reference-plane position for the atom-surface van der Waals interaction," Physical Review B **30**, 5669.

Polanyi, M. (1932), "Section III.-Theories of the adsorption of gases. A general survey and some additional remarks. Introductory paper to section III," Transactions of the Faraday Society **28**, 316.

Polanyi, M. (1963), "The Potential Theory of Adsorption," Science **141**, 1010.

Ponec, R. (2005), "Chemical bonding in solids. On the generalization of the concept of bond order and valence for infinite periodical structures," Theoretical Chemistry Accounts **114**, 208.

Ponec, R. (2011), "Electron localization and delocalization indices for solids," Journal of Computational Chemistry **32**, 3114.

Potthoff, M., G. Hilgers, N. Müller, U. Heinzmann, L. Haunert, J. Braun, and G. Borstel (1995), "Structure investigations of Xe-adsorbate layers by spin-polarized low-energy electron diffraction I. (3×33) R30°−Xe/Pt (111)," Surface Science **322**, 193.

Pouthier, V., C. Ramseyer, C. Girardet, V. Diercks, R. Halmer, R. David, and P. Zeppenfeld (1998), "Structure of Xe adsorbed on the highly corrugated Cu(110) – (2×1)O surface," Physical Review B **57**, 13149.

Ramseyer, C., V. Pouthier, C. Girardet, P. Zeppenfeld, M. Büchel, V. Diercks, and G. Comsa (1997), "Influence of mode polarizations on the inelastic He-scattering spectrum: High-order commensurate Xe monolayer adsorbed on Cu(110)," Physical Review B **55**, 13203.

Redhead, P. A. (1962), "Thermal desorption of gases," Vacuum **12**, 201.

Rehr, J., E. Zaremba, and W. Kohn (1975), "Van der Waals forces in the noble metals," Physical Review B **12**, 2062.

Ren, X., P. Rinke, V. Blum, J. Wieferink, A. Tkatchenko, A. Sanfilippo, K. Reuter, and M. Scheffler (2012a), "Resolution-of-identity approach to Hartree-Fock, hybrid density functionals, RPA, MP2 and GW with numeric atom-centered orbital basis functions," New Journal of Physics **14**, 053020.

Ren, X., P. Rinke, C. Joas, and M. Scheffler (2012b), "Random-phase approximation and its applications in computational chemistry and materials science," Journal of Materials Science **47**, 7447.

Richardson, D. D., and J. Mahanty (1977), "Van der Waals contribution to the binding energy of noble metals," Journal of Physics C: Solid State Physics **10**, 3971.

Rohlfing, M., and T. Bredow (2008), "Binding Energy of Adsorbates on a Noble-Metal Surface: Exchange and Correlation Effects," Physical Review Letters **101**, 266106.

Rohlfing, M., R. Temirov, and F. S. Tautz (2007), "Adsorption structure and scanning tunneling data of a prototype organic-inorganic interface: PTCDA on Ag(111)," Physical Review B **76**, 115421.

Romaner, L., D. Nabok, P. Puschnig, E. Zojer, and C. Ambrosch-Draxl (2009), "Theoretical study of PTCDA adsorbed on the coinage metal surfaces, Ag(111), Au(111) and Cu(111)," New Journal of Physics **11**, 053010.

Ruiz, V. G., W. Liu, and A. Tkatchenko (2016), "Density-functional theory with screened van der Waals interactions applied to atomic and molecular adsorbates on close-packed and non-close-packed surfaces," Physical Review B **93**, 035118.

Ruiz, V. G., W. Liu, E. Zojer, M. Scheffler, and A. Tkatchenko (2012), "Density-Functional Theory with Screened van der Waals Interactions for the Modeling of Hybrid Inorganic-Organic Systems," Physical Review Letters **108**, 146103.

Rydberg, H., B. Lundqvist, D. C. Langreth, and M. Dion (2000), "Van der Waals Density Functional for Layered Structures," Physical Review B **62**, 6997.

Sabbe, M. K., M.-F. Reyniers, and K. Reuter (2012), "First-principles kinetic modeling in heterogeneous catalysis: an industrial perspective on best-practice, gaps and needs," Catalysis Science & Technology **2**, 2010.

Savin, A., O. Jepsen, J. Flad, O. H. Andersen, H. Preuss, and H. G. von Schnering (1992), "A New Look at Electron Localization," Angewandte Chemie International Edition in English **31**, 187.

Schmitz-Hübsch, T. T., T. Fritz, F. Sellam, , R. Staub, and K. Leo (1997), "Epitaxial growth of 3,4,9,10-perylene-tetracarboxylic-dianhydride on Au(111): A STM and RHEED study," Physical Review B **55**, 7972.

Schuler, B., W. Liu, A. Tkatchenko, N. Moll, G. Meyer, A. Mistry, D. Fox, and L. Gross (2013), "Adsorption Geometry Determination of Single Molecules by Atomic Force Microscopy," Physical Review Letters **111**, 106103.

Seyller, T., M. Caragiu, R. D. Diehl, P. Kaukasoina, and M. Lindroos (1998), "Observation of top-site adsorption for Xe on Cu(111)," Chemical Physics Letters **291**, 567.

Seyller, T., M. Caragiu, R. D. Diehl, P. Kaukasoina, and M. Lindroos (1999), "Dynamical LEED study of Pt(111) $-(\sqrt{3}\times\sqrt{3})R30^\circ-$Xe," Physical Review B **60**, 11084.

Stadler, C., S. Hansen, A. Schöell, T.-L. Lee, J. Zegenhagen, C. Kumpf, and E. Umbach (2007), "Molecular distortion of NTCDA upon adsorption on Ag(111): a normal incidence x-ray standing wave study," New Journal of Physics **9**, 50.

Stadtmüller, B. (2013), *Study of intermolecular interactions in hetero-organic thin films*, Ph.D. thesis (Forschungszentrum Jülich).

Stahl, U., D. Gador, A. Soukopp, R. Fink, and E. Umbach (1998), "Coverage-dependent superstructures in chemisorbed NTCDA monolayers: a combined LEED and STM study," Surface Science **414**, 423.

Stanzel, J., W. Weigand, L. Kilian, H. Meyerheim, C. Kumpf, and E. Umbach (2004), "Chemisorption of NTCDA on Ag(111): a NIXSW study including non-dipolar and electron-stimulated effects," Surface Science **571**, L311.

Stone, A. J. (2013), *The Theory of Intermolecular Forces* (Oxford University Press).

Stradi, D., S. Barja, C. Díaz, M. Garnica, B. Borca, J. J. Hinarejos, D. Sánchez-Portal, M. Alcamí, A. Arnau, A. L. Vázquez de Parga, R. Miranda, and F. Martín (2011), "Role of Dispersion Forces in the Structure of Graphene Monolayers on Ru Surfaces," Physical Review Letters **106**, 186102.

Stremlau, S. (2015), *High Resolution Vibrational Spectroscopy of Functional Organic Molecules at Surfaces*, Ph.D. thesis (Freie Universität Berlin).

Szabo, A., and N. S. Ostlund (1996), *Modern Quantum Chemistry: Introduction to Advanced Electronic Structure Theory* (Dover).

Tait, S. L., Z. Dohnálek, C. T. Campbell, and B. D. Kay (2005), "*n*-alkanes on MgO(100). II. Chain length dependence of kinetic desorption parameters for small *n*-alkanes," The Journal of Chemical Physics **122**, 164708.

Tang, K. T. (1969), "Dynamic Polarizabilities and van der Waals Coefficients," Physical Review **177**, 108.

Tang, K. T., and M. Karplus (1968), "Padé-Approximant Calculation of the Nonretarded van der Waals Coefficients for Two and Three Helium Atoms," Physical Review **171**, 70.

Tao, J., J. P. Perdew, and A. Ruzsinszky (2010), "Long-range van der Waals attraction and alkali-metal lattice constants," Physical Review B **81**, 233102.

Tautz, F. S. (2007), "Structure and bonding of large aromatic molecules on noble metal surfaces: The example of PTCDA," Progress in Surface Science **82**, 479.

Tkatchenko, A., A. Ambrosetti, and R. DiStasio Jr. (2013), "Interatomic methods for the dispersion energy derived from the adiabatic connection fluctuation-dissipation theorem," The Journal of Chemical Physics **138**, 074106.

Tkatchenko, A., R. A. DiStasio Jr., R. Car, and M. Scheffler (2012), "Accurate and Efficient Method for Many-Body van der Waals Interactions," Physical Review Letters **108**, 236402.

Tkatchenko, A., L. Romaner, O. T. Hoffmann, E. Zojer, C. Ambrosch-Draxl, and M. Scheffler (2010), "Van der Waals Interactions Between Organic Adsorbates and at Organic/Inorganic Interfaces," MRS Bulletin **35**, 435.

Tkatchenko, A., and M. Scheffler (2009), "Accurate Molecular Van Der Waals Interactions from Ground-State Electron Density and Free-Atom Reference Data," Physical Review Letters **102**, 073005.

Tonigold, K., and A. Gross (2010), "Adsorption of small aromatic molecules on the (111) surfaces of noble metals: A density functional theory study with semiempirical corrections for dispersion effects," The Journal of Chemical Physics **132**, 224701.

van Lenthe, J. H., S. Faas, and J. G. Snijders (2000), "Gradients in the ab initio scalar zeroth-order regular approximation (ZORA) approach," Chemical Physics Letters **328**, 107.

van Ruitenbeek, J. (2012), "Metal/molecule interfaces: Dispersion forces unveiled," Nature Materials **11**, 834.

Vidali, G., G. Ihm, H.-Y. Kim, and M. W. Cole (1991), "Potentials of physical adsorption," Surface Science Reports **12**, 135.

Wagner, C., N. Fournier, V. G. Ruiz, C. Li, K. Müllen, M. Rohlfing, A. Tkatchenko, R. Temirov, and F. S. Tautz (2014), "Non-additivity of molecule-surface van der Waals potentials from force measurements," Nature Communications **5**, 5568.

Wagner, C., N. Fournier, F. S. Tautz, and R. Temirov (2012), "Measurement of the Binding Energies of the Organic-Metal Perylene-Teracarboxylic-Dianhydride/Au(111) Bonds by Molecular Manipulation Using an Atomic Force Microscope," Physical Review Letters **109**, 076102.

Wagner, C., and R. Temirov (2015), "Tunnelling junctions with additional degrees of freedom: An extended toolbox of scanning probe microscopy," Progress in Surface Science **90**, 194.

Wagner, T., A. Bannani, C. Bobisch, H. Karacuban, and R. Möller (2007), "The initial growth of PTCDA on Cu(111) studied by STM," Journal of Physics: Condensed Matter **19**, 056009.

Werner, W. S. M., K. Glantschnig, and C. Ambrosch-Draxl (2009), "Optical Constants and Inelastic Electron-Scattering Data for 17 Elemental Metals," Journal of Physical and Chemical Reference Data **38**, 1013.

Widdra, W., P. Trischberger, W. Frieß, D. Menzel, S. H. Payne, and H. J. Kreuzer (1998), "Rare-gas thermal desorption from flat and stepped platinum surfaces: Lateral interactions and the influence of dimensionality," Physical Review B **57**, 4111.

Windt, D. L., W. C. Cash, Jr., M. Scott, P. Arendt, B. Newman, R. F. Fisher, and A. B. Swartzlander (1988), "Optical constants for thin films of Ti, Zr, Nb, Mo, Ru, Rh, Pd, Ag, Hf, Ta, W, Re, Ir, Os, Pt, and Au from 24 Å to 1216 Å," Applied Optics **27**, 246.

Woodruff, D. P. (2005), "Surface structure determination using x-ray standing waves," Reports on Progress in Physics **68**, 743.

Woods, L. M., D. A. R. Dalvit, A. Tkatchenko, P. Rodriguez-Lopez, A. W. Rodriguez, and R. Podgornik (2015), "A materials perspective on casimir and van der waals interactions," ArXiv e-prints arXiv:1509.03338 [cond-mat.mtrl-sci] .

Zaremba, E., and W. Kohn (1976), "Van der Waals interaction between an atom and a solid surface," Physical Review B **13**, 2270.

Zegenhagen, J. (1993), "Surface structure determination with X-ray standing waves," Surface Science Reports **18**, 199.

Zeppenfeld, P., M. Büchel, R. David, G. Comsa, C. Ramseyer, and C. Girardet (1994), "Effect of the structural anisotropy and lateral strain on the surface phonons of monolayer xenon on Cu(110)," Physical Review B **50**, 14667.

Zhang, G.-X. (2014), *Understanding the role of van der Waals forces in solids from first principles*, Ph.D. thesis (Fritz-Haber-Institut der MPG).

Zhang, G.-X., A. Tkatchenko, J. Paier, H. Appel, and M. Scheffler (2011), "van der Waals Interactions in Ionic and Semiconductor Solids," Physical Review Letters **107**, 245501.

Zhang, Y., and W. Yang (1998), "Comment on Generalized Gradient Approximation Made Simple," Physical Review Letters **80**, 890.

Zhu, J. F., H. Ellmer, H. Malissa, T. Brandstetter, D. Semrad, and P. Zeppenfeld (2003), "Low-temperature phases of Xe on Pd(111)," Physical Review B **68**, 045406.

Ziroff, J., P. Gold, A. Bendounan, F. Forster, and F. Reinert (2009), "Adsorption energy and geometry of physisorbed organic molecules on Au(111) probed by surface-state photoemission," Surface Science **603**, 354.

Zou, Y., L. Kilian, A. Schöll, T. Schmidt, R. Fink, and E. Umbach (2006), "Chemical bonding of PTCDA on Ag surfaces and the formation of interface states," Surface Science **600**, 1240.